AD NUMBER

AD875378

LIMITATION CHANGES

TO:

Approved for public release; distribution is unlimited. Document partially illegible.

FROM:

**Distribution authorized to U.S. Gov't. agencies and their contractors;
Administrative/Operational Use; 15 JAN 1970.
Other requests shall be referred to Naval Electronics Lab., San Diego, CA. Document partially illegible.**

AUTHORITY

NELC ltr 22 Aug 1974

PROCEEDINGS OF THE CONFORMAL-ARRAY ANTENNA CONFERENCE

Sponsored by
NAVAL ELECTRONICS LABORATORY CENTER
and
NAVAL SHIP SYSTEMS COMMAND

Held at
NAVAL ELECTRONICS LABORATORY CENTER
San Diego, California 92152

February 1970

caa

CONTENTS

caa

IV. CIRCULAR-ARRAY APPLICATIONS

V. RELATED TECHNIQUES

CONTENTS (Continued)

caa

RECENT DEVELOPMENTS IN CIRCULAR AND CYLINDRICAL-ARRAY ANTENNAS

By J. H. Provencher

Naval Electronics Laboratory Center
San Diego, California 92152

Considerable interest in circular and cylindrical arrays has arisen in recent years, and extensions of planar-array technology to curved-aperture antennas have been demonstrated. For some applications, the use of the circular array has some advantages, especially where single rings are used to produce a fan beam in the vertical plane. In contrast to the linear or planar array, the radiated beam in the azimuthal plane of the circular array does not change with scan angle. In general, the amplitude and phase distributions required to produce given beam shapes for the circularly symmetric arrays are more complicated than those required for linear arrays, but the advent of the high-speed digital computer has eased the calculation of these distributions. The data hand-over problems generally related to the four-sided planar arrays are reduced for the circular and cylindrical arrays for the azimuth plane.

Other characteristics which are not obvious but which have been verified by experiment are:

1. Mutual interaction between adjacent antenna elements is reduced because of the curvature of the array.

2. Antenna input impedance for all azimuth beam positions is constant for any given elevation angle.

3. Element spacing restrictions are not so severe as for scanned planar arrays.

The elevation scanning properties of a large circular cylindrical array have not been fully investigated. Experimental arrays are being studied at NELC to verify predicted data. An alternate approach is to use the conical configuration to extend the high angular coverage. This approach also is being examined at NELC and some of the preliminary results obtained will be given here.

For some applications it is desirable to split the array aperture so that different parts of the complete array can be placed at widely separated positions on the ship. The circular array does not lend itself easily to this kind of separation. The technique is indeed possible with a circular array, but more radiating elements are required because of the step-scan beam steering which is used and this usually increases the overall array cost. The following discussions assume that the array aperture will be located at a single position on the ship.

The characteristic mentioned in paragraph 3 above has some implications involving the number of radiating elements required to form the radiated beam. In figure 1 the circular geometry is compared with the geometry of a four-sided linear configuration. Each array has the same number of elements and subtends the same angle. Since the limitation imposed upon the interelement spacing by scanning in linear arrays is not present in the circular array, the element spacing in an arc array can be increased. A maximum spacing of about 0.6 wavelength is required for linear arrays which scan to angles of 45° in order to suppress the grating lobes. The two arrays shown in the figure yield radiation patterns having similar characteristics. Each produces the same sidelobe level and beamwidth, has the same number of elements, and uses only 40 active elements. A major difference is in the wide-angle sidelobe structure; the arc array pattern contains energy in far-out sidelobes (fig. 2). This energy can be substantially lessened by reducing the element spacing, radius of curvature, and active sector.

In the arrays under discussion, now let us:

1. Increase the number of active elements for the arc array.

2. Increase the active sector (shaded region in fig. 3).

3. Decrease the element spacing and radius (fig. 3).

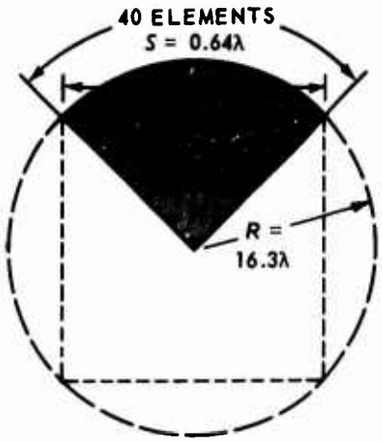

UNIFORM DISTRIB.	LINEAR	ARC
BW	2.15° (3.01°)	2.20°
SIDELOBE	-13.5 dB	-13.5 dB
GRATING LOBE	NONE	-23.4 dB AT 104°
TOTAL ELEMENTS	160	160

Figure 1. Comparison of linear and arc array – equal elements.

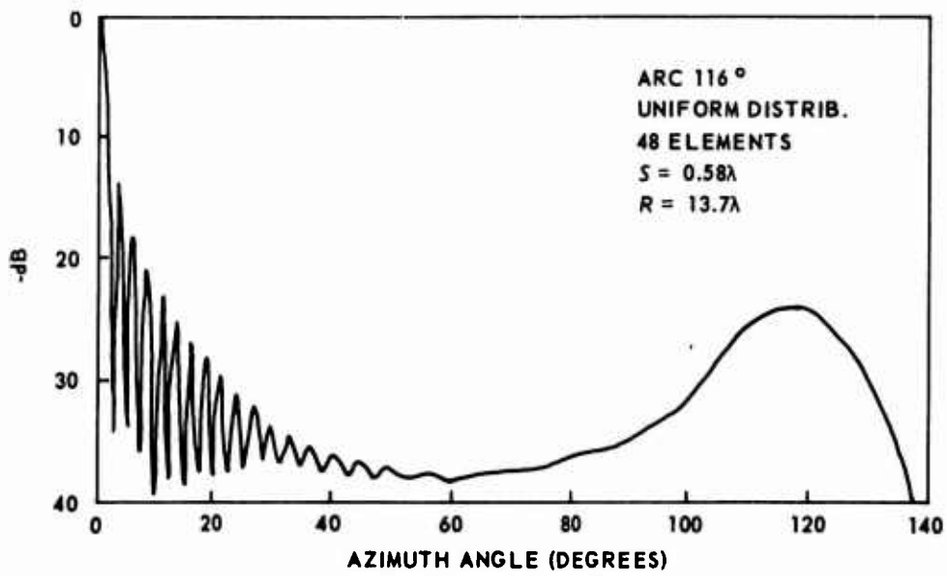

Figure 2. Radiation pattern of circular arc array.

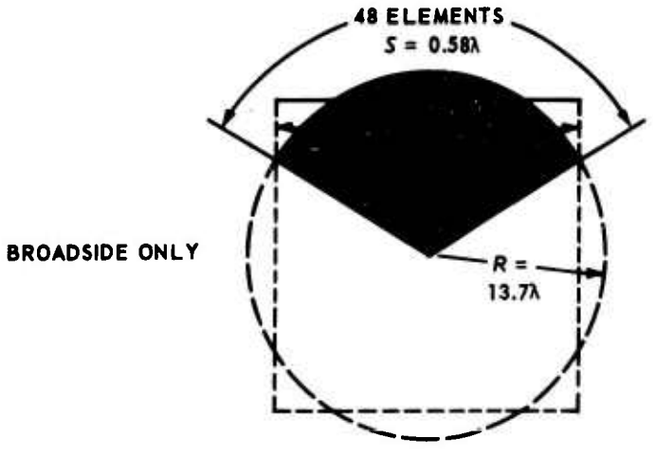

UNIFORM DISTRIB.	LINEAR	ARC
BW	215° (3.01°)	2.19°
SIDELOBE	-13.5 dB	-13.5 dB
GRATING LOBE	NONE	24.1 dB AT 118°
TOTAL ELEMENTS	160	150

Figure 3. Comparison of linear and arc array – unequal elements.

We find that the total number of elements of the ring array is now 150, while the four-sided planar configuration still contains 160 elements. This reduction in the number of total elements has been achieved while essentially maintaining the same radiation pattern characteristics as given in figure 2. All of these conditions assume that the beam of the linear array is at the broadside position. When the beam is scanned to an angle other than broadside, the beam broadens and the sidelobes increase. The number given in parentheses in figures 1 and 3 is the -3 dB beamwidth of the linear array patterns when scanned to an angle of 45°. The pattern of the ring array at all scan angles is the same.

The circular cylinder and the four-sided planar configuration with vertical sides fall into the general category of cylindrical, and can be made up by stacking the arrays previously discussed. Neither of these structures is optimum from the standpoint of vertical scanning, although the circular cylinder is superior for azimuthal scan. For the circular cylindrical array with an element spacing of 0.58 wavelength, the total number of radiating elements for a surface array of 40 elements in height is 6000. The radius is 13.7 wavelengths and the radiating aperture is on the order of 116° in azimuth. The total number of elements for a planar array of the same size and element spacing is 6400, with each planar face about 24 wavelengths square. If the spacing of the cylindrical array is increased to 0.64 wavelength in azimuth, then 5400 radiating elements are required to maintain the same beamwidth and sidelobe level. If a three-sided planar configuration is used, then the element spacing must be reduced in order to satisfy the grating lobe conditions for a 60° scan angle requirement. The total number of elements is 5400 and additional beam broadening will occur because of the larger scan angle.

Figures 4 and 5 are comparisons of radiation patterns from cylindrical and conical structures. The cone angle was 30°. The distribution used in both cases was Chebyshev for -30 dB sidelobes and cophasal. Patterns are given for main beam pointing angles of 0° and 60° above the horizontal. Two cuts are given for each beam position: an elevation

cut at constant azimuth angle and an azimuth cut with constant elevation angle. The elevation patterns indicate that the conical-array geometry has the capability of maintaining good patterns at higher elevation angles with only slight degradation in the horizontal plane. The sidelobe structure for the conical array azimuth patterns show some deviation from the patterns obtained from the selected Chebyshev distribution. This follows since both structures can be considered a collection of linear arrays phased in such a manner as to add constructively in the main beam direction. It is well known that a linear array forms a fan beam on a cone of constant angle to its axis. For the cylindrical array, all of the individual arrays have their axes aligned such that the "radiation cones" from all arrays coincide. The azimuth sidelobes of the cylinder are thus formed along this cone. This is not true for the conical array, since its constituent array axes are not aligned. The cophasal distribution is such that the "radiation cones" from all subarrays pass through the main beam position. This means that the sidelobe energy for the conical array is not concentrated as in the cylindrical array, but is "smeared out" over a larger region. For this reason, azimuth cuts of conical-array radiation patterns do not yield a satisfactory evaluation of the sidelobe structure. Techniques for experimental evaluation of the patterns are being investigated.

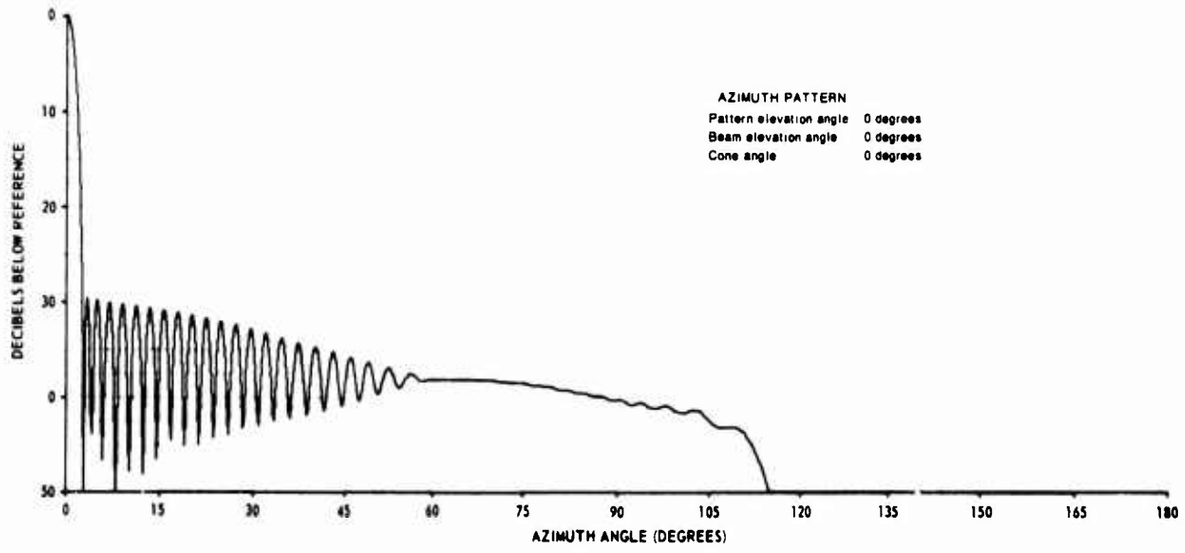

Figure 4. Azimuth patterns, various beam positions.

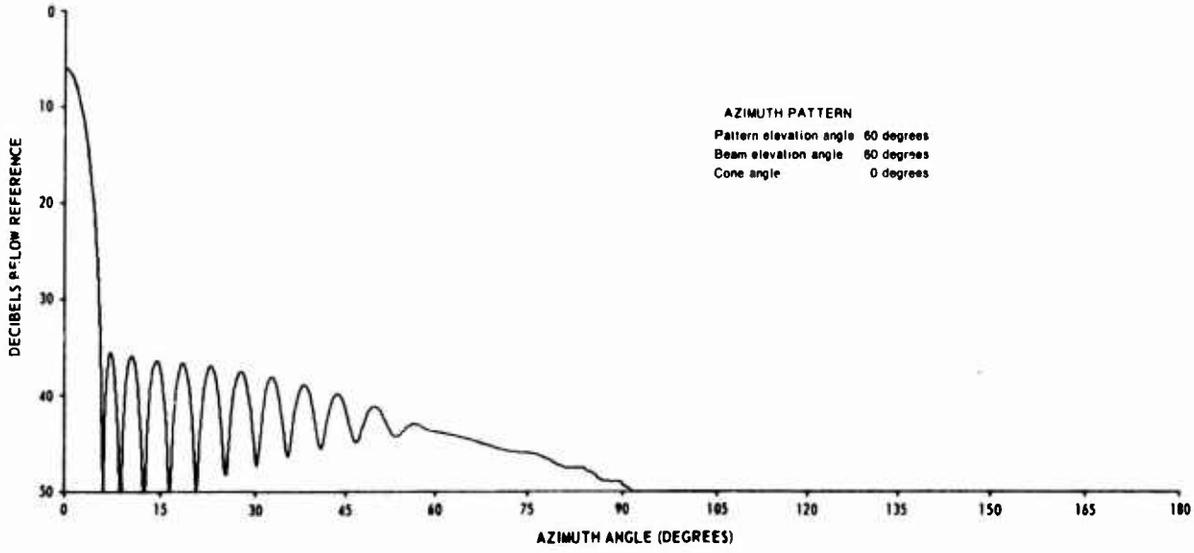

Figure 4 (Continued).

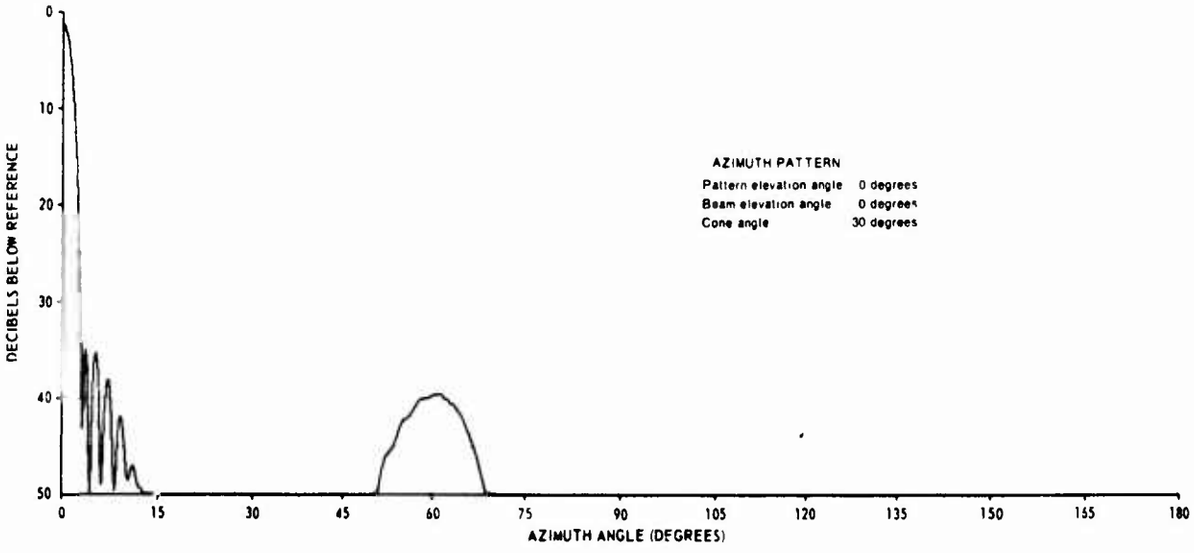

Figure 4 (Continued).

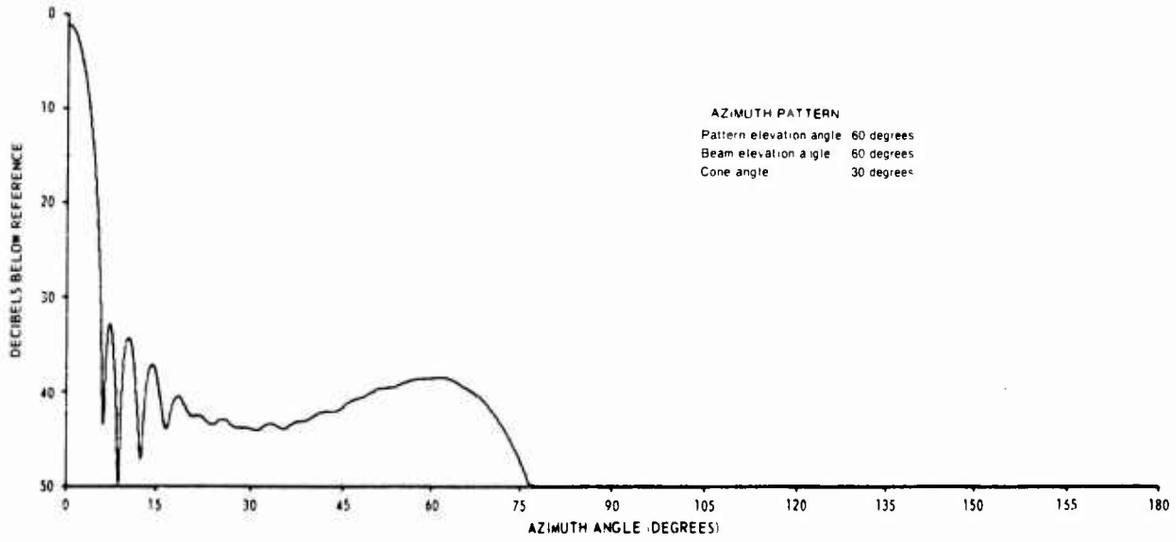

Figure 4 (Continued).

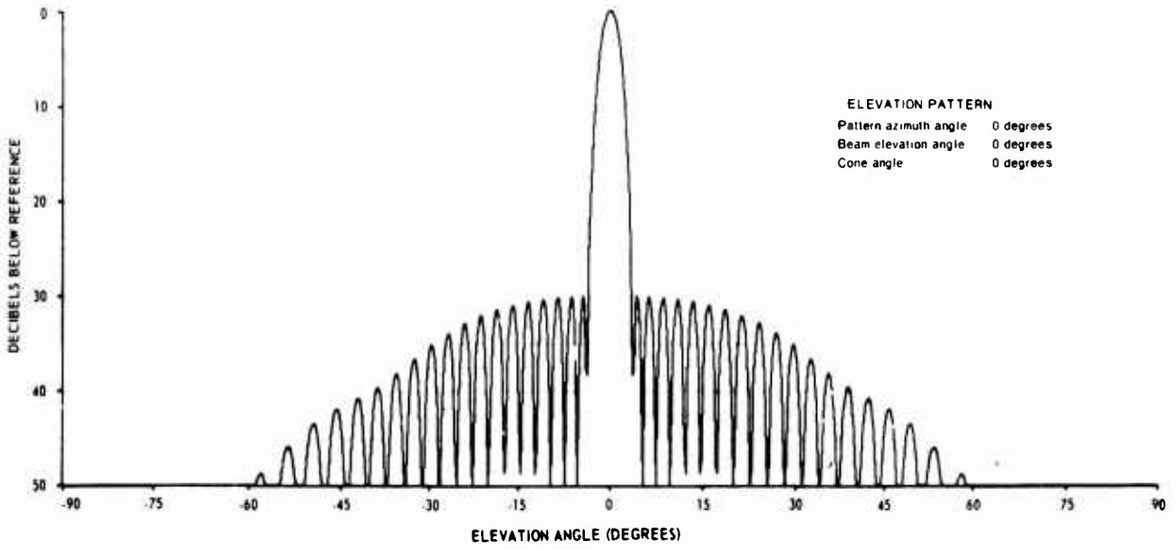

Figure 5. Elevation patterns, various beam positions.

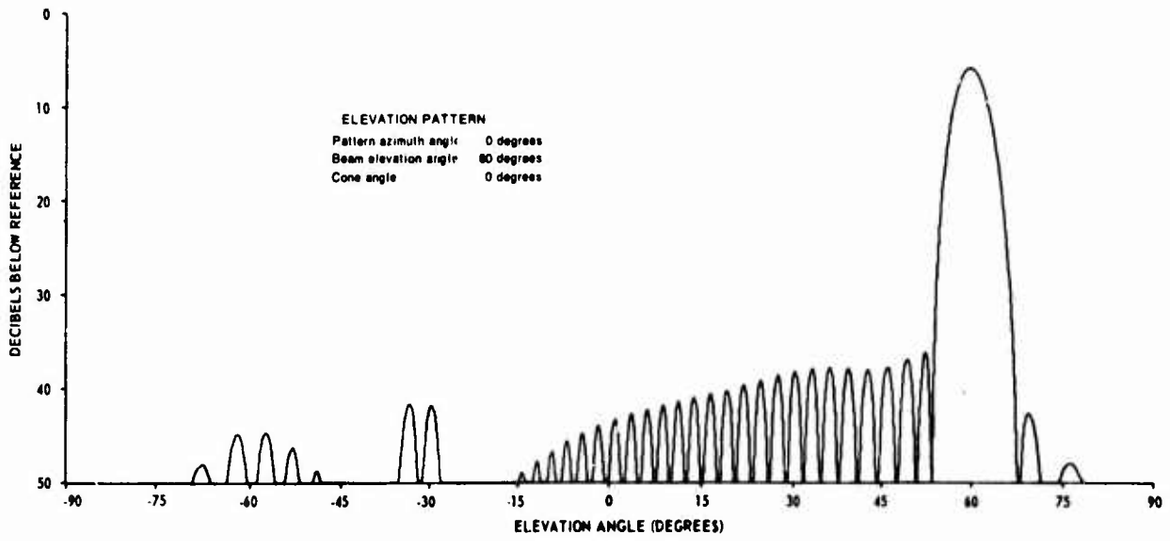

Figure 5 (Continued).

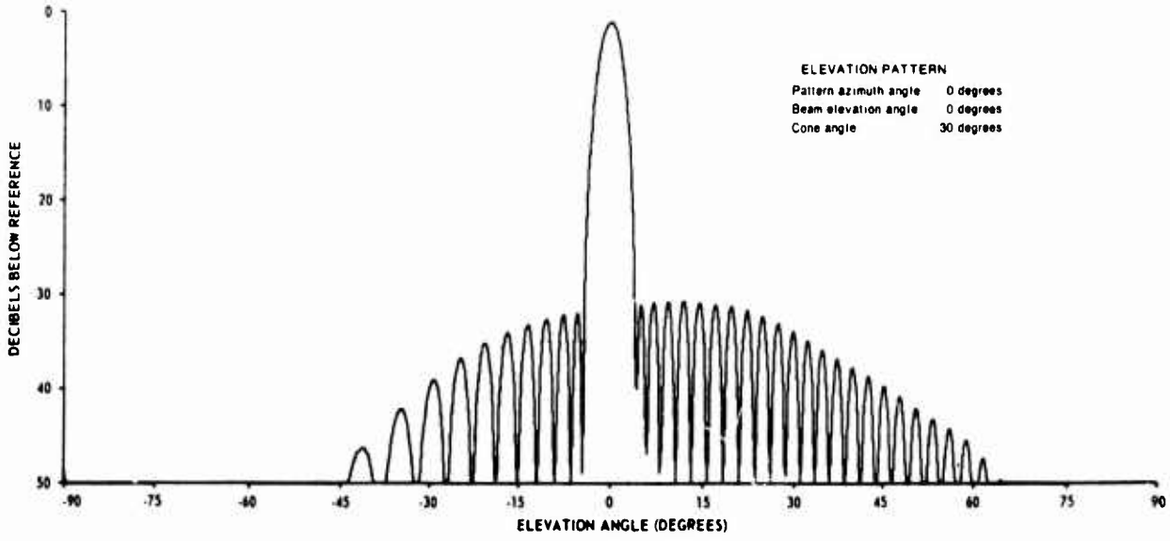

Figure 5 (Continued).

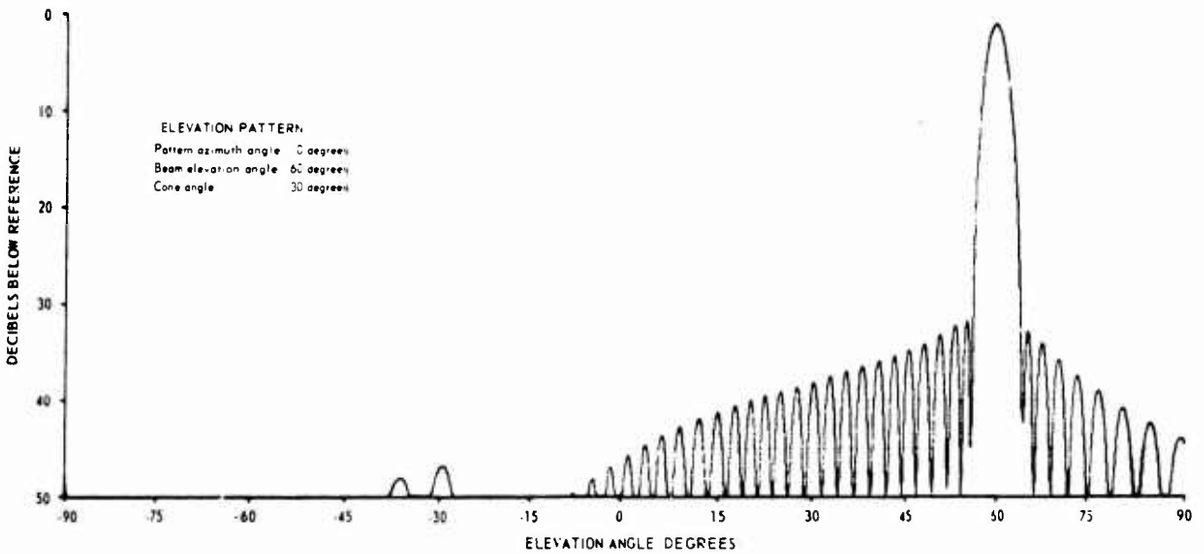

Figure 5 (Continued).

Many of the developments will be discussed at this conference and I would like to give a brief review of the more common general feeding and implementation techniques, as well as some promising analytical work concerning the effects of mutual coupling in cylindrical arrays. A major difference between the circular array and the linear array is the means used to steer the beam. In some approaches, for example, in addition to the usual devices such as the phase shifter used to steer the beam, the circular array requires some type of device such as a switch (fig. 6) to commute the amplitude and phase distributions around the ring of various elements. In order to produce low sidelobe beams, it is necessary that the amplitude have a taper and this further complicates the commutation process. In the earlier development of the Wullenweber arrays, the elements were uniformly excited. Later presentations to be given by Boyns of NELC, Gabriel of Scanwell, and Giannini of Wheeler Labs will give variations of these techniques.

The use of optical techniques which make use of microwave lenses to provide the proper amplitude and phase to feed a ring array or partial ring array has also been "borrowed" from the linear-array technology. The familiar R-2R lens approach has been applied to the ring array and will be discussed by Devan of NELC, and Zimmer of Georgia Tech will present another lens approach. Other uses of the lens have been made, and I am sure that they will be discussed later.

Another technique carried over from the linear-array technology is the use of a hybrid matrix as a means of beam forming by a superposition of modes. The technique has a wide bandwidth potential as well as a multiple beam potential. Sheleg of NRL, Chadwick and Van Wagoner of RSI will discuss applications of these techniques.

In the techniques previously discussed, the radiation pattern desired was not specifically mentioned. However, a narrow azimuth beam, a fan beam, or the pencil beam can be achieved by all of these techniques. An important application not requiring a narrow azimuth beam is TACAN. Considerable interest has been shown in the use of a phased array for the TACAN application. Several approaches to the solution of the TACAN problem using cylindrical phased arrays will be discussed. Present TACAN systems use a mechanically rotating antenna. Shestag of Rantec will give a description of TACAN and some background on the systems aspects. Hanratty of ITT Gilfillan, Greco of the NFSTEF, and Van Wagoner of RSI will give some recent developments in this area.

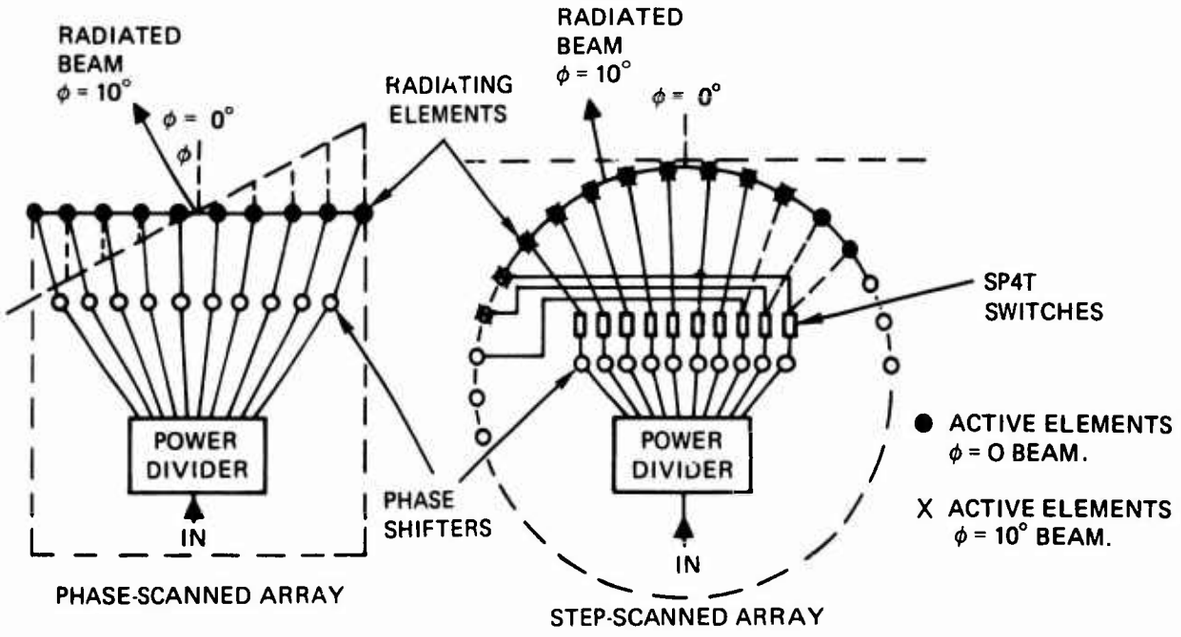

Figure 6. Phase-scanned and step-scanned arrays.

The previous discussion has presented some of the hardware aspects and applications of circular and cylindrical arrays. The ability to adequately design an operating array is highly dependent upon reliable mathematical techniques. Considerable work on these techniques is being done by many universities, and some of that work will be presented here. Hessel and Sureau of PIB, Gladman of ASWE, Great Britain and Munger of NELC will discuss the effects of mutual coupling on array excitations. Coleman of NRL, Butler of SMU, and Ma of ESSA will discuss analysis techniques and pattern synthesis. Another area, although not analytical, is of importance to antenna designers and that is the area of potential applications and the specific design requirements. Blake of FAA and Weis of NAVSEC will give some design considerations for proposed systems.

I have given a brief outline of some of the topics to be discussed but have not covered them all. I hope that in the next three days we can cover many topics and obtain a better understanding of circular and cylindrical arrays and their potential use as scanning arrays.

MUTUAL COUPLING ON CYLINDRICAL ARRAY ANTENNAS

By B. R. Gladman

Naval Electronics Laboratory Center
San Diego, California 92152

INTRODUCTION

The high cost and complexity of large phased arrays make it highly desirable to evaluate their performance prior to fabrication. Earlier methods of prediction usually ignored the effects of mutual coupling by assuming that the radiation patterns of the individual array elements were identical to the pattern of a single isolated element. Comparison between theory and experiment indicated that the effects of mutual coupling could significantly alter the behavior of phased arrays and that such effects must be accounted for in any reliable evaluation method. Fortunately, experimental methods of array evaluation that do not require large numbers of elements (array simulators) were developed and made a significant contribution to the understanding of large phased arrays. More recently it has become possible to completely analyze the infinite planar phased array in such a way as to yield the detailed behavior of its elements. As would be expected, the interaction effects are largest between closely spaced elements and an analysis of the infinite array gives results that apply to all elements except those on the edge of a practical phased array. This paper presents a similar analysis for the infinite cylindrical array, as shown in figure 1, for horizontally polarized excitation. The treatment of vertical polarization is somewhat more difficult, but equally possible.

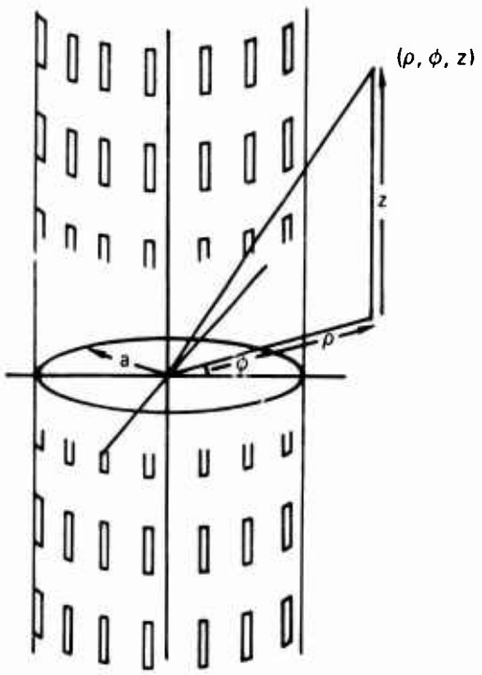

Figure 1. Cylindrical coordinate system.

ANALYSIS

The infinite cylindrical array (and all of space exterior to it) is split into "unit cells," each geometrically identical to all others. This is illustrated in figure 2. The basic array excitations studied are those which place all unit cells in an identical electrical environment, the fields in all unit cells being identical except for a constant phase shift from cell to cell along rings and columns. In principle, this is not a restriction since arbitrary excitations can be decomposed into sums of excitations of the above type. Along rings, the phase shift between cells must be such that a complete transversal of a ring produces a total phase change that is a multiple of 2π, thus ensuring that the fields are single-valued functions of azimuth angle. The array is subdivided into an infinite number of rings, each containing M unit cells. All such cells are identical and can contain more than one element; however, in this paper one element per cell is assumed. Allowance has been made for a possible dielectric filling within the waveguides.

An exact analysis would require that the feed waveguides have radial vertical sidewalls as illustrated in figure 3. An approximate analysis is used here in that the waveguides are assumed to possess uniform cross sections, the small difference between their plane ends and the cylindrical arc being neglected. This should be reasonable for all but the smallest arrays. A time dependence of the form $\exp(i\omega t)$ is assumed and all distances are normalized by using $\lambda/2\pi$ as the basic unit of length, where λ is the free-space wavelength. Also, electric fields are measured in a basic unit of η volts, where η is the impedance of free space. These adjustments allow the equations to be written in dimensionless form.

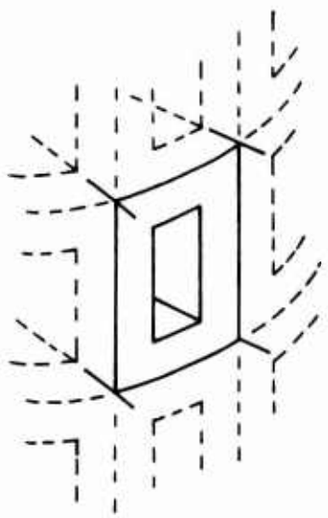

Figure 2. Unit cell.

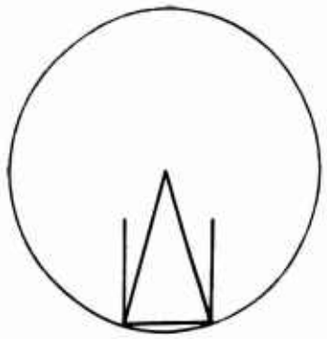

Figure 3. Approximation using uniform cross section waveguide instead of radial waveguide.

Fields in Space

Fields in cylindrical coordinates can be classified into two types - transverse electric (TE) or transverse magnetic (TM) to the z axis. For horizontally polarized excitation, only TE fields are generated. These can be obtained from a z-directed Hertz vector ψ_z, where

$$\mathbf{E} = -i\mu\nabla \times (\psi_z) \tag{1}$$

$$\mathbf{H} = \epsilon\mu\,(\psi_z) + \nabla[\nabla \cdot (\psi_z)] \tag{2}$$

$$\nabla^2 + \epsilon\mu\psi = 0 \tag{3}$$

In free space $\epsilon = \mu = 1$. Solution of (3) in cylindrical coordinates for free space gives

$$\psi = [AH_m^{\,2}(k_t\rho) + BH_m^{\,1}(k_t\rho)]\,\exp(ik_z z)\exp(im\phi) \tag{4}$$

with

$$k_t^{\,2} = 1 - k_z^{\,2} \tag{5}$$

The analysis will be conducted for the array as a transmitter, the space fields consisting of wave traveling in the positive ρ direction. These fields are represented by Hankel functions of the second kind, the solutions being of the form:

$$\psi = AH_m^{\,2}(k_t\rho)\exp(ik_z z)\exp(im\phi) \tag{6}$$

If k_z is greater than unity, k_t is taken to be negative imaginary and the solution is expressed in terms of the modified Bessel functions

$$\psi = AK_m\,(ik_t\rho)\exp(ik_z z)\exp(im\phi) \tag{7}$$

where the function $K_m\,(x)$ has been chosen to ensure that the fields at infinity are finite. Equations 6 and 7 give the basic spatial solutions which can be summed to yield more general solutions. For our purposes, we must exclude all solutions that do not yield the correct cell-to-cell phase shifts as discussed earlier. If the phase shift between the excitation fields in adjacent elements along columns is γ_z, then only modes with the same phase change between cells are allowed. Thus

$$k_z d = \gamma_z + 2n\pi \qquad -\infty \leq n \leq \infty \tag{8}$$

gives the allowed values of k_z. If we let the value be k_{zn}, we obtain

$$k_{zn} = k_{z0} + 2\pi n/d \qquad -\infty \leq n \leq \infty \tag{9}$$

The value of k_{z0} determines the elevation beam position being studied. Similarly, the azimuth phase shift between cells must be of the form $2\pi m_0/M$ where m_0 takes on any of M consequentive integer values (normally $0 \leq m_0 < M$). This phase shift between cells is required to ensure phase changes that are multiples of 2π for complete revolutions around the array. The cell-to-cell phase shift in the space modes must match this value, thus requiring that allowed m values satsify

$$\frac{2\pi m}{M} = \frac{2\pi m_0}{M} + 2\ell\pi \qquad -\infty < \ell < \infty \tag{10}$$

Denoting these values by m_ℓ, we obtain

$$m_\ell = m_0 + \ell M \qquad -\infty \leq \ell \leq \infty \tag{11}$$

We can now write down the allowed solutions $\psi_{\ell n}$ as

$$\psi_{\ell n} = A_{\ell n} H_{m_\ell}^{\ 2}(k_{tn}\rho) \exp(ik_{zn}z) \exp(im_\ell\varphi) \tag{12}$$

for

$$k_{tn}^{\ 2} = 1 - k_{zn}^{\ 2} \geq 0 \qquad (k_{tn} \text{ positive real}) \tag{13}$$

or

$$\psi_{\ell n} = A_{\ell n} K_{m_\ell}(k_{tn}\rho) \exp(ik_{zn}z) \exp(im_\ell\phi) \tag{14}$$

for

$$k_{tn}^{\ 2} = 1 - k_{zn}^{\ 2} \leq 0 \qquad (k_{tn} \text{ negative imaginary}) \tag{15}$$

Equations 1 and 2 can now be used to give E and H in the space surrounding the array. Specifically, H_z (z-directed magnetic field) and E_ϕ (ϕ-directed electric field) will be of use, the general solutions being obtained from sums over the above ψ modes. This gives

$$H_z = \sum_{\ell=-\infty}^{\infty} \sum_{n=-\infty}^{\infty} A_{\ell n} k_{tn}^{\ 2} \begin{Bmatrix} H_{m_\ell}^{\ 2}(k_{tn}\rho) \\ K_{m_\ell}(ik_{tn}\rho) \end{Bmatrix} \exp(ik_{zn}z) \exp(im_\ell\phi) \tag{16}$$

$$E_\phi = \sum_{\ell=-\infty}^{\infty} \sum_{n=-\infty}^{\infty} A_{\ell n} k_{tn} \begin{Bmatrix} H_{m_\ell}^{\ 2'}(k_{tn}\rho) \\ iK_{m_\ell}'(ik_{tn}\rho) \end{Bmatrix} \exp(ik_{zn}z) \exp(im_\ell\phi) \tag{17}$$

The upper or lower solution is taken if k_{tn} is real or imaginary respectively. k_{tn} is taken to be either positive real or negative imaginary.

Waveguide Fields

Figure 4 shows the "local" coordinate system used to obtain the expressions for the waveguide fields. Although it is more usual to divide the fields into two sets that are TE and TM to the guide axis, our purposes are more simply satisfied by using LSE modes (longitudinal section electric) which are TE to the z axis. These fields can be obtained by solving equations 1, 2, and 3 in rectangular coordinates with appropriate boundary conditions at the waveguide walls. The mode funct n ψ_{pq} (p half-cycle variations in y, q in z) is easily shown to be

$$\psi_{pq} = [B_{pq} \exp(-ik_{pq}x) + C_{pq} \exp(ik_{pq}x)]$$
$$\cos[p\pi(y+b)/2b] \sin[q\pi(z+c)/2c] \qquad (18)$$

Where

$$k_{pq}^2 = \epsilon - (p\pi/2b)^2 - (q\pi/2c)^2 \qquad (19)$$

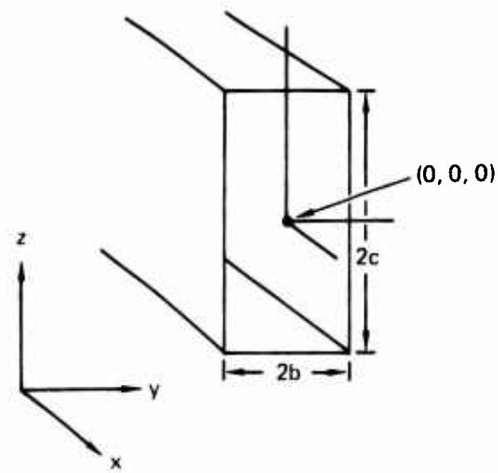

Figure 4. Coordinate system for waveguide.

Where k_{pq} is taken to be positive real or negative imaginary. With the former choice, the B_{pq} term represents a wave travelling towards the aperture, the C_{pq} term being a reflected field. With the latter choice, only the C_{pq} term is used, and represents evanescent waveguide fields. The y coordinate of the waveguide coordinate system is aligned with the ϕ coordinate of the cylindrical system. If the waveguide center is at an angle zero, its angular half-width being α, then, provided α is sufficiently small, $(y + b)/b$ can be replaced by $(\phi + \alpha)/\alpha$ at the x=0 plane. A general waveguide field is represented by a sum of the ψ_{pq} mode functions over p and q, equations 2 and 3 being used to obtain the fields. The E_ϕ and H_z fields in the waveguide apertures can be expressed as

$$H_z = \sum_{p=0}^{\infty} \sum_{q=1}^{\infty} (B_{pq} + C_{pq}) [\epsilon - (q\pi/2c)^2]$$
$$\cos[p\pi(\phi+\alpha)/2\alpha] \sin[q\pi(z+c)/2c] \qquad (20)$$

$$E_\phi = \sum_{p=0}^{\infty} \sum_{q=1}^{\infty} (B_{pq} - C_{pq}) k_{pq} \cos[p\pi(\phi+\alpha)/2\alpha]$$

$$\sin[q\pi(z+c)/2c] \tag{21}$$

with

$$k_{pq}^2 = \epsilon - (p\pi/2b)^2 - (q\pi/2c)^2 \tag{22}$$

Where k_{pq} is positive real or negative imaginary and B_{pq} is zero for all modes but those exciting the array (normally the $p = 0, q = 1$ mode only).

Field Matching at the Array Aperture

The surface of the array not occupied by waveguide elements is assumed to be a perfect conductor. Over the waveguide aperture the fields described by (16) and (17) for $\rho = a$ must match those described by (20) and (21) which are waveguide descriptions of the same field. In addition, the tangential electric field E_ϕ given by (17) must vanish over the array surface not occupied by the waveguide element. The tangential magnetic field H_z given by (16) cannot however be specified over the metallic region of the aperture. This matching can be specific within each unit cell as follows:

$$i \sum_{\varrho=-\infty}^{\infty} \sum_{n=-\infty}^{\infty} A_{\varrho n} k_{tn} \begin{Bmatrix} H_{m_\varrho}'(k_{tn}a) \\ K_{m_\varrho}'(ik_{tn}a) \end{Bmatrix} \exp(ik_{zn}z) \exp(im_\varrho\varphi)$$

$$= \sum_{p=0}^{\infty} \sum_{q=1}^{\infty} [B_{pq} - C_{pq}]\, k_{pq} \cos[p\pi(\varphi-\alpha)/2\alpha]\, \sin[q\pi(z+c)/2c]$$

over aperture of waveguide.

$$= 0 \qquad \text{over surface not occupied by waveguide.} \tag{23}$$

$$\sum_{\varrho=-\infty}^{\infty} \sum_{n=-\infty}^{\infty} A_{\varrho n} k_{tn}^2 \begin{Bmatrix} H_{m_\varrho}'(k_{tn}a) \\ K_{m_\varrho}(ik_{tn}a) \end{Bmatrix} \exp(ik_{zn}z) \exp(im_\varrho\phi)$$

$$= \sum_{p=0}^{\infty} \sum_{q=1}^{\infty} [B_{pq} + C_{pq}]\, [\epsilon - (q\pi/2c)^2] \cos[p\pi(\phi+\alpha)/2\alpha]$$
$$\sin[q\pi(z+c)/2c]$$

over aperture of waveguide

$$= \text{unspecified over surface not occupied by waveguide.} \tag{24}$$

If both sides of equation 23 are multiplied by $\exp(ik_{zs}z)\exp(-im_Q\phi)$ and the resultant equation is integrated over the entire unit cell aperture surface, we obtain after some manipulation:

$$\frac{2\pi d}{M} ik_{ts} A_{rs} \begin{Bmatrix} H_{m_r}{}^{2'}(k_{ts}a) \\ iK_{m_r}{}'(k_{ts}a) \end{Bmatrix} = \sum_{p=0} \sum_{q=1} k_{pq}(B_{pq} - C_{pq})$$

$$2\alpha \exp[-i(m_r\phi - p\pi/2)]\ V_1(m_r\alpha, -p)$$

$$2(-i)c \exp[-i(k_{zs}z - q\pi/2)]\ V_2(k_{zs}c, -q) \qquad (25)$$

Where

$$\left.\begin{matrix} V_1(x, n) \\ V_2(x, n) \end{matrix}\right\} = \frac{1}{2}\left\{\frac{\sin(x+n\pi/2)}{x+n\pi/2} \pm (-1)^n \frac{\sin(x-n\pi/2)}{x-n\pi/2}\right\} \qquad (26)$$

The subscripts 1 and 2 indicate addition or subtraction respectively. In a similar manner equation 24 can be multiplied by

$$\cos[P\pi(\phi+\alpha)/2\alpha]\ \sin[Q\pi(z+c)/2c]$$

and integrated over the aperture of the waveguide. This gives the equation

$$[B_{PQ} + C_{PQ}]\ [\epsilon - (Q\pi/2c)^2]\ (1 - \delta_{0Q})(1 + \delta_{0P})\, c\alpha$$

$$= \sum_{Q=-\infty}^{\infty} \sum_{n=-\infty}^{\infty} A_{Qn} k_{tn}{}^2 \begin{Bmatrix} H_{m_Q}{}^2(k_{tn}a) \\ K_{m_Q}(ik_{tn}a) \end{Bmatrix}$$

$$2\alpha \exp[i(m_Q\phi + P\pi/2)]\ V_1(m_Q\alpha, P)$$

$$2ic \exp[i(k_{zn}z + Q\pi/2)]\ V_2(k_{zn}c, Q) \qquad (27)$$

$$0 \leqslant P \leqslant \infty$$

$$1 \leqslant Q \leqslant \infty$$

Finally, substituting for A_{Qn} in (27) using (25) gives after considerable reorganization

$$\sum_{p=0}^{\infty} \sum_{q=1}^{\infty} \Big[S(p, q\,;\, P, Q) + D(p, q\,;\, P, Q)\Big] F_{pq} = G_{PQ} \qquad (28)$$

$$0 \leqslant P < \infty$$

$$1 \leqslant Q < \infty$$

where

$$S(p, q\,;\, P, Q) = M \sum_{Q=-\infty}^{\infty} \sum_{n=-\infty}^{\infty} k_{tn}a \begin{Bmatrix} H_{m_Q}{}^2(k_{tn}a)/H_{m_Q}{}^{2'}(k_{tn}a) \\ -iK_{m_Q}(ik_{tn}a)/K_{m_Q}{}'(ik_{tn}a) \end{Bmatrix}$$

$$V_1(m_Q\alpha, p)\ V_1(m_Q\alpha, P)\ V_2(k_{zn}c, q)\ V_2(k_{zn}c, Q) \qquad (29)$$

$$D(p, q, P, Q) = \frac{i\pi ad(1 - \delta_{0q})(1 + \delta_{0p})\left[\epsilon - (q\pi/2c)^2\right]\delta_{pP}\delta_{qQ}}{8c\,\alpha\,k_{pq}} \tag{30}$$

$$F_{pq} = 4c\,\alpha\,k_{pq}\,(-i)^{p+q}\,(B_{pq} - C_{pq}) \tag{31}$$

$$G_{PQ} = i\pi ad\,(1 - \delta_{0q})(1 + \delta_{0p})\left[\epsilon - (q\pi/2c)^2\right](-i)^{p+q}\,B_{PQ} \tag{32}$$

Equation 28 is an infinite matrix equation for the amplitudes of all waveguide modes in terms of the incident mode amplitudes. Spatial mode amplitudes can be obtained from the solution of (28) by use of (25). In practice, the infinite matrix is truncated (as is the sum over ℓ and n in equation 29) and the resultant set of equations solved for the lower modes only using a digital computer.

Normally G_{pq} is zero for all but the p=0, q=1 mode, this being the waveguide mode that excites the array. Solution of (28) gives the waveguide reflection coefficient and far-field amplitude for the specified aperture phasing (as determined by m_0 and k_{z0}). Equation 25 gives the space-mode amplitudes in terms of the F_{pq}:

$$A_{\ell n} = \frac{-a\,M}{2\pi c\left\{\begin{matrix} k_{tn}a\,H_{m_\ell}^{2\prime}(k_{tn}a) \\ ik_{tn}a\,K_{m_\ell}^{\prime}(ik_{tn}a)\end{matrix}\right\}}\sum_{p=0}^{\infty}\sum_{q=1}^{\infty}V_1(m_\ell\alpha, p)\,V_2(k_{zn}c, q)\,F_{pq} \tag{33}$$

where, as before, the actual sum is taken over those modes included in the solution of (28) rather than the infinite number indicated.

MUTUAL INTERACTION EFFECTS IN AZIMUTH

A single element in each unit cell is assumed with excitation in the $p = 0, q = 1$ waveguide mode, all other B_{pq}'s being zero. The pq subscript will therefore be dropped from B_{pq}, $B(m_0)$ being understood to mean the incident waveguide field amplitudes for an excitation that exhibits a phase of $2\pi m_0/M$ from cell to cell (this excitation will be referred to as azimuth excitation mode m_0). Since the phase between adjacent cells in azimuth is $2\pi m_0/M$, the incident field in waveguide s is

$$B(m_0)\exp\left(\frac{2\pi i m_0 s}{M}\right) \quad 0 \leqslant s \leqslant M - 1 \tag{34}$$

the waveguides being labelled with the subscript s which ranges from 0 through M-1 as a ring of array elements is traversed. Similarly, the reflected field in the $p = 0, q = 1$ mode in waveguide s has the form:

$$C(m_0) = \exp\left(\frac{2\pi i m_0 s}{M}\right) \quad 0 \leqslant s \leqslant M - 1 \tag{35}$$

Alternatively, this can be written in terms of the waveguide reflection coefficient for excitation mode m_0, $R(m_0)$, as

$$B(m_0)\,R(m_0)\exp\left(\frac{2\pi i m_0 s}{M}\right) \quad 0 \leqslant s \leqslant M - 1 \tag{36}$$

The incident and reflected fields of waveguide s when more than one azimuth excitation mode is present are simply

$$\mathrm{Inc}(s) = \sum_{m_0=0}^{M-1} B(m_0) \exp\left(\frac{2\pi i m_0 s}{M}\right) \quad 0 \leqslant s \leqslant M-1 \tag{37}$$

$$\mathrm{Ref}(s) = \sum_{m_0=0}^{M-1} B(m_0)\, R(m_0) \exp\left(\frac{2\pi i m_0 s}{M}\right) \quad 0 \leqslant s \leqslant M-1 \tag{38}$$

A most important excitation is one for which all azimuth excitation modes are excited with an equal amplitude of $1/M$. Equation 37 gives

$$\mathrm{Inc}(s) = \frac{1}{M} \sum_{m_0=0}^{M-1} \exp\left(\frac{2\pi i m_0 s}{M}\right) \quad 0 \leqslant s \leqslant M-1$$

$$= 1 \text{ if } s = 0$$

$$= 0 \text{ if } s \neq 0 \tag{39}$$

Thus, this type of excitation corresponds to the excitation of a single column of elements in the array (the s=0 column). Under these conditions, equation 38 shows that

$$\mathrm{Ref}(s) = \frac{1}{M} \sum_{m_0=0}^{M-1} R(m_0) \exp\left(\frac{2\pi i m_0 s}{M}\right) \quad 0 \leqslant s \leqslant M-1 \tag{40}$$

Clearly, since Inc(0) is unity, Ref (0) is simply the reflection coefficient of an element on a ring when all others are not excited. When s is not zero, $R(s)$ must be interpreted as the field coupled from the s=0 element into the element s. Thus (40) gives the relationship between the modal reflection coefficients $R(m_0)$ and the coupled fields. These will be denoted by $U(s)$, the field coupled into waveguide element s when element zero is excited with unit amplitude. $U(0)$ is the element reflection coefficient as described above.

$$U(s) = \frac{1}{M} \sum_{m_0=0}^{M-1} R(m_0) \exp\left(\frac{2\pi i m_0 s}{M}\right) \quad 0 \leqslant s \leqslant M-1 \tag{41}$$

The far-field pattern of a single excited column is clearly obtained by combining the spatial modes in the far field.

COMPUTED RESULTS

Since the behavior of linear and planar arrays is fairly well understood, this section will concentrate on the effects of coupling between the columns of a cylinder (i.e., on the mutual interactions effects in azimuth). These results apply to an array of the

type shown in figure 1 where the horizontal and vertical dimensions of the element are 0.25 and 0.75 wavelength respectively and the vertical-element spacing is 0.8 wavelength. The waveguides are not loaded with dielectric material and the phase shift in the vertical direction is zero.

As previously explained, there are M possible cell-to-cell phasings of the form $2\pi m_0/M$ ($0 \leq m_0 \leq M-1$) on a cylindrical array with M elements on each of its rings. An important factor in the performance of such an array is the waveguide reflection coefficient for each of these modes of excitation. This is plotted against excitation mode number (i.e., m_0) for various numbers of elements on a four-wavelength radius array in figure 5. The spacing of the elements in wavelengths is given in parentheses. This figure indicates that azimuth modes of excitation above about 25 are completely unusable since much or all of the incident power undergoes reflection at the aperture. This cutoff effect is common to all cylindrical antennas. The rapid rise in the reflection coefficient occurring when m_0 is of the order of the normalized radius of the cylinder (25.13 in this case). If the behavior for high modes is not important, it would appear that closely spaced elements have a better match.

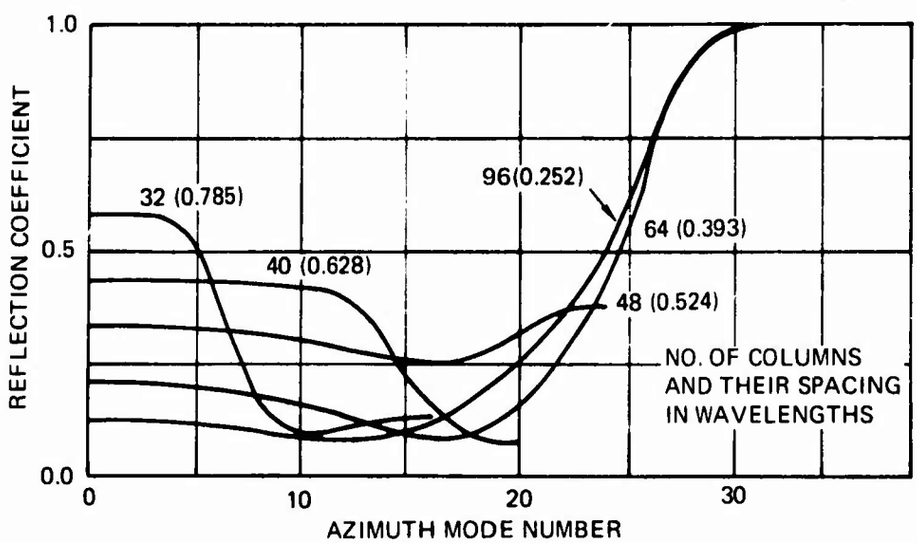

Figure 5. Waveguide reflection coefficient vs. azimuth mode number on a four-wavelength radius cylinder.

Figure 6 shows the efficiency with which the same array generates spatial modes. Modal efficiency, as plotted, is defined as the voltage for 100 percent efficiency and is therefore really the square root of the true generation efficiency. The curves are only plotted for positive mode numbers as it is easy to show that the modal efficiency does not depend on the sign of the mode number.

Although the efficiency is given for all modes, it should be remembered that the actual modes generated depend upon the number of elements on a ring and the cell-to-cell phase shift of the excitation. For example, excitation with azimuth mode m_0=0 for a 32-element array produces modes 0, -32, +32, -64, +64 etc., while excitation with mode m_0=16 yields 16, -16, 48, -48, etc. In general, excitation mode m_0 yields far-field space modes m_0, m_0-M, m_0-2M, etc., on an M-element array. These facts have a number of consequences. First, it is clear that only M far-field modes can be independently controlled, it being normal to choose these to be the modes -(M/2)+1 through (M/2). Secondly,

there is a limitation of the efficiency of certain modes. For example, excitation with mode $m_0=M/2$ also produces mode $m_0-M = -M/2$. Since these modes are known to have equal efficiency, the upper limit to the power efficiency of each of these modes is 50 percent. Thus, the maximum modal efficiency (i.e., voltage) of the $(M/2)$ and $-(M/2)$ modes is $\sqrt{2}$ or 0.707. These modes are shown dotted on figure 6 and clearly illustrate this effect.

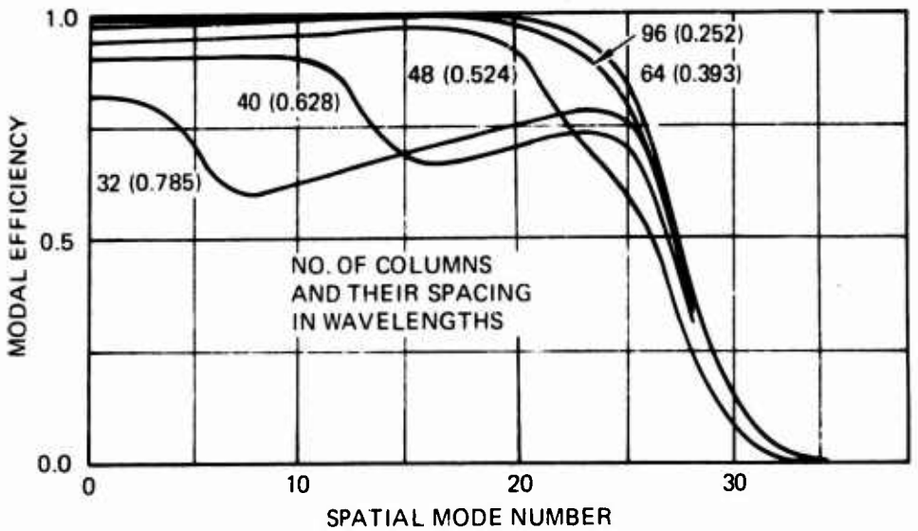

Figure 6. "Voltage efficiency" vs. spatial mode number on a four-wavelength radius cylinder.

The curves of figure 6 illustrate the modal efficiencies on a 4-wavelength cylinder containing different numbers of columns of elements, the spacing of these columns being given in parentheses. For spacings less than about 0.5 wavelength these curves are little different. At a spacing of about 0.5 wavelength, however, the curves start to distort and spacings greater than 0.6 wavelength severely degrade the modal efficiencies. This effect is the cylindrical array analogue of the appearance of a grating lobe on a linear array. Although these effects begin to show at small spacings, they are more gradual than the linear-array equivalents and do not actually limit spacings to the range below 0.5 wavelength. As detailed above, on a 40-element array it would be normal to obtain a desired far-field pattern by controlling the amplitudes of modes -19 through 20. However, modes -19 and 21, -18 and 22, etc., are coupled and figure 6 indicates that modes 21 and 22, which are unwanted, will have higher amplitudes than modes -18 and -19. The effect of these undesired modes is discussed at length in references 1 and 2, the main result being unwanted sidelobes ("grating lobes") at large pattern angles. In practice this limits array spacing to the region below about 0.65 wavelength.

The results of the analysis can also be used to predict the azimuth pattern of a singly excited column of elements. Typical patterns are illustrated in figure 7 where the normalization is such as to reflect the true gain including reflection losses. For column spacings less than 0.5 wavelength the curves are near to being smooth. At spacings over 0.5 wavelength, however, the patterns exhibit an increasing amount of variation with angle and rapid changes in gain on axis. This can be attributed to the parasitic excitation of adjacent columns in the array with a phase that is dependent upon the distance between columns. The reradiated energy will thus sometimes add and sometimes subtract from the

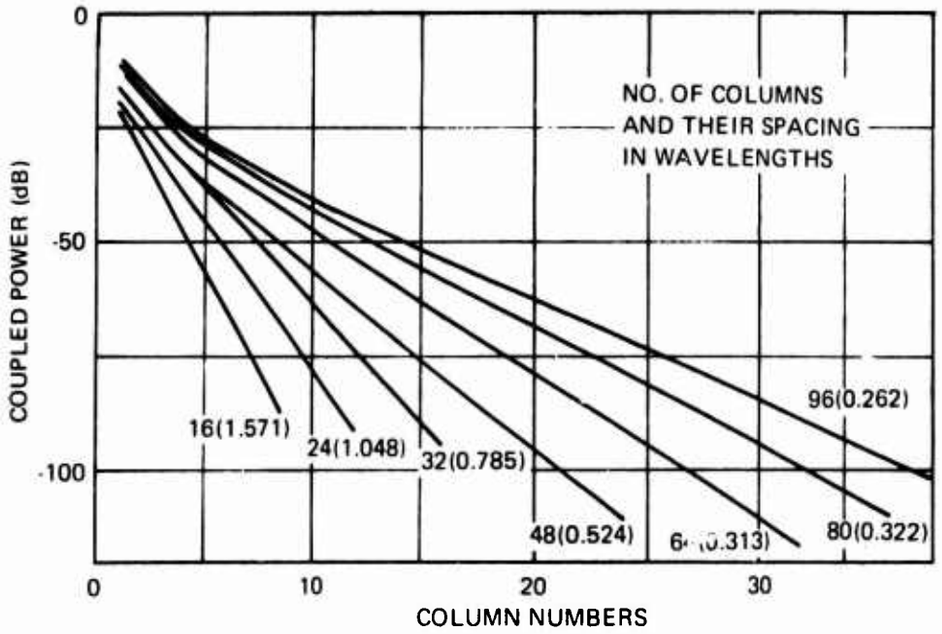

Figure 8. Power coupled from a singly excited column into adjacent columns on a four-wavelength cylindrical array.

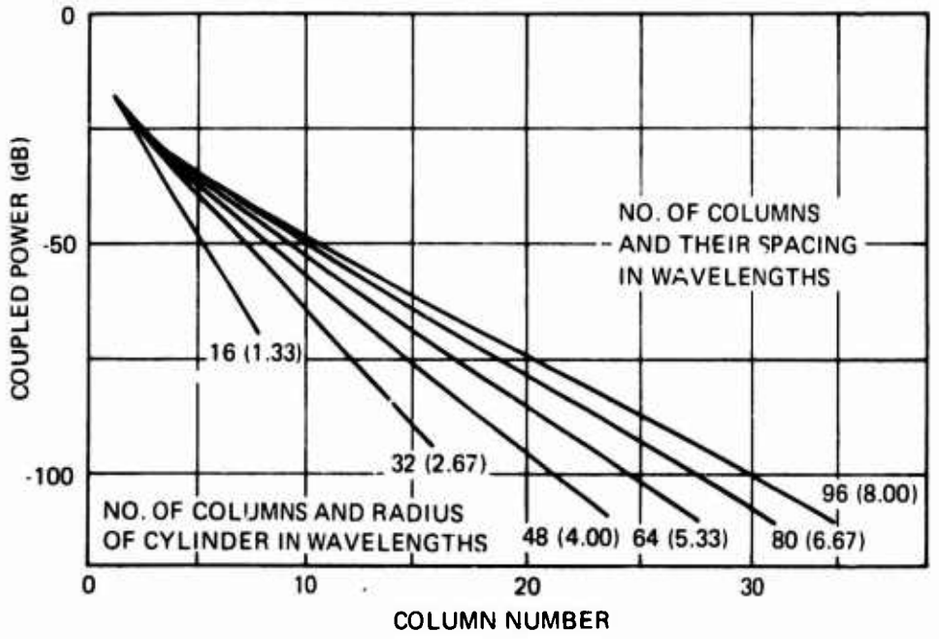

Figure 9. Power coupled from a singly excited column into adjacent columns for columns with fixed spacing on varying radii cylinders. Column spacing, 0.524 wavelength.

field of the primary column, producing changes in gain with column spacing. With larger spacings, "the aperture" of the parasitic array is larger and it is capable of producing more rapid angular changes of far-field intensity. These effects are clearly illustrated in figure 7. A further point of interest is that the pattern for a 96-column array contains less total far-field energy then the other patterns, indicating that the use of too many elements on a cylinder of given size is not useful. This is a result of the bad reflection coefficient of and the heavy coupling between such closely spaced elements.

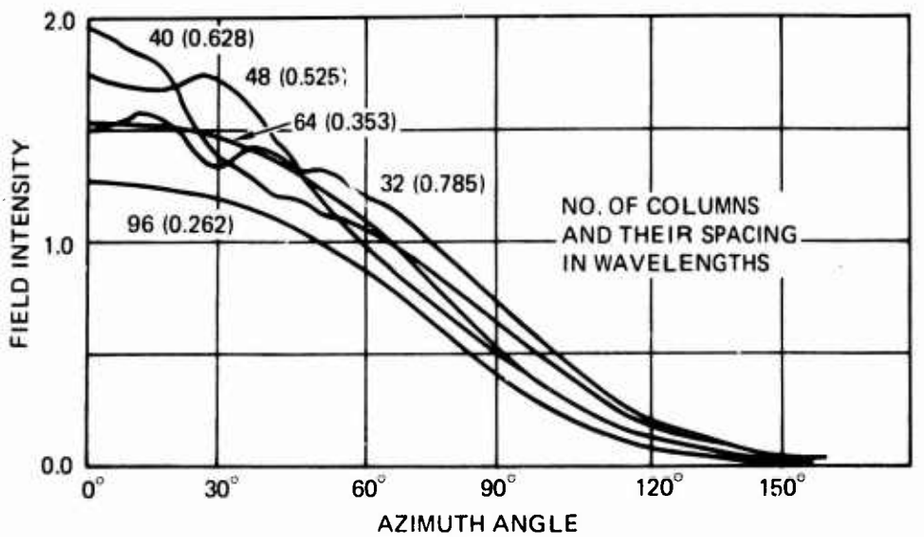

Figure 7. Azimuth patterns of singly excited column on a four-wavelength cylinder.

The power coupled from a single excited column into other columns on the array is shown in figure 8. Except for the immediately adjacent columns, the coupling is clearly linear with increasing element number. This is strong evidence for the presence of a surface wave travelling from the excited column around the array, this wave suffering the same fractional loss at each column it encounters. Further evidence for such a surface wave is provided by an investigation of the phase of the applied power which is again found to be linear with element number. Furthermore, it is indicated that for spacings above 0.5 wavelength, the coupling decay rate is proportional to column spacing. In other words, the fraction of the incident surface-wave power lost from column to column is proportional to the spacing of the column.

Figure 9 illustrates the coupled power as a function of cylinder radius. The numbers of columns on the cylinders have been altered in such a way as to maintain a constant column-to-column spacing, thus making figure 9 a true indication of the effects of cylinder radius. As can be seen, the coupling between closely spaced columns is almost independent of radius, but coupling to elements located further around the cylinder is definitely reduced by increasing the curvature of the aperture surface. It is clear that the behavior of cylindrical arrays of practical size will be essentially the same as that of a planar array with the same spacing. Significant reduction of coupling effects is evident only on cylinders with radii less than a few wavelengths.

CONCLUSIONS

A method for the prediction of mutual coupling effects on cylindrical arrays has been developed and tested. Using such computer programs, it should prove possible to accurately predict the performance of such arrays prior to fabrication. This in turn will lead to the use of optimum elements in such arrays and improve array performance.

REFERENCES

1. Naval Electronics Laboratory Center Report 1521, *Current Distributions and Radiation Patterns for Circular-Array Radar Antenna: Theory*, by A. D. Munger, 26 October 1967.

2. Naval Electronics Laboratory Center Report 1608, *Circular-Array Radar Antenna: Cylindrical-Array Theory*, by A. D. Munger, 15 January 1969.

PATTERN ANALYSIS FOR CYLINDRICAL AND CONICAL ARRAYS

by A. D. Munger and B. R. Gladman

Naval Electronics Laboratory Center
San Diego, California 92152

ANALYSIS OF CYLINDRICAL ARRAY

General

The cylindrical array can be considered to consist of a stack of identical ring arrays. We denote the complex excitation of the p^{th} element in the q^{th} ring by $I_{pq} = I(\alpha_p, z_q)$, where α_p is the angular location of the p^{th} and z_q is the z-axis location of the q^{th} ring. The coordinate system is shown in figure 1. The beam is assumed to be pointed in the $\varphi = 0$ direction in azimuth, corresponding to the $\alpha = 0$ reference point of the element location. The beam is stepped around the cylinder by redefining the $\alpha = 0$ reference to the desired position.

All elements are assumed identical, symmetrical, equally spaced, and pointed along the radius vector. Thus, the azimuth element pattern can be expressed as a function of $|\varphi - \alpha|$. In general, the azimuth pattern depends on the elevation angle θ. The complex element pattern is denoted by $G(\varphi - \alpha, \theta)$, with the phase referenced to the center of the ring in which it lies. Thus, if it is assumed that the phase center is at the element,*

$$G(\varphi-\alpha,\theta) = |G(\varphi-\alpha,\theta)| \exp[jk\rho\cos\theta\cos(\varphi-\alpha)] \tag{1}$$

The far field is

$$E(\varphi,\theta) = \sum_p \sum_q I_{pq}\, G(\varphi-\alpha_p,\theta) \exp[jqu] \tag{2}$$

where

$u = kd \sin\theta$
d = spacing between elements in vertical direction
$k = 2\pi/\lambda$

A beam can be formed in the direction $\varphi = 0$, $\theta = \theta_0$ by exciting all elements to add in phase in that direction (beam cophasal excitation). Thus, in view of (1) and (2) we require

$$I_{pq} = |I_{pq}| \exp[-jk\rho\cos\theta_0\cos\alpha_p - jqu_0] \tag{3}$$

where $u_0 = kd \sin\theta_0$.

Separable Aperture

In (3) the phase terms are separated in α_p and z_q, where $z_q = qd$. This allows us to assume a current distribution of the form

$$I(\alpha_p, z_q) = I^{(a)}(\alpha_p)\, I^{(e)}(z_q) = I_p^{(a)}\, I_q^{(e)} \tag{4a}$$

with

$$I_p^{(a)} = I_p^{(a)}[\exp -jk\rho\cos\theta_0\cos\alpha_p] \tag{4b}$$

and

$$I_q^{(e)} = |I_q^{(e)}| \exp[-jqu_0] \tag{4c}$$

---

*This is not strictly true for an element on a ground plane, but the deviation is significant only where the amplitude is small – that is, past 90° – so the assumption has negligible effect on computed result.

The superscripts (a) and (e) indicate azimuth and elevation distributions, respectively. Note that the azimuth distribution depends on the beam-pointing angle in both azimuth and elevation, whereas $I_q^{(e)}$ depends only on θ_o. Writing the current distribution in the form (4a) allows us to write the pattern (2) in the form

$$E(\varphi,\theta) = E^{(a)}(\varphi,\theta)\, E^{(e)}(\theta) \tag{5a}$$

where

$$E^{(a)}(\varphi,\theta) = \sum_p I_p^{(a)}\, G(\varphi-\alpha_p,\theta) \tag{5b}$$

and

$$E^{(e)}(\theta) = \sum_q I_q^{(e)} \exp\,[\,jqu] \tag{5c}$$

$E^{(a)}(\varphi,\theta)$ is just the pattern of a single ring excited by $I_p^{(a)}$. $E^{(e)}(\theta)$ is the space factor of a single vertical column of elements excited by $I_q^{(e)}$.

Thus, the analysis can be simplified by assuming the separable-aperture distribution and considering the cylindrical-array pattern to be the product of a ring-array pattern and a linear-array pattern. A pencil beam can be formed by selecting $I_p^{(a)}$ to form a beam at $\varphi = 0$ in the azimuth cone $\theta = \theta_o$, and by selecting $I_q^{(e)}$ to form a beam at θ_o in the elevation plane $\varphi = 0$. Since the pencil beam is the product of two fan beams, the principal sidelobes will lie on the cone and plane in which the fan beams were shaped.

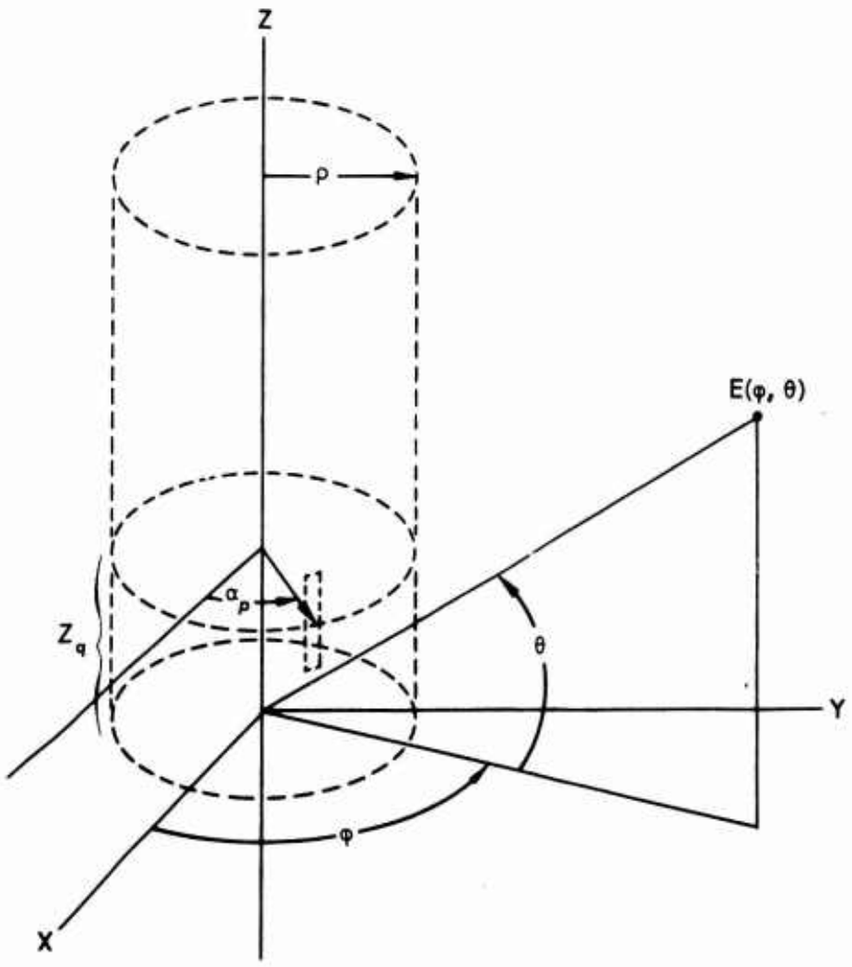

Figure 1. Coordinate system.

Synthesis on Ring with Continuous Current

Synthesis on a ring can be carried out by assuming that there is a continuous current density $I(\alpha)$ exciting the ring and further that the full 360 degrees is excited. The pattern is

$$E(\varphi, \theta) = \frac{M}{2\pi} \int_0^{2\pi} I(\alpha)\, G(\varphi - \alpha, \theta)\, d\alpha \tag{6}$$

M is the number of elements which the continuous distribution replaces. If $I(\alpha)$ is symmetrical, it may be written

$$I(\alpha) = \sum_{n=0}^{\infty} I_n \cos n\alpha \tag{7}$$

The I_n are the complex-current-mode amplitudes. The element factor $G(\varphi - \alpha, \theta)$ may also be expanded as

$$G(\varphi - \alpha, \theta) = f(\theta) \sum_{m=0}^{\infty} F_m(\theta) \cos m(\varphi - \alpha) \tag{8}$$

Substitution of (7) and (8) into (6) and integrating yield

$$E(\varphi, \theta) = Mf(\theta) \sum_{n=0}^{\infty} \frac{1}{\epsilon_n} I_n F_n(\theta) \cos n\varphi \tag{9}$$

where $\epsilon_n = 1$ if $n = 0$, $\epsilon_n = 2$ if $n \neq 0$. The I_n are determined from the desired azimuth pattern expanded in a Fourier series. We call the desired pattern $T_n(\varphi)$ to indicate an N^{th}-order Chebyshev pattern, though any pattern may be used if it can be put in the following form:

$$T_n(\varphi) = \sum_{n=0}^{N} C_n^N \cos n\varphi \tag{10}$$

Equating (10) and (11) at $\theta = \theta_0$ yields

$$I_n^{(\theta_0)} = \frac{\epsilon_n C_n^N}{Mf(\theta) F_n(\theta)} \tag{11a}$$

and

$$I^{(\theta_0)}(\alpha) = \sum_{n=0}^{N} I_n^{(\theta_0)} \cos n\alpha \tag{11b}$$

The superscript (θ_0) has been introduced to emphasize that I_n and $I(\alpha)$ give the optimum azimuth pattern $T_n(\varphi)$ only in the cone $\theta = \theta_0$. At a general elevation angle θ the pattern is

$$E^{(\theta_0)}(\varphi, \theta) = Mf(\theta) \sum_{n=0}^{N} I_n^{(\theta_0)} F_n(\theta) \cos n\varphi \tag{12}$$

Reference 2 gives details for computing C_n^N and the $F_n(\theta)$ for various element types,* plus some criteria for selecting the pattern order N. It is found necessary to let $N^{(\theta_0)} = N \cos \theta_0$, where $N_0 \approx k\rho$ is N at $\theta_0 = 0$. This selection of $N^{(\theta_0)}$ gives approximately the same amplitude distribution for all θ_0, and a beam cophasal phase. For a given sidelobe level, the beamwidth is approximately proportional to $\frac{1}{N}$. Thus

*Mutual coupling may be simply taken into account by use of $F_n(\theta)$ computed for elements in the array environment. See reference 1 for details.

$$\text{azimuth beamwidth} \approx \text{beamwidth at broadside}/\cos\theta_0 \tag{13}$$

This broadening of the beamwidth is only apparent, however. It is due to the fact that the azimuth pattern is measured on a cone $\theta = \theta_0$, and the ratio of the perimeter of the cone base at θ_0 to that at $\theta = 0$ is just $(\cos\theta_0)^{-1}$. The actual spatial extent of the beam in the plane perpendicular to the $\varphi = 0$ plane remains approximately constant to near zenith.

Figures* 2 and 3 show the behavior of (12) for $\theta_0 = 0$ and $\theta_0 = 45°$. The distribution is for a –50-dB Chebyshev pattern, so only the beam shape appears in the plot (all sidelobes are at –50 dB for $\theta = \theta_0$). The extensive beam broadening (beyond the $(\cos\theta_0)^{-1}$ factor) and gain loss for $\theta \neq \theta_0$ are due to the deviation of the phase from the optimum (which is essentially identical to (4b)). Figure 4* shows elevation patterns through the beam $\varphi = 0$ direction with the azimuth pattern optimized at various θ_0. They are compared with the element elevation pattern, since this represents the maximum possible for each curve. For a linear array the curves would all coincide with the elevation element pattern. For the ring array they coincide with the elevation element pattern only at θ_0, where all elements add in phase to form the beam.

Discrete-Current Distribution

The continuous distribution can be replaced by M elements located at

$$\alpha_p = \frac{2\pi}{M}(p+f) \qquad p = 0, 1, 2, \ldots, M-1$$

where f is a fraction that indicates the position of the beam with respect to the first element. It can be shown[2] that

$$E(\varphi,\theta) = M \sum_{n=0}^{N} \frac{1}{\varepsilon_n} I_n^{(\theta_0)} \{ F_n(\theta) \cos n\varphi + \sum_{r=1}^{\infty} F_{rM-n}(\theta) \cos[(rM-n)\varphi - 2\pi rf] \} \tag{14}$$

(14) is the desired pattern plus an error term. For spacing $s = \frac{2\pi\rho}{M}$ of less than a half wavelength, only the $r = 0$ term is significant. For spacing less than one wavelength, only $r = 0$ and $r = 1$ contribute, and so forth. The error term's primary contribution to the pattern is in the form of a grating lobe.

---

*Figures 2, 3, and 4 use $N^{(\theta_0)} = N_0 \cos\theta_0$, $N_0 = 128$, and $f(\theta)F_n(\theta)$ for an axial slot in a cylindrical ground plane of radius $\rho = 26.3\lambda$. The height of the slot is 0.72λ.

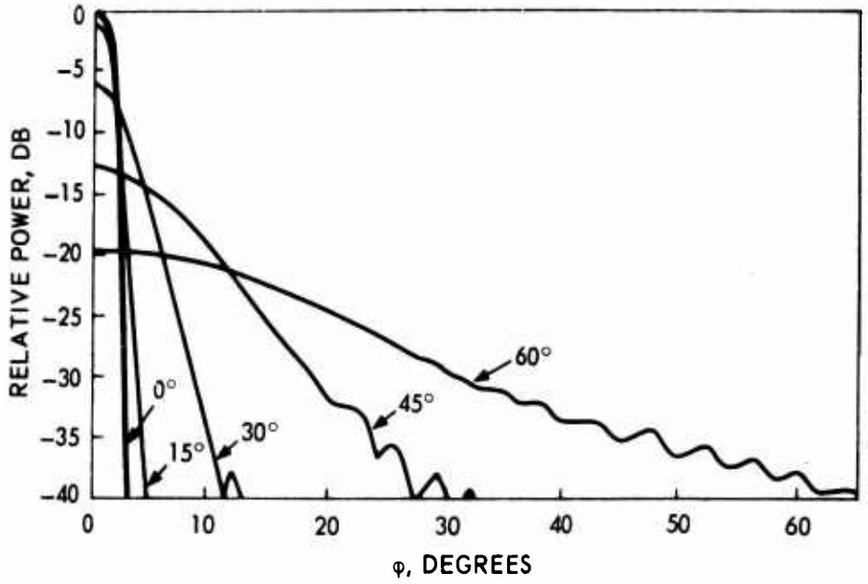

Figure 2. Ring-array pattern for $\theta_0 = 0°$, −50-dB continuous Chebyshev distribution. $N^{(\theta_0)} = N_0 \cos \theta_0$, $N_0 = 128$, and element is axial slot in cylindrical ground plane of radius $\rho = 26.3\,\lambda$

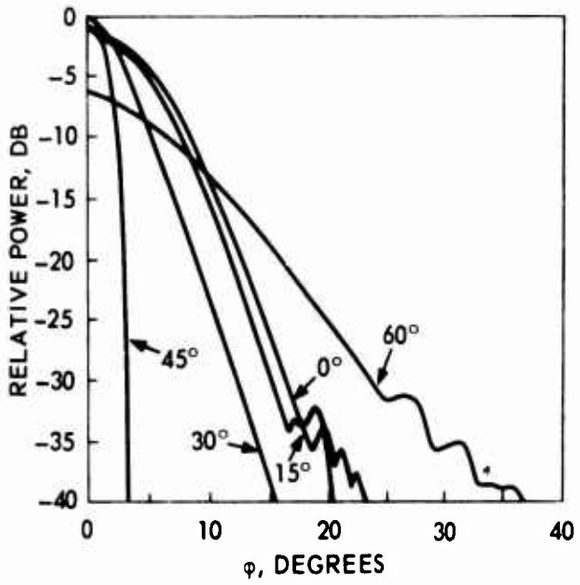

Figure 3. Ring-array pattern for $\theta_0 = 45°$. Other parameters same as in figure 2.

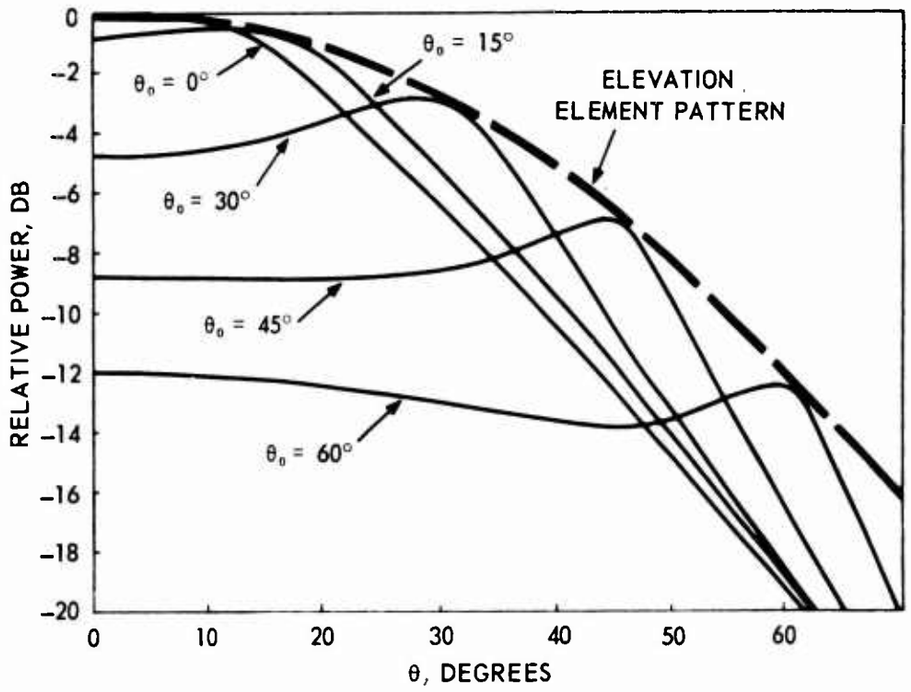

Figure 4. Ring-array elevation patterns through the beam for azimuth pattern optimized at various θ_0 compared with element elevation pattern. Parameters same as in figure 2.

GRATING LOBE FOR CYLINDRICAL ARRAY

Regular Array

Elevation scan to θ_0 is achieved by adding the phase $-qkd \sin \theta_0$ to the q^{th} ring. The performance of the array pattern in the plane $\varphi=0$ is now the same as for a linear array with ring-array "elements" with patterns such as those in figure 4. In particular, a grating lobe appears at θ when

$$\frac{d}{\lambda}(\sin\theta - \sin\theta_0) = \pm m \qquad m = 1, 2, \ldots \tag{15}$$

The lobe is at $\varphi = 0$ in azimuth because $E^{(a)}(\varphi, \theta)$ has its maximum at $\varphi = 0$ (or nearly so) for all θ. The grating lobe as it arises from $E^{(e)}(\theta)$ has unit magnitude (equal to main beam), but is reduced by $E^{(a)}(\varphi = 0, \theta)$.

Staggered Array

Staggering alternate columns of elements on the cylinder is an effective means of extending the elevation-scanning angle for a given ring-to-ring spacing d and maintaining a small grating lobe.

Consider the staggered array as a superposition of two regular arrays, each with the normal number of rings Q but only half the number of elements in each ring $\frac{M}{2}$. The subarrays are identical except one is rotated by half a spacing in azimuth and is raised by half a spacing in the vertical direction, with the phase compensating for the dislocation. The ring-array patterns for the subarrays can be written as follows, from (14):

Array I – The beam in the direction of the first element; that is, $f = 0$.

$$EI = f(\theta) \sum_n I_n^{(\theta_0)} F_n(\theta) \cos n\varphi + f(\theta) \sum_n I_n^{(\theta_0)} F_{\frac{M}{2}-n}(\theta) \cos\left(\frac{M}{2} - n\right) \varphi$$

$$+ f(\theta) \sum_n I_n^{(\theta_0)} F_{M-n} \cos (M - n) \varphi \qquad (16)$$

The $r = 2$ term, which ordinarily would not contribute (for $s < \lambda$) is included, because the spacing is now double the normal spacing.

Array II – The beam is in a direction halfway between two elements; that is, $f = 0.5$.

$$EII = f(\theta) \sum_n I_n^{(\theta_0)} F_n(\theta) \cos n\varphi - f(\theta) \sum_n I_n^{(\theta_0)} F_{\frac{M}{2}-n}(\theta) \cos\left(\frac{M}{2} - n\right) \varphi$$

$$+ f(\theta) \sum_n I_n^{(\theta_0)} F_{M-n} \cos (M - n) \varphi \qquad (17)$$

If the array were not staggered, each ring would have M elements and a pattern

$$E^{(a)}(\varphi, \theta) = f(\theta) \sum_n I_n^{(\theta_0)} F_n(\theta) \cos n\varphi + f(\theta) \sum_n I_n^{(\theta_0)} F_{M-n}(\theta) \cos (M-n) \varphi \qquad (18)$$

The grating-lobe term that arises because of the doubling of the spacing is

$$E^{g.\ell.}(\varphi, \theta) = \sum_n I_n F_{\frac{M}{2}-n} \cos\left(\frac{M}{2} - n\right) \varphi \qquad (19)$$

Assume Array II is raised with respect to Array I by $\frac{d}{2}$ and multiplied by exp $[jk\frac{d}{2}(\sin\theta - \sin\theta_0)]$ to account for the phase. The patterns of cylindrical Arrays I and II are then

$$EI(\varphi,\theta) = \sum_{q=1}^{Q} |I_q| \exp[jqkd(\sin\theta - \sin\theta_0)] \; [E^{(a)}(\varphi,\theta) + E^{g.\ell.}(\varphi,\theta)]$$

and

$$EII(\varphi,\theta) = \exp[jk\frac{d}{2}(\sin\theta - \sin\theta_0)] \sum_{q=1}^{Q} |I_q| \exp[jqkd(\sin\theta - \sin\theta_0)]$$

$$X[E^{(a)}(\varphi,\theta) - E^{g.\ell.}(\varphi,\theta)] \tag{20}$$

The sum of EI and EII is the pattern of the staggered array. It may be put in the form

$$E(\varphi,\theta) = \left\{\sum_{q=1}^{2Q} |I_q| \exp[jqk\frac{d}{2}(\sin\theta - \sin\theta_0)]\right\} \cdot E^{(a)}(\varphi,\theta)$$

$$+ \left\{\sum_{q=1}^{Q} |I_q| \exp[jqkd(\sin\theta - \theta_0)]\right\} \cdot \left\{1 - \exp[jk\frac{d}{2}(\sin\vartheta - \sin\theta_0)]\right\}$$

$$\cdot E^{g.\ell.}(\varphi,\theta) \tag{21}$$

The first term of (21) is the pattern of an array of $2Q$ rings spaced at half the normal spacing with M elements on each ring; that is, the staggered array with the "holes" filled in. This term should give no grating lobe because of the half spacing in elevation and the normal spacing in azimuth.

The second term accounts for the grating lobe. The factor

$$\sum_{q=1}^{Q} |I_q| \exp[jqkd(\sin\theta - \sin\theta_0)]$$

is the linear-array pattern for normal elevation spacing, and gives a grating lobe when

$$\frac{d}{\lambda}(\sin\theta - \sin\theta_0) = \pm 1 \tag{22}$$

This gives

$$1 - \exp[jk\frac{d}{2}(\sin\theta - \sin\theta_0)] = 2$$

Thus, the grating lobe of the cylindrical staggered array is equal to the grating lobe of the linear array, with spacing d, times the grating lobe of a ring array, with spacing $2s$. The elevation and azimuth positions of the product lobe are the positions of the linear- and ring-array lobes, respectively. The staggered-array lobe appears at the same elevation angle as the lobe of the regular array but is removed from $\varphi = 0$ to $\varphi = \varphi^{g.\ell.}$ as determined from a ring array with every other element removed. The advantage gained is the amount the grating lobe of the ring subarrays is down from the main beam.

In obtaining (21), we started with equation (14). However, we could as well have started with (5b), using $\alpha = \frac{2\pi}{M}(p+f)$. Also, we assumed $f=0$ for Array I and $f=0.5\lambda$ for Array II. (21) depends only on the fact that $E^{g.\ell.}(\varphi,\theta)$ for Array I is equal to $-E^{g.\ell.}(\varphi,\theta)$ for Array II, which is true for any orientation of the first element with respect to the main beam. Thus, (21) is valid for cylindrical-arc arrays in general. Furthermore, we may easily identify $E^{g.\ell.}(\varphi,\theta)$ from patterns computed directly from (5b) with alternate elements excited.

Figure 5 shows $E^{(a)}(\varphi,\theta) + E^{g.\ell.}(\varphi,\theta)$ and for comparison $E^{(a)}(\varphi,\theta)$ for $\theta_0 = 30°$. These patterns are computed from (5b),* and the contribution from $E^{g.\ell.}(\varphi,\theta)$ is easily identified.

Principal Sidelobes

For the regular array the principal sidelobes will lie on the plane $\varphi=0$ and the cone $\theta=\theta_0$, because the regular-array pattern, for the separable distribution, can be thought of as the product of two fan beams.

For the staggered array we can consider equation (21). The first term is the product of a linear-array fan beam and a ring-array fan beam, giving principal sidelobes as a regular array on the plane $\varphi=0$ and the cone $\theta=\theta_0$. The second term gives another set of axes, however. The first two factors of the second term give the linear-array grating lobe (without the main beam); the third factor gives the ring-array grating lobe (with double spacing). Thus, another set of principal sidelobes lies on the cone $\theta=\theta^{g.\ell.}$ and the warped plane $\varphi=\theta^{g.\ell.}(\theta)$ where $\theta^{g.\ell.}$ is given by (22) and $\varphi^{g.\ell.}(\theta)$ gives a maximum to $E^{g.\ell.}(\varphi,\theta)$.

For the regular array, then, the full cylindrical-array pattern is well represented by two contours through φ, θ space, (φ,θ_0) and $(0,\theta)$. For the staggered array, the full pattern is well represented by the four contours (φ,θ_0), $(0,\theta)$, $(\varphi,\theta^{g.\ell.})$ and $(\varphi^{g.\ell.}(\theta),\theta)$. Figure 6 presents the patterns for regular and staggered arrays at various θ_0. The same single-ring parameters are assumed as for figure 5; in addition, 32 rings spaced at 0.72λ are used with a 30-dB Chebyshev distribution for $I_q^{(e)}$. The contour $(\varphi^{g.\ell.}(\theta),\theta)$ was determined from the patterns of figure 5 by interpolation between the maximum points on the grating lobe.

The grating lobe can be reduced and elevation scan extended by reducing the azimuth and/or elevation spacing of the staggered array. For example, reducing the azimuth spacing from 0.65λ to 0.5λ (with $d = 0.72\lambda$) increases the scan-angle limit from 30° to about 40° to maintain a grating lobe of 30 dB, and further reduction to 0.4λ allows scanning to above 75° with the grating lobe below 40 dB. Reduction of elevation spacing (with $s = 0.65\lambda$) from 0.72 to 0.6λ allows scanning to above 50° for a grating lobe below 40 dB.

---

*Figures 5 and 6 are for 44 active elements spaced at 0.65λ on a radius of 26.3λ. A projected 30-dB Chebyshev distribution is assumed with an element pattern $|G(\varphi-\alpha,\theta)| = \cos(\varphi-\alpha)\cos\theta$. All patterns are normalized to the beam at $\theta_0=0$. The patterns are symmetrical about both $\theta=0$ and $\varphi=0$.

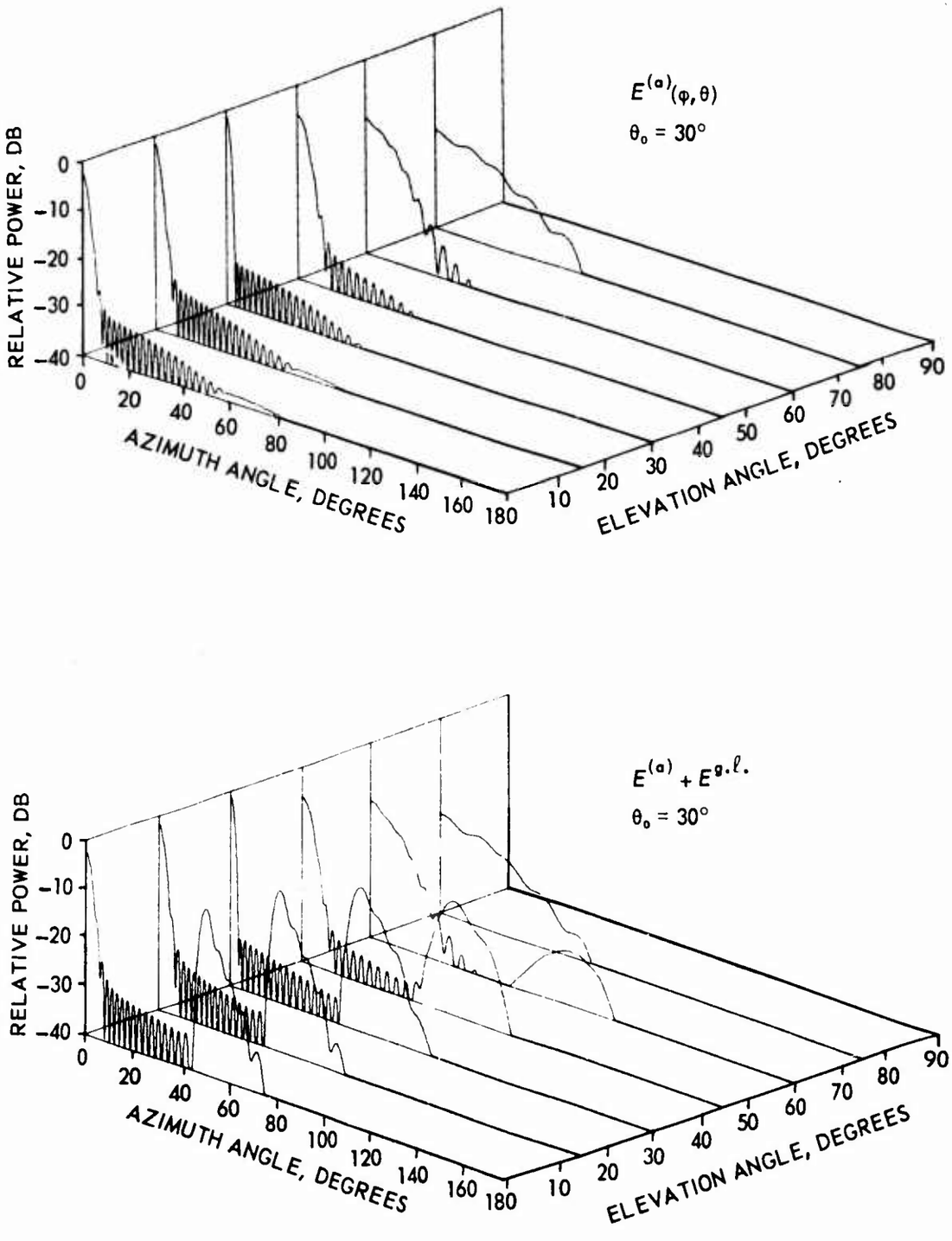

Figure 5. $E^{(a)}(\varphi, \theta) + E^{g.\ell.}(\varphi, \theta)$ and $E^{(a)}(\varphi, \theta)$ for $\theta_0 = 30°$. Forty-four active elements spaced at 0.65λ on a radius of 26.3λ, with a projected 30-dB Chebyshev distribution and cosine element pattern.

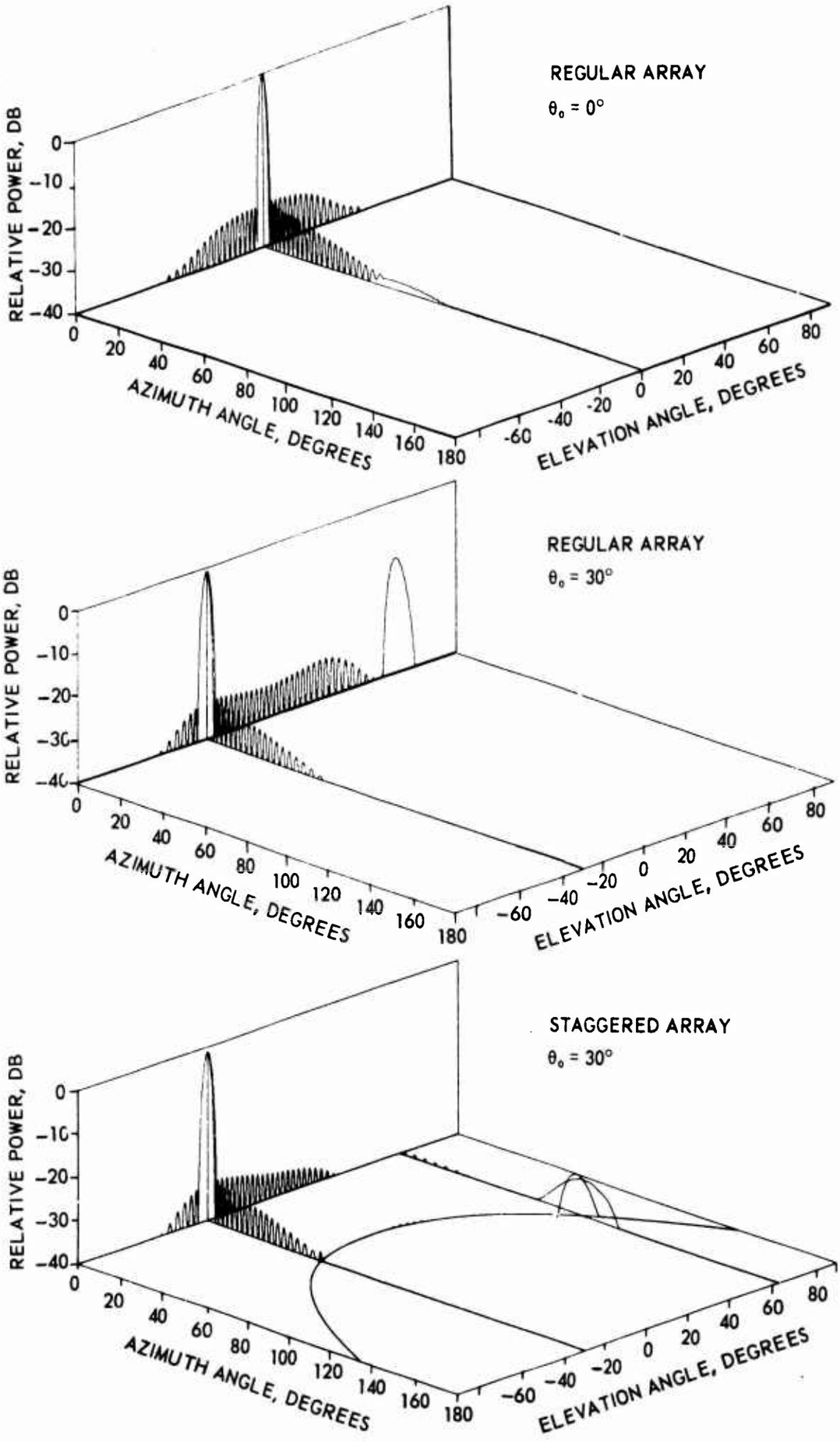

Figure 6. Patterns for regular and staggered arrays at various θ_0. Ring-array elements as in figure 5. Vertical spacing is 0.72λ, and 32 rings are assumed with a 30-dB Chebyshev distribution.

ANALYSIS OF CONICAL ARRAY

It was shown that the cylindrical array aperture is partially separable and that as a result the elevation and azimuth patterns could be controlled by factoring the aperture into linear and ring array distributions. The required phase correction from the conical surface to a planar phase front does not allow this for the conical array. Nevertheless, it is reasonable to assume a separation of amplitude distributions if the cone angle is not too large. For this analysis, the parameters will be the same as for the cylindrical array of figure y, with beam cophasal phase and a mean radius equal to the radius of the cylindrical array. The staggered configuration is assumed as shown in figure 7.

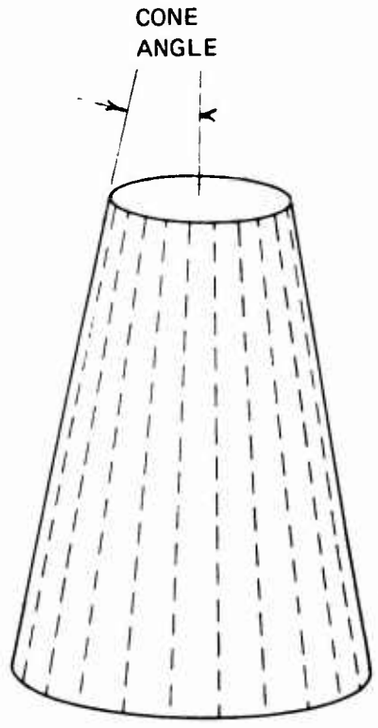

Figure 7. Staggered-element configuration used for the pattern-analysis

Beamwidth Performance

The variation of elevation beamwidth with scan angle for cone angles of 0, 15, and 30 degrees is shown in figure 8. In each case the beamwidth is a minimum when the beam is formed in a direction normal to the cone surface. In fact, except for a displacement, the curves are so similar that it can be concluded that performance in this respect can be easily predicted from the behavior of a constituent linear array on the conical surface at the same azimuth angle as the beam. The variation of the azimuth beamwidth as a function of the same parameters is shown in figure 9. In this case there is little or no dependency on cone angle, each curve exhibiting a minimum value in the horizontal plane. As described in the cylindrical array analysis section, there is inherently a beam broadening factor of $1/\cos\theta_0$ due to coordinate system. The variation shown in figure 9 is close to this, irrespective of cone angle, thus indicating that the azimuth beamwidth measured in the plane of the beam is close to constant, being independent of both the scan angle and the angle of the cone in the range covered. In summary, the beamwidths of the conical array exhibit no unusual characteristics, the position of optimum behavior being in a direction normal to the surface of the cone.

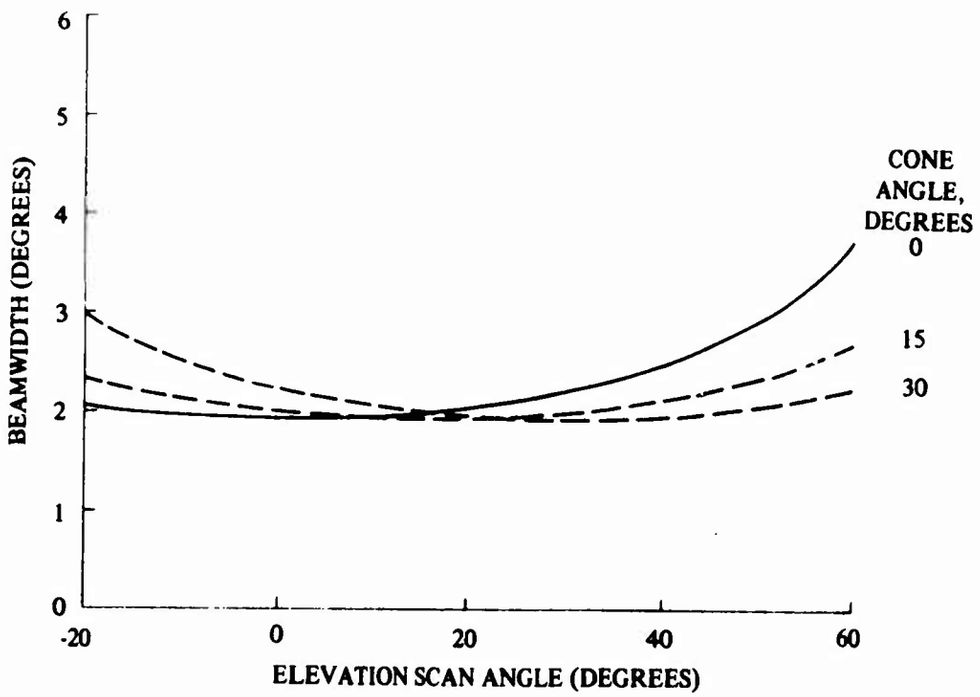

Figure 8. Elevation beamwidth as a function of scan angle for various cone angles.

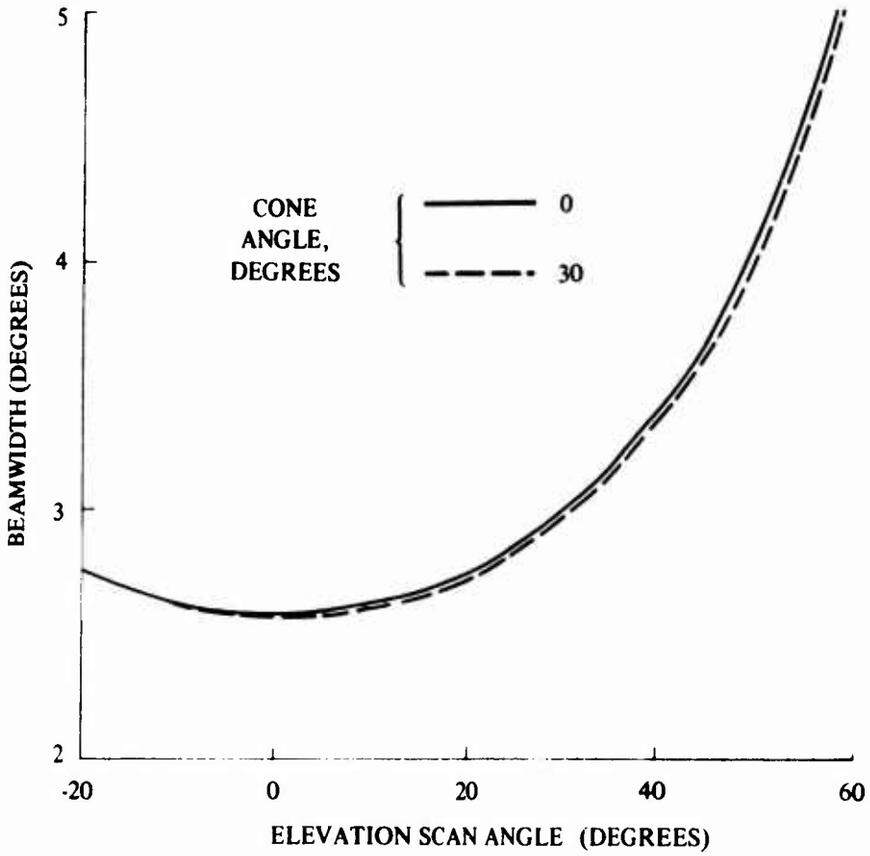

Figure 9. Azimuth beamwidth as a function of elevation scan angle for cylindrical and conical arrays.

Sidelobe Levels

The structure of the sidelobes of planar and cylindrical arrays can be easily established because the radiation patterns of these structures can be written as a product of two factors. These factors individually control the sidelobe behavior in orthogonal directions. The radiation pattern of the conical array has no similar product representation and consequently there is no easy method of predicting sidelobe levels. The vertical plane through the center of the active sector, however, being a plane of symmetry, will contain the elevation sidelobes. Radiation patterns in this plane for a cone angle of 30 degrees and a number of elevation beam angles are given in figure 10. For comparison, corresponding patterns for a cylindrical array with a radius equal to the mean radius of the conical structure were given in figure 6. These diagrams indicate that the conical array is little different from the cylinder in regard to elevation sidelobe levels. This result is to be expected since their behavior in this plane is almost entirely controlled by the vertical linear arrays that make up both geometries.

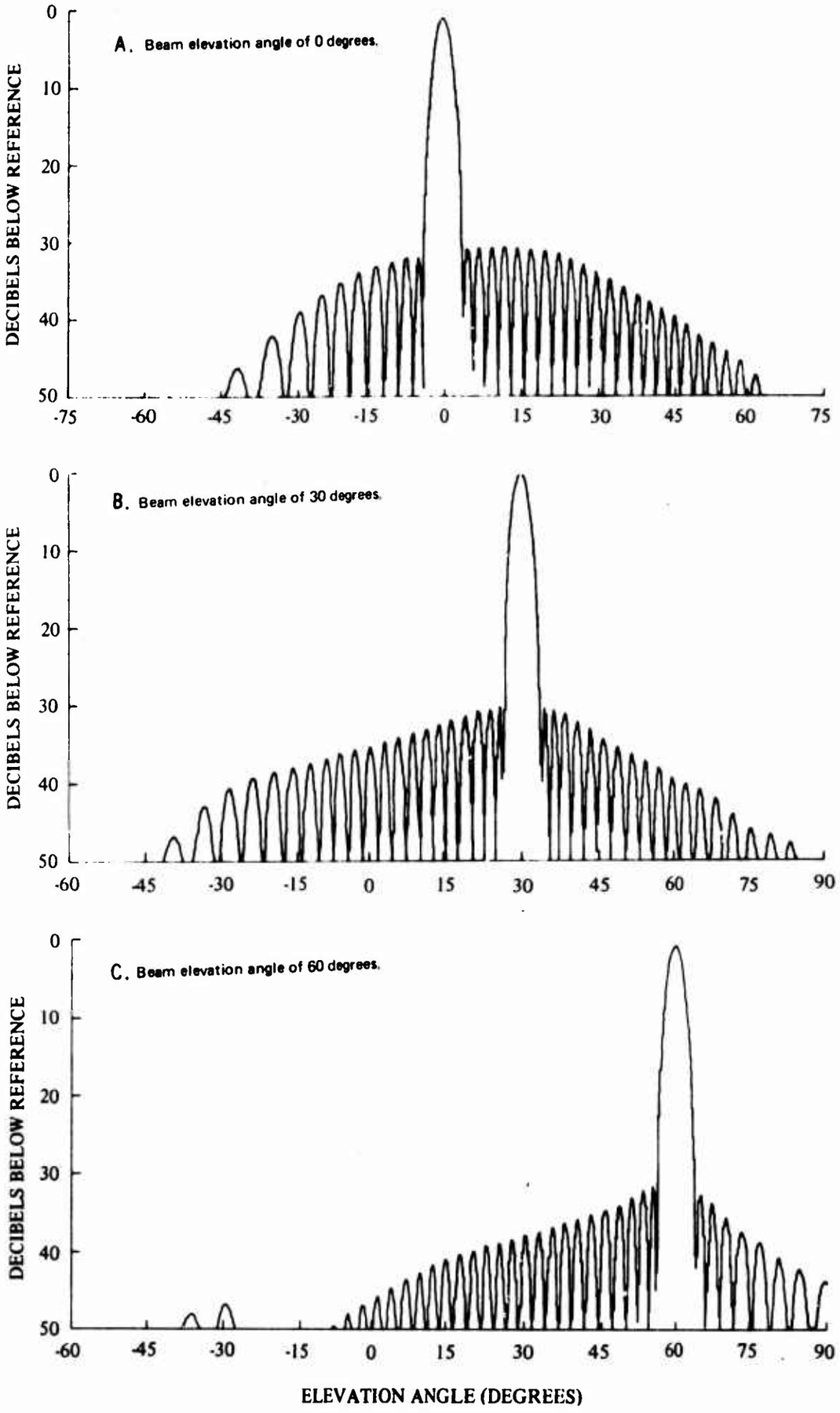

Figure 10. Elevation patterns of the conical array of 30-degree angle for various beam elevation angles.

In contrast, sidelobe structure in azimuth shows significant differences; the reasons are most easily understood by accepting the premise that the total pattern consists of a summation of contributions from the individual linear arrays. On a cylinder such arrays have their axes aligned. When a beam is formed at a particular elevation angle, each array is phased to produce a maximum contribution in this direction. Individually the linear arrays form fan beams at a constant angle to their axes, with each of these fan beams passing through the main beam direction. The axial alignment of all vertical arrays results in the coincidence of all such "radiation cones," the azimuth sidelobes and the main beam being formed within this surface. For the cylindrical array, therefore, the azimuth sidelobes lie on a conical surface about the axis of the array, its zenith angle being the same as that of the main beam. The main beam of the conical array is formed in the same manner, each vertical linear array forming a fan beam on a radiation cone passing through the beam location. In this case, however, the nonalignment of the array axes causes these cones to diverge from one another at points away from the main beam. This is illustrated in figure 11 where the location of these radiation cones in terms of spherical coordinates is shown for vertical arrays spaced five degrees apart in the active sector (the angle of the conical array is 30 degrees, the main beam elevation angles being 0, 30, and 60 degrees respectively). In the array under study this sector extends 30.23 degrees either side of center so that the outer curves in these diagrams give an indication of the

A. Beam elevation angle of 0 degrees.

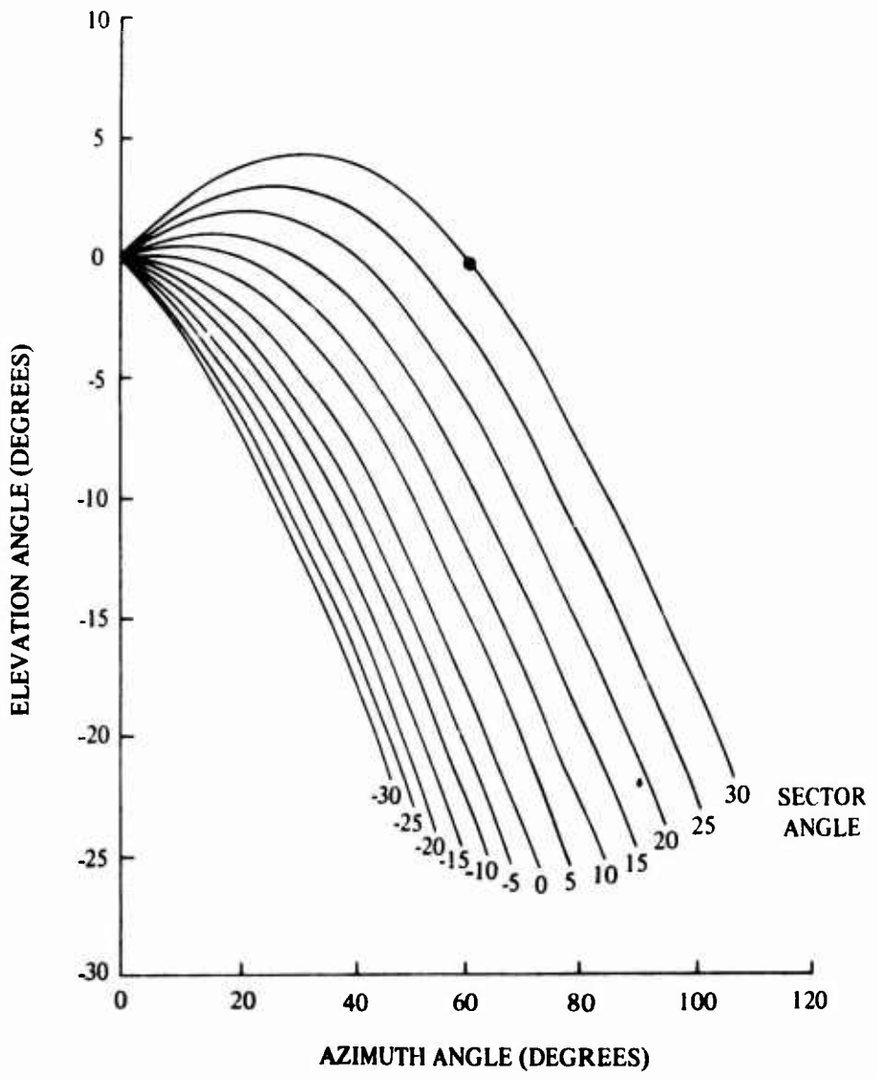

Figure 11. Contours of the linear array radiation cones from a 30-degree conical array for various beam elevation angles.

C. Beam elevation angle of 60 degrees.

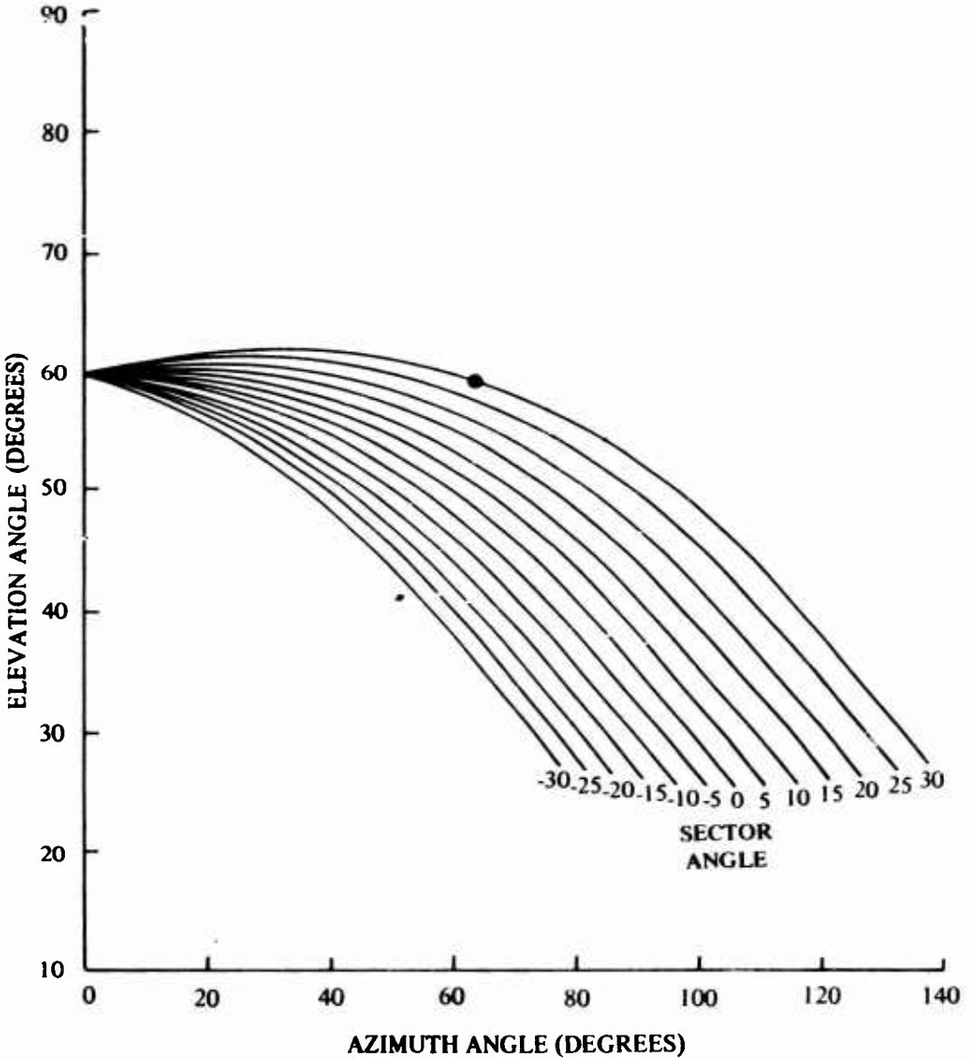

Figure 11. (Continued)

B. Beam elevation angle of 30 degrees.

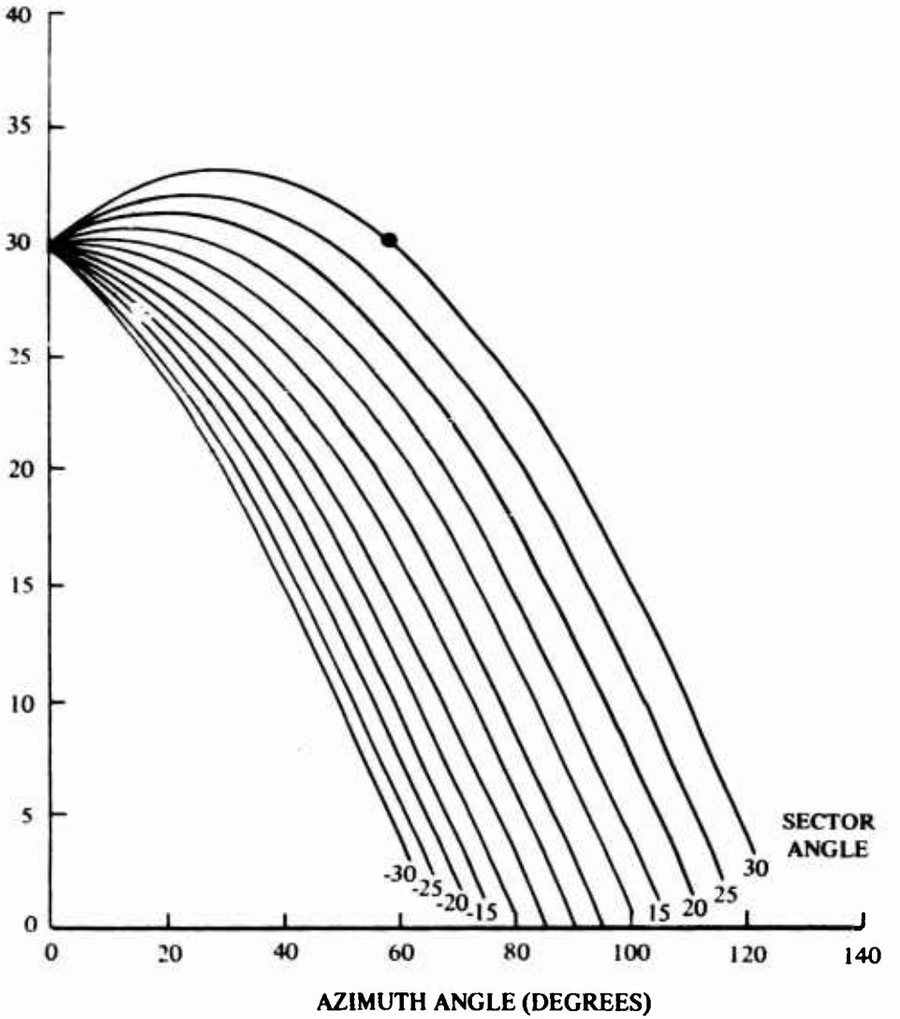

Figure 11. (Continued)

spread of the azimuth sidelobe energy. On figure 11 the cuts along which these patterns are taken are horizontal lines through the beam positions. Since the sidelobe energy is spread out, it may be more meaningful to plot azimuth patterns on a contour through the center of the curves given in these diagrams. Figure 12 gives the azimuth patterns (i.e., taken at a constant elevation angle) of the conical array for beam positions of 0, 30, and 60 degrees in elevation. The sharp decline of the sidelobes with azimuth angle is a direct consequence of the spreading described above. Figure 6 gave the corresponding patterns for a cylindrical array. Figure 13 shows patterns plotted along the center contours of figure 11 (i.e., sector angle of zero) for each of the three beam elevation angles being used. There is little difference between figures 12 and 13 as far as close-in sidelobes are concerned. However, patterns in figure 12 do show subsidiary peaks not present in the patterns of figure 13. The circles on figure 11 show the location of these peaks that are seen to lie on the contours of the radiation cones of the outer arrays of the active sector. These arrays have twice the amplitude of their neighbors due to the Chebychev distribution, and this is an explanation for the higher sidelobe energy on the outer contours.

A. Beam elevation angle of 0 degrees.

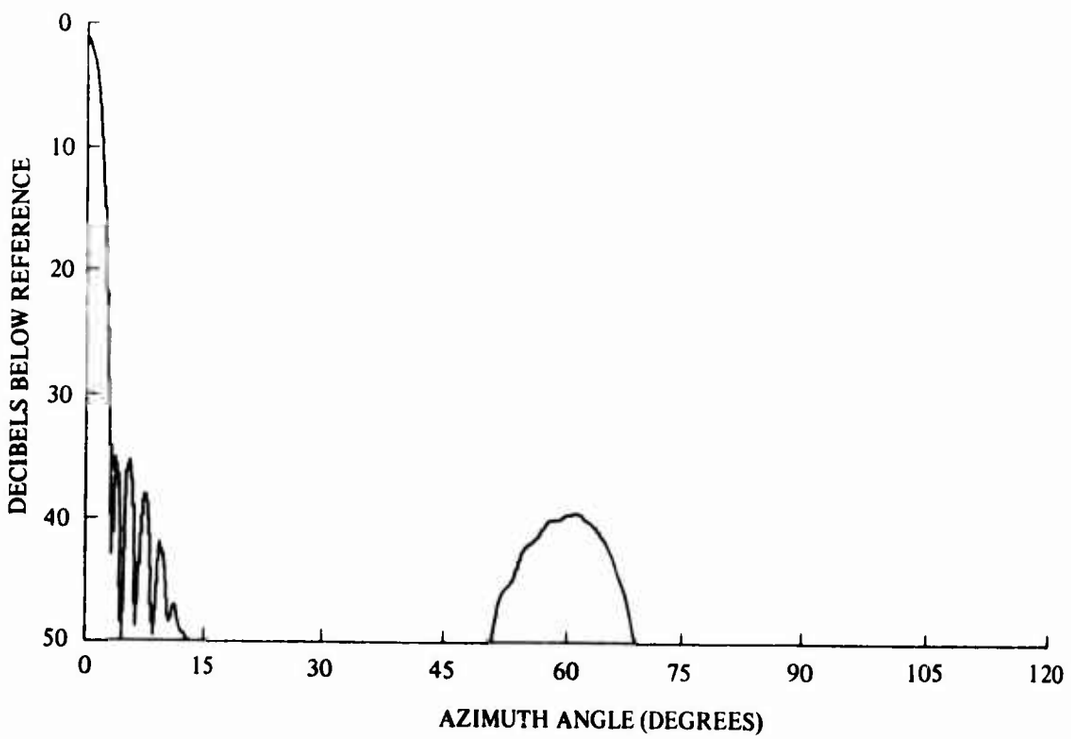

Figure12. Azimuth patterns of the conical array (30-degree angle) for various beam elevation angles.

B. Beam elevation angle of 30 degrees.

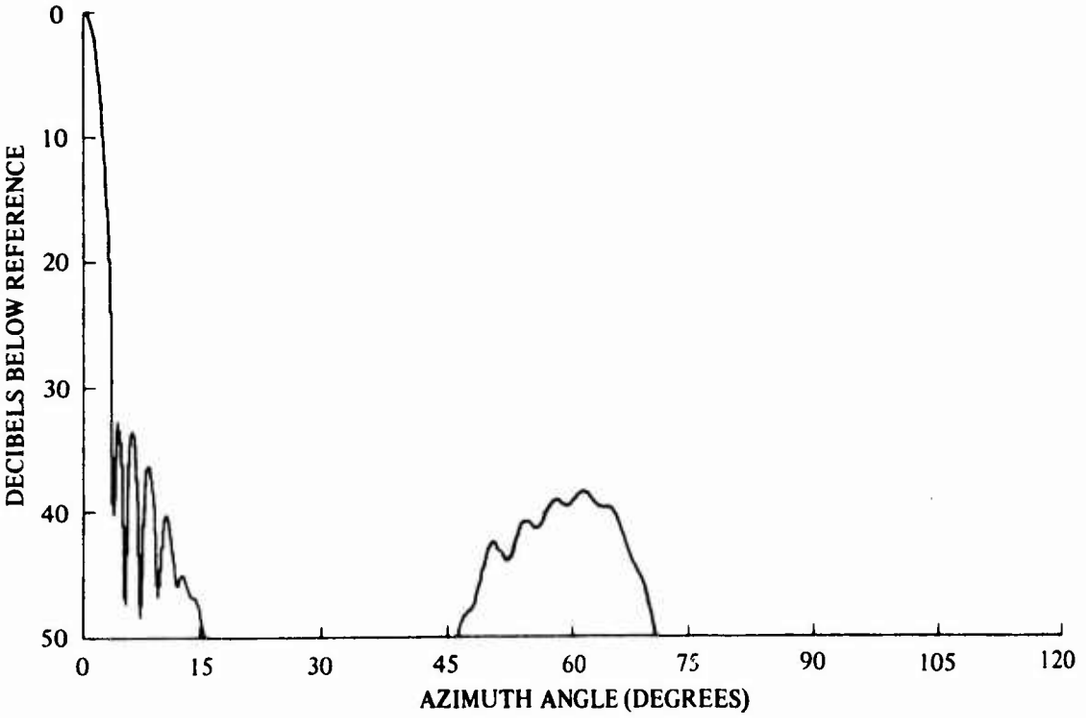

C. Beam elevation angle of 60 degrees.

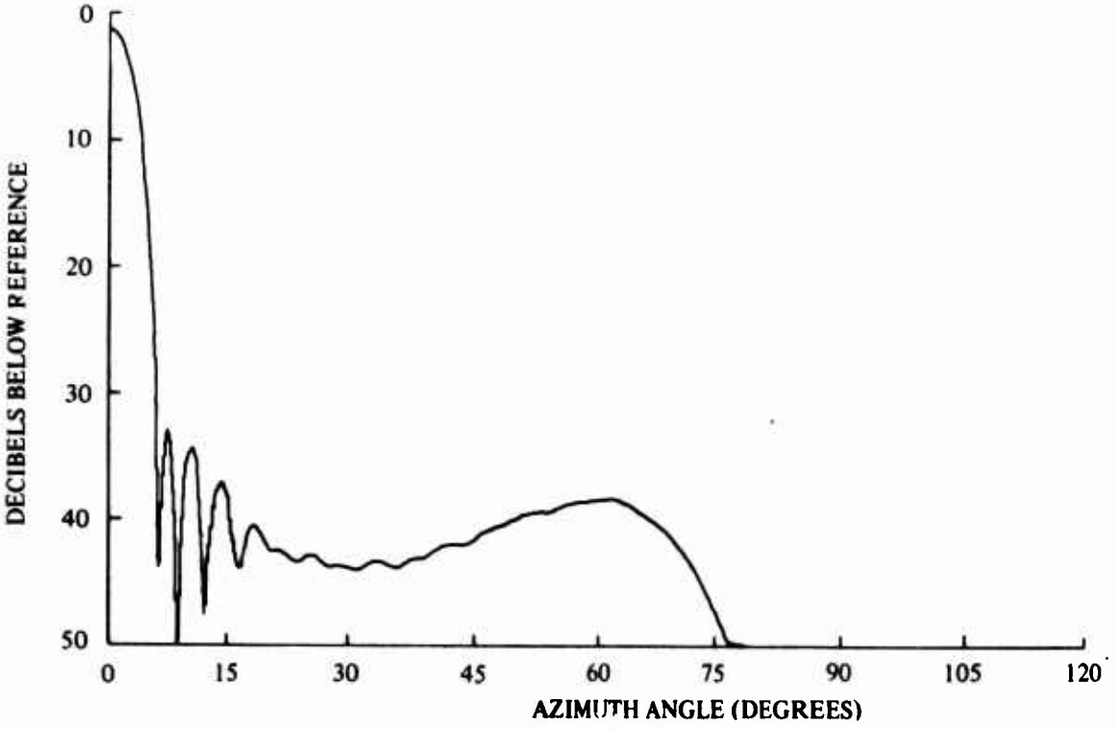

Figure 12. (Continued).

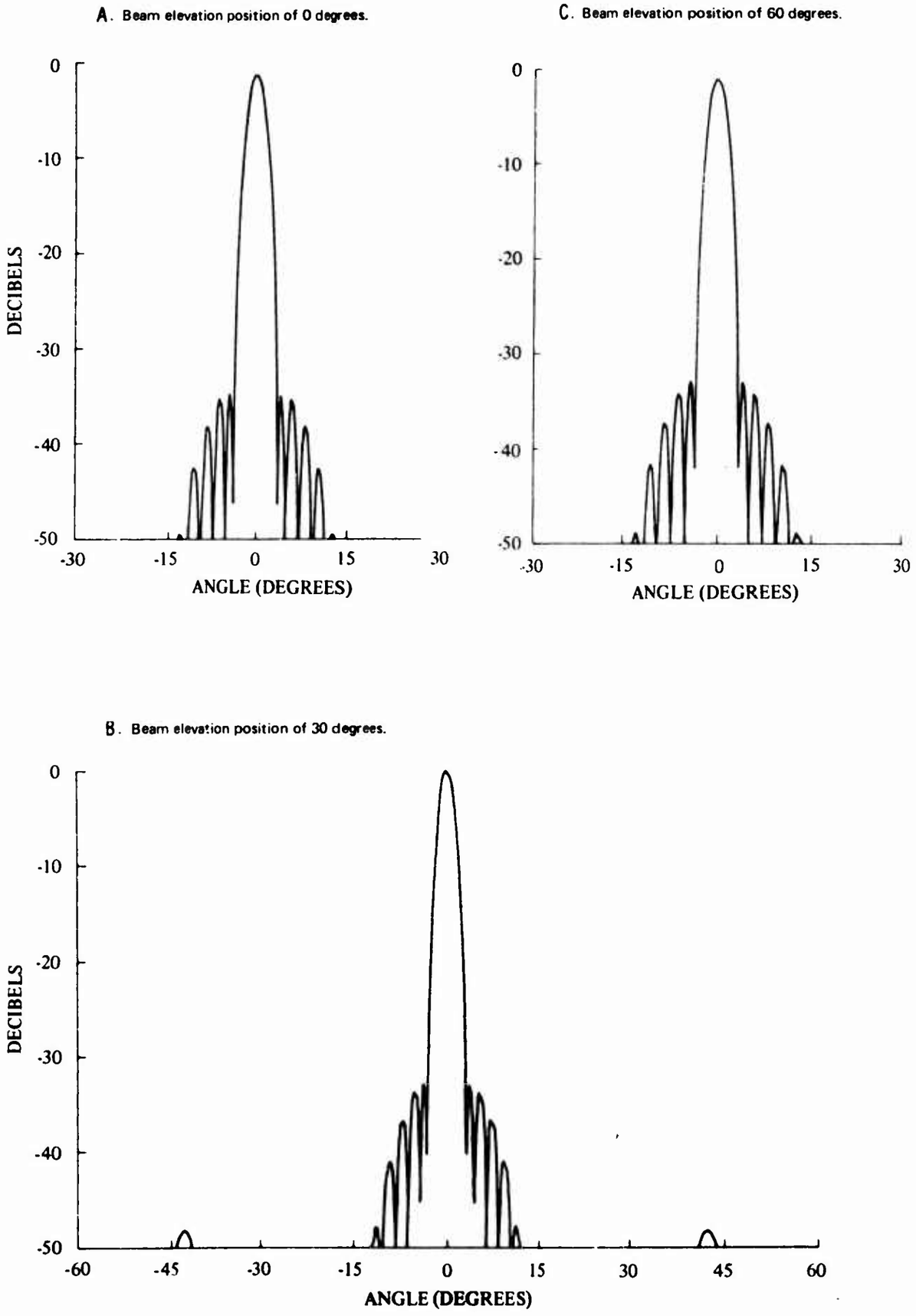

Figure 13. Patterns through the center of the azimuth energy distribution for a 30-degree conical array at various elevation beam positions.

The Grating Lobe

The grating lobes formed by individual linear arrays on a cylinder are coincident; the grating lobes formed by the linear arrays on a cone are dispersed. Typical contours of these grating lobes are shown in figure 14. It is reasonable to assume that this dispersal will result in a reduction of the grating lobe in the radiation pattern of the conical array when compared to that of the cylindrical array.

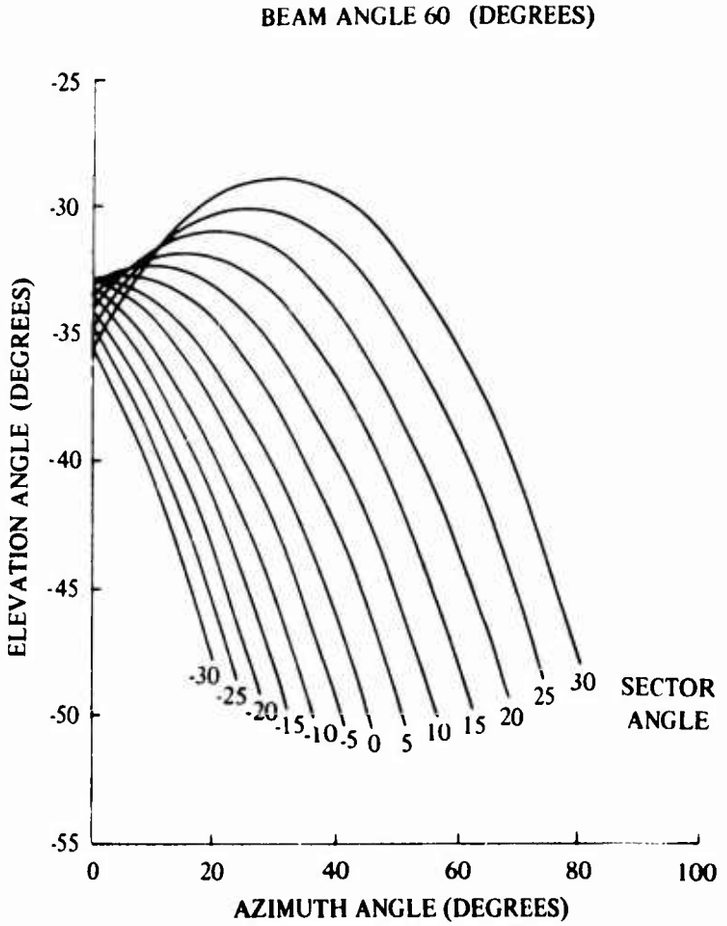

Figure 14. Contours of the grating lobes from linear arrays making up a cone of 30-degree angle.

REFERENCES

1. "Mutual Coupling on Cylindrical Arrays", by B. R. Gladman, this symposium record.

2. Naval Electronics Laboratory Center Report 1521, *Current Distributions and Radiation Patterns for Circular-Array Radar Antenna: Theory*, by A. D. Munger, 26 October 1967.

3. Naval Electronics Laboratory Center Report 1608, *Circular-Array Radar Antenna: Cylindrical-Array Theory*, by A. D. Munger, 15 January 1969.

4. Naval Electronics Laboratory Center Report 1630, *Multifunction Multi-frequency Integrated Arrays; Conical Array Studies*, by B. R. Gladman, 24 June 1969.

SCANNING A MULTI-LOBED PATTERN WITH A CYLINDRICAL ARRAY

Prepared for

CONFORMAL ARRAY ANTENNA CONFERENCE

January, 1970

NELC

San Diego, California

L. N. Shestag

Rantec Division, Emerson Electric Company

ABSTRACT

The application of a cylindrical array to forming and scanning a multi-lobed but nearly omni-beam will be discussed. Much of the information will be based on a computer simulation model that accurately predicts the array performance, including the scanning modulation, for a wide range of antenna parameters. The inter-relationships of antenna radius, frequency, and elevation angle will be emphasized. Curves showing the n-lobe mode behavior for radius versus frequency at a fixed angle will be presented. Likewise, the particular case of n = 9 will be discussed for radius versus frequency over a range of elevation angles. Both amplitude and phase modulation will be examined. Application of this technique to TACAN ground antenna design and performance will be presented, and will include a discussion of considerations unique to this problem such as incidental phase modulation, mutual coupling, and array radiator configuration.

SCANNING A MULTI-LOBED PATTERN WITH A CYLINDRICAL ARRAY

INTRODUCTION

The application of a cylindrical array to forming and scanning a multi-lobed quasi-omnidirectional pattern will be discussed. Work in this field has progressed slowly during the past half-dozen years and has lately received increasing attention. Recent results will be presented, however a good deal of the material is based on previous work dating to 1963.[1] It should be emphasized that the primary pattern for this application is omni-directional in the azimuth plane with a multi-lobed pattern superimposed on it. This is significantly different from applications requiring a pencil beam, and most of the design considerations reflect that difference. The application of this technology to the TACAN antenna will be discussed. In this case a nine-lobed, nearly omniazimuth pattern must be generated and rotated. The rotation causes the carrier signal to be amplitude modulated, and the behavior of this modulation is critical to the system performance. Most of the discussion will be concerned with the generation of precise azimuth modulation characteristics.

The initial portion of this discourse will be based on a mathematical model of a cylindrical array and computer simulation of its performance. The model allows the array's theoretical behavior to be studied, and accurately predicts performance, including the scanning modulation.

The primary terms of the model which influence the array characteristics will be outlined. Graphical data is presented which illustrates how the modulation behavior depends on the antenna radius, frequency, and elevation angle.

Two design examples are given which indicate how the fundamental array characteristics are analyzed and design parameters are chosen in order to achieve specific performance for TACAN antenna applications. A brief discussion is also included that considers problems unique to a cylindrical array used for this application. Such problems are due to the array element lattice, mutual coupling, and composite amplitude and phase excitation on the aperture. Consideration of these factors is important to understanding the performance of an actual antenna system. Much of the information included in this report is based on work done for the following contracts: (AF19(628)-3824, AF30(602)-4012, AF19(628)-67-C-0222).

MATHEMATICAL MODEL

The expected performance and the basic characteristics of this array antenna are based on computer simulation and analysis. Likewise, the design of such an antenna can be based largely on study of computer data that predicts its behavior for a wide range of design parameters. A mathematical model of the antenna was formulated which includes all the factors known to influence its behavior. This model has been programmed for computer analysis which will give the performance at any point in space or time and at any point in space as a function of time.

Furthermore, by means of Fourier analysis, it will give a complete description of the modulation. That is, the waveshape which is formed at any point in space is analyzed for its harmonic content and the phase of those harmonics.

The mathematical model represents an exact replica of the antenna. It gives the total dynamic vector field as generated from all the elements on the cylinder. The vector value of the radiation from each element on the aperture is added at any point in space as a function of time, and exactly represents the physical situation which occurs. An alternative technique would be to formulate a model of the antenna with analytical functions based on idealized field theory using integral equations. Typically, this has resulted in equations that are both too cumbersome and require too many simplifying assumptions to produce detailed, accurate analysis.

The equation used in the model can be written, for present purposes as follows:

$$F(\theta, \phi, t, R, Z) = \sum^{MN} \Sigma E(\theta)E(\phi)V(Z, \lambda)M(\phi, t)C(R, \lambda, \theta, \phi)$$

where:

θ = Elevation coordinate

ϕ = Azimuth coordinate

t = Time

R = Array Radius

Z = Vertical coordinate

M = Number of radiators vertically

N = Number of radiators circumferentially.

See Figure 1 for the array geometry.

(a) Nine Lobed Rotating Pattern

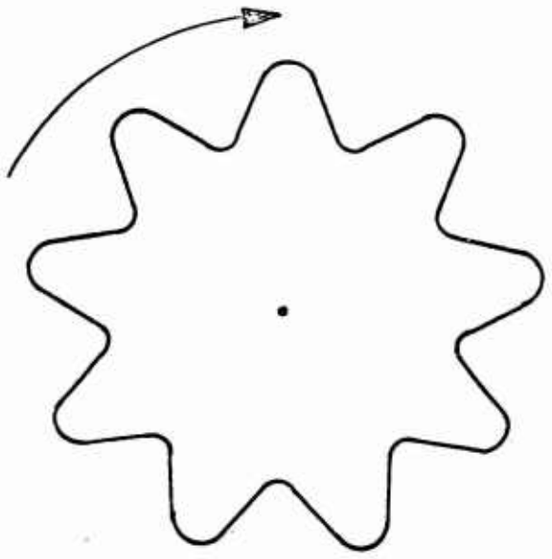

(b) System Geometry

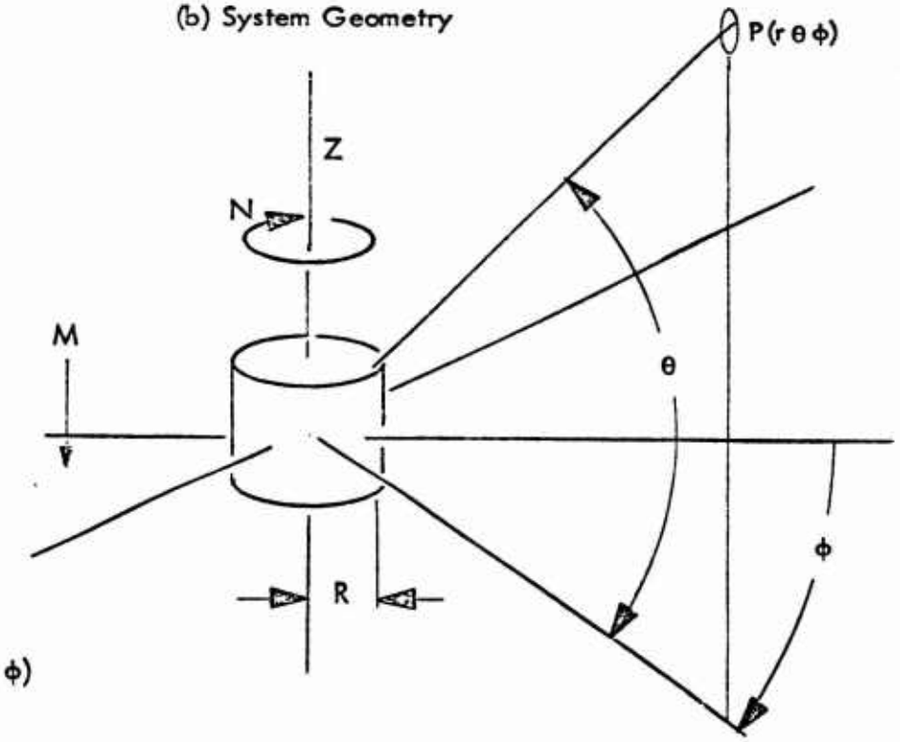

$$F(\theta, \phi, t, R, Z) = \sum_{M} \sum_{N} E(\theta) E(\phi) V(Z, \lambda) M(\phi, t) C(R, \lambda, \theta, \phi)$$

where

θ	= Elevation coordinate	$E(\theta)$	is the radiator's elevation radiation pattern
ϕ	= Azimuth coordinate	$E(\phi)$	is the radiator's azimuth radiation pattern
t	= Time	$V(Z, \lambda)$	is the vertical distribution
R	= Radius coordinate	$M(\phi, t)$	is the azimuth modulation
Z	= Vertical coordinate	$C(R, \lambda, \theta, \phi)$	is the cylindrical array phase term
M	= Number of radiators vertically		
N	= Number of radiators circumferentially		

Figure 1. Geometry and Equations

$E(\theta)$, the element elevation pattern, can be specified in many ways. If possible, values measured in the mutual coupling environment should be used since the measured pattern shape may vary significantly from that of an isolated element in a cylinder. However, this is not usually a critical factor in the model and simply helps shape the elevation pattern, which is basically determined by the vertical distribution on the cylinder. For the purposes of this discussion, $E(\theta) = \cos\theta$ was used so that the basic array behavior can be clearly seen.

The radiator's azimuth pattern is the $E(\phi)$ term. It is a good example of a factor that must be experimentally determined. Mutual coupling distorts the pattern, which is normally described with a

$$\left[1-\cos\left(\phi - \frac{(n-1)360}{N}\right)\right]^{P}$$

term. This term is for the nth element away from the reference angle, ϕ. Measured patterns contain higher terms, $U_n\cos(n\phi)$ and these must be included in the model to insure accurate performance predictions. The azimuth element pattern has a strong influence on the multi-lobed pattern. Here again, in order to not obscure the basic behavior, the simplified term shown above has been used throughout. It should be noted that this term, as well as the others, vary with frequency and this variation must also be accounted for in an actual design task.

The vertical aperture distribution is described by the $V(Z, \lambda)$ term. This is the R-F amplitude and phase that is formed on the cylindrical array by the elevation feed circuits. It is constant along the circumference at a given height from the base. This term is important in the

model and is important to the antenna's performance. The vertical amplitude and phase distribution determines the elevation plane radiation pattern characteristics. For the TACAN application this includes important features such as the horizon slope, side lobes, and beam uptilt. It is relatively easy to measure the distribution of a feed circuit and include this in the equation. The factors which are important in specifying this pattern shape are well known[2] and are not difficult to achieve. Also for purposes of clarity and simplicity, the data presented here are for either a single ring or for a uniform vertical distribution.

$M(\phi, t)$ describes the modulation function that is impressed on the antenna. It is an azimuth function and is constant along any vertical line on the aperture. This term contains modulation drive amplitudes to generate the lobed azimuth pattern, and any residual distortion. It also contains the phase modulation, if any is generated in the modulator. This term is readily included in the formulation, since it simply requires measurements on the modulator which is to be used.

The most important term in the equation is the one that accounts for the fundamental radiation characteristics of a cylindrical array, $C(R, \lambda, \theta, \phi)$. This term gives the phase of each of the vectors representing the radiation from all elements in the aperture at any point in space. The basic argument in this term can be written as

$$fR \cos\theta \left[(1 - \cos(\phi - (n-1)\frac{360}{N}) \right] .$$

This illustrates the interrelationship between antenna size (R), bandwidth (f), and elevation coverage (θ). It is primarily this term in the

model that allows the antenna radius to be chosen for optimum performance.

Each of the parameters in the equation may be varied in any way and in any combination with other parameters and the analysis generally can be used to study all aspects of the characteristics and behavior of any cylindrical array. For the purposes of this program, the model has been specially tailored to investigate the TACAN application. The analysis provides more detailed information than any other known technique.

COMPUTER ANALYSIS

Figure 2 shows the characteristic behavior of a cylindrical array as generated by the computer simulation for seven, nine, and eleven lobe azimuth patterns, using $1 + 0.35 \cos(L\phi)$ as the modulation function. Percent modulation is used in the usual sense:

$$m = \frac{(V_{max} - V_{min})\,100}{2V_{avg}}$$

The number of elements around the array was chosen to maintain the circumferential spacing close to one-half wavelength for the various radii used. This is an important consideration. For larger spacings the rotating pattern will exhibit amplitude variation in azimuth with a period of 360/N. Note that for a given cylinder radius, increasing elevation angle corresponds to moving left along the curve, and increasing frequency is indicated by movement to the right on the curve. These curves illustrate that the behavior is described in terms of the argument $\frac{R \cos\theta}{\lambda}$, and that if the pattern lobing or modulation is to be larger than

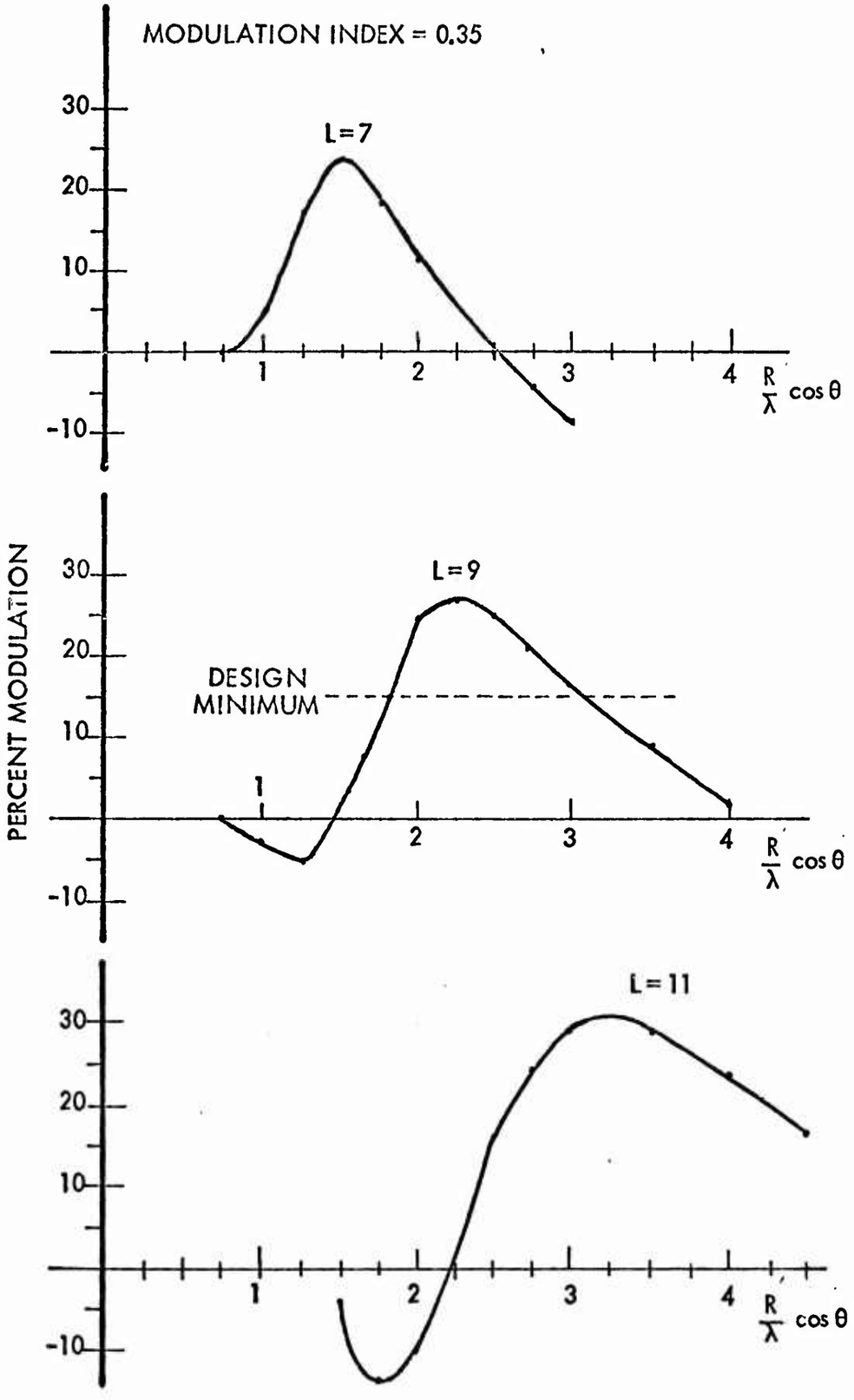

Figure 2. Amplitude Modulation Characteristic

some design minimum, only a limited range of antenna size, frequency, and elevation angle can be used.

Application of this technology to the TACAN antenna requires a nine-lobed azimuth pattern. It also requires a single-lobed cardiod but design considerations for this pattern are negligible as long as the basic requirements for omni-directional coverage are maintained. The modulation which is generated as the azimuth pattern is rotated is limited by system performance criteria to be between 12 and 30 percent. It is also desirable to maintain the modulation to as high an elevation angle as possible. Curves such as shown in Figure 2 allow these design requirements to be balanced and an optimum antenna radius to be chosen. An important feature of this technique which is evident from the characteristic curve is that an all-band TACAN antenna can be realized. For design purposes, the minimum modulation and elevation angle will be chosen to be 15 percent and 45 degrees, to provide a reasonable margin. Using the L=9 curve and starting at the lowest frequency and maximum elevation angle:

$$\frac{R}{\lambda_{max}} \cos \theta_{max} = 1.75, \quad R = 30.5'' \text{ at } f = 960 \text{ MHz}$$

Then at the other limit: $\frac{R}{\lambda_{min}} \cos \theta_{min} = 3.15$, and for $\theta = 0$ the high frequency is 12.15. Thus over the TACAN band, between 960 and 1215 MHz, and for angles up to at least 45 degrees, the modulation will be no less than 15 percent.

The simulated performance of an antenna with a 30.5 inch radius is shown in Figure 3. Having chosen this radius as indicated above, the behavior is readily determined from the mathematical model.

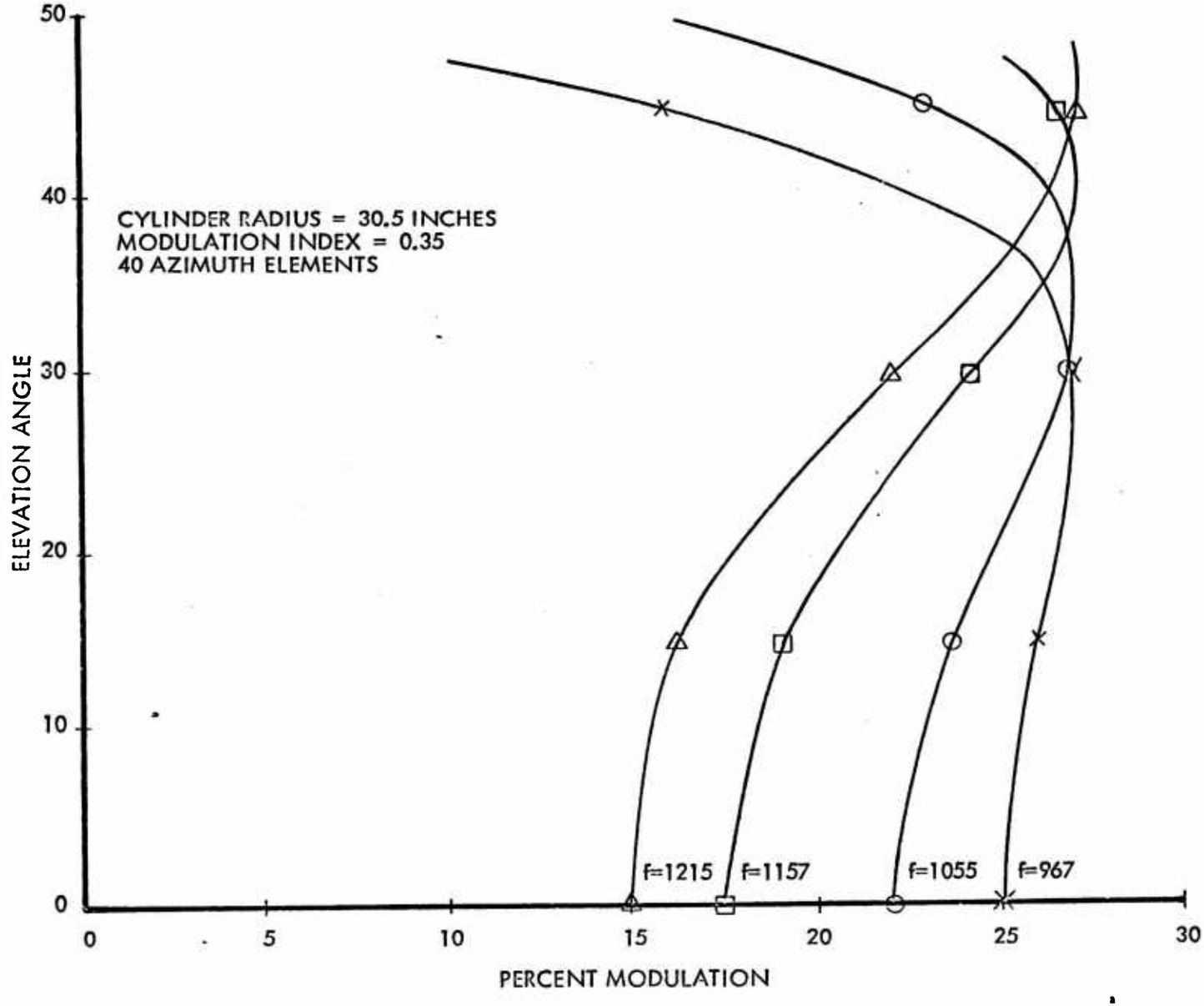

Figure 3. Ideal All-Band TACAN Antenna Behavior

An interesting characteristic of a cylindrical array operating in the multi-lobe, quasi-omni mode is that it can be a phase-amplitude modulation transducer. Specifically, Figure 4 shows the amplitude modulation generated by the rotating multi-lobed pattern when the aperture is excited with phase modulation. For the case shown, the phase distribution varied sinusoidally between ±13 degrees with 9 periods on the array circumference. Likewise, amplitude excitation on the aperture can generate a phase modulated signal in the far field. It can be seen from Figure 4 that phase modulation on the antenna can be an important factor for the TACAN application. When both amplitude and phase modulation are present on the aperture, the effects are essentially additive. It is also important to note that the far field signal will not have pure amplitude modulation in either case. Various amounts of phase modulation are generated, which is typically negligible (10 degrees peak to peak). However, it is a factor which must be checked for any practical design.

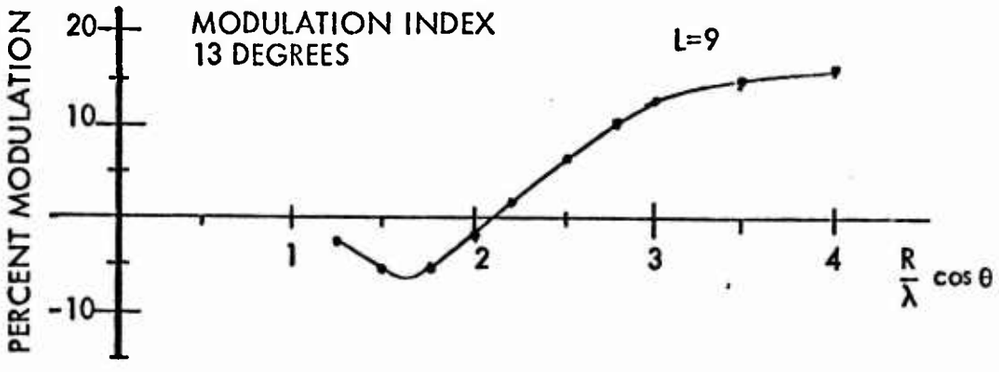

Figure 4. Phase Modulation Characteristic

A design example will now be discussed wherein both amplitude and phase excitation are used together for a particular application. If the excitation used in Figure 4 is reversed and used with that for the L = 9 case of Figure 2, a characteristic curve will be generated which reaches its peak for relatively small values of $(R \cos\theta)/\lambda$. This indicates that a small array can be designed and a "Manpack" antenna will be discussed. In this case the design criteria are taken to be 20 percent modulation minimum at the horizon and only nominal coverage at higher elevations. From the smallest value of $(R \cos\theta)/\lambda$ which yields 20 percent modulation on the modified characteristic curve, a radius is determined for $\theta = 0$, and $\lambda = 12.3''$ (f = 960 MHz). This radius is 21 inches. Using 27 elements insures that the spacing will be less than one-half wavelength at 1215 MHz. These specific values are then used in the computer simulation to predict the antenna performance in detail. A sample of this prediction is shown in Figure 5. It shows 19.75 percent modulation on the horizon at 960 MHz and that the 12 to 30 percent modulation requirement can be met for the entire TACAN band for reasonable elevation angles. The maximum azimuth bearing error was predicted to be 1° for this example.

SPECIAL CONSIDERATIONS

Some peculiarities of the cylindrical array for the TACAN application will be briefly discussed, since they are quite important to the design and can result in serious trouble in antenna performance if not properly handled. There are three factors which are: (1) the use of a rectangular

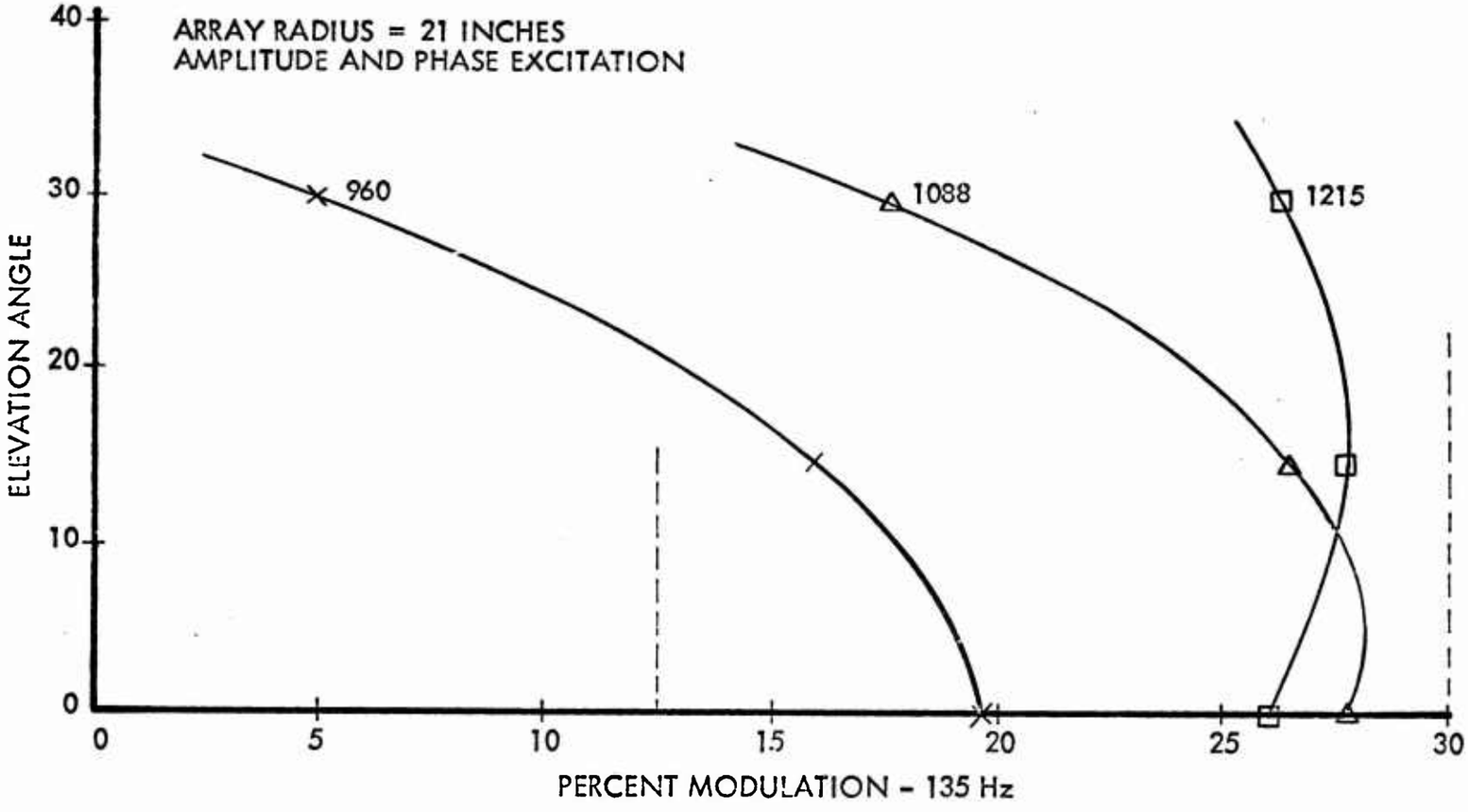

Figure 5. Design Example Antenna Characteristics

lattice rather than a triangular lattice in the array, (2) phase distortion of the element radiation pattern due to mutual coupling, and (3) incidental phase excitation mixed with pure amplitude excitation on the aperture. These factors were discovered and explored during the course of recent work[3].

A triangular element lattice is widely used in planar array applications without unusual effects. However, in this application where a cylindrical array is used to generate a rotating, multi-lobe, quasi-omni-beam, a rectangular lattice was found to be necessary. The triangular lattice, rather than acting as a composite array as might be expected, acts as two rectangular arrays displaced from each other. This is indicated by a granularity in the azimuth modulation behavior. The modulation magnitude and phase vary with a periodicity of $(360/\frac{N}{2})$. This phenomenon is apparently unexplained, and peculiar to this application. With a rectangular lattice the phenomenon does not occur.

Mutual coupling, of course, is a serious consideration for an array antenna. In this case the considerations are quite unique. Phase scanning is not a factor as in many array applications, and the radiators have been reasonably well matched over the 25 percent TACAN band even in the presence of mutual coupling. Furthermore, the effects of E-plane coupling, which is strongest, are effectively suppressed by using isolated output power dividers in the vertical feed network. Also, E-plane coupling effects do not appear to be critical to generation of the azimuth modulation. The azimuth pattern of the individual elements can be distorted by mutual coupling and this must be accounted for in the mathematical

model if realistic performance characteristics are to be obtained. The most important problem related to mutual coupling is that of phase front distortion in the radiation from the individual elements. The phase front has been found to be other than spherical, as expected, and the effective center of radiation may not be in the element aperture. This results in the cylinder's electrical diameter being different than its physical diameter. Since the performance for this application is fundamentally dependent on the cylinder's size as previously shown, this can lead to behavior other than predicted by the mathematical model. This problem can be eliminated by measuring the element's phase center in a small test array and correcting the array radius accordingly.

As discussed previously it is important to account for both the amplitude and phase excitation on the aperture. Ignoring one or the other or assuming pure excitation when that is not the case can lead to unexpected behavior. This is an important consideration because modulators typically used for this application may not generate pure amplitude or phase excitation. However, as shown previously a combination of both excitations can be effectively used to tailor an array design for a particular design requirement.

DEVELOPMENTAL MODEL ANTENNA

An Advanced Development Model electronically modulated cylindrical array was flight checked with a TRN-17 beacon at Fontana, California, on March 26 and 27, 1968. Flight tests were made on channels 16 and 61. Analysis of the results show that the system was within the requirements of AFM 55-8 in all categories. These flight checks were done as

a part of the evaluation of the Advanced Development Model antenna system and also to demonstrate for the first time an all electronically scanned TACAN antenna. In this respect an important step in TACAN antenna development was accomplished. The flight tests permitted the opportunity to observe this new antenna system operating in normal environmental conditions.

The Fontana site is far from ideal, being situated within 10 nm of a large mountain range and within 15 nm of a 10,000-foot peak. There are also local obstructions since the site is an antenna test facility with several tall towers; however, the nearest obstructions were 650 feet from the beacon site. These site considerations limited the region of the flight checks.

The Course Deviation Indicator (CDI) signal was chart-recorded while orbits, radials, approaches, and cross-polarization tests were flown by an AFCS Flight Crew using a C-47. The antenna system performed satisfactorily. In spite of the relatively poor site, no out-of-tolerance conditions or unlocks were observed. This series of flight checks successfully demonstrated that this new antenna technique can satisfy the requirements of the TACAN system.

SUMMARY

The preceding discussion has shown how a mathematical model and computer simulation is used to analyze and design a cylindrical array, in particular for the TACAN application. The computer-predicted performance of two ideal antennas were shown as examples.

Design considerations unique to this application of cylindrical array were discussed and the results of a flight check on a developmental antenna were presented.

REFERENCES

(1) Shestag, L. N., and Thomas, D. L., "A Design Study of an Antenna for an Air-Transportable TACAN Ground Station," ESD-TDR-64-526, July 1964.

(2) Greco, S. V., and Reed, H. R., "TACAN, Principles and Siting Criteria," NESTEF, September 1968.

(3) TACAN Antenna Techniques, November 1969, AF19(628)-67-C-0222.

AN ELECTRONICALLY STEERED ARRAY ANTENNA FOR TACAN

by R. J. Hanratty
ITT Gilfillan Inc.
Los Angeles, California

The Tactical Air Navigation System (TACAN) is a navigational aid designed to provide an aircraft with bearing and distance information with respect to a ground reference point. There are two essential components to the system: an airborne transmitter/receiver, called an interrogator; and a ground-based beacon antenna and transponder. Continuous bearing information at the aircraft is determined by measuring the electrical phase of specially modulated signals transmitted by the ground-based beacon and received by the airborne interrogator. Distance information, on the other hand, is determined by measuring the time interval between the transmission of an interrogation pulse from the aircraft, and subsequent reception of a beacon reply pulse; the distance-measuring function is not pertinent to this discussion.

The "bearing signal" is generated by rotating a multi-lobed azimuthal radiation pattern from the beacon antenna. Currently operational versions of the beacon antenna form and rotate the required multi-lobed radiation pattern by mechanical rotation of two rings of parasitic radiators about a centrally excited radiator. The difficulties with the present arrangement, that of providing the required bearing signals over the full TACAN frequency band of 960 to 1215 MHz and also over an elevation angle range from the horizon up to 50 degrees, has been instrumental in fostering development of an electronically steered cylindrical array antenna for TACAN, which can overcome these difficulties. This paper describes the design principles

of such an electronically steered array antenna, and the results achieved for an experimental array constructed generally in accordance with these principles.

Figure 1 shows the detected envelope of the bearing signal required to be generated at a point in space by the beacon antenna. The envelope consists of three distinct components: a bias or carrier level, a 15 Hz component of audio modulation, and a 135 Hz component of audio modulation. (Note that the audio components are related by a factor of nine.) Upon reception of such a signal, the aircraft interrogator determines the bearing by measuring the audio phase of the 15 Hz and 135 Hz components relative to timing reference signals transmitted by the beacon antenna at selected times during rotation of its multi-lobed radiation pattern.

The bearing signal shown in Figure 1 is generated by rotating a multi-lobed azimuthal radiation pattern from the beacon antenna. Figure 2 illustrates the three required components of the composite azimuthal pattern: an omnidirectional "carrier" pattern, a dual-lobed "15 Hz" pattern, and an 18-lobed "135 Hz" pattern, all with the relative RF phases indicated. Time rotation of the latter two patterns at 15 revolutions per second develops the 15 and 135 Hz audio components of the bearing signal.

The azimuthal radiation patterns shown in Figure 2 can be generated by exciting a cylindrical aperture circumferentially with similar amplitude functions, since, for a cylindrical wavefront, a one-to-one correspondence generally exists between aperture excitation and far-field radiation pattern. The three components of circumferential aperture excitation, corresponding to the three radiation patterns of Figure 2, are illustrated in Figure 3. The three components are a uniform amplitude and phase "carrier" excitation, a single-cycle "15 Hz" excitation, and a nine-cycle "135 Hz"

excitation; time rotation of the latter two excitations at 15 revolutions per second is again implied. The modulation phases indicated in Figure 3 are those to develop the radiation-pattern phases of Figure 2 in a practical design.

From this brief discussion, it appears the designer's tasks is relatively simple, a matter of selecting the parameters of the cylindrical array--i.e., the array radius and relative amplitudes of the three modes of excitation--to develop the required modulation of the bearing signal over the full TACAN frequency band of 960 MHz to 1215 MHz, and also over an elevation angle range from the horizon up to 50 degrees. For those unacquainted with TACAN, MIL-STD-291B states the requirements for modulation of the bearing signal as follows: the 15 Hz and 135 Hz components, taken individually, shall have a modulation index between 12 and 30 percent; and the composite modulation index shall never exceed 55 percent. Other requirements, such as harmonic distortion of the bearing signal, are not germane to the discussion herein.

That the designer's task is not necessarily a simple one, however, is illustrated in Figure 4, which shows, for a single elemental "ring" of the cylindrical array, typical elevation radiation patterns of the three component modes of excitation shown in Figure 3. For convenience, a peak amplitude of unity has been assumed for all three modes of excitation. It is entirely acceptable to concern ourselves with only a single ring element of the cylindrical array since the radiation patterns of the array are separable into a vertical array factor and a ring element factor. All the time-dependent pattern characteristics are contained in the ring element factor; the vertical array factor only shapes the time-independent carrier elevation pattern. The azimuthal characteristics of the array at any

elevation angle are, therefore, identical to those of a single ring element. This presumes of course, identical elemental rings, which is the case here.

Referring to Figure 4, the radiation patterns of the three component modes of excitation are in general different, as should be expected with circular geometry; and the relative amplitude between them is, therefore, a function of elevation angle. Since the modulation index of either the 15 Hz or 135 Hz component of bearing signal depends on the amplitude of that particular component relative to the amplitude of the carrier component, the modulation indices of the 15 and 135 Hz components will in general also be a function of elevation angle. The designer's task, therefore, is to select an array radius, and hence a set of patterns for the three component modes of excitation, that will maintain the required modulation indices over the desired elevation angle range, and over the frequency band as well. This task is aided by the use of curves such as illustrated in Figure 5.

Figure 5 shows typical "modulation" patterns calculated for a cylindrical TACAN antenna. These modulation patterns are the variation in modulation index of the 15 Hz and 135 Hz component graphed against a parameter involving the radius of the antenna, elevation angle to the observation point, and wavelength of operation. As such, these modulation patterns are a measure of the relative amplitude variation between component elevation radiation patterns of the type illustrated in Figure 4, but for a wide range of electrical array radii. For convenience, a peak amplitude of unity has again been assumed for all three modes of excitation. Although the modulation patterns illustrated were calculated for a continuously excited aperture, they are equally valid for an array with a finite number of circumferential elements, as long as the element spacing is under a half-wavelength. The principal effect of fewer elements circumferentially--or element spacings greater than a half-wavelength--is

the development of periodic audio phase errors, which translate into errors of bearing angle. This will not be discussed further here. Superimposed or these graphs are the extent of acceptable modulation indices as established by MIL-STD-291B, as well as the extent of the horizontal-axis parameter corresponding to an elevation angle range of 0 degrees (horizon) to 50 degrees, and a wavelength range for operation between 960 and 1215 MHz.

Referring to Figure 5, it is observed that there is very little difficulty in selecting an array radius to obtain the required index of 15 Hz modulation over the full TACAN frequency band and range of elevation angles. However, only an extremely limited range of array radii will enable the required index of 135 Hz modulation to be obtained over the frequency band and range of elevation angles. This points out the necessity of carefully selecting the array radius to optimize the 135 Hz performance, and furthermore illustrates the difficulty of extending acceptable modulation performance to elevation angles greater than 50 degrees. It is interesting to note that if the correct array radius is not selected, the 135 Hz modulation can "disappear" completely from the bearing signal at certain elevation angles; or perhaps it can reverse sense, which will cause an error in bearing angle of 20 degrees.

An experimental cylindrical array constructed generally in accordance with the above-described principles is shown in Figures 6, 7, and 8. The array contains a total of 336 elements, arranged in 42 columns of 8 elements each. Adjacent columns are staggered vertically to achieve an effective circumferential element spacing smaller than could be achieved with the elements in a simple rectangular arrangement. Elements in each column were connected by a stripline feed network. The input to each column contained a PIN-diode amplitude modulator, which was connected through a 42-way power divider to a single input port. The circumferential array excitation,

provided by time-phased bias-voltage control of the diode amplitude modulators, consisted of the three components illustrated earlier in Figure 3, but in ratio to develop the correct modulation indices. The vertical array excitation was selected to form the desired "shaped" elevation pattern.

The experimental array underwent an extensive series of electrical tests, including a flight check in the lower half of the TACAN frequency band. However, because of a non-judicious choice of the parameters of the array early in the development, the array did not meet all the requirements established for it, particularly in regard to maintaining the modulation index of the 135 Hz component at its required level over the full frequency band and range of elevation angles. The measurements did demonstrate, however, the feasibility of the particular amplitude modulation technique for developing TACAN bearing signals. The experience gained with this array, plus the results of extensive subsequent analyses, have shown that a full-band electronically steered array antenna for TACAN is achievable in a practical configuration.

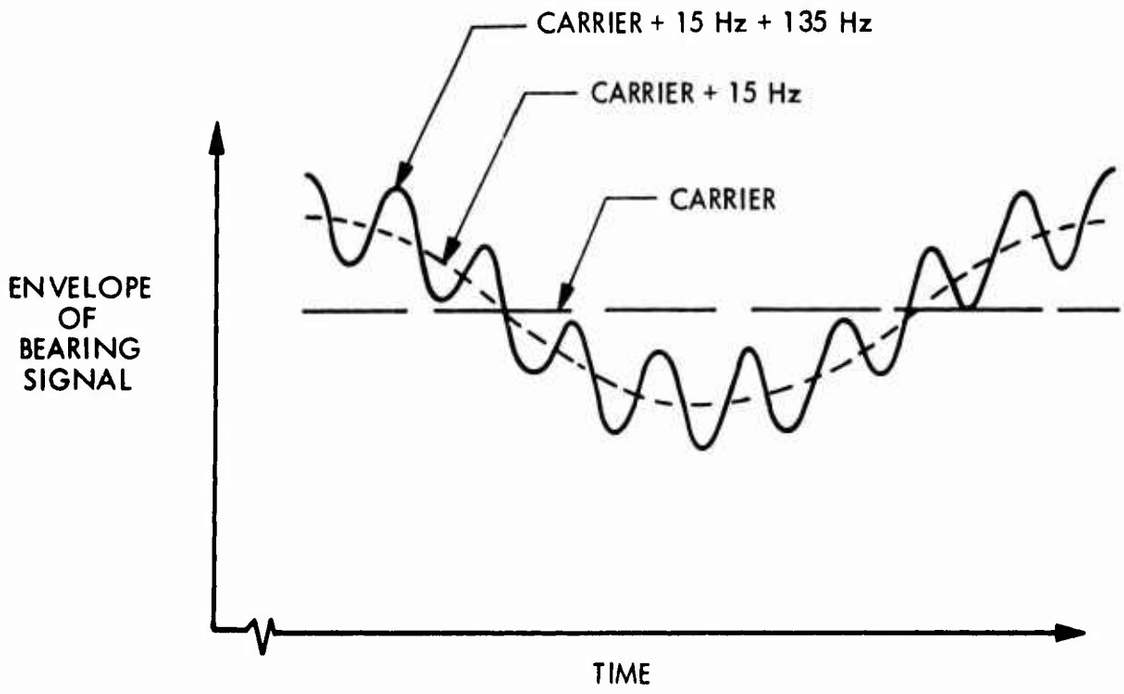

199 - 3A

Figure 1. Detected Envelope of Bearing Signal Required at a Point in Space

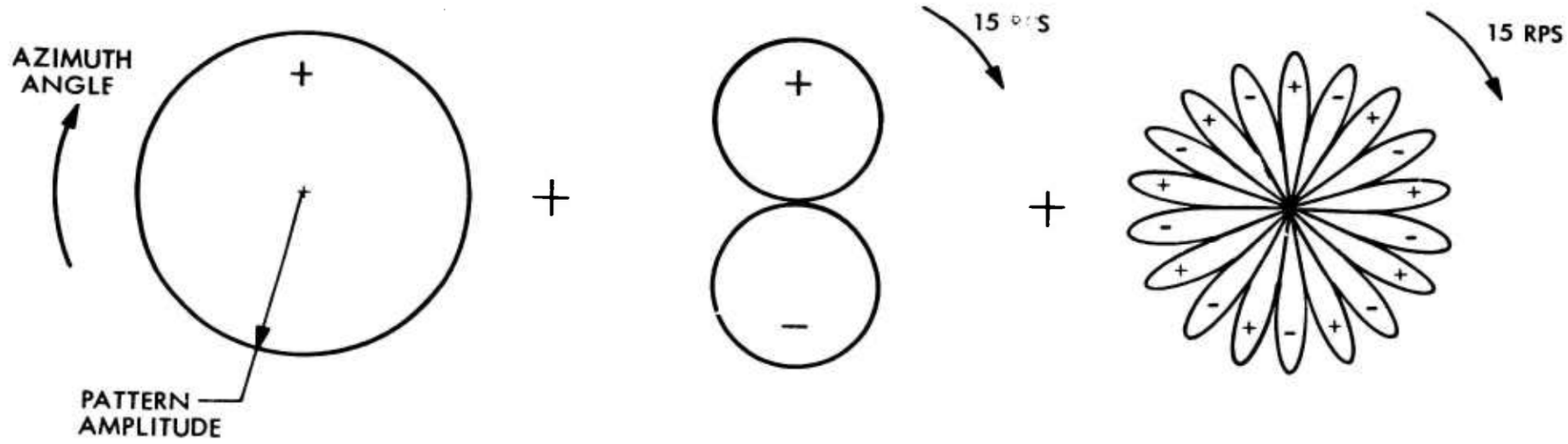

199 - 4A

Figure 2. Generation of Required Bearing Signal by Rotating Azimuthal Radiation Patterns

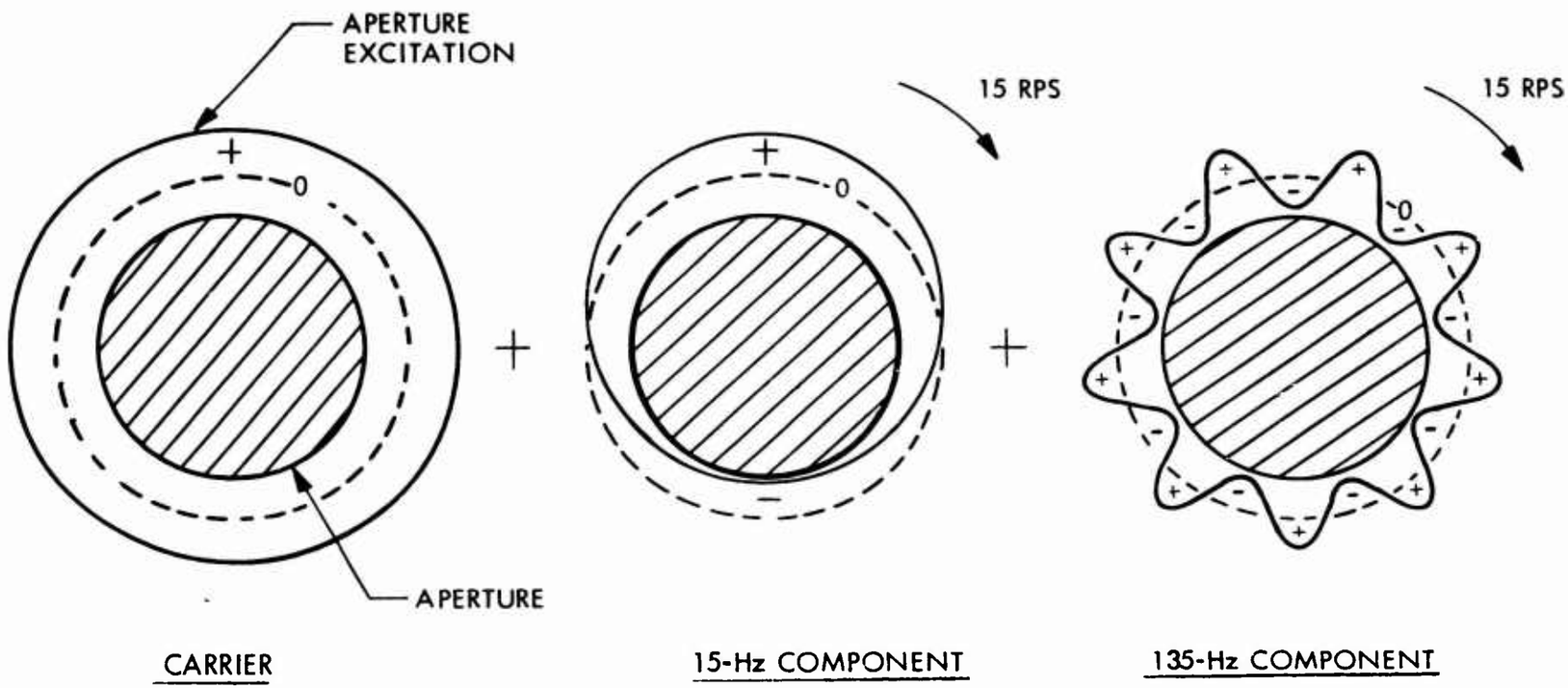

199 - 5A

Figure 3. Generation of Required Azimuthal Radiation Patterns by Modulation of Aperture Excitation

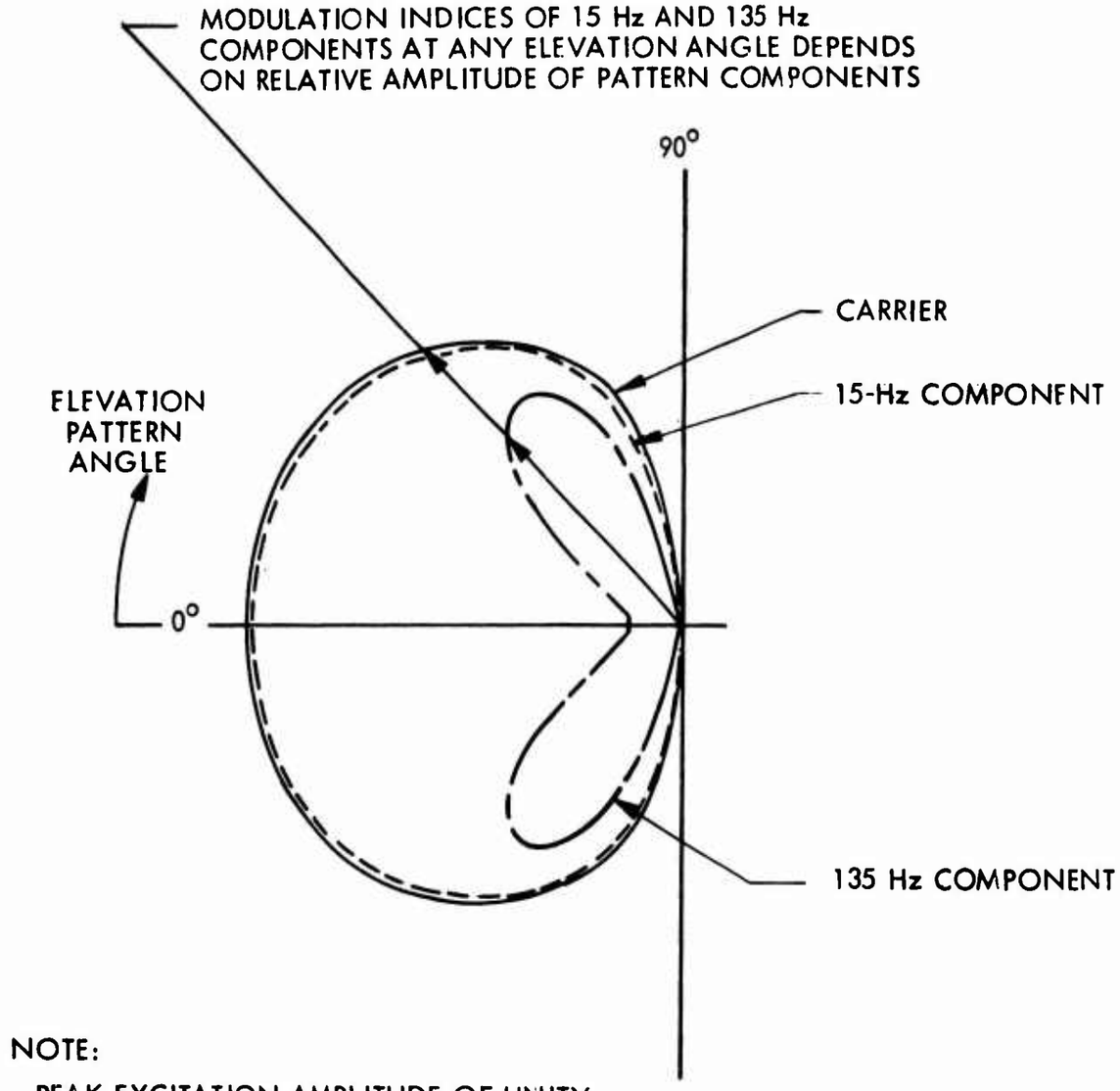

Figure 4. Typical Elevation Radiation Patterns of Component Aperture Excitations

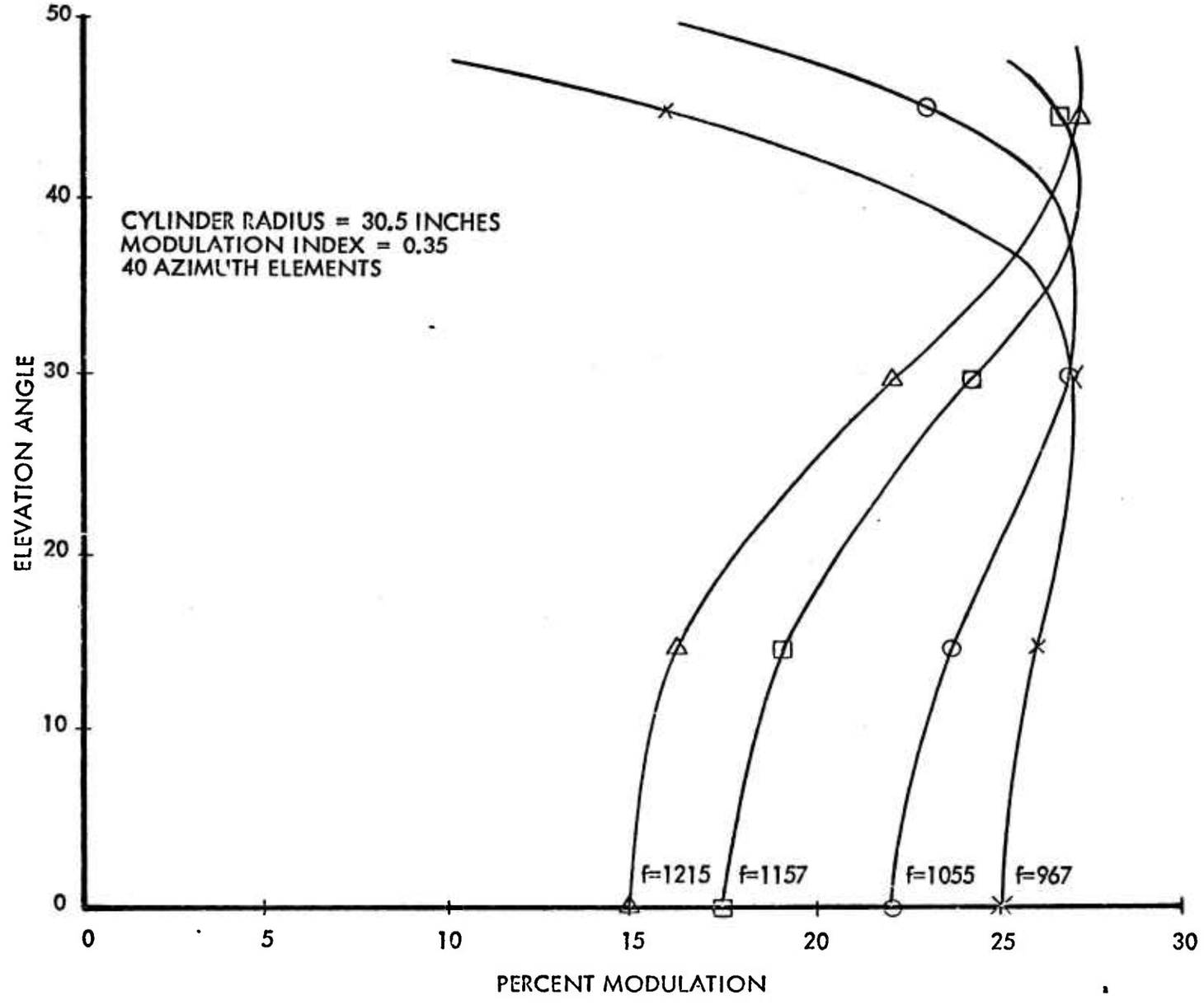

Figure 3. Ideal All-Band TACAN Antenna Behavior

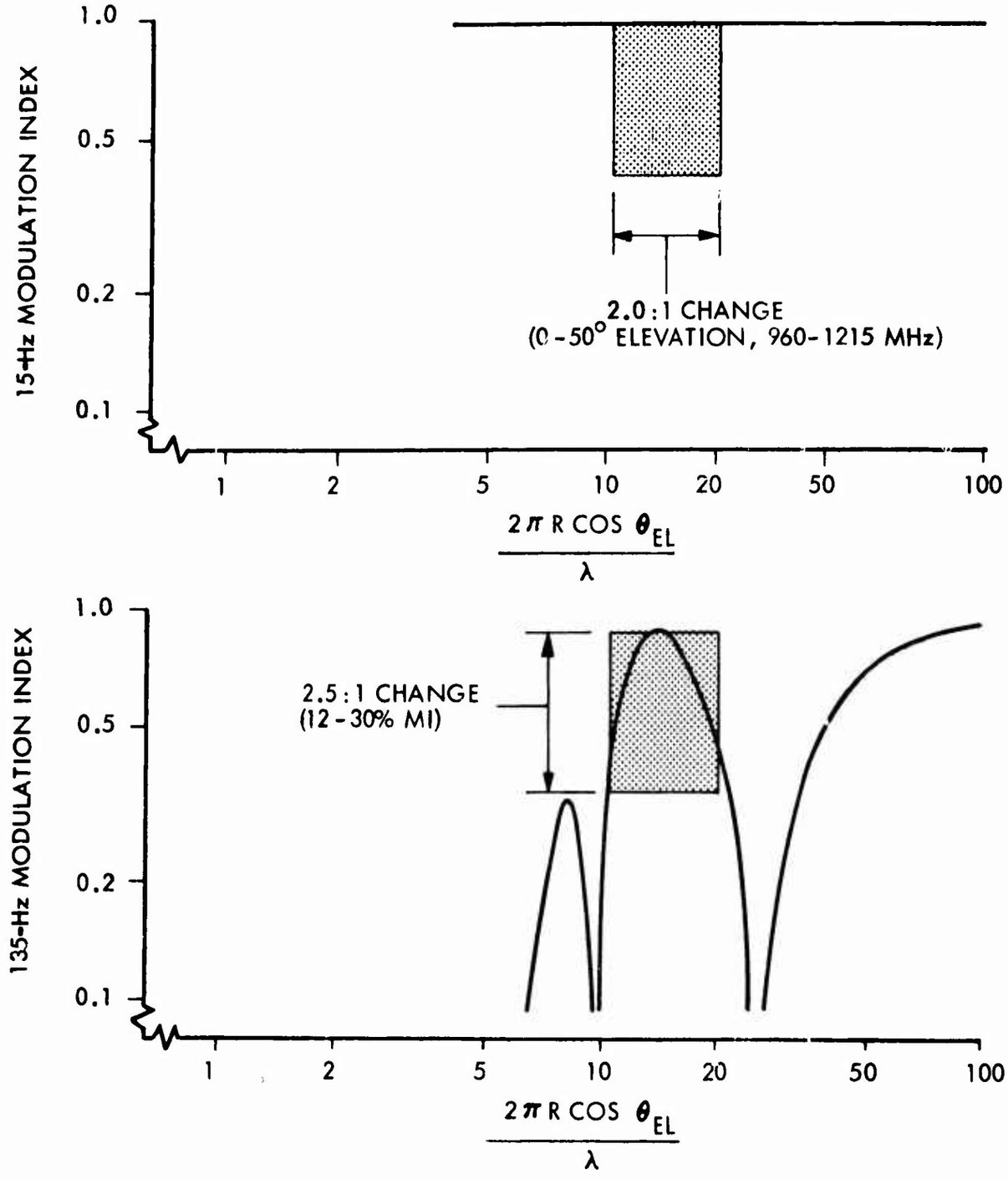

KEY:
R = RADIUS OF CYLINDRICAL ARRAY
θ_{EL} = ELEVATION ANGLE TO OBSERVATION POINT
λ = WAVELENGTH OF OPERATION

NOTE: PEAK EXCITATION AMPLITUDE OF UNITY ASSUMED FOR EACH COMPONENT.

199 - 7A

Figure 5. Typical "Modulation Patterns" of Cylindrical TACAN Antenna

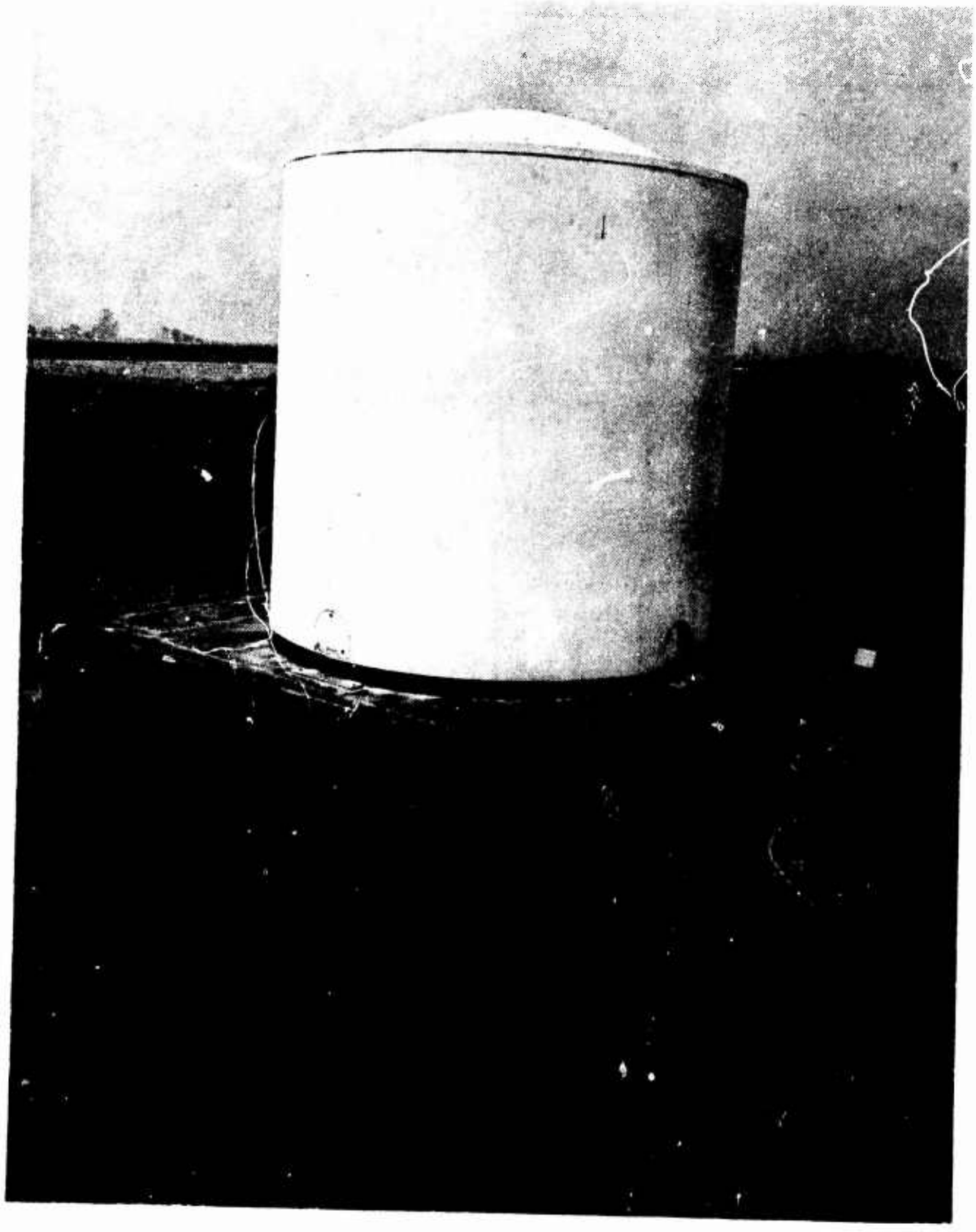

Figure 6. TACAN Antenna Exterior View

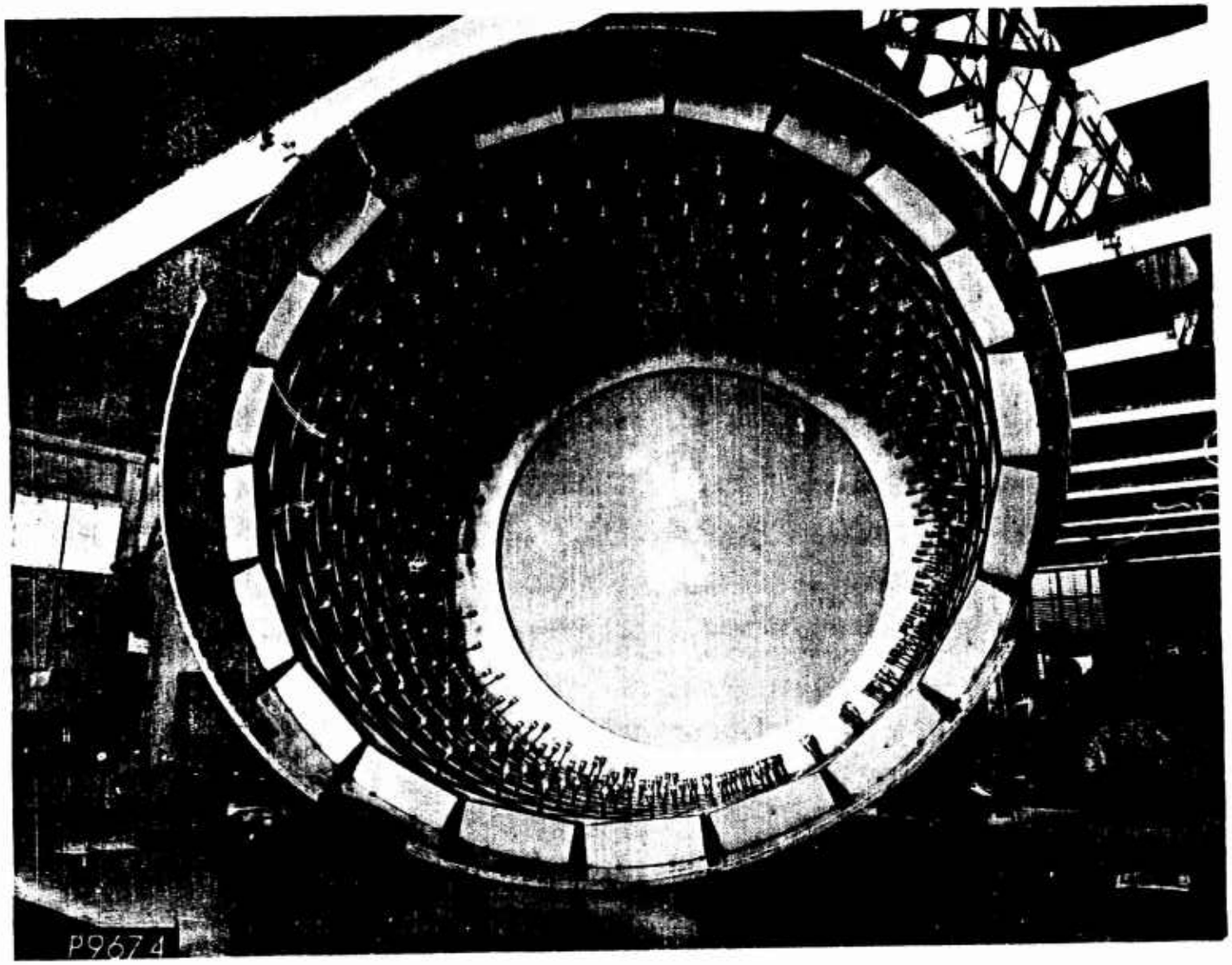

Figure 7. Interior View Showing Arrangement of Radiating Elements

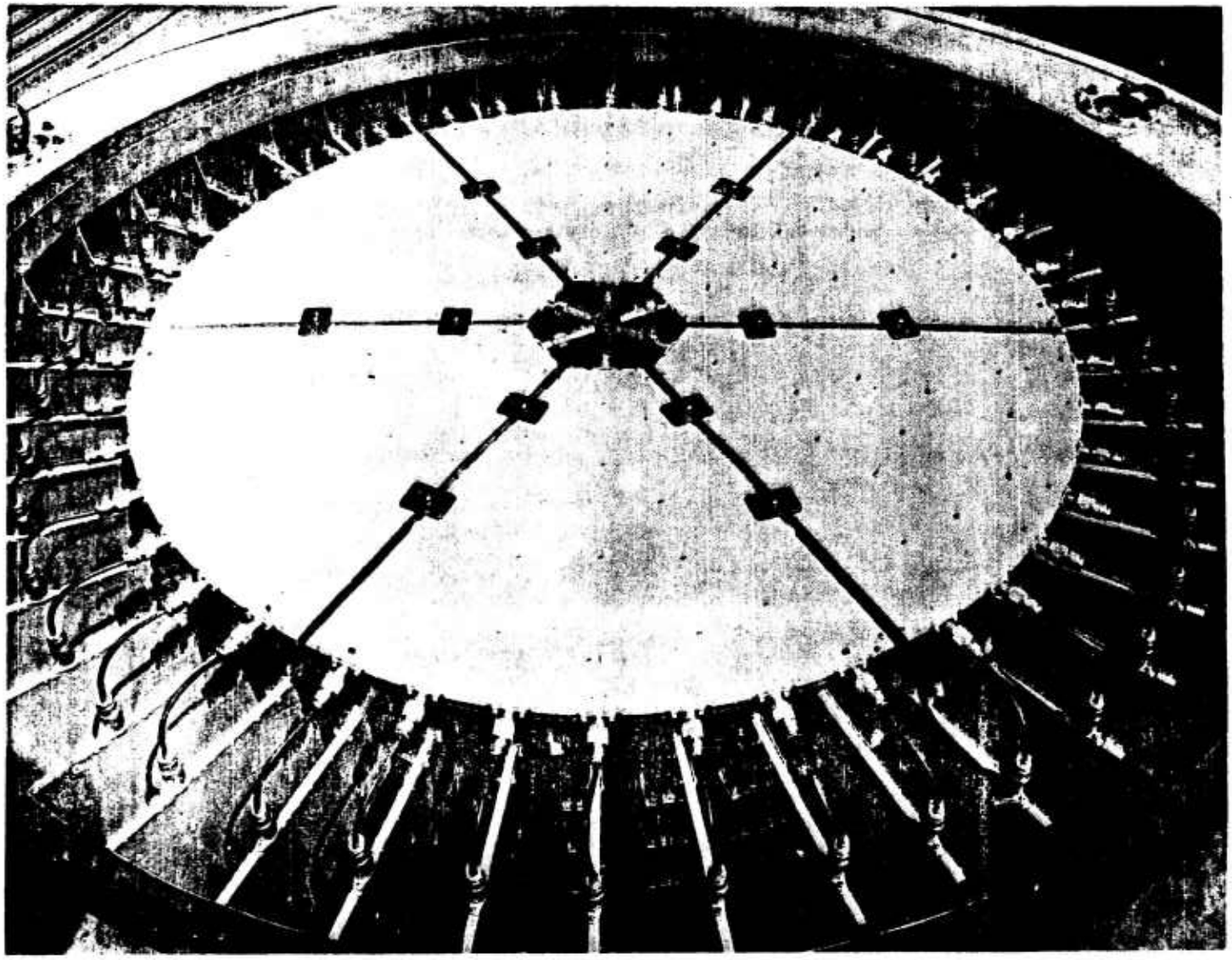

Figure 8. Top Interior TACAN Antenna Showing Stripline Feed Network

AN ELECTRONICALLY SCANNED CYLINDRICAL ARRAY SWITCHED IN AZIMUTH AND FREQUENCY SCANNED IN ELEVATION

B.Sheleg and B.D.Wright
Naval Research Laboratory
Washington, D.C. 20390

INTRODUCTION

By virtue of its symmetry, a cylindrical array has obvious appeal when an antenna is needed for high-speed scanning of a pencil beam 360 degrees in azimuth and over some range of elevation angles. With such an array, the radiation pattern is formed by establishing the proper currents on the elements (ordinarily on just a sector of the cylinder), and is then scanned in azimuth by moving the excitation around the cylinder, and in elevation by varying the phases of the currents. Previous work at the Naval Research Laboratory on circular arrays [1] resulted in the development of a matrix of diode switches capable of performing the first function, permitting switching from beam to beam in azimuth in less than a microsecond. To demonstrate 3-D scanning with a cylindrical array, a 256-element, S-band array consisting of 32 8-element linear arrays has been built and tested at NRL (Fig.1). The diode switch matrix was used for azimuth steering and frequency change for elevation scanning.

AZIMUTH NETWORK

Eight of the 32 linear arrays were excited at a time. The currents to be applied were first established by a corporate structing having 8 outputs equal in phase and having a 25 dB Tchebyscheff amplitude distribution. Shielded stripline was used for the corporate structure and, to provide sum and difference ports, the two halves were fed with a magic tee. The amplitude taper was achieved by the use of isolated tees. To obtain cophased currents (phases corrected to the line tangent to the circle), coaxial lines of the proper lengths were used to connect the corporate structure to the switch matrix. The matrix, which was in turn connected to the 32 linear arrays by coaxial cables of equal length, was designed to route the currents to any 8 adjacent linear arrays, keeping the currents in the proper order, with relative amplitudes and phases preserved in all switch states. For a cylindrical array, the azimuth phases should ideally be changed as the beam is scanned in elevation, unlike the planar array for which azimuth and elevation scans are independent. However, this array was small enough that the azimuth phase adjustment with elevation scan could be neglected since the resultant phase error for 45 degree elevation scan was only 11 degrees.

The switch matrix was a network of diode transfer switches (44 in all) built by Microwave Associates to an NRL design under NAVELEX Contract NObsr 95014. The matrix consisted of two parts--the first, an 8-input, 8-output network (an 8-by-8) of 12 transfer switches was used to provide as outputs all the cyclic permutations of the input currents. These outputs served as inputs to 8 4-by-4 networks whose 32 outputs were connected in interlaced fashion to the 32 linear arrays. The 4-by-4's served to move the excitation around the array, the 8-by-8 to keep the currents in the proper order. The most difficult problem in the design and fabrication of the switch matrix was that of keeping constant pathlengths for all paths for all switching states. At the center frequency, 3.2 GHz, the difference in phase between any of the 8 inputs and any of the 32 outputs was within ± 12 degrees. Each path contained 5 transfer switches in series and the total insertion loss was about 3.7 dB. The individual transfer switches were made in shielded stripline and consisted of a loop 2λ in circumference with ports at 90-degree intervals. Midway between the ports were diode-loaded stubs which were biased in pairs to obtain the two switch states. Over the range 3.1 to 3.3 GHz the switch isolation was better than 25 dB. Tests at Microwave Associates showed a switching time of .5 microseconds and a peak power capability of more than 1 kw. Although the switch matrix was used to excite only a quadrant of the array, the same number of switches in a different configuration could be used to excite as many as half the elements and to move the excitation around the array.

FREQUENCY SCANNED LINEAR ARRAYS

The 32 arrays making up the cylinder each consisted of 8 vertically polarized dipoles series fed from a serpentine transmission line by means of directional couplers which acted to mitigate the effects of mutual coupling. The large number of components involved and the desirability of minimizing the number of transitions dictated the use of printed circuits for the arrays. Three layer stripline (using copper-clad Tellite) was chosen primarily because directional couplers having the required values of coupling could most easily be made in this line.

The radiating elements were a new type ("sandwich dipoles") fed directly from the transmission line and occupying just a single surface. For a balun, the dipole used a rat-race hybrid which was collapsed from its usual circular shape into a narrow oval to fit the dipole geometry. The rat-race was fed at its difference port and quarter wavelength stubs attached to its out-of-phase outputs became the dipole radiator. The sum port was terminated in a load. The virtue of this dipole is its simplicity--no transition was required and, once designed, there was no necessity for trimming to match.

The directional couplers were of the offset parallel-coupled type [2] and were spaced about 7 wavelengths apart on the serpentine line. The couplers prevent coupled currents from recirculating through the linear array to be reradiated. Each linear array required 17 50-ohm terminations--these were made by placing a thin resistive film across a gap one-quarter wavelength from the open end of the line. They were well matched over the frequency band of the array and had the advantage of requiring no transition.

The tolerances on the offset directional couplers required that there be very precise registry between the two transmission lines on opposite sides of the center layer of the stripline. This problem was solved by using a computer-controlled coordinatograph to scribe the serpentine line and the couplers at four times size on peel-coat material. Each linear array was made by printed circuit techniques from a master negative which included transmission line, couplers, dipoles, and terminations--the only machining operation was for mounting a single coaxial input connector. The three layers of the board were bonded together with an adhesive under pressure. This process was found to be critical. The propagation constant is a function of the plate spacing and some boards had to be discarded because their boresight frequency was incorrect. Slight variations in the intrinsic phase of the linear arrays were compensated for by trimming the cables connecting the arrays to the switch matrix.

PATTERN MEASUREMENT

The array was scanned in elevation from -20 to +40 degrees by varying the frequency from 3.07 to 3.37 MHz, a somewhat greater frequency excursion than the switch matrix was originally designed to cover (3.1 to 3.3 GHz). The worst azimuth sidelobes occurred at 40 degrees elevation--Fig.2 shows these beams, with sidelobes generally 16 to 18 dB down. Azimuth patterns for 0 degrees elevation were 19 to 21 dB down--typical sum and difference patterns are shown in Fig.3. Elevation patterns are shown in Fig.4--the relative gains are probably not accurate since the transmitter was not leveled.

CONCLUSION

The azimuth and elevation scanning of the pencil beam formed by a cylindrical array were demonstrated. The diode switching matrix used to steer the beam through 360 degrees in azimuth was shown to have sufficient bandwidth to accommodate frequency scan in elevation, but improvement in isolation and pathlength stability of the switches is

necessary if better patterns are to be obtained. Finally, for larger arrays, variable phase shifters will be required to adjust the azimuth phase of at least some of the elements as the beam is scanned in elevation.

REFERENCES

[1] R.M.Brown, "Cylindrical Array," Meeting on Phased Array Technology, Naval Research Laboratory, September 1968.

[2] J.A.Mosko, "Calculating the Strip Geometry of Offset Parallel-Coupled Strip Transmission Lines Using an IBM 1620 Computer," U.S.N.O.T.S., China Lake, March 1966.

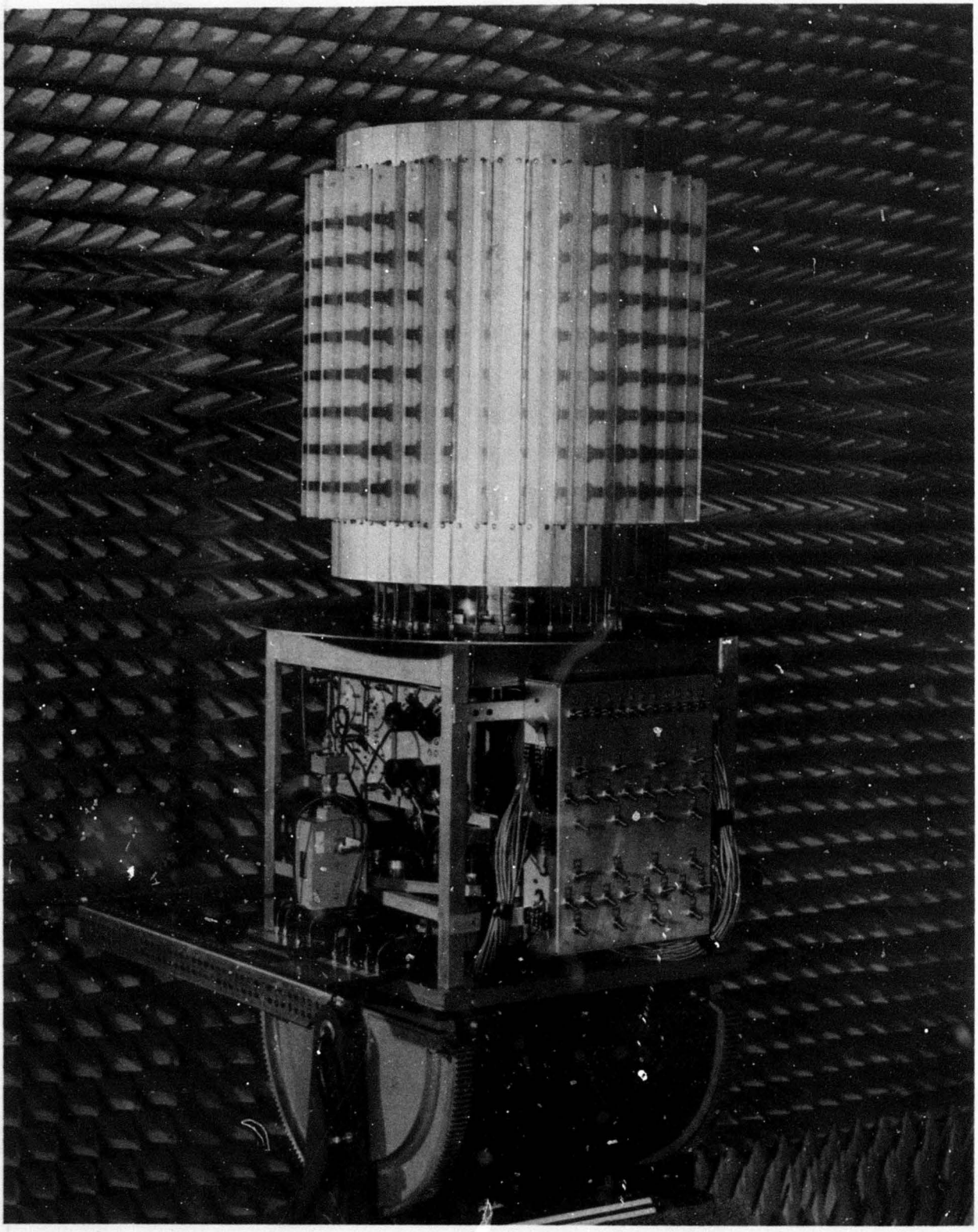

Figure 1

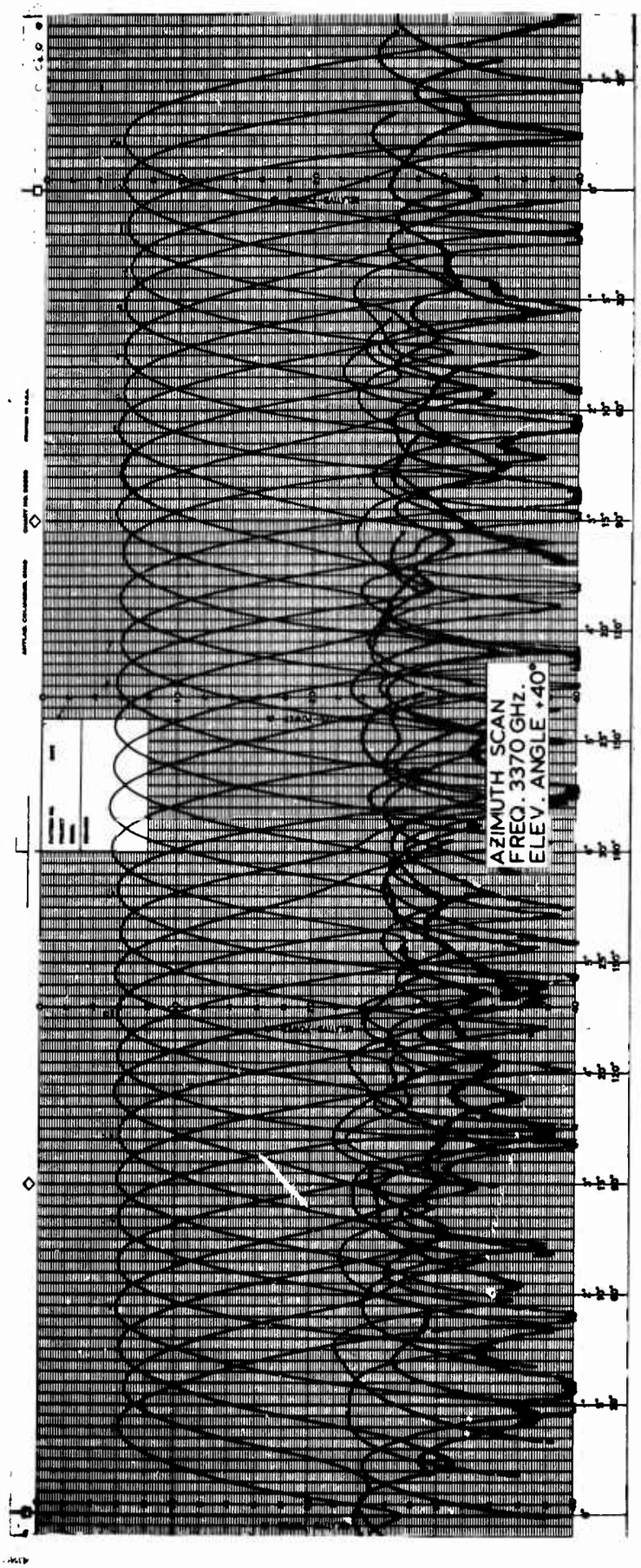

Figure 2

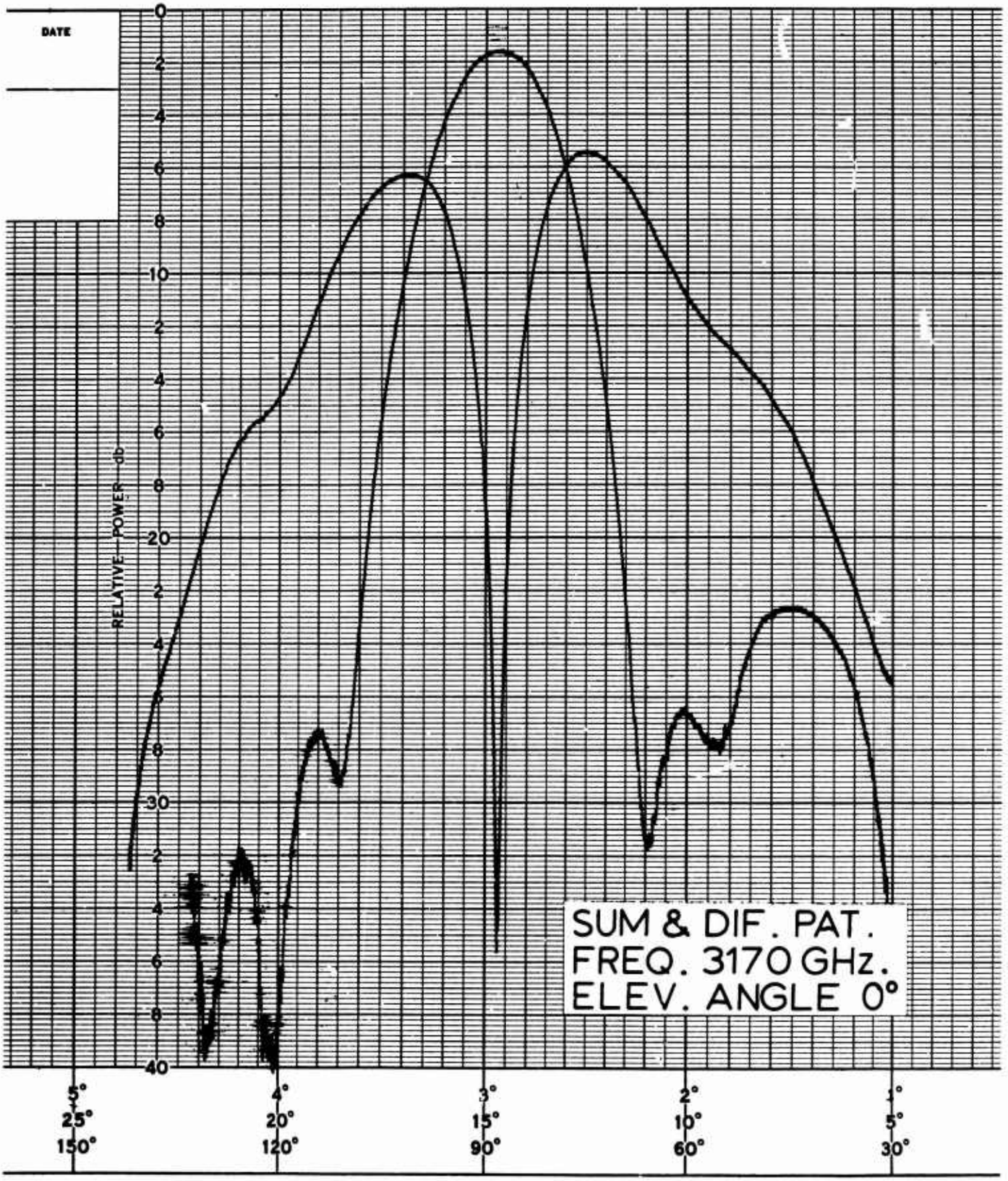
DATE
RELATIVE—POWER—dB
0
2
4
6
8
10
2
4
6
8
20
2
4
6
8
30
2
4
6
8
40
SUM & DIF. PAT.
FREQ. 3170 GHz.
ELEV. ANGLE 0°
5°
25°
150°
4°
20°
120°
3°
15°
90°
2°
10°
60°
1°
5°
30°

Figure 3

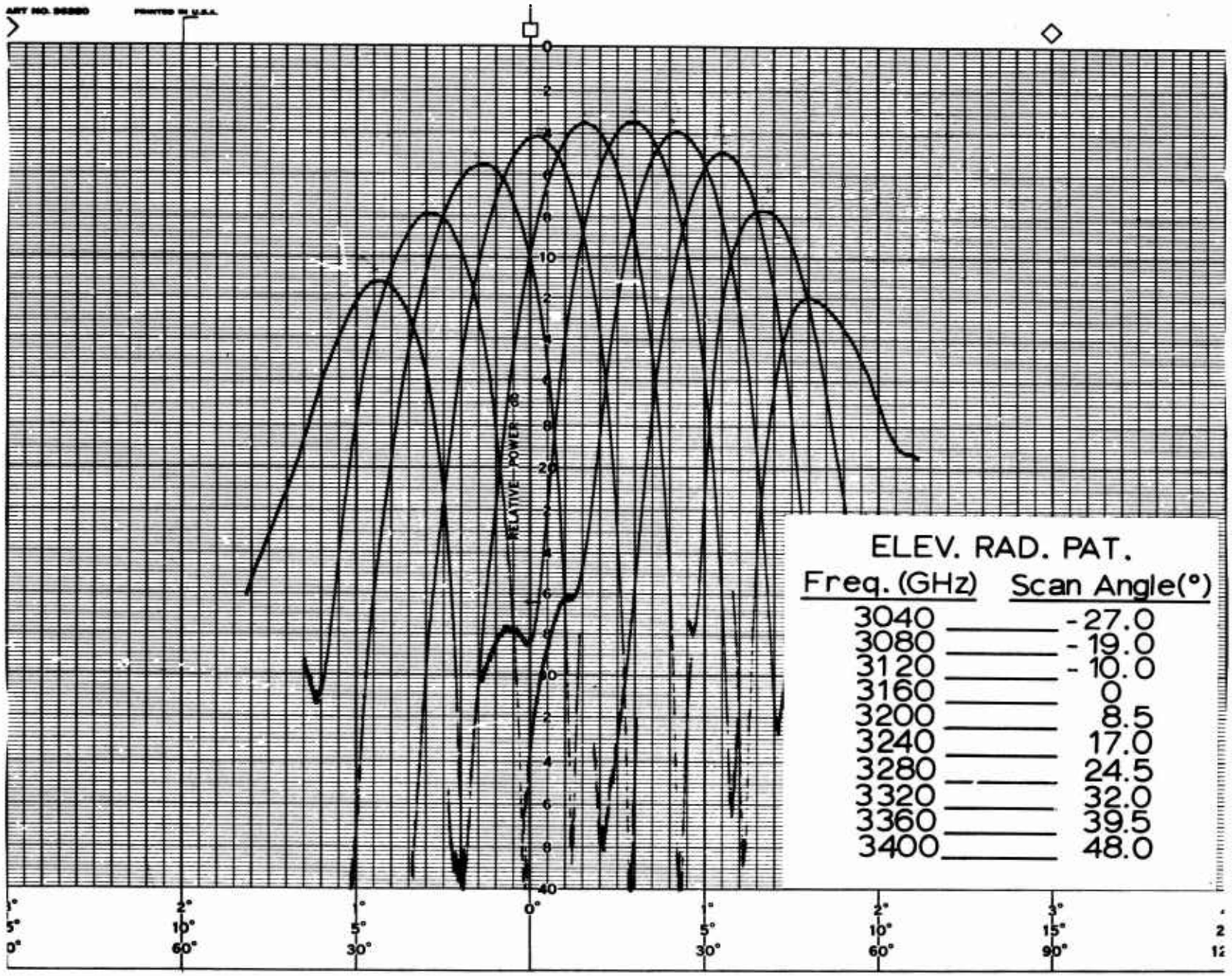
RELATIVE POWER
ELEV. RAD. PAT.
Freq. (GHz) Scan Angle(°)
3040 -27.0
3080 -19.0
3120 -10.0
3160 0
3200 8.5
3240 17.0
3280 24.5
3320 32.0
3360 39.5
3400 48.0

Figure 4

Theoretical Methods for Computing Characteristics of Wullenweber Antennas

by

M. T. Ma and L. C. Walters
Institute for Telecommunication Sciences
ESSA Research Laboratories
Boulder, Colorado 80302

and

Thomas M. Counts
Naval Electronic Systems Command
Washington, D. C.

Abstract

The Wullenweber antenna considered here is essentially an array of two concentric rings of discrete elements. Each ring is placed in front of a concentric screen. The inner ring is designed to operate at 3-10 MHz while the outer ring is at 8-32 MHz. The radiator used for the high-band ring is a sleeve antenna, and that for the low-band ring is a three-wire folded monopole.

A theoretical method is formulated to calculate input and mutual impedances, total field radiated, and power gain of a Wullenweber antenna above a lossy flat earth. Impedances are derived by the commonly used induced emf method with different forms of current distribution assumed on elements of different bands. Radiated fields and power gains are obtained from the known propagation theory.

Numerical results on all of these characteristics are given as a function of frequency, ground constants, element dimensions, array geometries, elevation and azimuth angles. Optimization of the array performance with respect to the ring radii and element-to-screen distances is also shown.

Key Words: arrays, computation, impedances, power gain, radiation, Wullenweber antennas.

1. INTRODUCTION

Many Wullenweber antennas have been experimentally designed for the receiving purpose. No systematic theoretical work has been formulated to check measured characteristics or as a design guideline. This paper provides a theoretical method to calculate input and mutual impedances, fields radiated, and power gains of a Wullenweber antenna above a lossy flat earth. The antenna considered here is essentially an array of two concentric rings of discrete elements. Each ring is placed in front of a concentric screen. The inner ring, consisting of 40 three-wire folded monopoles, operates at 3-10 MHz while the outer ring of 120 sleeve antennas operates at 8-32 MHz. Details of the array geometry are shown in figure 1.

Impedances are derived by the commonly used induced emf method with different forms of current distribution assumed on elements on different bands. Radiated fields and power gains are obtained from known propagation theory. Numerical results on all these characteristics are given as a function of frequency, ground constants, element dimensions, array geometries, elevation and azimuth angles. Optimization of the array performance with respect to the ring radii and element-to-screeen distances is also demonstrated.

2. HIGH-BAND ELEMENTS

2.1 Impedance and current distribution.

The particular radiator used for the high-band (8-32 MHz) ring is a cylindrical sleeve antenna that consists of a vertically extended inner conductor of height h and radius a_i, and an outer conductor of the coaxial line of height s and radius a_o over a horizontal conducting plane (see fig. 2a). It differs from the conventional base-driven monopole in that the sheath of the coaxial line does not end at the conducting plane but extends above it a distance s to form a sleeve. This essentially moves the feed point upward from $z = 0$ to $z = s$. However, the discontinuity at $z = s$

does cause considerable difficulty in the rigorous solution of the problem. Accordingly, an approximation for considering the antenna with a uniform height h, and equivalent radius a_e ($a_i < a_e \leq a_o$), and the excitation at $z = s$ as shown in figure 2b has been suggested (King, 1956).

Using this approximation, one can derive the input impedance at $z = s$ through the conventional induced emf method with appropriate boundary conditions (Taylor, 1951):

$$Z_{in} = \frac{-\mu}{4\pi I^2(s)} \int_0^h I(z)\, dz\, L_z \int_{-h}^{h} I(z')\, K(z, z')\, dz' \quad , \tag{1}$$

where

$$L_z = -\frac{j\omega}{\kappa^2}\left(\frac{\partial^2}{\partial z^2} + k^2\right) \quad , \tag{2}$$

$$K(z, z') = e^{-jk\sqrt{(z-z')^2 + a_e^2}} \Big/ \sqrt{(z-z')^2 + a_e^2} \quad , \tag{3}$$

μ = permeability,

and $I(z)$, the current distribution over the antenna, is still unknown. An approximate Z_{in} can usually be determined by assuming a suitable form for $I(z)$. When considering the conditions that $I(z)$ must be continuous in the interval $0 \leq z \leq h$, $I(h) = 0$, and $\partial I(z)/\partial z$ must be continuous except at the driving point $z = s$, Taylor (1951) concluded that the following form should be a good approximation for $I(z)$:

$$I_1(z) = 1 + C(-\cos ks + \cos kz) \quad , \quad 0 \leq z \leq s \quad ,$$

and

$$I_2(z) = \delta[1 - \cos k(h - z)] + D\{\sin k(h - z) + \epsilon[1 - \cos k(h - z)]\} \quad , \quad s \leq z \leq h \quad , \tag{4}$$

where

$$\delta = 1/[1 - \cos k(h - s)] \ ,$$

$$\epsilon = -\sin k(h - s)/[1 - \cos k(h - s)] \ ,$$

C and D are complex constants to be determined, and the current has been normalized to unity at $z = s$. Current forms assumed in (4) have also been verified experimentally and have proved very satisfactory provided that

$$h - s < \lambda \ , \ \text{and} \ \ s < \lambda/2 \tag{5}$$

are satisfied.

Since the h and s specified in this study do meet the requirement in (5), we will follow Taylor's approach. With (4), the input impedance of the sleeve antenna becomes approximately

$$\bar{Z}_{in} = j30(\gamma_o + \gamma_c C + \gamma_d D + \gamma_{cc} C^2 + \gamma_{dd} D^2 + \gamma_{cd} CD) \ , \tag{6}$$

where

$$\gamma_o = \delta^2 (B_o + j C_o) \ , \tag{7}$$

$$\gamma_c = \delta (B_1 + j C_1) \ , \tag{8}$$

$$\gamma_d = 2\delta^2 (B_2 + j C_2) \ , \tag{9}$$

$$\gamma_{cc} = B_3 + j C_3 \ , \tag{10}$$

$$\gamma_{dd} = 2\delta (B_4 + j C_4) \ , \tag{11}$$

$$\gamma_{cd} = 2\delta (B_5 + j C_5) \ , \tag{12}$$

and the B_i and C_i in (7) through (12) are complicated combinations of trigometric functions and the generalized sine- and cosine-integrals; the latter are available in tables (Tables of generalized sine and cosine integral functions, 1949). The readers are referred to Taylor (1951) for details about these functions. From (6) we can see that $\bar{Z}_{in}$ is an analytic

function of both C and D; therefore, the values of C and D for the best approximation of $\bar{Z}_{in}$ to the true Z_{in} are given by the conditions

$$\frac{\partial \bar{Z}_{in}}{\partial C} = 0, \quad \text{and} \quad \frac{\partial \bar{Z}_{in}}{\partial D} = 0 , \tag{13}$$

which yield

$$C = (\gamma_d \gamma_{cd} - 2\gamma_c \gamma_{dd})/(4\gamma_{cc} \gamma_{dd} - \gamma_{cd}^2) , \tag{14}$$

$$D = (\gamma_c \gamma_{cd} - 2\gamma_d \gamma_{cc})/(4\gamma_{cc} \gamma_{dd} - \gamma_{cd}^2) . \tag{15}$$

Using (14) and (15), we can calculate the approximate input impedance from (6) and the current distribution from (4). The technique adopted here is actually an extension of Storer's (1950) variational formulation. Equation (6) is also good for the mutual impedance between two parallel identical sleeve antennas, when the equivalent radius a_e is replaced by d, center-to-center separation of the two antennas.

2.2 Field and power gain.

The field radiated from an isolated sleeve antenna is given by (Ma and Walters, 1967)

$$E_\theta^h = -j30\, k \frac{e^{-jkr}}{r} \sin\theta \int_o^h I(z)\, e^{jkz\cos\theta} (1 + R_v\, e^{-j2kz\cos\theta})\, dz$$

$$= -j30\, k \frac{e^{-jkr}}{r} \sin\theta \int_o^s I_1(z)(e^{jkz\cos\theta} + R_v\, e^{-jkz\cos\theta})\, dz$$

$$-j30k \frac{e^{-jkr}}{r} \sin\theta \int_s^h I_2(z)(e^{jkz\cos\theta} + R_v\, e^{-jkz\cos\theta})\, dz$$

$$= -j30 \frac{e^{-jkr}}{r} \sin\theta\, (E_{\theta 1} + E_{\theta 2} + E_{\theta 3} + E_{\theta 4} + E_{\theta 5}) , \tag{16}$$

where

R_v = vertically polarized ground reflection coefficient

$$= \frac{\cos\theta - \frac{k}{k_2}\left[1 - \left(\frac{k}{k_2}\sin\theta\right)^2\right]^{\frac{1}{2}}}{\cos\theta + \frac{k}{k_2}\left[1 - \left(\frac{k}{k_2}\sin\theta\right)^2\right]^{\frac{1}{2}}} \quad , \tag{17}$$

θ is the angle measured from the antenna axis (z-axis),

$$k_2 \cong k\left[\epsilon_r - j\frac{18\sigma(10^3)}{f_{MHz}}\right]^{\frac{1}{2}} \quad , \tag{18}$$

f_{MHz} = operating frequency in MHz,

ϵ_r = relative dielectric constant of the ground,

σ = conductivity of the ground in mho/m.

The component fields in (16) are

$$E_{\theta 1} = \int_o^s (1 - C\cos ks)(e^{jkz\cos\theta} + R_v e^{-jkz\cos\theta})\, dz$$

$$= \frac{1 - C\cos ks}{j\cos\theta}\left(e^{jks\cos\theta} - R_v e^{-jks\cos\theta} - 1 + R_v\right) , \tag{19}$$

$$E_{\theta 2} = C\int_o^s \cos kz\,(e^{jkz\cos\theta} + R_v e^{-jkz\cos\theta})\, dz$$

$$= \frac{C}{\sin^2\theta}\left\{e^{jks\cos\theta}(j\cos\theta\cos ks + \sin ks) - j\cos\theta\right.$$

$$\left. + R_v\left[e^{-jks\cos\theta}(-j\cos\theta\cos ks + \sin ks) + j\cos\theta\right]\right\} , \tag{20}$$

$$E_{\theta 3} = (\delta + D\epsilon) \int_s^h (e^{jkz\cos\theta} + R_v e^{-jkz\cos\theta})\, dz$$

$$= \frac{(\delta + D\epsilon)}{j\cos\theta} (e^{jk\cos\theta} - R_v e^{-jkh\cos\theta} - e^{jks\cos\theta} + R_v e^{-jks\cos\theta}), \tag{21}$$

$$E_{\theta 4} = \left[D\sin kh - (\delta + D\epsilon)\cos kh \right] \int_s^h \cos kz\, (e^{jkz\cos\theta} + R_v e^{-jkz\cos\theta})\, dz$$

$$= \frac{D\sin kh - (\delta + D\epsilon)\cos kh}{\sin^2\theta} \left[e^{jkh\cos\theta} (j\cos\theta\cos kh + \sin kh) \right.$$

$$- e^{jks\cos\theta} (j\cos\theta\cos ks + \sin ks)$$

$$+ R_v e^{-jkh\cos\theta} (-j\cos\theta\cos kh + \sin kh)$$

$$\left. - R_v e^{-jks\cos\theta} (-j\cos\theta\cos ks + \sin ks) \right], \tag{22}$$

and

$$E_{\theta 5} = -\left[D\cos kh + (\delta + D\epsilon)\sin kh \right] \int_s^h \sin kz\, (e^{jkz\cos\theta} + R_v e^{-jkz\cos\theta})\, dz$$

$$= -\frac{D\cos kh + (\delta + D\epsilon)\sin kh}{\sin^2\theta} \left[e^{jkh\cos\theta} (j\cos\theta\sin kh - \cos kh) \right.$$

$$- e^{jks\cos\theta} (j\cos\theta\sin ks - \cos ks)$$

$$- R_v e^{-jkh\cos\theta} (j\cos\theta\sin kh + \cos kh)$$

$$\left. + R_v e^{-jks\cos\theta} (j\cos\theta\sin ks + \cos ks) \right]. \tag{23}$$

Since there are 120 antennas on the circumference of the high-band ring and eight elements are actually excited at a time for scanning, the array factor contributed from the eight excited elements and the next two pairs of parasitic elements caused by mutual coupling can be written (see fig. 3)

$$E_{h1} = \sum_{i=-6}^{6} I_{hi}\, e^{jk\, a_{h1} \sin\theta \cos(\varphi-\varphi_i)} \quad , \quad (i \neq 0) \tag{24}$$

where a_{h1} is the radius of the high-band ring, θ the angle measured from the z-axis (normal to the array plane), φ measured from the axis shown in figure 3, φ_i the location of the ith element, and I_{hi} the current of the ith element at its feed point. In arriving at (24), we have only considered two parasitic pairs closest to the excited elements and neglected the remaining parasitic elements since they are farther away from the excited antennas and the induced currents on them should be insignificant. Because of symmetry and the special way of voltage excitation discussed later, we have

$$I_{hi} \text{ (for positive i)} = I_{hi} \text{ (for negative i)}. \tag{25}$$

Similarly, the contribution from the image ring whose radius is a_{h2} should be

$$E_{h2} = \sum_{i=-6}^{6} (-I_{hi})\, e^{jk\, a_{h2} \sin\theta \cos(\varphi-\varphi_i)} \quad , \quad (i \neq 0) \ . \tag{26}$$

The currents I_{hi} in (24) and (26) can be determined from the circuit consideration:

$$
\begin{bmatrix}
\bar{Z}_{in}-Z_{11'}+Z_{12}-Z_{12'} & Z_{12}-Z_{12'}+Z_{13} & Z_{13} & 0 & 0 & 0 \\
Z_{12}-Z_{12'}+Z_{13} & \bar{Z}_{in}-Z_{11'} & Z_{12}-Z_{12'} & Z_{13} & 0 & 0 \\
Z_{13} & Z_{12}-Z_{12'} & \bar{Z}_{in}-Z_{11'} & Z_{12}-Z_{12'} & Z_{13} & 0 \\
0 & Z_{13} & Z_{12}-Z_{12'} & \bar{Z}_{in}-Z_{11'} & Z_{12}-Z_{12'} & Z_{13} \\
0 & 0 & Z_{13} & Z_{12}-Z_{12'} & \bar{Z}_{in}+50-Z_{11'} & Z_{12}-Z_{12'} \\
0 & 0 & 0 & Z_{13} & Z_{12}-Z_{12'} & \bar{Z}_{in}+50-Z_{11'}
\end{bmatrix}
$$

$$
\times \begin{bmatrix} I_{h1} \\ I_{h2} \\ I_{h3} \\ I_{h4} \\ I_{h5} \\ I_{h6} \end{bmatrix} = \begin{bmatrix} \bar{Z}_{in}\, e^{-j\alpha_1} \\ \bar{Z}_{in}\, e^{-j\alpha_2} \\ \bar{Z}_{in}\, e^{-j\alpha_3} \\ \bar{Z}_{in}\, e^{-j\alpha_4} \\ 0 \\ 0 \end{bmatrix}, \qquad (27)
$$

where $\bar{Z}_{in}$ is the open-circuit self impedance of an isolated antenna, Z_{12} the open-circuit mutual impedance between No. 1 and No. 2 antennas with $d = 2a_{h1} \sin 1.5^\circ$, Z_{13} is that between No. 1 and No. 3 antennas with $d = 2a_{h1} \sin 3^\circ$, $Z_{11'}$ is that between No. 1 antenna and its own image with $d = a_{h1} - a_{h2} = 2$ (distance between the high-band ring and the screen), $Z_{12'}$ is that between No. 1 antenna and the image of No. 2 antenna with $d = (a_{h1}^2 + a_{h2}^2 - 2a_{h1}\, a_{h2} \cos 3^\circ)^{\frac{1}{2}}$. Here again we have only considered mutual couplings between relatively close pairs of elements.

A resistance of 50 ohms has been added to the parasitic elements (No. 5 and No. 6), since they both are unexcited but terminated with a resistor of 50 ohms. The voltage excitation on the right side of (27) has been multiplied by $\bar{Z}_{in}$ to make $|I_{hi}| = 1$ should the mutual impedances be ignored. This is required in order to be consistent with the current normalization assumed in (4). The phase α_i associated with the voltage is given according to

$$\alpha_i = k\, a_{h1} \sin\theta_o \cos(\varphi_o - \varphi_i) \quad , \tag{28}$$

where $70^\circ \le \theta_o \le 80^\circ$ and $\varphi_o = 0^\circ$ define the desired direction of beam maximum.

After obtaining the I_{hi} from (27) and substituting them into (24) and (26), we have the total field radiated from the portion of the high-band array under consideration,

$$E_t^h = E_\theta^h (E_{h1} + E_{h2}) \quad . \tag{29}$$

The power gain relative to a loss less isotropic source with the same power input (Kraus, 1950) thus becomes

$$g^h(\theta,\varphi) = \frac{4\pi r^2 \times \frac{1}{120\pi} |E_t^h|^2}{P_{in}}$$

$$= \frac{30 \sin^2\theta \left| \left(\sum_{n=1}^{5} E_{\theta n} \right) (E_{h1} + E_{h2}) \right|^2}{P_{in}} \quad , \tag{30}$$

or

$$G^h(\theta,\varphi) = 10 \log(g^h) \text{ in dB} \quad , \tag{31}$$

where $E_{\theta n}$, n = 1, 2, 3, 4 and 5 are given in (19) through (23), E_{h1} and E_{h2} are from (24) and (26), and P_{in} representing the total power input is

$$P_{in} = 2 \sum_{i=1}^{4} |I_{hi}|^2 \, \mathrm{Re}(z_i) = 2 \, \mathrm{Re} \sum_{i=1}^{4} V_i \, I_{hi}^*$$

$$= 2 \, \mathrm{Re} \sum_{i=1}^{4} \overline{Z}_{in} \, e^{-j\alpha_i} \, I_{hi}^* \quad . \tag{32}$$

Numerical results for $G^h(75^\bullet, \varphi)$ and $G^h(\theta, 0^\bullet)$ as a function of frequency and ground constants with a specified element dimension and array geometry are given in figure 4.

3. LOW-BAND ELEMENTS

3.1 Impedance and current distribution.

The radiator used for the low-band (3-10 MHz) ring is a three-wire folded monopole excited against a horizontal ground plane, as shown in figure 2c. Characteristics of this antenna may be conveniently analyzed through an equivalent folded dipole formed by the antenna and its image, which in turn can be represented by an equivalent circuit shown in figure 2d (Tai, 1961; Guertler, 1950). The transmission mode is represented by Z_f, which can be calculated according to

$$Z_f = 200 + j \, Z_o \tan kh \quad , \tag{33}$$

where

$$Z_o = 60 \left[\ell n \frac{2h}{a_2} - 2 \frac{\left(\ell n \frac{\sqrt{4h^2 + d^2}}{d} \right)^2}{\ell n \frac{2h\sqrt{h^2 + d^2}}{a_1 d}} \right] , \tag{34}$$

with h the height of the monopole, a_1 and a_2 radii of the out down-wire and center pipe, respectively, and d now the half distance between the two downwires. The radiation mode is represented by Z_r,

which is the corresponding free-space input impedance of an equivalent dipole of length $2h$ and radius $a'_e = [a_2 + 2a_1)d^2/3]^{\frac{1}{3}}$.

Because kh may be equal to π for a frequency in the designed frequency range, which would cause difficulty in evaluating Z_r if the ordinary sinusoidal current distribution is assumed on the antenna, we use the three-term theory developed by King and Wu (1965) for the current distribution; that is

$$I_\ell = \frac{j \cdot V}{60\, \psi_{dR} \cos kh} \left[\sin k(h - |z|) + T_U (\cos kz - \cos kh) + T_D \left(\cos \frac{kz}{2} - \cos \frac{kh}{2} \right) \right] \quad kh \neq \pi/2 , \quad (35)$$

or

$$I_\ell = \frac{-j \cdot V}{60\, \psi_{dR}} \left[\sin k|z| - 1 + T'_U \cos kz - T'_D \left(\cos \frac{kz}{2} - \cos \frac{\pi}{4} \right) \right] \quad kh = \pi/2 , \quad (36)$$

where V = the impressed voltage, ψ_{dR}, T_U, T_D, T'_U, and T'_D can also be expressed in terms of the generalized sine- and cosine-integrals with arguments functions of a'_e and h. The details are given in a paper by King and Wu (1965).

Equations (35) and (36) give the input impedance of the dipole:

$$Z_r = -j\,60\, \psi_{dR} \cos kh \Big/ \left[\sin kh + T_U(1 - \cos kh) + T_D \left(1 - \cos \frac{kh}{2} \right) \right] , \quad kh \neq \frac{\pi}{2} , \quad (37)$$

or

$$Z_r = j\,60\, \psi_{dR} / (-1 + T'_U - 0.293\, T'_D) , \quad kh = \frac{\pi}{2} . \quad (38)$$

The equivalent input impedance of the original folded monopole then becomes (see fig. 2d)

$$Z'_{in} = \frac{\frac{3}{2}(2m+1)^2 Z_r Z_f}{(2m+1)^2 Z_r + 3 Z_f}, \tag{39}$$

where

$$m = \log \frac{d}{a_1} \Big/ \log \frac{d}{2a_2} \quad . \tag{40}$$

Note that Z'_{in} reduces to $\frac{1}{2}(2m+1)^2 Z_r$ when $kh = \frac{\pi}{2}$ $(Z_f = \infty)$. The parameter m in (40) becomes unity when $2a_2 = a_1$.

The mutual impedance between two parallel identical low-band elements can also be calculated by (37) or (38) if a'_e in Ψ_{dR}, T_U, T_D, T'_U and T'_D is replaced by the separation between the two antennas.

3.2 Field and power gain.

The field radiated by a single low-band antenna, based on the current forms given in (35) and (36), is

$$E^{\ell}_{\theta} = -j30 \frac{I_{\ell}(0)}{\sin kh + T_U(1 - \cos kh) + T_D(1 - \cos \frac{kh}{2})} \times$$

$$\frac{e^{-jkr}}{r} E_{\theta 6}, \quad kh \neq \pi/2 \tag{41}$$

or

$$E^{\ell}_{\theta} = -j30 \frac{I_{\ell}(0)}{-1 + T'_U - 0.293\, T'_D} \cdot \frac{e^{-jkr}}{r} E_{\theta 7}, \quad kh = \pi/2 \ , \tag{42}$$

where

$$E_{\theta 6} = \frac{1}{\sin\theta}\left[B_6 + j\,C_6 + R_v(B_6 - j\,C_6)\right]$$

$$+ \frac{T_U}{\sin\theta}\left[B_7 + j\,C_7 + R_v(B_7 - j\,C_7)\right]$$

$$- (T_U \cos kh + T_D \cos\frac{kh}{2})\tan\theta\left[B_8 + j\,C_8 + R_v(B_8 - j\,C_8)\right]$$

$$+ \frac{2\,T_D \sin\theta}{1 - 4\cos^2\theta}\left[B_9 + j\,C_9 + R_v(B_9 - j\,C_9)\right] , \qquad (43)$$

$$E_{\theta 7} = \frac{1}{\sin\theta}\left[B_{10} + j\,B_{10} + R_v(B_{10} - j\,C_{10})\right]$$

$$+ \frac{T'_U}{\sin\theta}\left[B_7 + j\,C_7 + R_v(B_7 - j\,C_7)\right]$$

$$+ (-1 + 0.707\,T'_D)\tan\theta\left[B_8 + j\,C_8 + R_v(B_8 - j\,C_8)\right]$$

$$- \frac{2T'_D \sin\theta}{1 - 4\cos^2\theta}\left[B_9 + j\,C_9 + R_v(B_9 - j\,C_9)\right] , \qquad (44)$$

$B_6 = \cos(kh\cos\theta) - \cos kh$,

$C_6 = \sin(kh\cos\theta) - \cos\theta \sin kh$,

$B_7 = \sin kh \cos(kh\cos\theta) - \cos\theta \cos kh \sin(kh\cos\theta)$,

$C_7 = \sin kh \sin(kh\cos\theta) + \cos\theta \cos kh \cos(kh\cos\theta) - \cos\theta$,

$B_8 = \sin(kh\cos\theta)$,

$C_8 = 1 - \cos(kh\cos\theta)$,

$B_9 = \sin\frac{kh}{2}\cos(kh\cos\theta) - 2\cos\theta\cos\frac{kh}{2}\sin(kh\cos\theta)$,

$$C_9 = \sin\frac{kh}{2}\sin(kh\cos\theta) + 2\cos\theta\cos\frac{kh}{2}\cos(kh\cos\theta) - 2\cos\theta \quad ,$$

$$B_{10} = 1 - \cos kh\cos(kh\cos\theta) - \cos\theta\sin kh\sin(kh\cos\theta) \quad ,$$

$$C_{10} = -\cos kh\sin(kh\cos\theta) + \cos\theta\sin kh\cos(kh\cos\theta) \quad .$$

Once we know how to calculate the element field and impedances, determining the field contributed by the array of eight excited elements and two neighboring parasitic pairs follows that for the high-band ring. Namely, the low-band ring and its image ring will contribute, respectively,

$$E_{\ell 1} = \sum_{i=-6}^{6}{}' I_{\ell i}\, e^{jk\, a_{\ell 1}\sin\theta\cos(\varphi-\varphi_i)} \quad , \quad i \neq 0 \qquad (45)$$

and

$$E_{\ell 2} = \sum_{i=-6}^{6}{}' (-I_{\ell i})\, e^{jk\, a_{\ell 2}\sin\theta\cos(\varphi-\varphi_i)} \quad , \quad i \neq 0 \quad , \qquad (46)$$

where the $I_{\ell i}$ are the terminal currents determined by the following matrix equation with a procedure similar to that of (27),

$$\left[Z_\ell\right]\left[I_{\ell i}\right] = \left[e^{-j\alpha'_i}\right] \quad . \qquad (47)$$

In (47), $\alpha'_i = k\, a_{\ell 1}\sin\theta_o\cos(\varphi_0-\varphi_i)$, and $\left[Z_\ell\right]$ is a 6×6 impedance matrix with Z_r given in (37) or (38) replacing $\bar{Z}_{in}$ in the main diagonal in (27). Since the actual termination resistance at the input of parasitic elements is now 200 ohms, the equivalent resistor termination experienced by the radiating mode should be (see fig. 2d)

$$Z_t = \frac{1}{(2m+1)^2} \cdot \frac{1200 Z_f}{400 + 3Z_f} \quad . \tag{48}$$

This equivalent termination impedance Z_t should be used to substitute 50 in (5, 5) and (6, 6) positions in (27).

The power gain expression is therefore

$$g^{\ell}(\theta, \varphi) = \frac{30 \left| E_{\theta 6} (E_{\ell 1} + E_{\ell 2}) \right|^2}{\left| \sin kh + T_U (1 - \cos kh) + T_D (1 - \cos \frac{kh}{2}) \right|^2 P'_{in}}$$

$$\text{for } kh \neq \pi/2 \ , \tag{49}$$

or

$$g^{\ell}(\theta, \varphi) = \frac{30 \left| E_{\theta 7} (E_{\ell 1} + E_{\ell 2}) \right|^2}{\left| -1 + T'_U - 0.293 T'_D \right|^2 P'_{in}} \quad \text{for } kh = \pi/2 \ , \tag{50}$$

where

$$P'_{in} = \mathrm{Re} \sum_{i=1}^{4} (2m+1) V_i I^*_{in} = \mathrm{Re} \sum_{i=1}^{4} V_i \left[I_{\ell i} + \frac{(2m+1)^2 V_i}{3Z_f} \right]^* . \tag{51}$$

Numerical examples for $G^{\ell}(75^\circ, \varphi)$ and $G^{\ell}(\theta, 0^\circ)$ are given in figure 5 with a specified element dimension and array geometry.

4. FURTHER IMPROVEMENTS

Clearly, the performance given in figures 4 and 5, according to a certain set of specified dimensions, is not the best in any sense. Further improvements by varying some parameters are definitely possible. In this paper, we only consider the case of varying the array radii and element-to-screen distance (a_{h1}, a_{h2}, $a_{\ell 1}$, $a_{\ell 2}$). Some of the improved

results are shown in figure 6, which can be compared with those presented in figures 4 and 5 to get a general idea for "optimization" as design guideline.

5. CONCLUDING REMARKS

A theoretical method has been formulated for numerically calculating impedances, field radiated, and power gain of a Wullenweber antenna above a lossy flat earth. Typical results of these characteristics are given as a function of frequency, ground constants, element dimensions, array geometries, elevation and azimuth angles. Optimization of the array performance with respect to the ring radii and element-to-screen distance is also demonstrated with supporting numerical results. In this study, we have assumed current distributions on both low-band and high-band elements, and a perfect current image of the screen. Possible interactions between the screens and elements of different bands have been neglected.

6. REFERENCES

Guertler, R. (1950), Impedance transformation in folded dipoles, IRE Proc. 38, No. 9, 1042-1047.

King, R. W. P. (1956), The Theory of Linear Antennas, 407-419 (Harvard University Press, Cambridge, Mass.)

King, R. W. P. and T. T. Wu (1965), Currents, charges, and near fields of cylindrical antennas, Radio Sci. 69D, No. 3, 429-446.

Kraus, J. D. (1950), Antennas, 26 (McGraw-Hill Book Co., Inc, New York).

Ma, M. T. and L. C. Walters (1967), Computed radiation patterns of log-periodic antennas over lossy plane ground, ESSA Tech. Rept. IER 54-ITSA 52.

Storer, J. E. (1950), Variational solution to the problem of the symmetrical cylindrical antenna, Tech. Rept. No. 101, Cruft Laboratory, Harvard University.

Tai, C. T. (1961), Characteristics of Linear Antenna Elements, 3-13, Edited by H. Jasik (McGraw-Hill Book Co., Inc., New York).

Taylor, J. (1951), The sleeve antenna, Tech. Rept. No. 128, Cruft Laboratory, Harvard University.

Tables of generalized sine and cosine integral functions, Vol. I and II, (Harvard University Press, Cambridge, Mass., 1949).

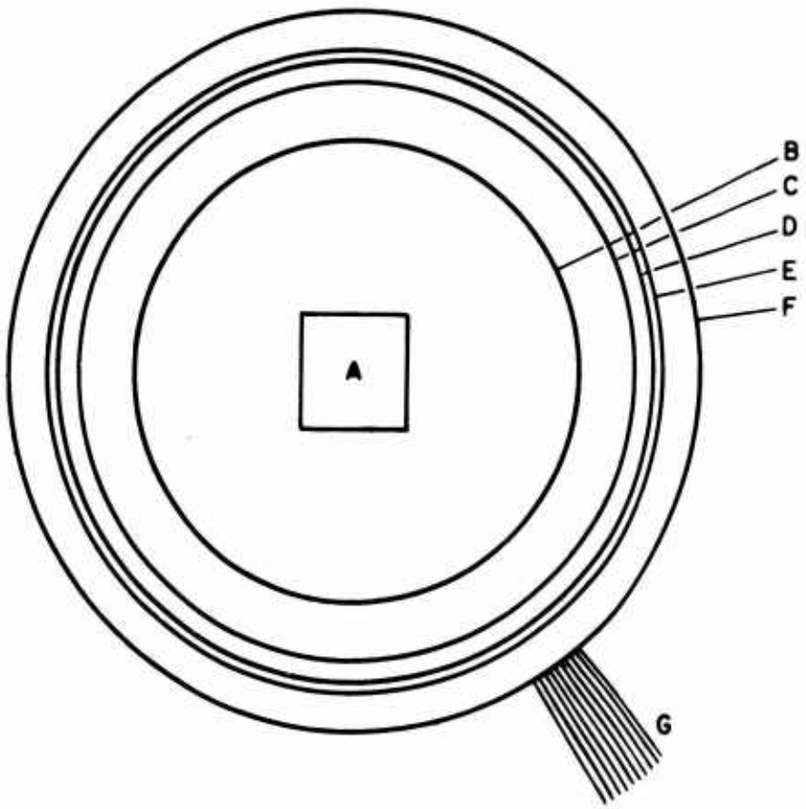

A. Operations Building
B. Low Band Screen (Radius 366 feet)
C. Low Band Antennas (40 folded three-wire monopole; Radius 393.5 feet)
D. High Band Screen (Radius 423.5 feet)
E. High Band Antennas (120 sleeve antennas; Radius 436.75 feet)
F. Outer Edge of Ground Mat (Extends 127.5 feet from Inner Edge)
G. Radials (One every degree extending 150 feet in length from Outer Edge of Ground Mat; Only 10 radials of 360 are shown)

Figure 1. Array geometry (top view).

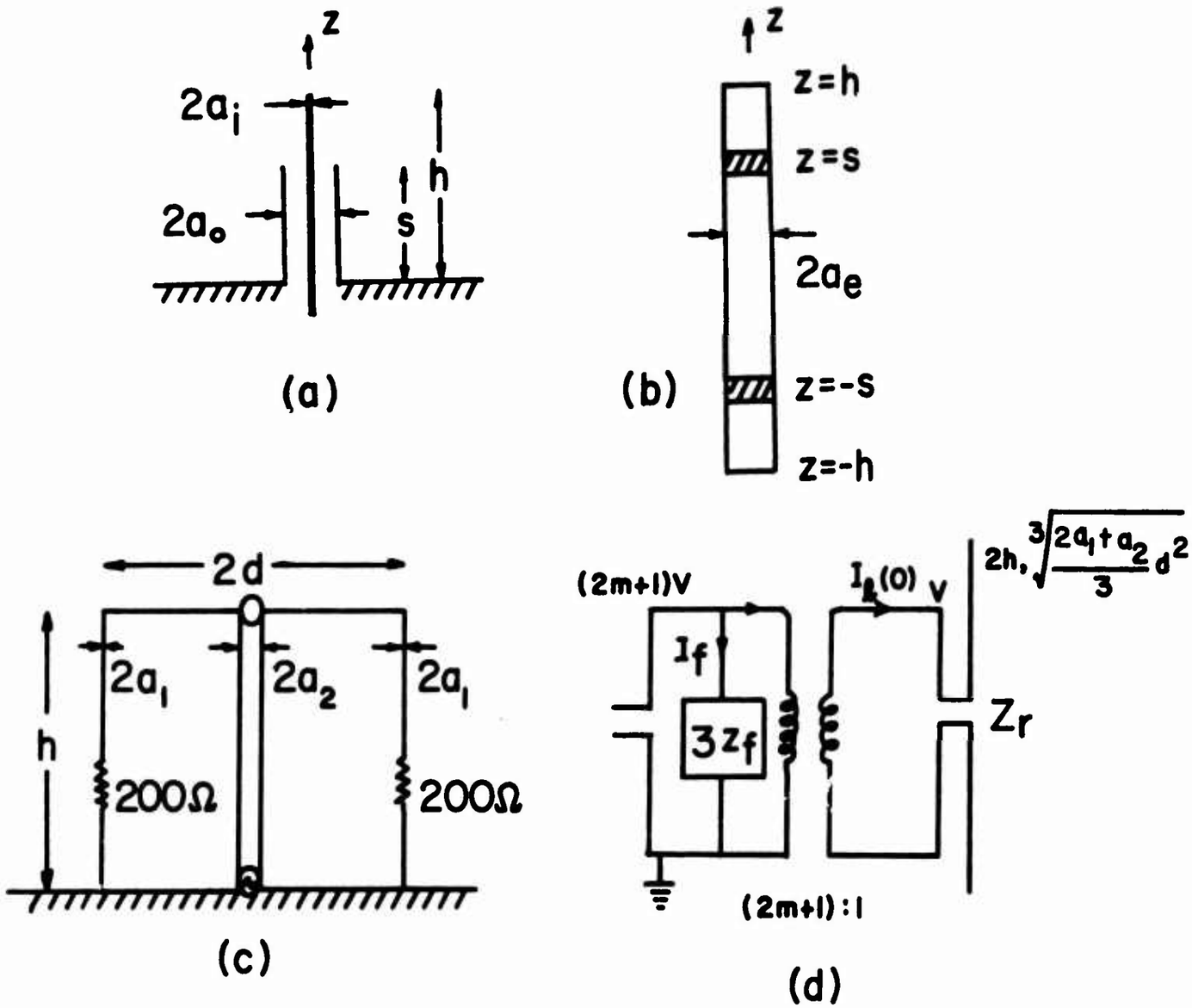

Figure 2. Sketches of antenna elements:
(a) sleeve antenna, (b) approximate equivalent of (a),
(c) three-wire folded monopole, (d) equivalent circuit of (c).

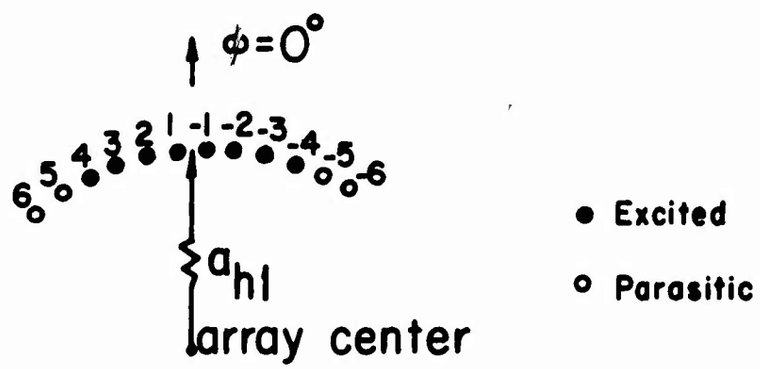

Figure 3. Top view of the high-band ring with 8 of 120 elements excited.

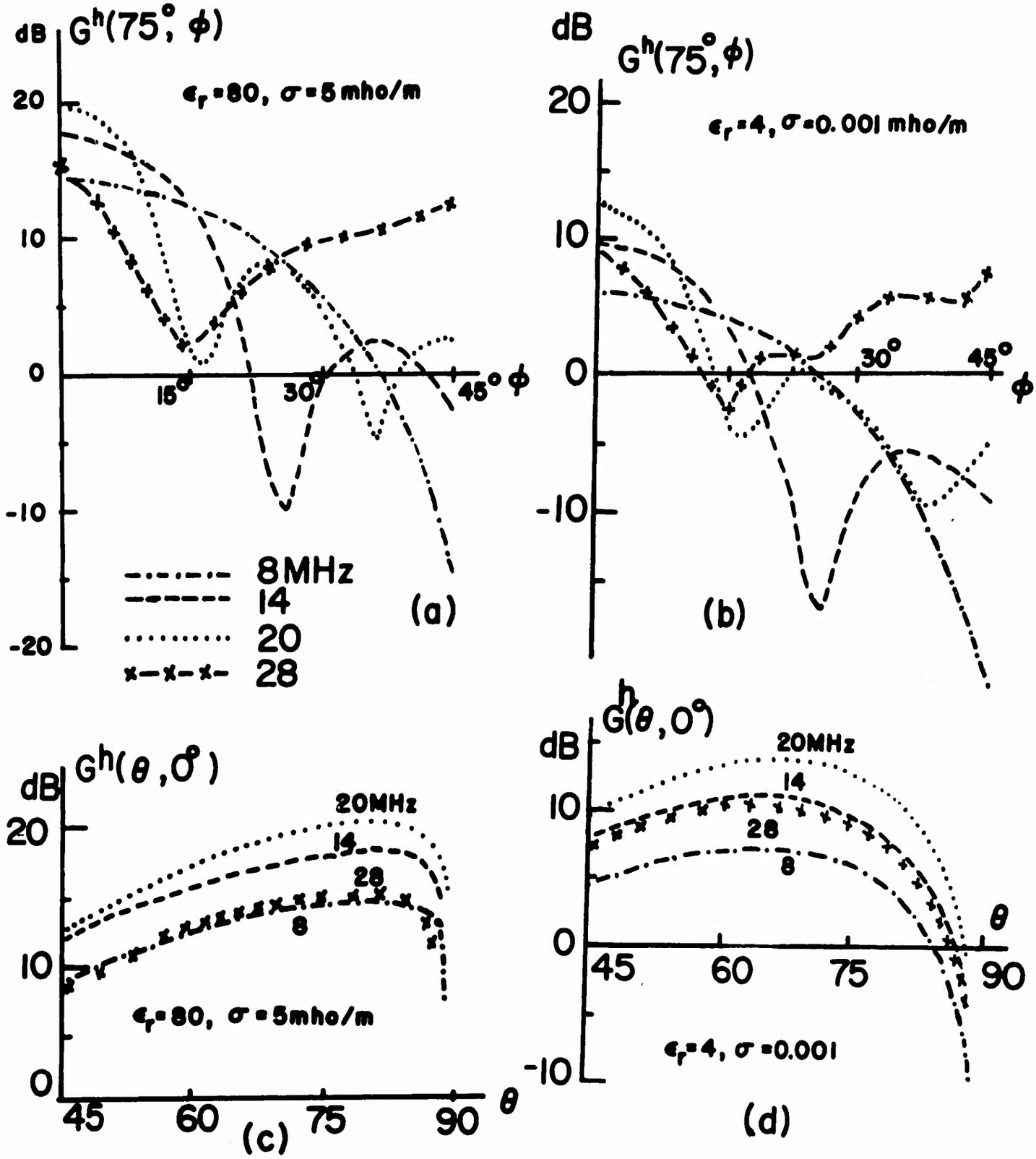

Figure 4. High-band power gain of a Wullenweber antenna for two grounds: (a) and (b) as a function of φ; (c) and (d) as a function of θ.

(h = 7.239 m, s = 2.515 m, a_{h1} = 133.121 m, a_{h2} = 125.044 m, a_e = 0.105 m)

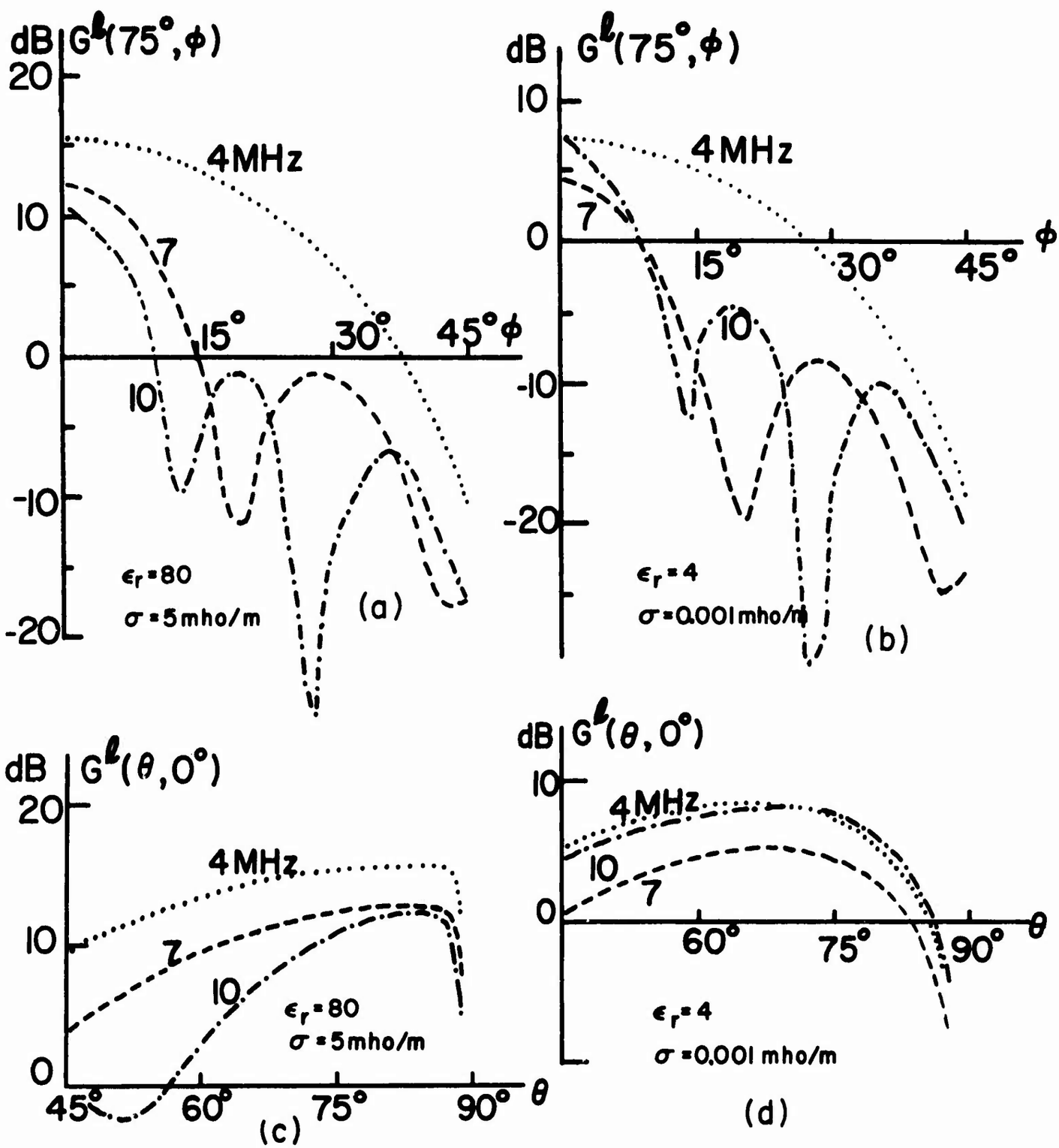

Figure 5. Low-band power gain of a Wullenweber antenna for two grounds: (a) and (b) as a function of φ; (c) and (d) as a function of θ.

($h = 17.399$ m, $d = 0.381$ m, $a_1 = 0.0016$ m, $a_2 = 0.0508$ m, $a_{\ell 1} = 119.939$ m, $a_{\ell 2} = 103.175$ m).

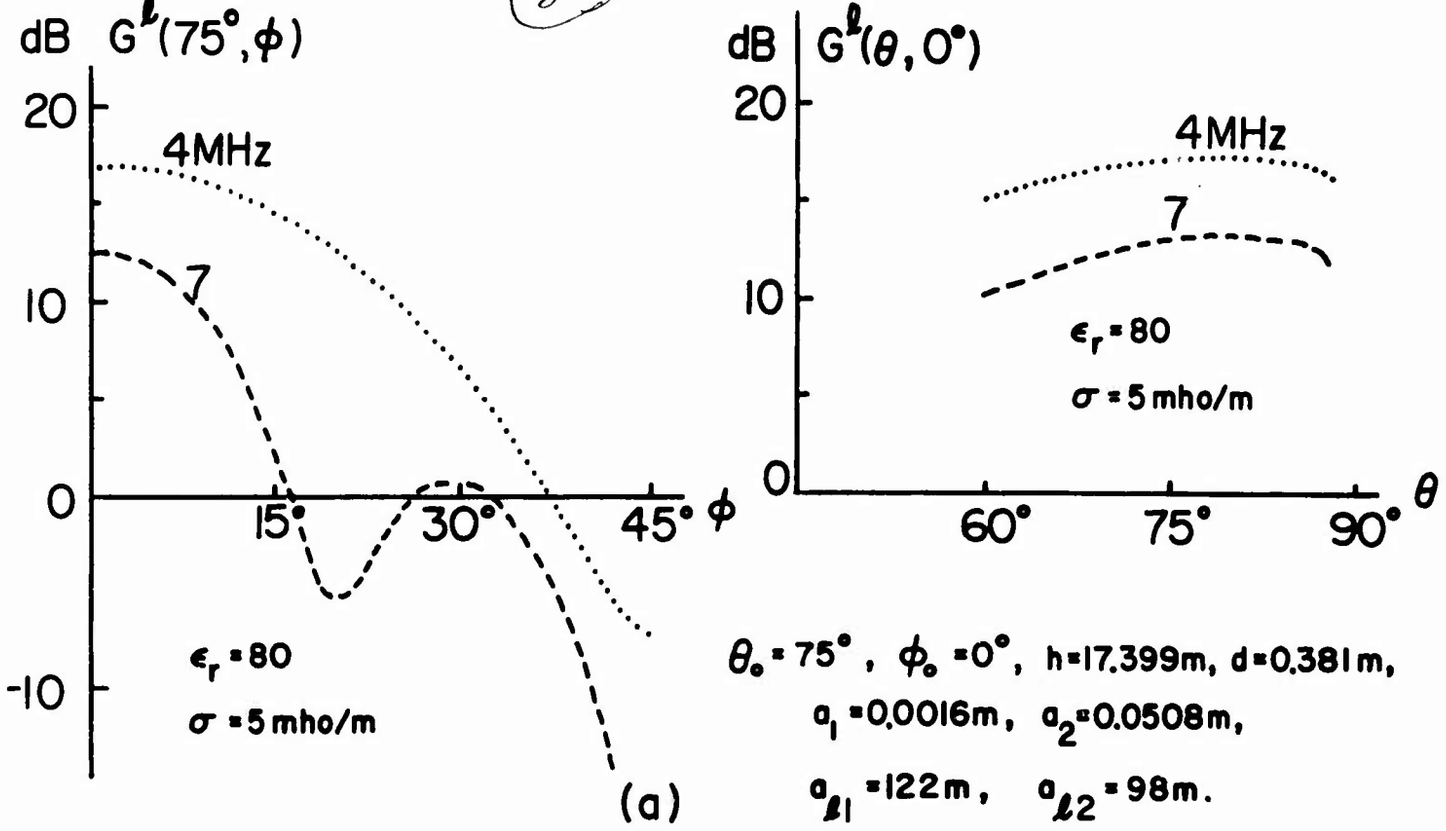

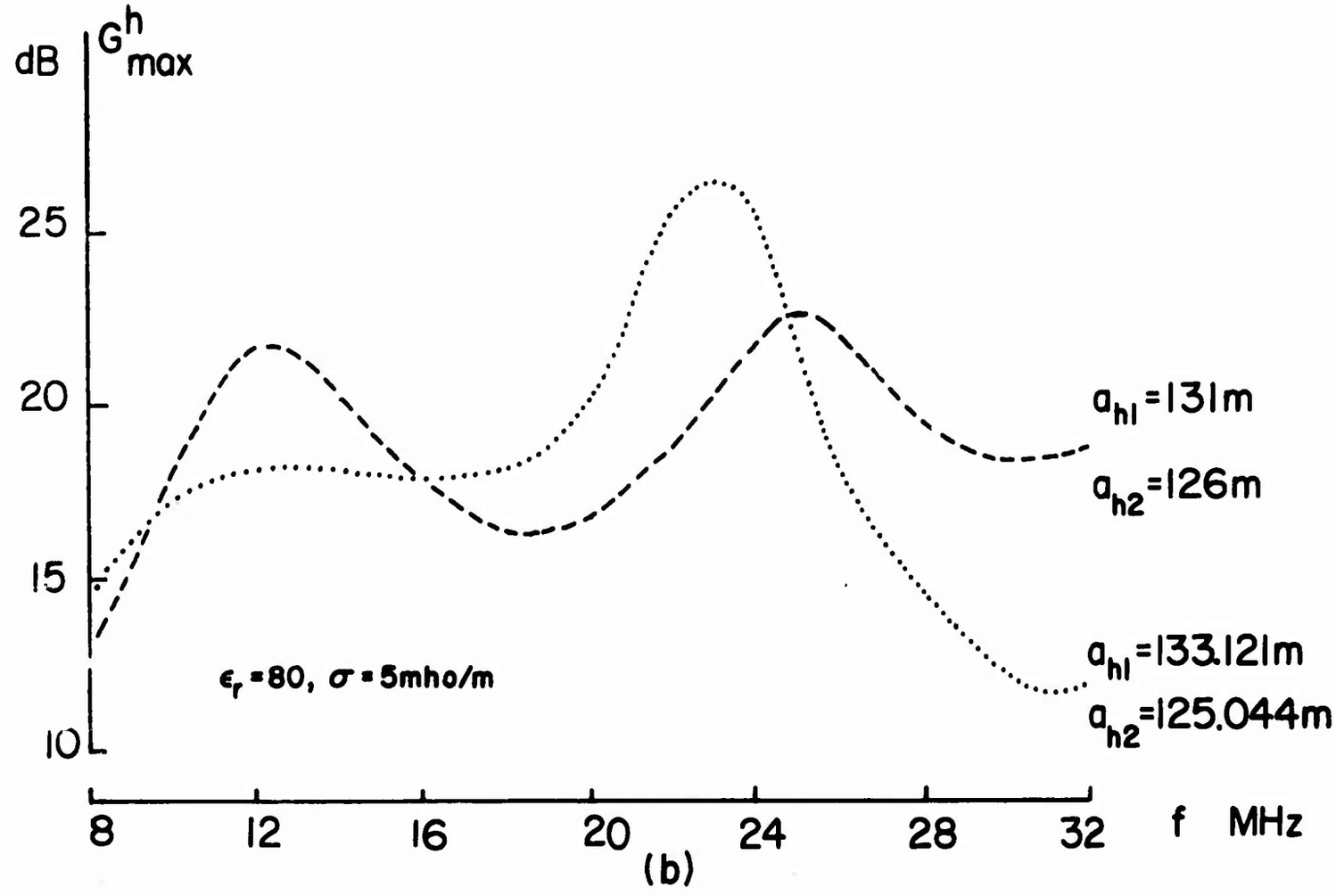

Figure 6. "optimum" power gain of a Wullenweber antenna with revised ring radii and element-to-screen distance: (a) low band, (b) high band.

A BROADBAND OPTICAL FEED FOR CIRCULAR ARRAYS

By

J. M. Devan, J. E. Boyns, and A. D. Munger

Naval Electronics Laboratory Center
San Diego, California 92152

ABSTRACT

This paper describes the optical characteristics of the R-2R parallel-plate lens which make it useful as a broadband feed system for circular arrays featuring multiple beams, DF, and/or sidelobe-suppression techniques. Experimental results are given for lens systems designed to operate over frequency ranges of 2-4, and 2.9-3.5 GHz.

REVERSE SIDE BLANK

1/2

CONTENTS

ILLUSTRATIONS

ILLUSTRATIONS (CONTINUED)

INTRODUCTION

A circular array will provide identical beams at all beam positions around its circumference. However, phase correction is inherently necessary if the radiators on a curved surface are to produce a planar phase front. In practice, energizing a sector of approximately 90° (plus and minus 45° from the beam axis) will produce the desired beam; energizing additional elements contributes little to beam quality. As with the planar array, some form of amplitude taper distribution may be used to reduce sidelobes as required or establish a desired adjacent-beam crossover level.

A feed system for circular arrays must therefore provide these basic functions: (1) energized-element phase correction to produce the required aperture ph se distribution for a planar phase front, (2) suitable amplitude taper distribution, and (3) commutation of the beam around the array while maintaining correct element amplitude and phase relationships. The accomplishment of functions (1) and (2) with the R-2R parallel plate lens is the primary topic of this paper.

THEORETICAL CONSIDERATIONS

The 2-R2 parallel-plate lens is essentially a dielectric region of radius R bounded by parallel conducting surfaces and a circumferential conducting st rface at radius R. Energy may be inserted at any location around the circumference, such as point "A" in figure 1A, by one element or an array of elements; all remaining elements are then available for use as output ports. These input/output elements are commonly either horns located around the circumference or probes spaced ¼ wavelength in front of the circumferential ground plane. The distance between the parallel conducting plates must be no greater than ½ wavelength at the highest frequency of interest in order to propagate only the electric-field component perpendicular to the plates.

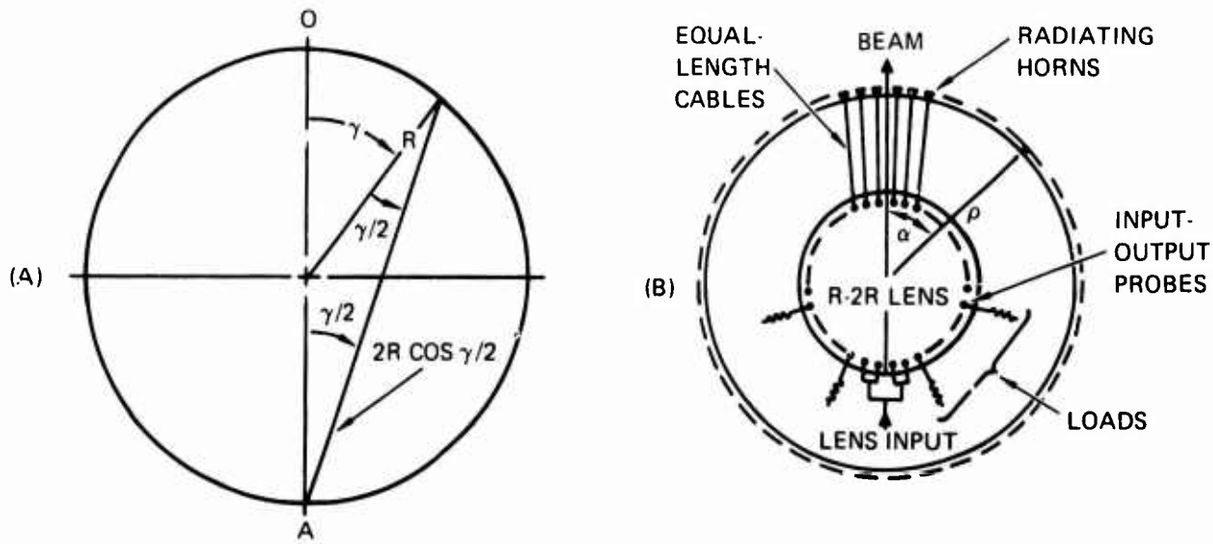

Figure 1. Parallel-plate lens. A, geometry; B, schematic of completed array.

The phase delay required for a circular array of elements to produce a planar phase front is given by

$$\phi_D = \frac{2\pi}{\lambda} \rho \cos \alpha \tag{1}$$

where ρ is the radius of the array and α is the element angular location referenced to the beam direction as shown in figure 1B. The phase delay distance, d_D, is then given by

$$d_D = \rho \cos \alpha \tag{2}$$

The distance traveled, d_T, by energy inserted into the lens at port "A" of figure 1A and extracted at some other port around the lens is given by

$$d_T = 2R \cos \frac{\gamma}{2} \tag{3}$$

where R is the radius of the lens and γ is the angular location of the output port referenced to the radius of the lens passing through the center of the output array. Equating d_D to d_T shows that the phase delay distance required for the proper circular-array phase distribution will be provided by the lens if

$$R = \tfrac{1}{2} \rho \tag{4}$$

and

$$\gamma = 2\alpha \tag{5}$$

That is, the lens radius must be one-half the array radius,[1] the lens angle to any output port will be twice the array angle to the corresponding antenna element, and the number of ports around the lens is one-half the number of antenna elements. Thus a lens of N ports can provide the desired phase correction for N M elements of a $2N$-element antenna, where M is the number of lens ports used for the input. All elements of the array can be fed with the lens by making each lens port switchable to one of two elements separated 180° around the array and by connecting adjacent lens ports to adjacent elements on the array with equal length cables

The normalized amplitude pattern for a probe feed spaced ¼λ in front of the circumferential ground plane at point "A" of figure 1A can be approximated by that of a probe on a flat ground plane,

$$E_N(\gamma) = \sin\left(\frac{\pi}{2} \cos \frac{\gamma}{2}\right) \tag{6}$$

However, the use of a single lens input results in a fixed distribution around the lens output ports. If only a 90° sector of the circular array is illuminated to form the beam, then only a 180° sector of lens outputs need be used. It is therefore desirable to direct or focus the beam within the lens so that maximum input energy is available at the selected output ports. Also, since the receive pattern of a probe is the same as its radiating pattern, it will not absorb energy at high angles of incidence. Therefore, energy incident on probe near the input will cause reflection within the lens even when these probes are terminated. Such reflections can destroy the optical properties of the lens. Providing a directive input pattern will therefore minimize reflections as well as maximize output energy.

Some control over the directivity of the lens input pattern can be achieved by using a small array of input probes and by tapering the amplitude distribution to the probes. The normalized amplitude pattern for any single input probe located at an angle β with respect to center of the input array can be approximated by

$$E_N(\gamma) = \sin\left(\frac{\pi}{2} \cos \frac{\gamma+\beta}{2}\right) \tag{7}$$

The output amplitude on a probe located at an angle γ can be approximated by summing over the inputs,

$$E(\gamma) = \sum_{\beta} I(\beta) \frac{\sin^2\left(\frac{\pi}{2}\cos\frac{\gamma+\beta}{2}\right)}{\sqrt{2R\cos\frac{\gamma+\beta}{2}}} \exp\left(-j2\pi R\cos\frac{\gamma+\beta}{2}\right) \qquad (8)$$

The sidelobe level of a circular-array antenna pattern can be minimized by application of an amplitude taper to the energized elements. The R-$2R$ parallel-plate lens can provide various amplitude distributions depending on the lens input arrangement. The computed results for various input arrangements are given with the measured experimental results obtained for several lenses.

Commutation of the input around the lens will result in scanning or stepping the beam around the antenna. To accomplish this, switching circuitry must be added between the transmitter or receiver and the lens input and also between the lens output and the circular array.[2]

EXPERIMENTAL LENSES

One-foot-diameter Lens

A 1-foot-diameter lens designed to operate over a bandwidth of 2 to 4 GHz is shown in figure 2A. The lens has 16 input/output ports and is to be used with a 2-foot-diameter circular array of 32 elements. Figure 2B is a photograph of the inside structure and probe arrangement of the lens. The lens consists of two circular plates with diameters of three free-space wavelengths, separated by 0.344 wavelength of air dielectric at the center frequency of 3.0 GHz. A stepped probe is used with lucite dielectric to provide satisfactory operation over the 67 percent bandwidth. Details of the probe feed are shown in figure 3.

Single and four-probe-tapered (1-3-3-1) inputs were used to excite the lens. Figure 4 is a plot of the measured and calculated phase distribution at the lens output ports for both types of inputs. Measured and calculated amplitude distributions are given in figures 5A and 5B for single-probe and four-probe-tapered inputs, respectively. The difference between the calculated and measured curves for the single-probe input is due primarily to uncontrolled reflections within the lens. The discrepancy in the curves for the four-probe-tapered input is due to several factors: the small size of the lens causes near-field coupling to the output; the use of one-fourth of the lens probes for the input severely compromises the approximation of a linear array in front of a ground plane; and mutual coupling between input probes increases as diameter decreases. The unused ports of the lens were terminated in the characteristic impedance of 50 ohms for these test measurements.

Impedance measurements of both input arrangements showed that the single-probe input provided a better match over the 2-4 GHz band, remaining within a 2.5:1 SWR circle. The four-probe-tapered input maximum SWR measured was at 4.3:1.

Predicted antenna patterns using calculated and measured phase and amplitude data for the lens are shown in figure 6. The pattern predicted from calculated lens data features an 16° HPBW and -32-dB sidelobes. The pattern predicted from measured lens data features a 18° HPBW and -24-dB sidelobes.

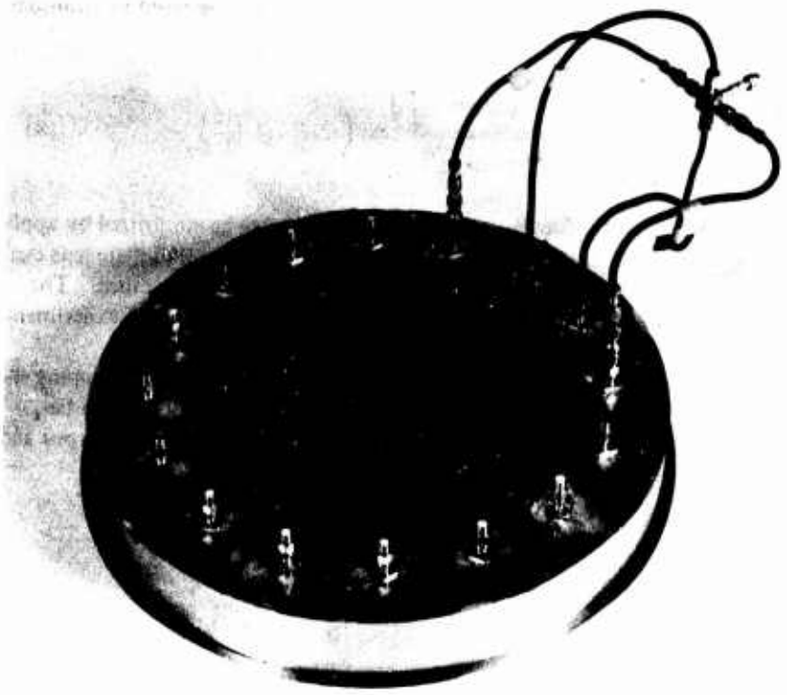

(A)

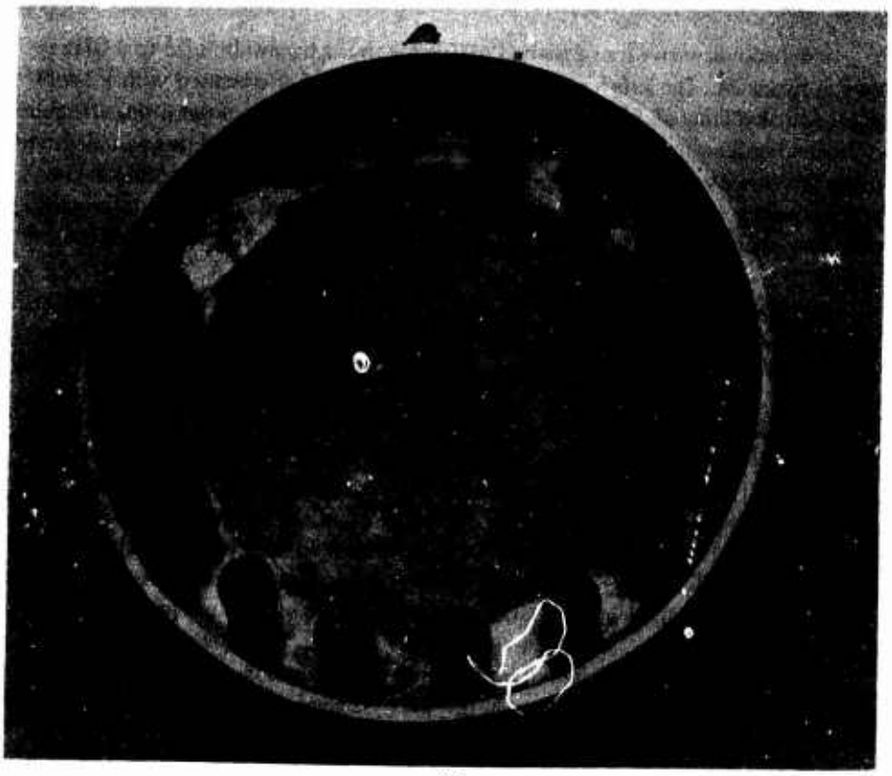

(B)

Figure 2. The 1-foot-diameter lens probes. A, exterior view; B, inside structure and probe arrangement.

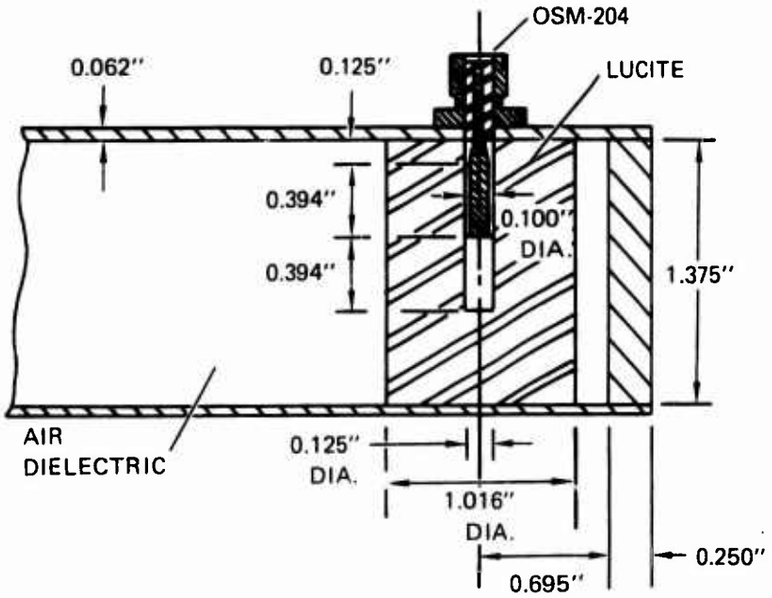

Figure 3. Probe-feed detail for the 1-foot-diameter lens.

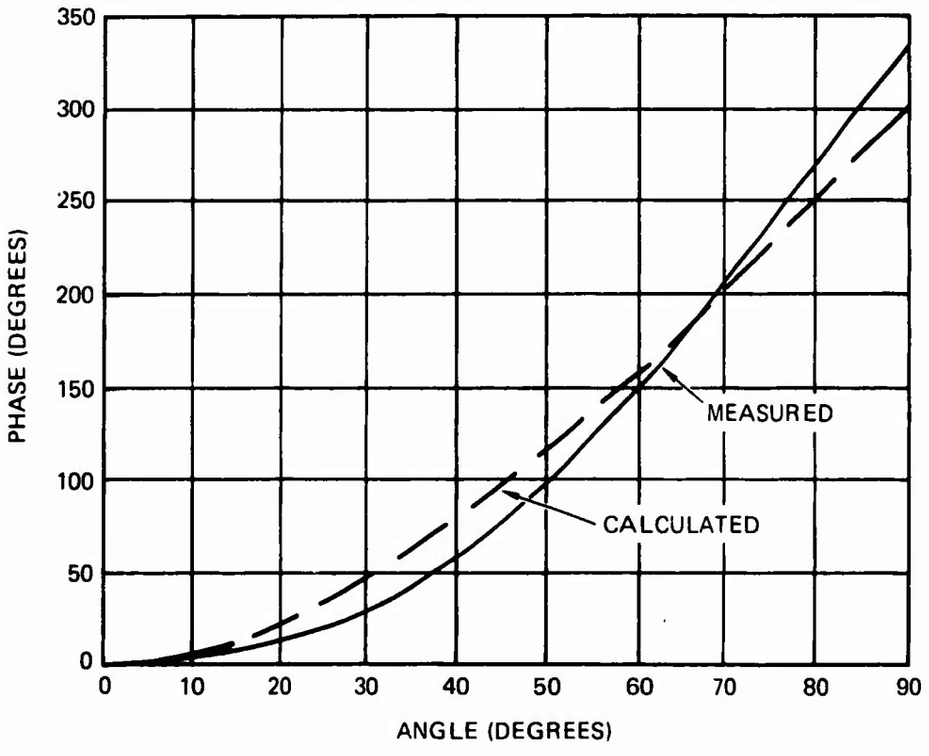

Figure 4. Plot of measured and calculated phase distribution vs. angle from lens zero, for 1-foot-diameter lens.

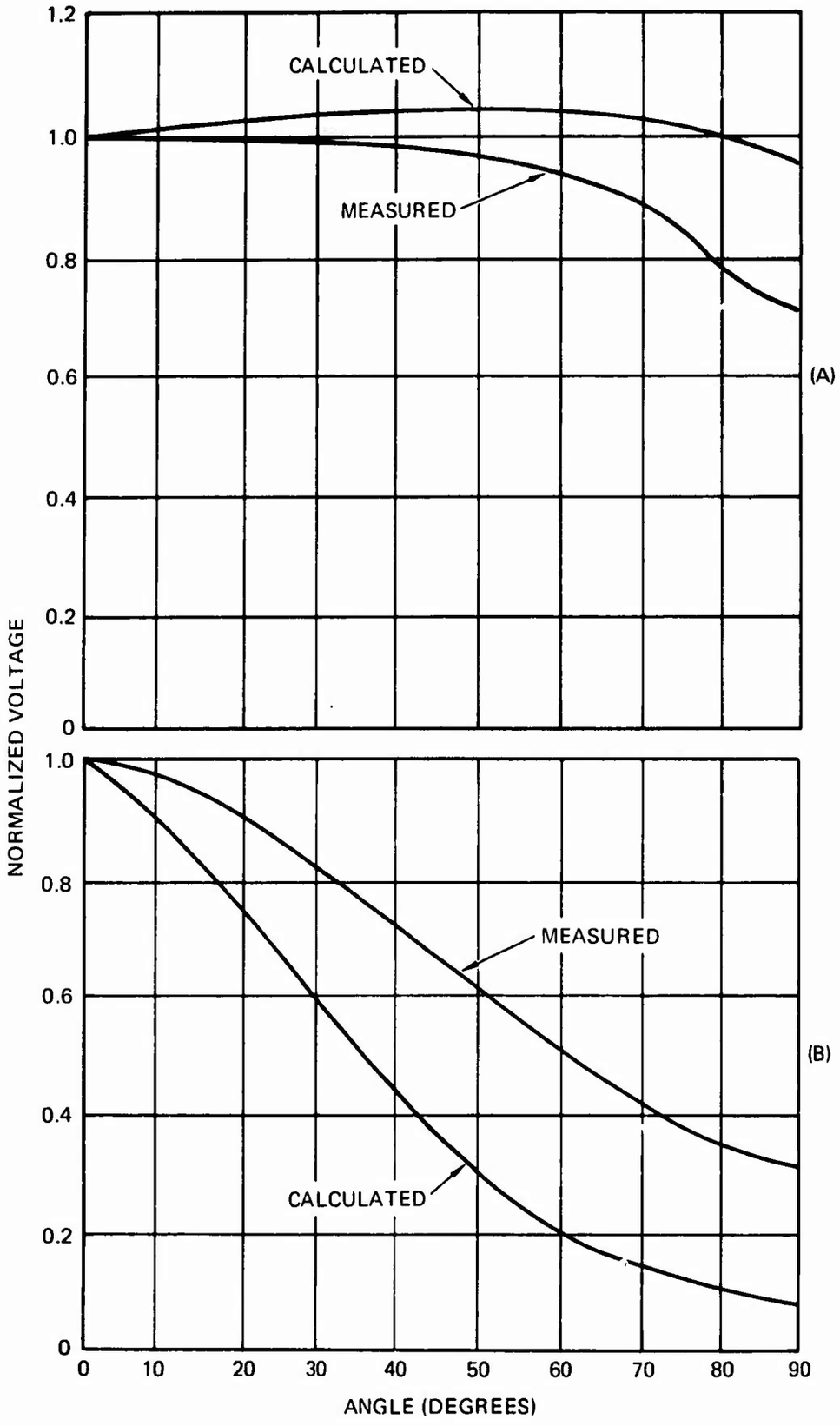

Figure 5. Measured and calculated amplitude distributions vs. angle from lens zero. 1-foot-diameter lens. A, single probe input, B, four-probe-tapered input.

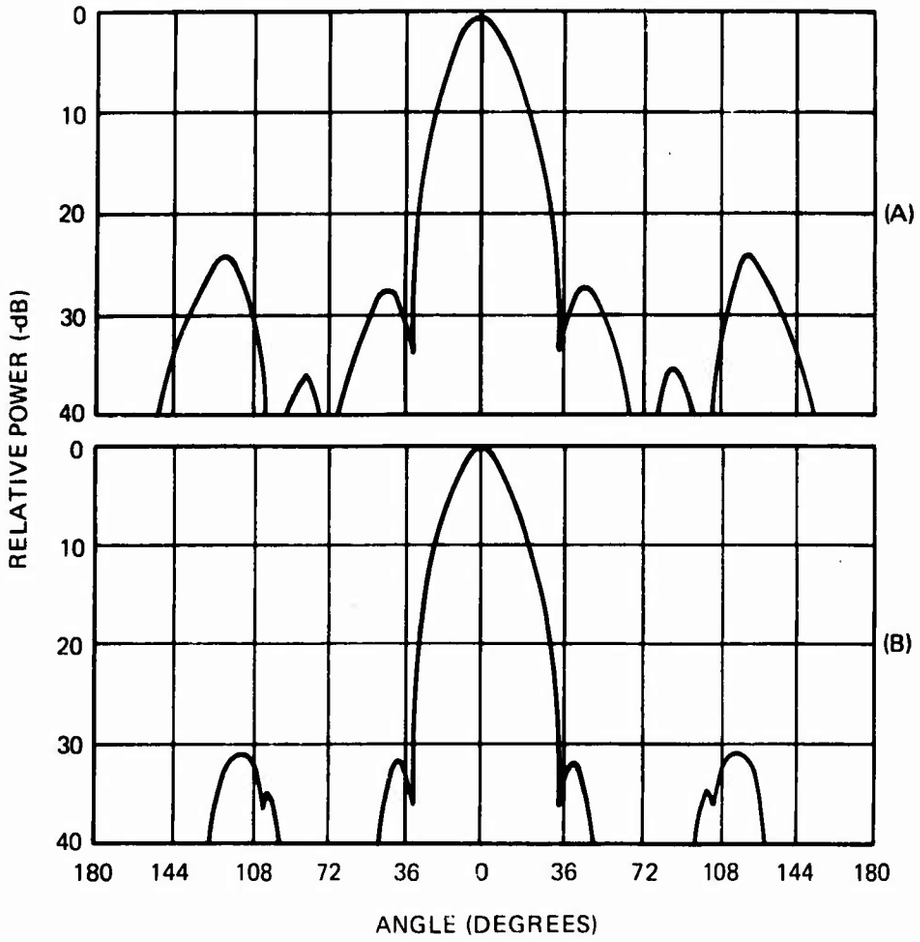

Figure 6. Predicted radiation patterns for 1-foot-diameter lens, using (A) measured lens distributions and (B) calculated lens distributions.

Four-foot-diameter Lens

The 4-foot-diameter R-2R lens is shown in figure 7A with some of the phase-measurement test equipment.[3] The lens consists of two circular metal plates 6.45 free-space wavelengths in radius spaced 3/8 of a free-space wavelength at 3.2 GHz. The bandwidth to be covered by the lens is 2.9-3.5 GHz. There are 64 probe terminals equi-spaced around the circumference of the lens with 1/4 of a free-space wavelength at 3.2 GHz spacing between the probes and the enclosing ground plane of the lens. Figure 7B is a photograph of the inside structure of the lens. A cross section of the lens construction including the probe feed is shown in figure 8.

Various small, linear arrays were used at the input portion of the lens in an attempt to determine the configuration that would best provide the desirable amplitude distribution. Single-probe, two-probe, three-probe, three-probe-tapered (1-2-1), four-probe, and four-probe-tapered (1-2-2-1) configurations were used. Figure 9A is a plot of the average measured phase distribution and the required phase distribution at the output terminals of the lens, considering all input configurations except four-probe. Good agreement is achieved between the calculated and measured phase distributions, with

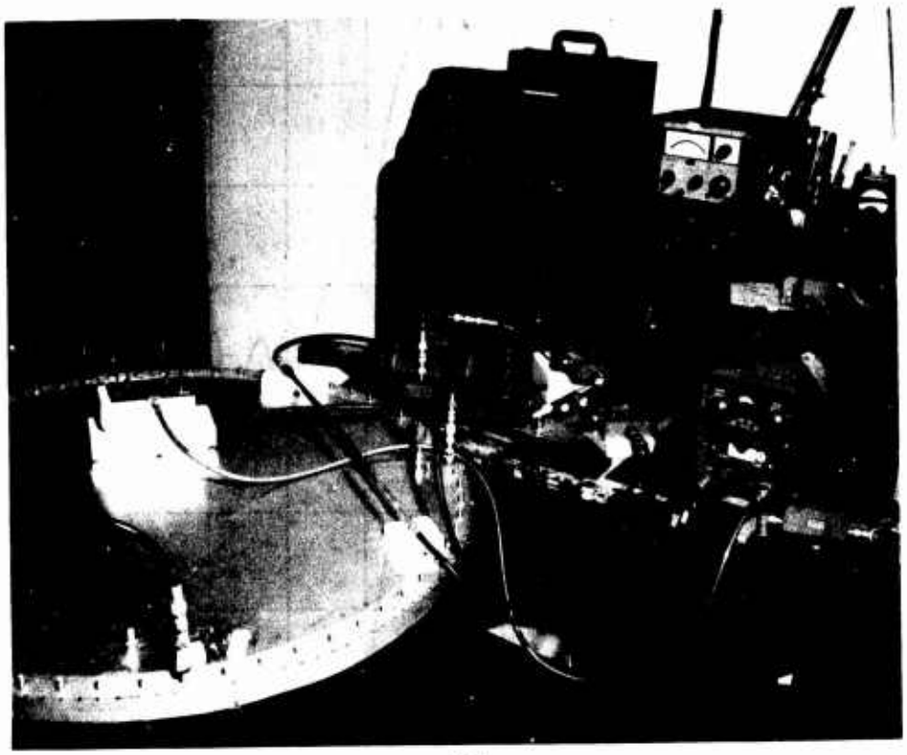

(A)

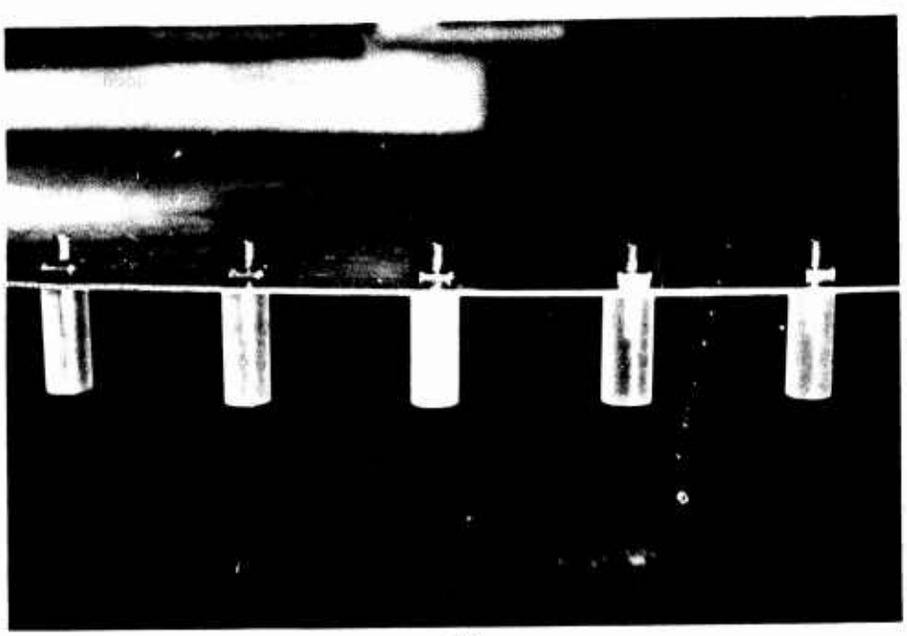

(B)

Figure 7. The 4-foot-diameter R-2R lens. A, with some of the phase-measurement test equipment; B, partial view of inside structure.

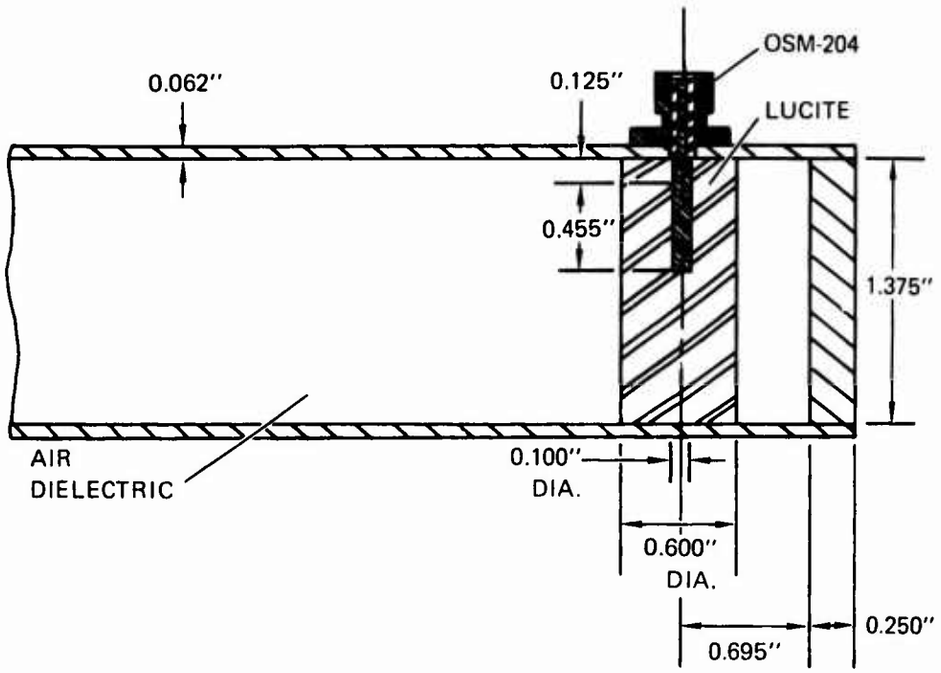

Figure 8. Internal construction of 4-root-diameter lens, including probe feed.

differences due to uncontrolled reflections inside the lens and unequal cable lengths at the lens input. Figure 9B is a plot of the phase distribution using a four-probe input. The large difference between the calculated and measured phases is due to the untapered input to the lens, which produces high lobes, phase reversals, and reflections inside the lens. Figure 10 shows the calculated and measured amplitude distributions for the various input configurations to the lens. Impedance tests for the lens using single-probe and four-probe-tapered inputs showed the single-probe input SWR to be within a 1.4:1 circle and the four-probe-tapered input SWR to be within a 1.8:1 circle. This lens was originally designed for a single-probe input and the time schedule did not allow for lens modification to improve the four-probe-tapered input which provided the better lens output.

Figure 11 shows predicted and measured antenna patterns using a (1-2-2-1) input to the lens. The predicted half-power beamwidth (HPBW) is 5.9° and the measured HPBW is 5.2°. The predicted maximum sidelobe level is -28 dB and the measured maximum sidelobe level is -24 dB.

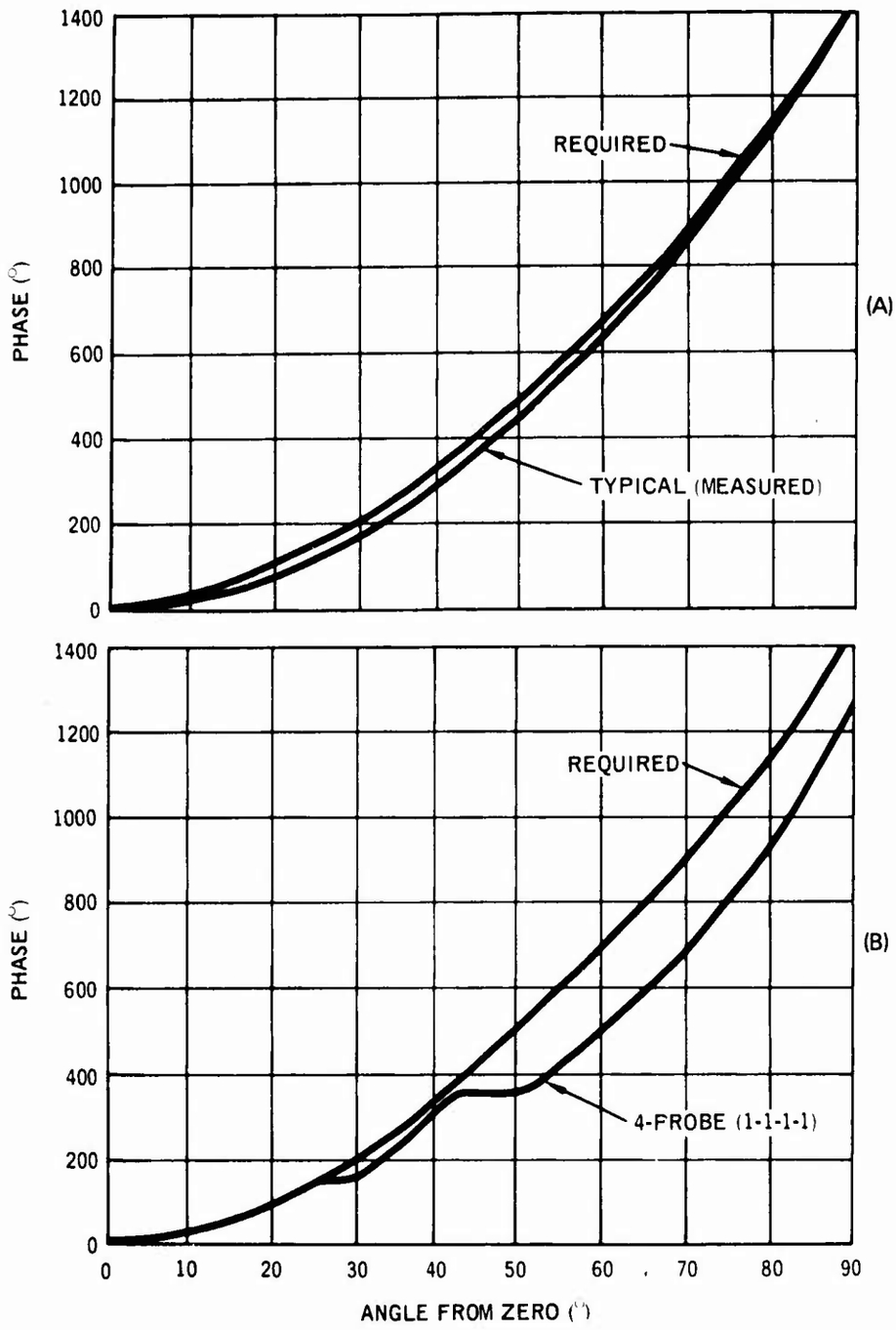

Figure 9. Plots of measured and predicted phase distributions vs. angle from zero for 4-foot-diameter lens. (A) Average of all input arrangements except four-probe, and (B) with four-probe input to lens.

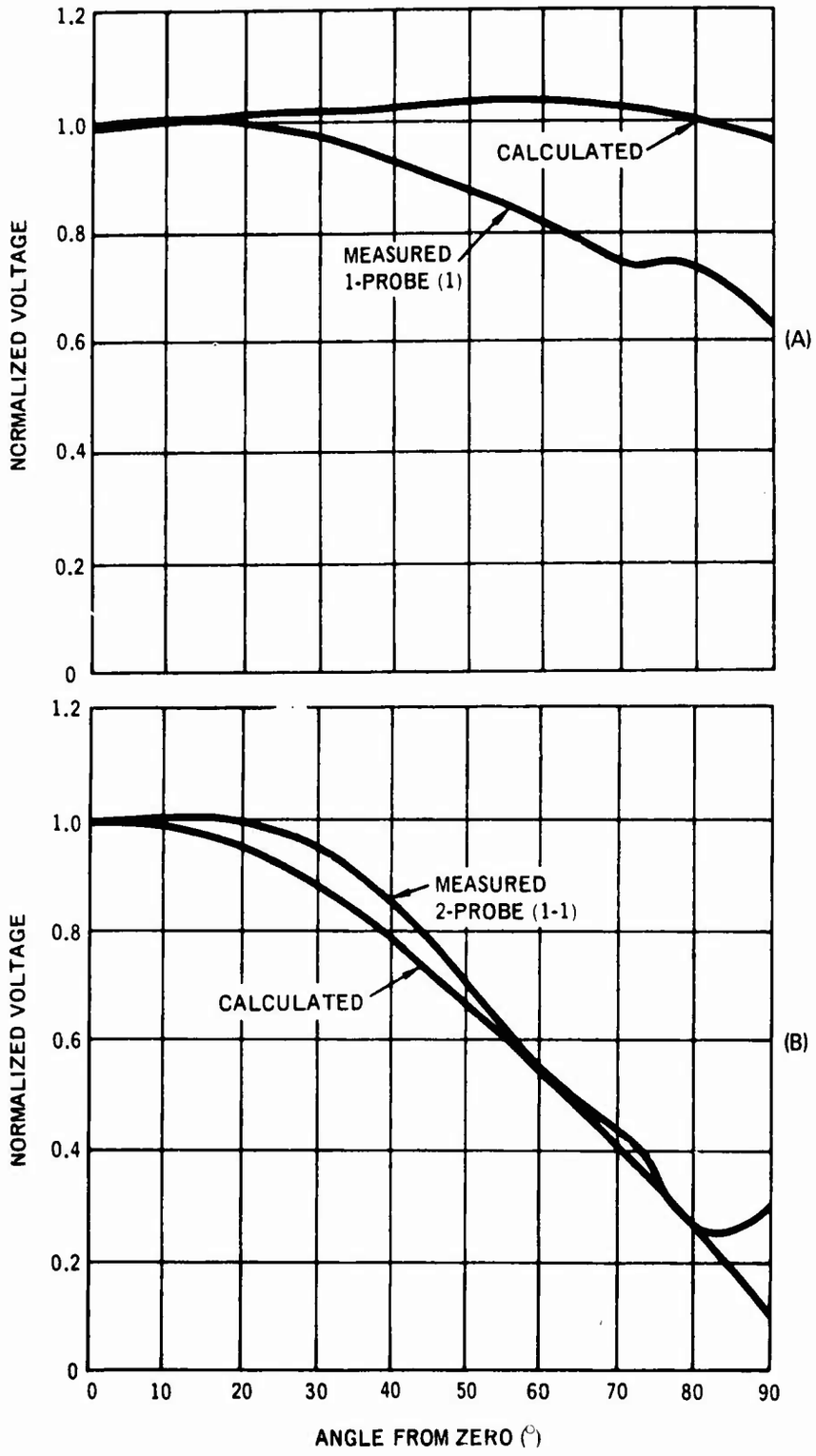

Figure 10. Plots of measured and predicted amplitude distributions vs. angle from lens zero, with various input configurations to 4-foot-diameter lens.

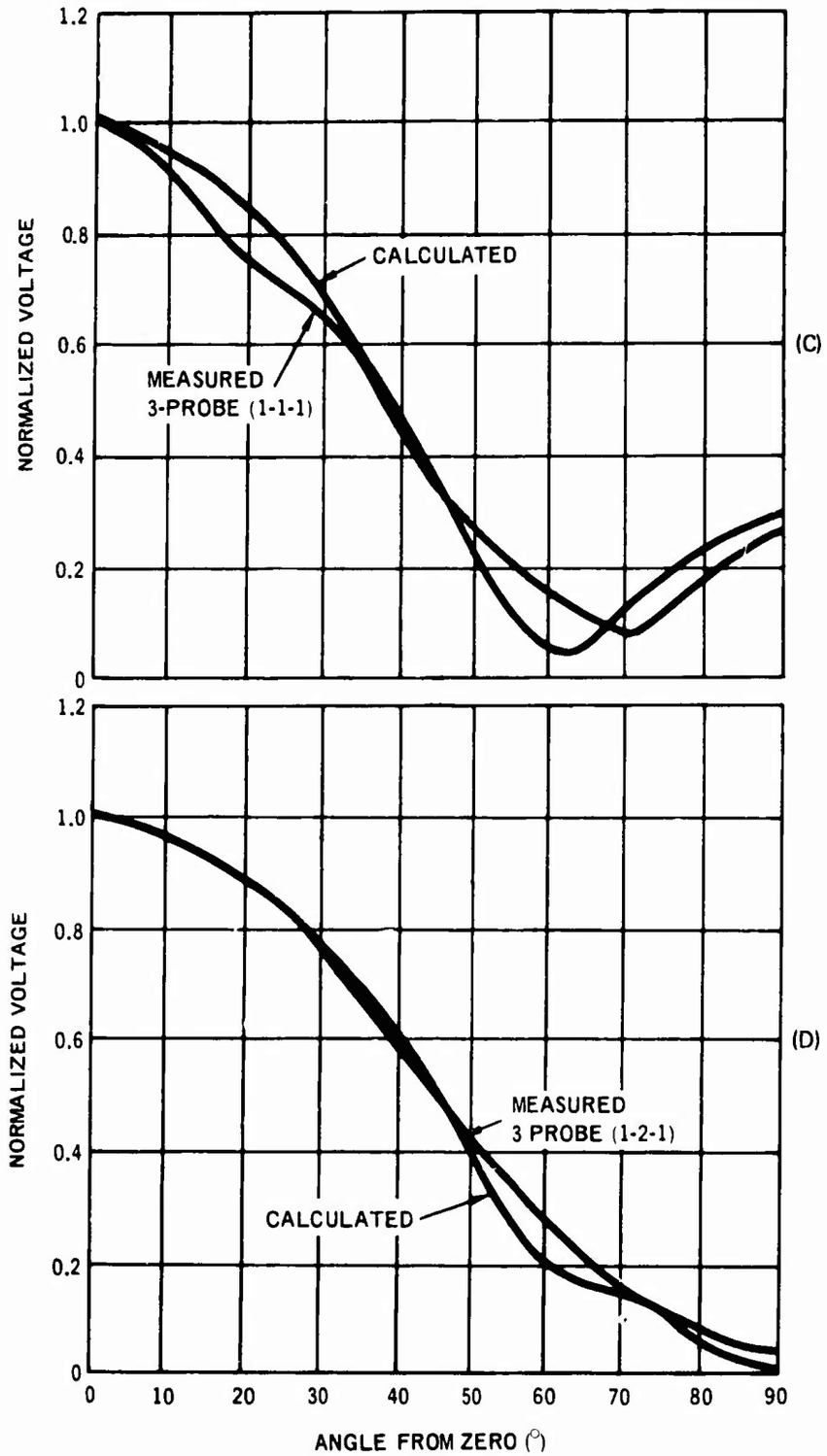

Figure 10. (Continued)

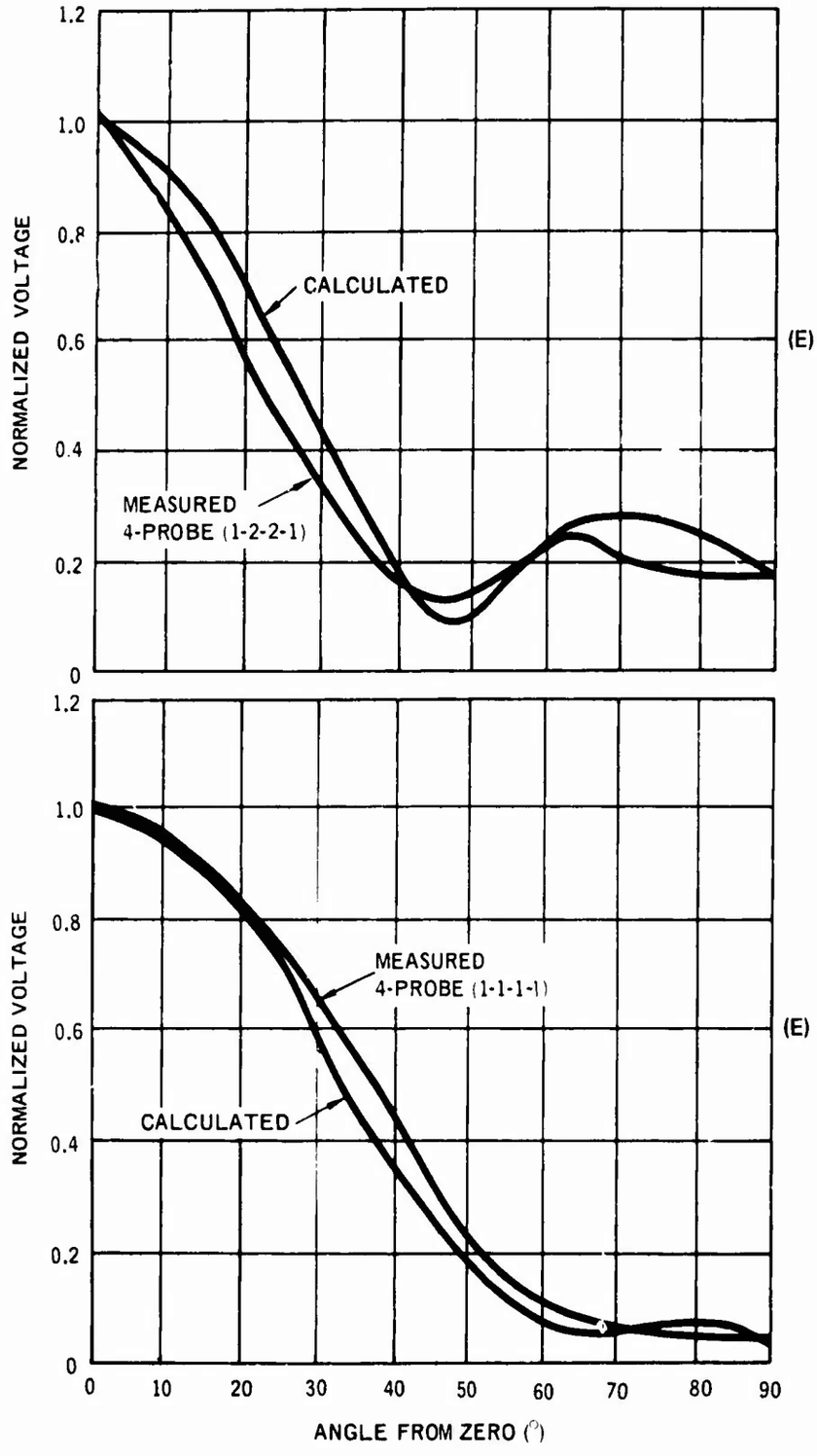

Figure 10. (Continued)

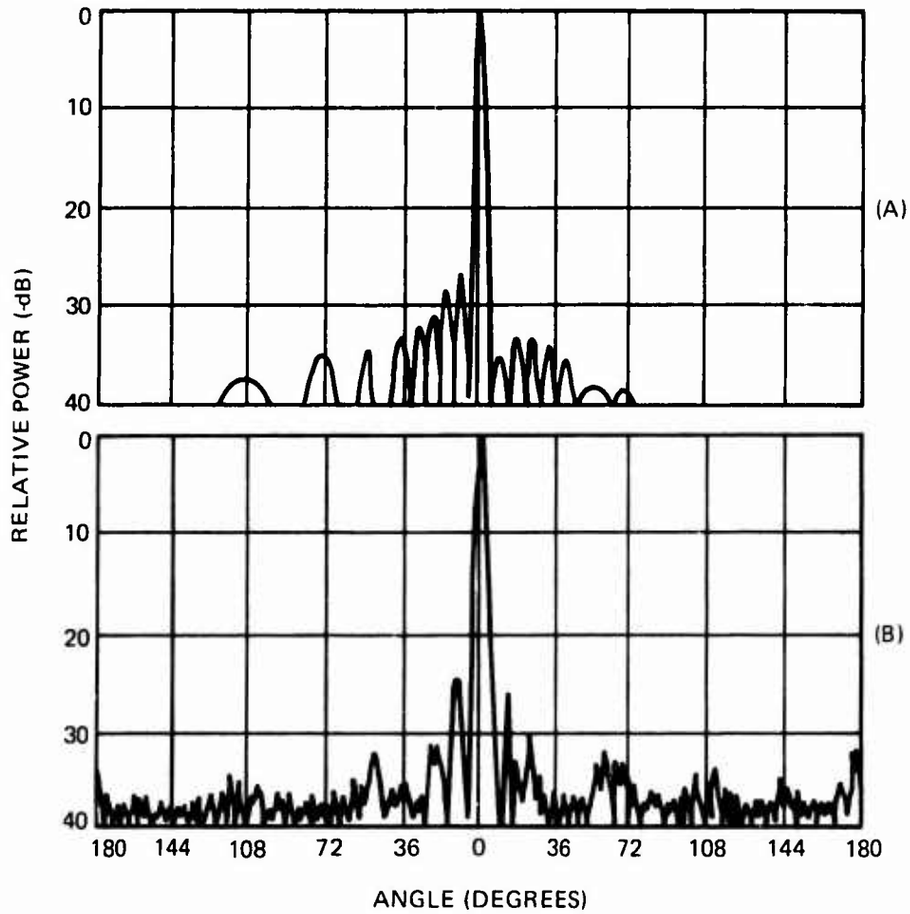

Figure 11. Radiation patterns for 4-foot-diameter lens. A, predicted, using measured lens distributions; B, measured, taken with 8-foot array.

Five-foot-diameter Lucite Lens

The 5-foot diameter lens was constructed to examine the lens characteristics in a dielectric and to reduce the physical size of the lens. This lens has 128 input-output ports and is lucite-coated with a metal spray.[4] It should have the correct phase for a 16-foot diameter radiating array. To facilitate ease of handling and construction, the lens was constructed from a 5-foot disc of lucite 7/8-inch thick. Electrically the lens appears 8 feet in diameter and less than 1/2 a free-space wavelength thick. Measurements on a similar piece of lucite indicated that a 3-dB loss (one-way) could be expected using this lens, but for studies in techniques this loss can be tolerated. Figure 13 shows the internal construction of the lens. The probe is stepped similar to that of the 1-foot-diameter lens to improve the impedance match and bandwidth characteristics. This lens was designed to operate over a 2.9-3.5 GHz bandwidth. Impedance measurements using single and four-probe-tapered inputs were taken with all unused ports terminated in the characteristic impedance of 50 ohms. The SWR of the single-probe input was shown to be within a 1.4:1 circle and that of the four-probe-tapered input was shown to be within a 1.7:1 circle.

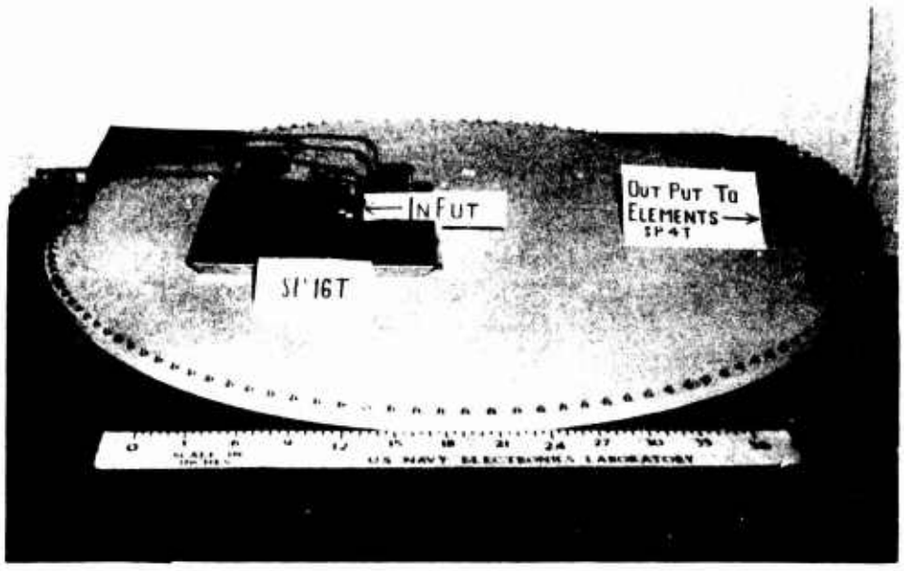

Figure 12. The 5-foot-diameter R-2R lens.

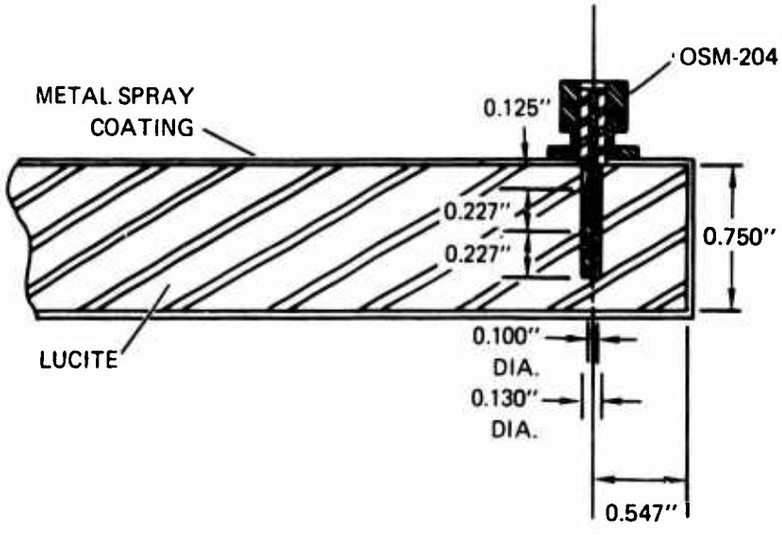

Figure 13. Internal construction of 5-foot-diameter lens.

Figure 14 is a plot of measured versus calculated phase distributions at the output ports of the lens for single and four-probe-tapered inputs. Figure 15 shows measured versus calculated amplitude distributions at the output terminals using a four-probe-tapered (1-2-2-1) input.

Predicted and measured antenna patterns are shown in figure 16. Figure 16A is a predicted antenna pattern using measured lens phase and amplitude data. Figure 16B is a measured pattern using a sector of the 3-D radar antenna. The predicted HPBW using measured lens data is 3.0° and the measured HPBW is 6.0°. The predicted maximum sidelobe level using measured lens data is -20 dB and the measured maximum sidelobe level is -18 dB.

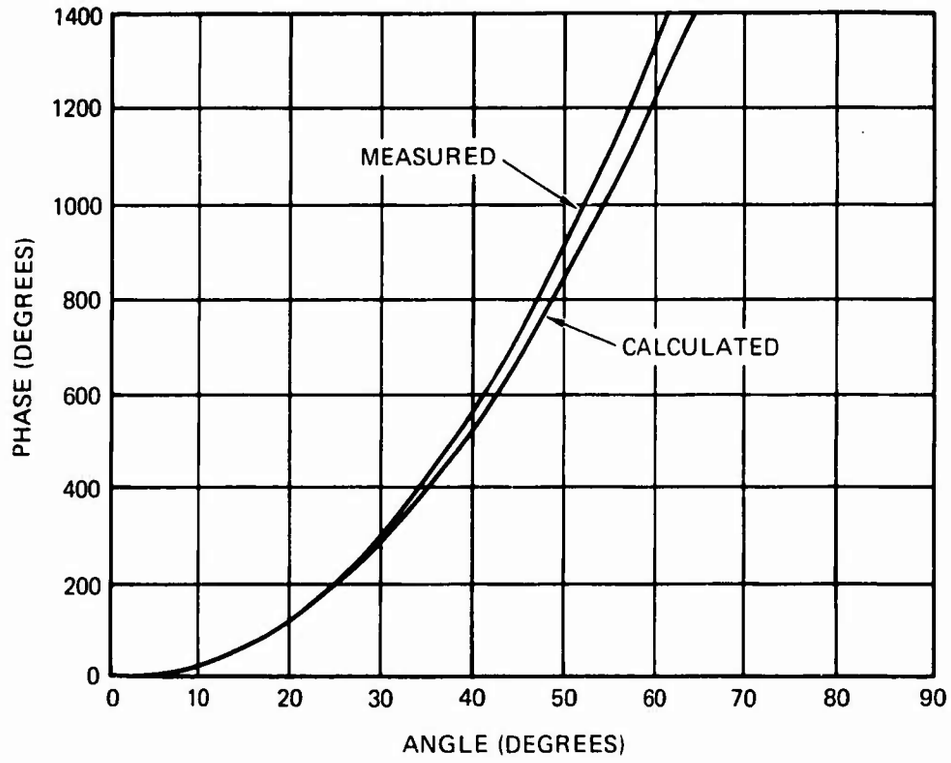

Figure 14. Measured and predicted phase distributions vs. angle from lens zero for 5-foot-diameter lens.

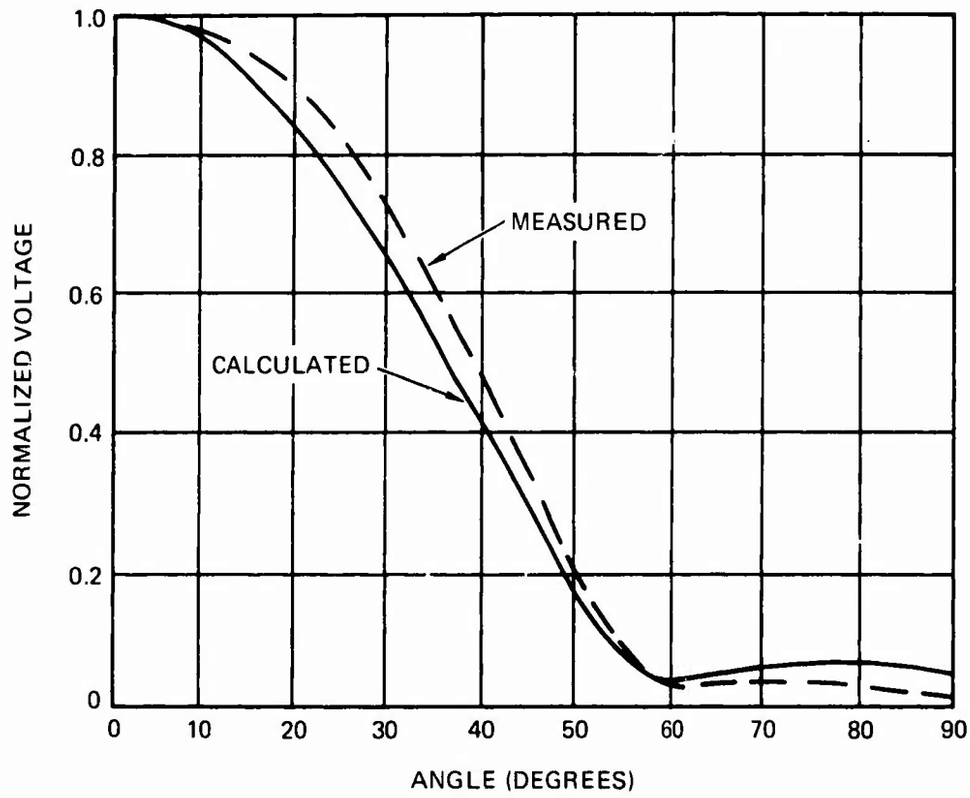

Figure 15. Measured and predicted amplitude distributions vs. angle from lens zero using four-probe-tapered input for 5-foot-diameter lens.

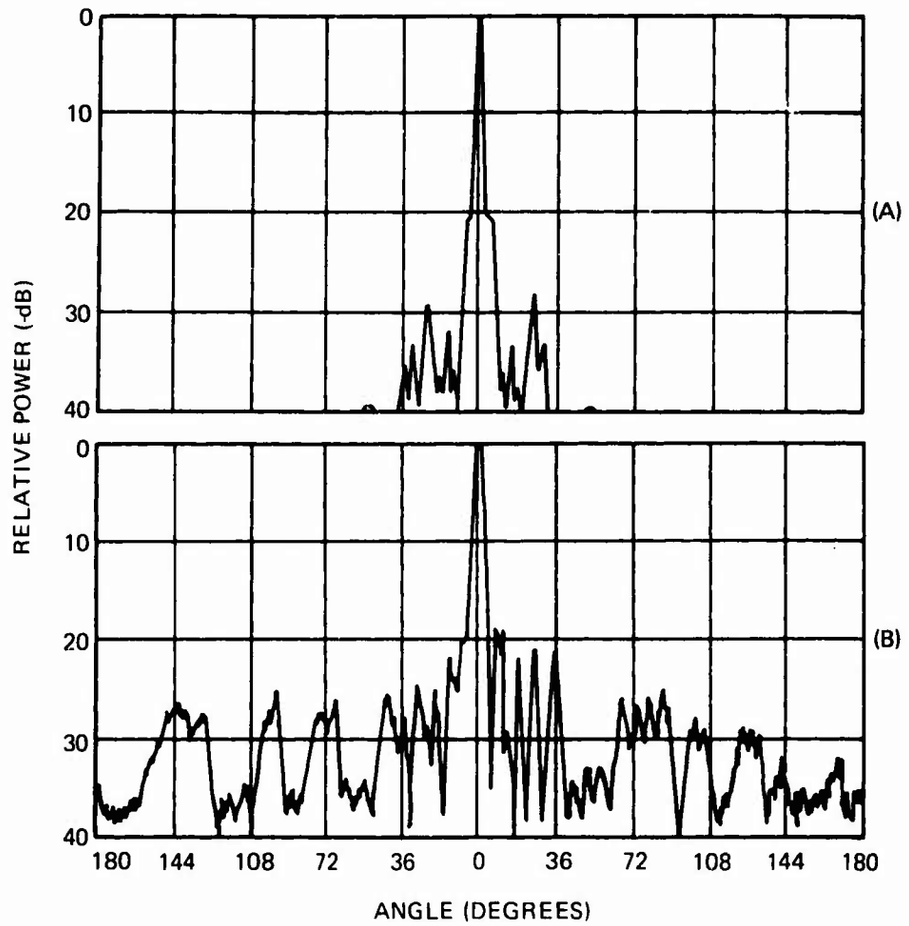

Figure 16. Antenna patterns for 5-foot-diameter lens. A, predicted, using measured lens phase and amplitude data. B, measured, using a sector of the 3-D radar antenna.

MULTIPLE BEAM TECHNIQUES

The feasibility of using a parallel-plate lens to achieve orthogonal beams from a circular array has been investigated (fig. 17). The 128-element ring-array antenna was excited using the 4-foot-diameter R-2R lens. Two single-probe inputs connected in parallel were used, separated 22.48° and 174.22°. Figure 17A is a measured pattern from the array with two beams being present separated 11.24°. The summation of sidelobes produces a higher sidelobe at -4 dB between the two beams. Two beams separated 87.11° are shown in figure 17B. The beam shape in both cases approximates expected results for an array with uniform amplitude distribution and a cophasal distribution. The HPBW is 2.5° in both cases. Figure 17C is a typical antenna pattern using a single-probe input to the lens. The HPBW is 2.5° and the maximum sidelobe level is -1.0 dB.

Further study is necessary to accurately determine the feasibility of orthogonal beams using parallel-plate lens feed systems. Successful results will allow for multitarget tracking.

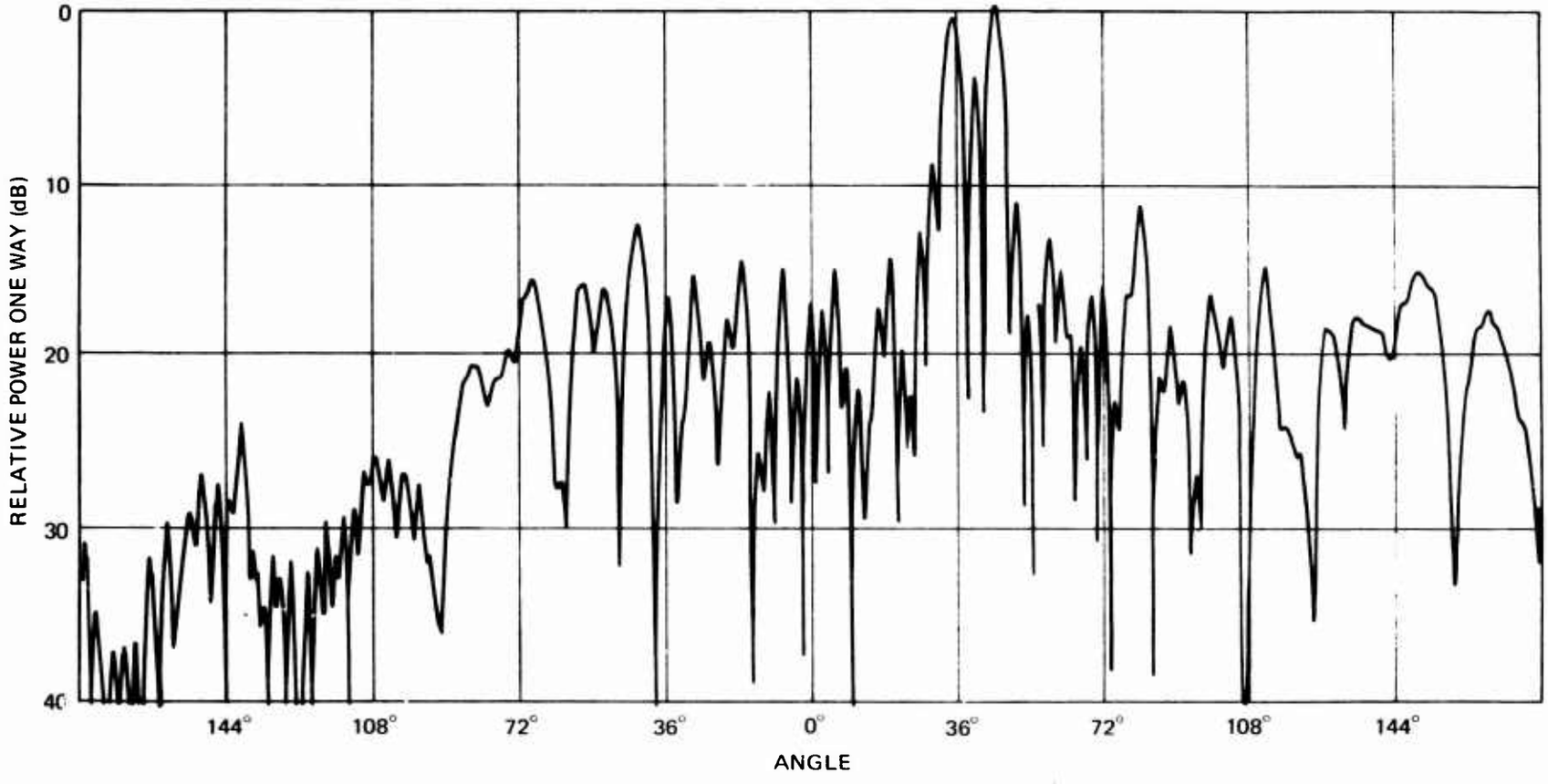

Figure 17. Measured radiation patterns from a circular array, using 4-foot-diameter lens. A, with two single-probe inputs separated 22.48°; B, with two single-probe inputs separated 174.22°; using one single-probe input.

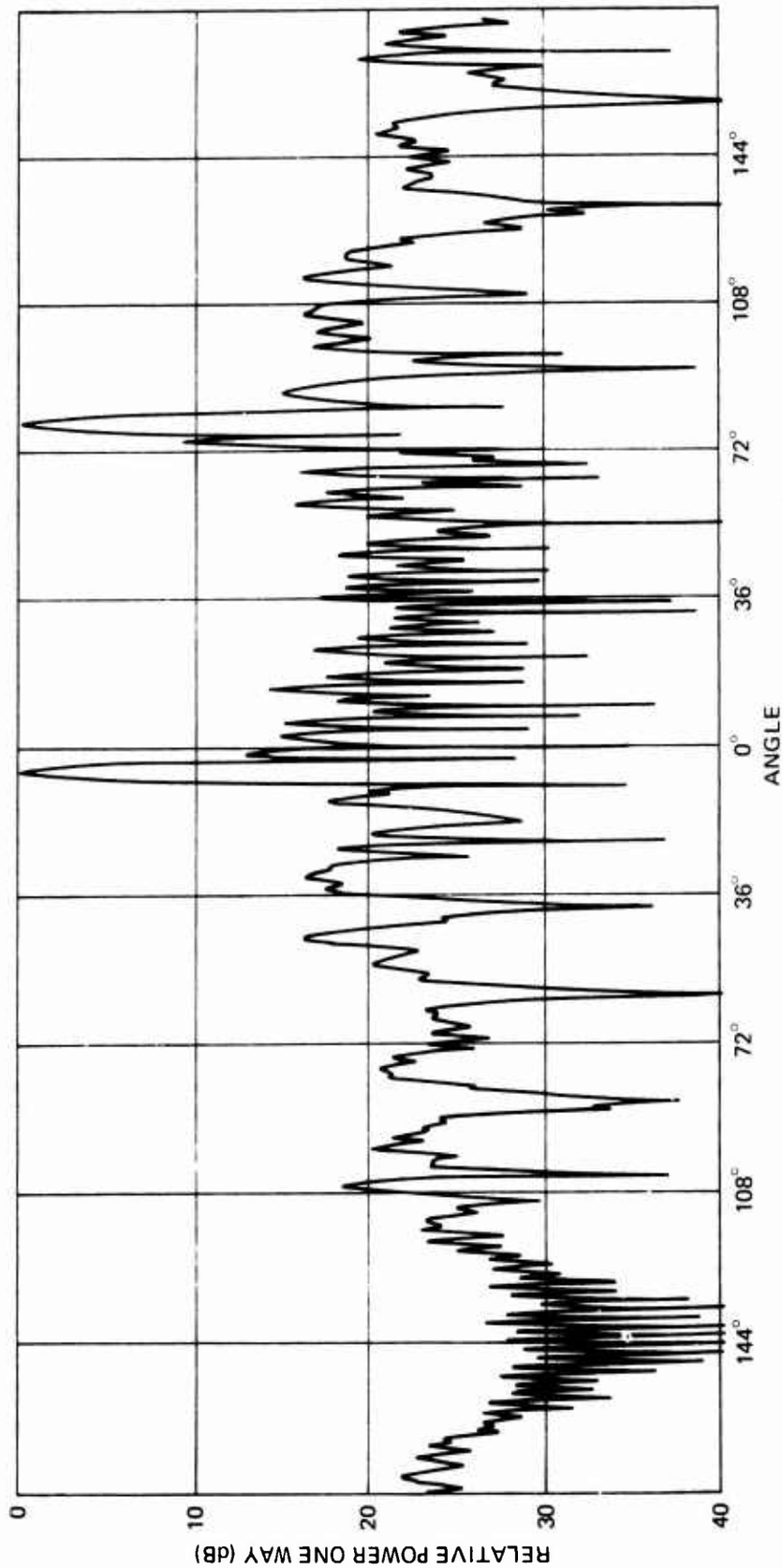

Figure 17. (Continued).

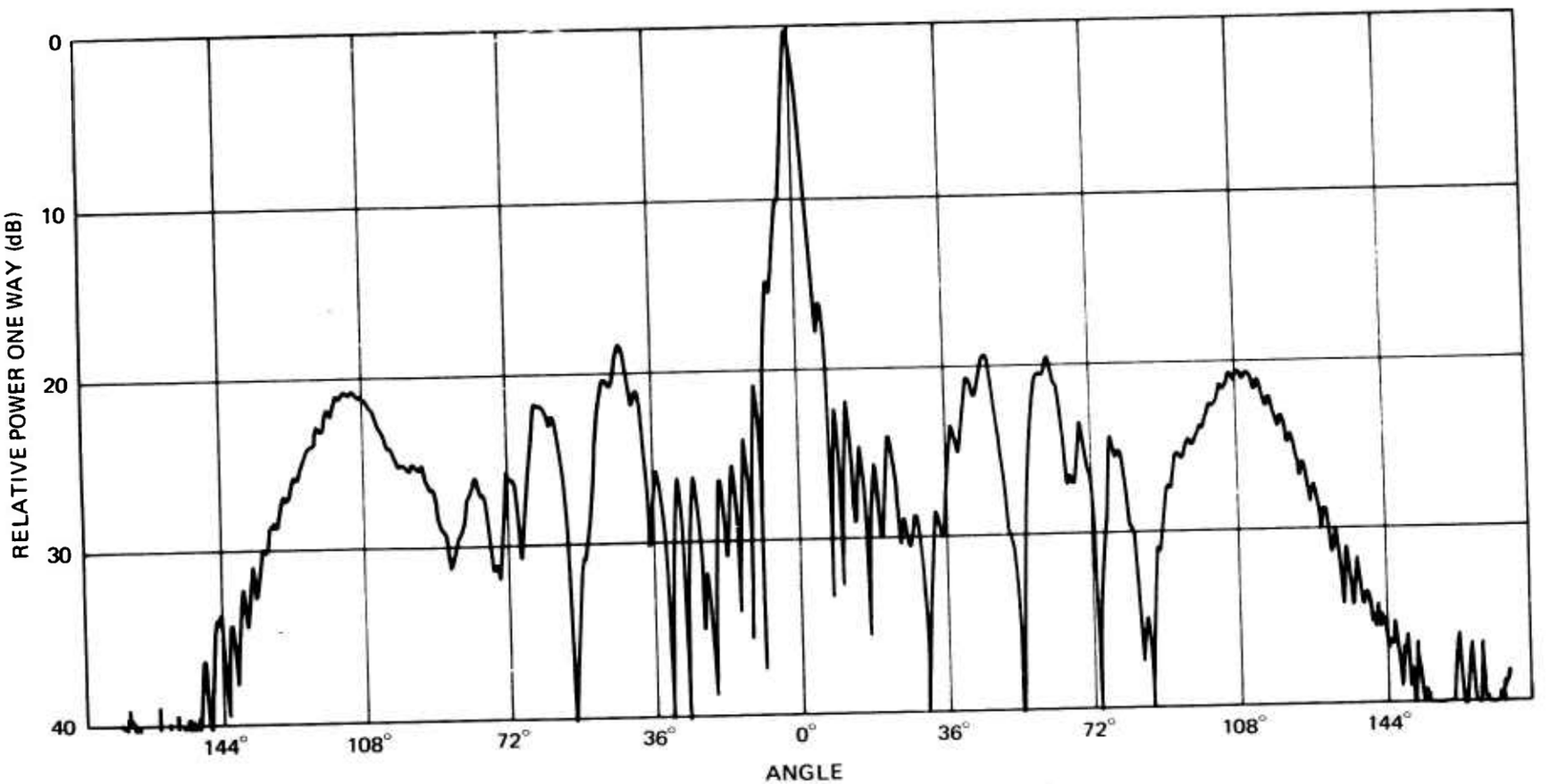

Figure 17. (Continued).

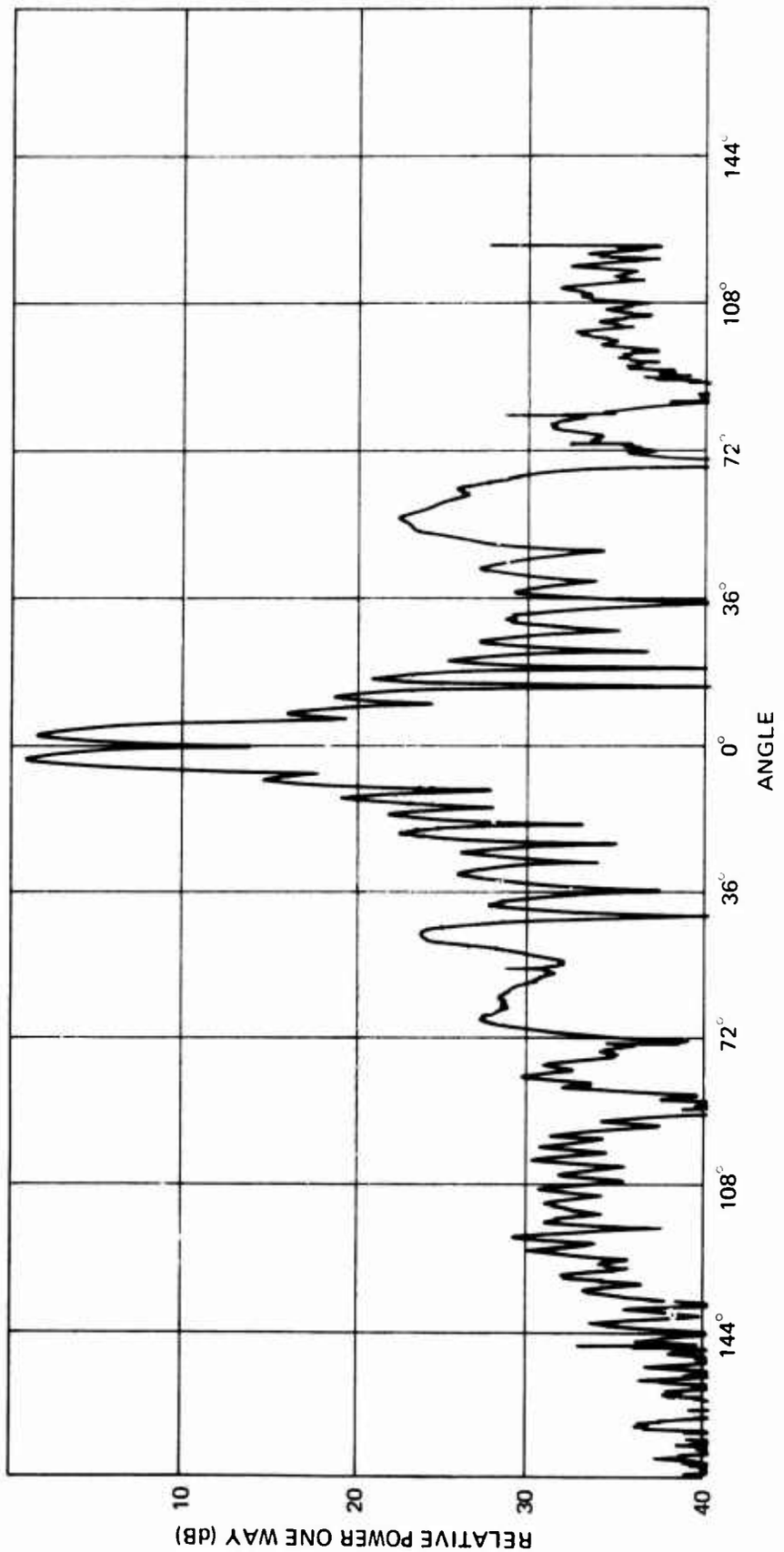

Figure 18. Measured difference patterns using 4-foot-diameter lens at (A) 2.9 GHz, (B) 3.2 GHz, and (C) 3.5 GHz.

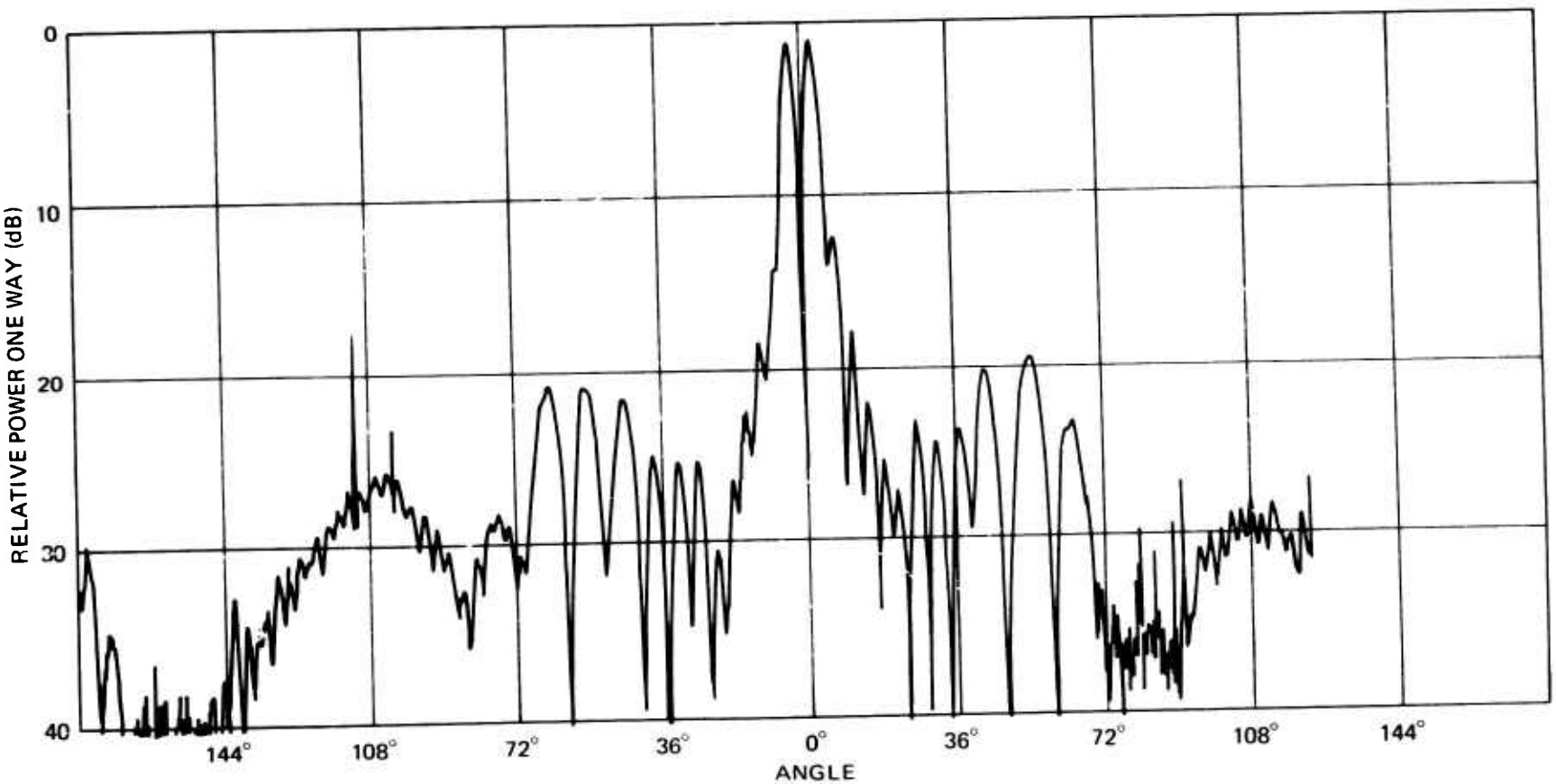

Figure 18. (Continued).

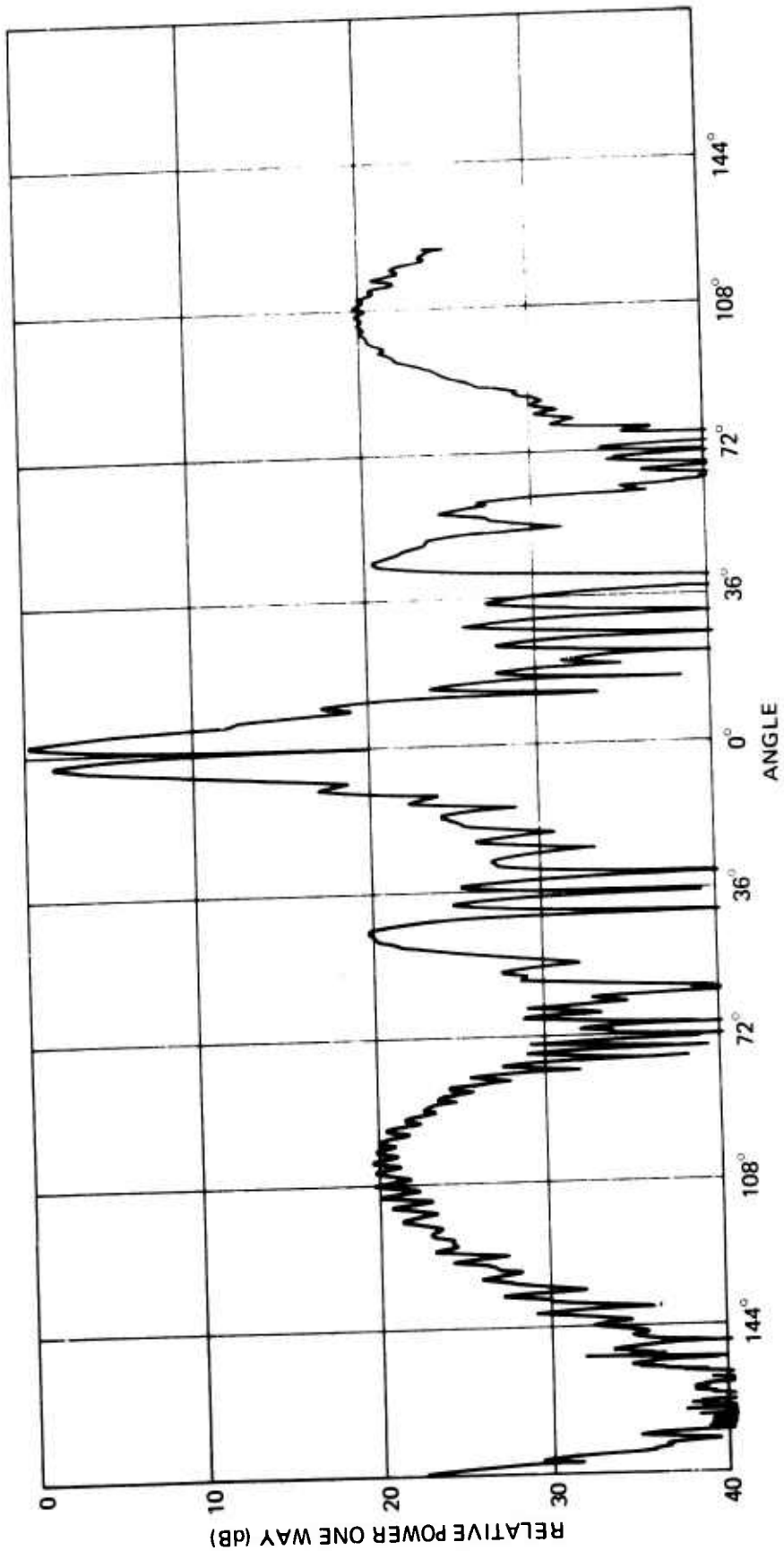

Figure 18. (Continued).

MONOPULSE TECHNIQUES

Monopulse patterns from a circular array excited with a parallel-plate lens have been measured as shown in figure 18. A four-probe-tapered (1-2-2-1) input was used as the input to the 4-foot R-2R lens. One-half of the input was shifted 180° in phase with respect to the other half at 3.2 GHz. Measurements were made over a 20-percent frequency band with the measurements taken at both ends and the center of the band being presented in figure 18. At the design frequency the null between beams occurs at -24 dB. Figure 19 is a typical sum pattern from the circular array excited with the 4-foot diameter lens.

Further investigation should show the feasibility of using the monopulse techniques in conjunction with orthogonal beam techniques for achieving multiple beams from the circular array for multiple-target tracking.

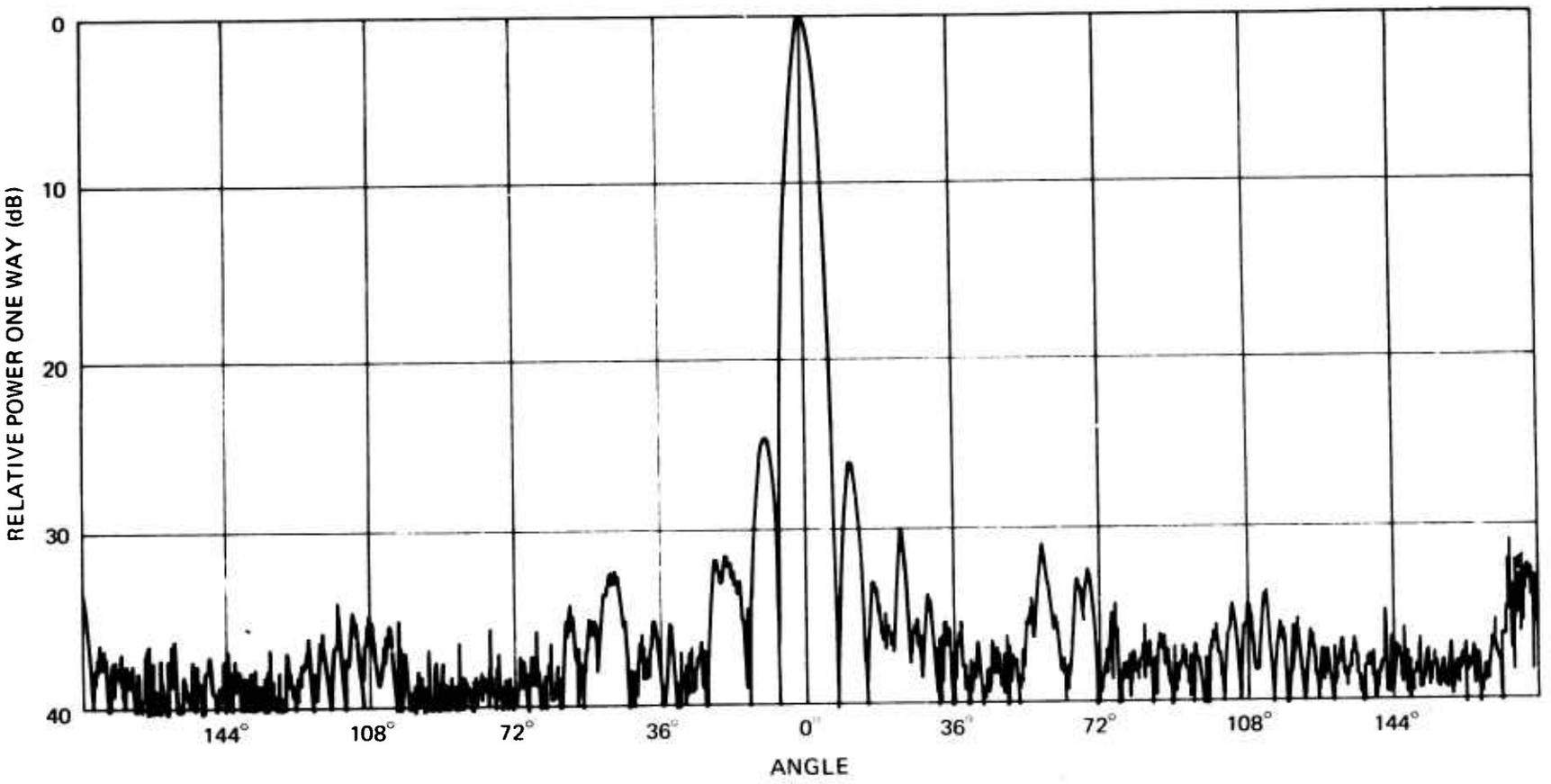

Figure 19. Typical sum pattern using 4-foot-diameter lens.

CONCLUSIONS

The R-2R parallel-plate lens readily provides a cophasal distribution when connected through equal-length cables to circular-array elements. Measured patterns are in good agreement with predicted results. The parallel-plate lens is easily constructed, rugged, reliable, and bandwidth-limited only by the physical limitations of the input-output probes.

The investigations into the feasibility of orthogonal beams showed that a large amount of interaction and coupling exists between lens probes. Techniques of improving probe isolation need to be investigated.

Further investigations are needed to improve probe design to increase the bandwidth of the lenses for multiprobe inputs. The need for this improvement is indicated by the impedance plots for each lens.

Monopulse patterns are easily obtained by adding phase control to one-half of the the input to the lens.

REFERENCES

1. Boyns, J. E. and others, "A Lens Feed for a Ring Array", *Institute of Electrical and Electronic Engineers, Transactions: Antennas and Propagation*, v. AP-16, p. 264-267, March 1968.

2. Naval Electronics Laboratory Center Report 1535, *Circular-Array Radar Antenna: CARAMBA I Experimental Results*, by J. E. Boyns, 2 February 1968.

3. Naval Electronics Laboratory Center Report 1594, *Circular-Array Radar Antenna: Final Report*, by J. E. Boyns, J. Reindel, and C. W. Gorham, 15 November 1968.

4. Naval Electronics Laboratory Center Technical Note TN 1460, *3-D Radar Antenna: Array Elements, Feed Systems, and Mutual Coupling*, by J. E. Boyns, 16 January 1969.

AN ITERATIVE TECHNIQUE FOR REDUCING SIDELOBES OF CIRCULAR ARRAYS

H. P. Coleman
Naval Research Laboratory
Washington, D. C. 20390

INTRODUCTION

Circular and cylindrical arrays of radiating elements can be used to produce beam patterns which may be rotated through 360 degrees by a cyclic permutation of the element currents, making them an attractive choice for numerous applications in radio, radar, and sonar. The successful design of these arrays requires a method for determining the element currents which will yield a desired radiation pattern. A method of approximate synthesis, due to DuHamel [1] is the primary basis for this element current determination. In this method, an exact synthesis for a continuous cylindrical current distribution is first derived and this continuous distribution is then approximated by a finite array of discrete sources on the cylinder. This approach works well if a large number of closely spaced elements is used to approximate the continuous distribution, even for high resolution low sidelobe beam patterns. However, if the method is used to attempt synthesis of a pattern having nearly optimum resolution for a given sidelobe level, with element spacings of about one-half wavelength, substantial differences may exist between the desired pattern and the performance attained. An iterative method has been devised, and computer-implemented, which progressively improves the sidelobe level of the radiation pattern of such a circular or cylindrical array.

THE ITERATIVE METHOD

As an example of the use of this method, results are shown for the attempted synthesis of a Tchebycheff pattern of order 16 with 30 dB sidelobes. This pattern is taken as the objective pattern, in the principal plane, of a circular array of thirty-two dipoles equally spaced around a conducting cylinder with a radius of 2.2965 wavelengths. The dipoles are arranged on a circle of 2.5465 wavelengths radius. In Figure 1, the objective pattern and the pattern resulting from using DuHamel's approximate synthesis for this array are plotted. The interval of computation is 2 degrees, and both patterns are symmetric about 0 degrees. A Tchebycheff pattern of order Q has 2Q maxima. It is to be noted that, although the approximate synthesized pattern has sidelobes as high as -20.8 dB, it still has the characteristic thirty-two maxima. The essential feature of the developed iterative technique is the numerical determination of the positions of these maxima and the solution of a system of simultaneous equations which impose constraints on the pattern of these positions. Provision is made in the computer algorithm for substituting pairs of symmetrically located constraints on the main beam for missing positions of maxima in the event that less than 2Q maxima exist.

The principal plane far-field pattern of a circular array of 2Q current elements arranged, if desired, around a perfectly conducting cylinder may be written in the form [2]

$$E(\varphi) = \sum_{k=1}^{2Q} I_k \sum_{n=1}^{\infty} G_n \cos[(n-1)(\varphi-\alpha_k)] \ . \tag{1}$$

Here $E(\varphi)$ is proportional to the total E-field at the angle φ. The current on the k^{th} element (located on the circle at an angle α_k) is I_k. The set of I_k are normalized so that E is real and equal to 1 at the peak of the main beam. The coefficients, G_n, depend only upon the dimensions of the array, in terms of wavelength, and upon the type of current element.

In the present technique, Equation (1) is used to determine numerically the 2Q positions of maxima in the far field radiation pattern. The expression for the value of the pattern function at these 2Q positions then becomes:

$$E_j = E(\bar{\varphi}_j) = \sum_{k=1}^{2Q} I_k \sum_{n=1}^{\infty} G_n \cos[(n-1)(\bar{\varphi}_j-\alpha_k)] \tag{2}$$

$$j = 1,2, \ldots, 2Q$$

where the positions of maxima are represented by the set of $\bar{\varphi}_j$. Making the substitution

$$A_{jk} = \sum_{n=1}^{\infty} G_n \cos[(n-1)(\varphi_j-\alpha_k)] \tag{3}$$

$$\begin{cases} j = 1,2, \ldots, 2Q \\ k = 1,2, \ldots, 2Q \end{cases}$$

yields

$$E_j = \sum_{k} I_k A_{jk} \ . \tag{4}$$

The range of j and k in this and subsequent equations is the same as in Equation (3).

We next consider a set of perturbations, Δ_k, applied to the original set of currents, I_k. These perturbations result in new values for E_j, redesignated $\tilde{E}_j$, for the 2Q far-field positions corresponding to the maxima of the original pattern

$$\tilde{E}_j = \sum_k (I_k + \Delta_k) A_{jk} \tag{5}$$

Substituting from Equation (4) and transposing results in

$$\sum_k \Delta_k A_{jk} = E_j - \tilde{E}_j \, . \tag{6}$$

The values of E_j are known from Equation (4); the 2K values of $\tilde{E}_j$ may be arbitrarily chosen and this set of equations solved for the 2Q perturbations of the element currents.

As currently implemented, the far field magnitude is set equal to its previous value at the main beam maximum and at the 2Q-1 sidelobe positions, a new level, in general lower than in the previous pattern, and equal at all sidelobe positions, is chosen. Far field phase is currently established as a strict 180-degree alternation between adjacent lobes; starting with 0 phase for the main beam. By substituting the perturbed currents for the element currents in Equation (1) and repeating the above procedure a number of times, an iterative method for sidelobe reduction results.

Current distributions yielding far field patterns with sidelobe levels equal to and also below the levels of the original objective function (in the example, a Tchebycheff pattern of order 16 with 30 dB sidelobes) have been attained for the cases examined to date. In the example, sidelobes were initially reduced to 24 dB and subsequently reduced in 1 dB increments. Figure 2 shows typical results for this array; an intermediate sidelobe reduction to 26 dB, reduction to 30 dB and an ultimate reduction to 33 dB, are shown.

For a given sidelobe level the current distributions obtained by using the above method are not unique, but depend, for instance, on the choice of starting current distribution. Utilizing the method, an entire family of current distributions, resulting in patterns with equal sidelobe levels, but differing in detail, may be generated.

ADDITIONAL RESULTS

Figure 3 presents plots of half-power beamwidth versus sidelobe level. In this figure, and subsequently, an abbreviated notation is utilized.

The notation $T^{16}(20)$ refers to an order 16 Tchebycheff with 20 dB lobes. A superposed bar, e.g., $T^{16}(\bar{20})$ indicates the result of DuHamel's approximate synthesis of $T^{16}(20)$. In this figure, all beamwidth data were obtained by linear interpolation in calculated tables of voltage versus far-field angle. Two separate iterative paths are plotted. The path starting with $T^{16}(\bar{30})$ has been discussed above; the path starting with $T^{16}(\bar{20})$ results from an initial sidelobe leveling to 16 dB and subsequent sidelobe reduction in 1 dB increments. At each iterative step the pattern was calculated in 3 degree increments of far-field angle. The best sidelobe level obtained was, in this case, 29 dB.

Figure 3 also includes plotted values for $T^{16}(20)$, $T^{16}(25)$ and $T^{16}(30)$; these plotted data allow comparison of the azimuth resolution of the patterns obtained from the current distributions on discrete arrays, obtained by the iterative technique, with the resolution of the exact Tchebycheff patterns of order 16 having corresponding sidelobe levels. It is interesting to note that only approximately 0.25 dB less resolution is obtained from the derived discrete current distributions then from the corresponding exact Tchebycheff pattern.

The iterative procedure starting with $T^{16}(20)$ was terminated at the 29 dB sidelobe level because, due to the relatively coarse computation interval, an apparent shoulder, rather than a maximum, appears adjacent to the main beam. Due to the method of assigning far field phase currently implemented, this causes a reassignment of far field phase at all determined positions of sidelobes, the new values differing by exactly 180 degrees from the previous values. This requirement of drastic change in the far field pattern, of course, destroys the perturbational method. The iterative procedure starting with $T^{16}(30)$ was terminated, rather arbitrarily, at the 33 dB sidelobe level. Beyond the 33 dB level, although the general sidelobe level continued to decrease, occasional lobes, higher in amplitude than the assigned objective level appear; and, in general the positions of maxima begin to change rapidly from one iterative step to the next. This effect is thought to stem from loss of accuracy in the solution of the set of simultaneous equations; this conjecture, however, has not yet been verified.

Figure 4 gives representative current distributions obtained during the iteration starting with $T^{16}(\bar{20})$ while Figure 5 gives corresponding data from the iteration starting with $T^{16}(\bar{30})$. The difference in phase variation on the rearward elements between the two cases is noteworthy.

CONCLUSION

An iterative technique has been presented which is capable of deriving low sidelobe current distributions for circular or cylindrical arrays of elements. Examples were given of the use of this technique to

suppression of sidelobes in the principal plane patterns of two circular arrays of 32 dipole elements, spaced a half wavelength apart, around a conducting cylinder. In one case a current distribution yielding 29 dB sidelobes was obtained; in the other case 33 dB sidelobe patterns were obtained. Both of these patterns, as in other examples of array of 2Q elements considered to date, exhibit azimuthal directivity only about 0.25 dB less than the order Q Tchebycheff pattern with the same sidelobe level.

REFERENCES

[1] R.DuHamel, "Pattern Synthesis for Antenna Arrays on Circular, Elliptical, and Spherical Surfaces," University of Illinois Electrical Engineering Research Technical Report No.16, pp.27-59, Urbana, Ill., May 1952.

[2] P.S.Carter, "Antenna Arrays Around Cylinders," Proc.I.R.E., Vol.31, No.12, pp.671-693, December 1943.

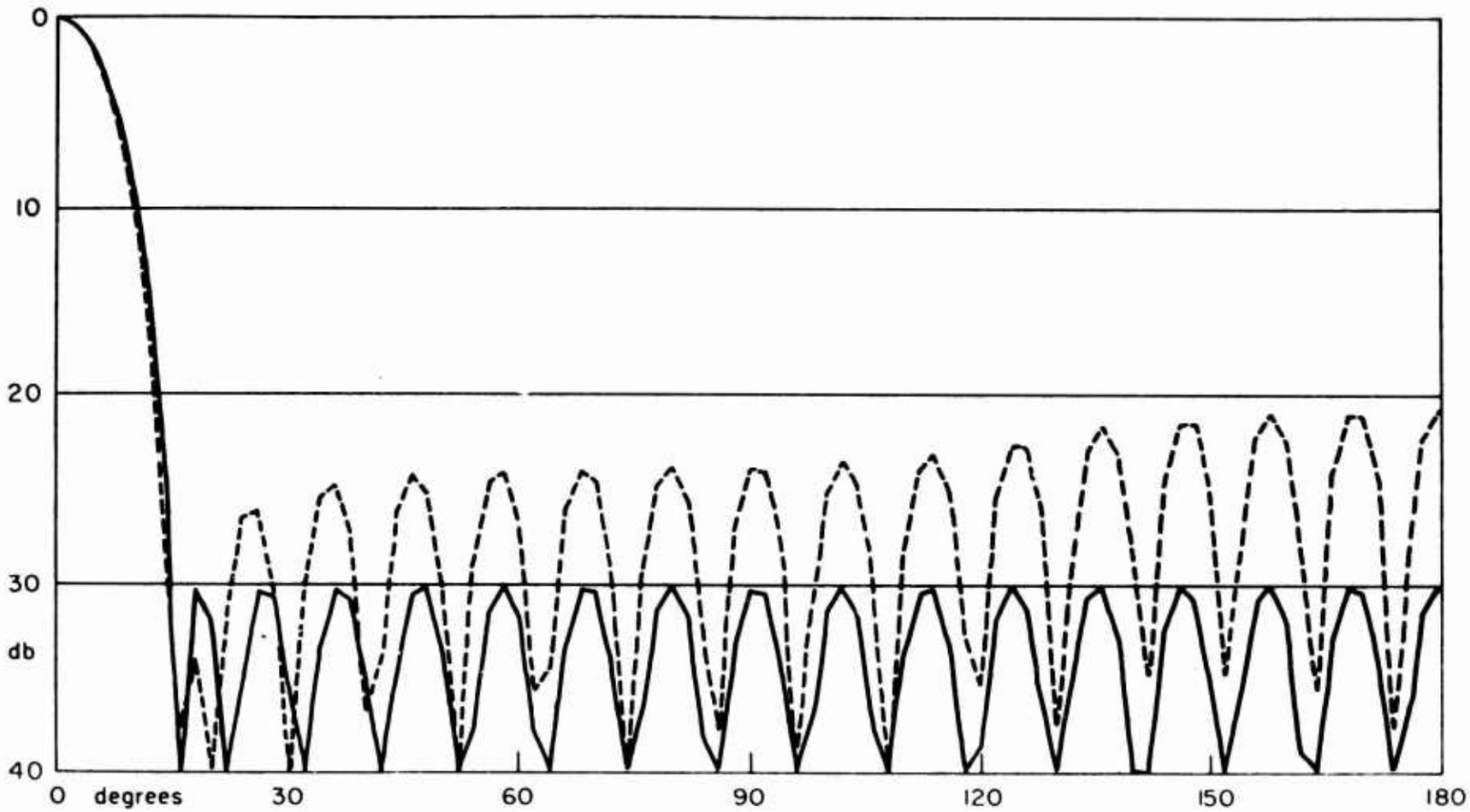

FIG 1

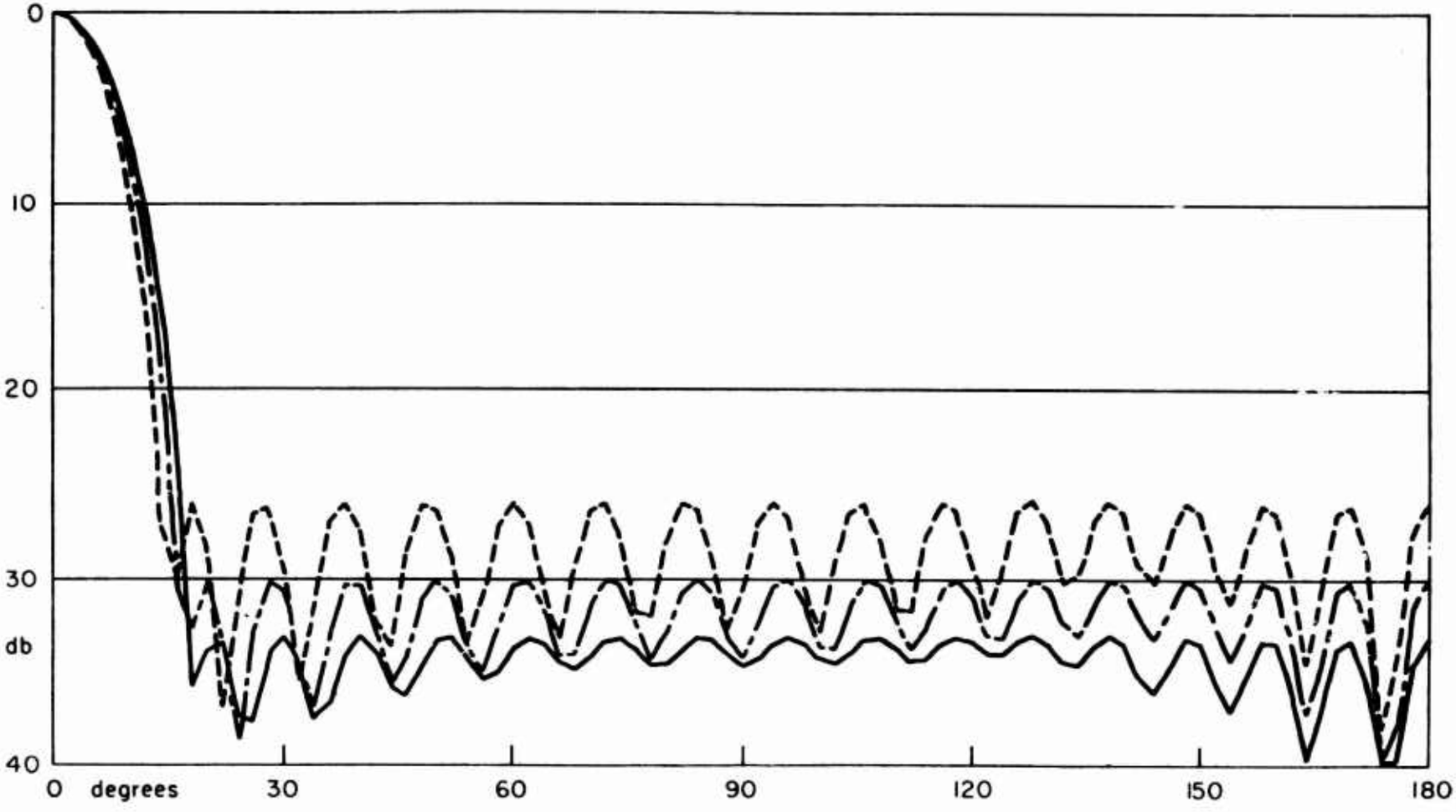

FIG 2

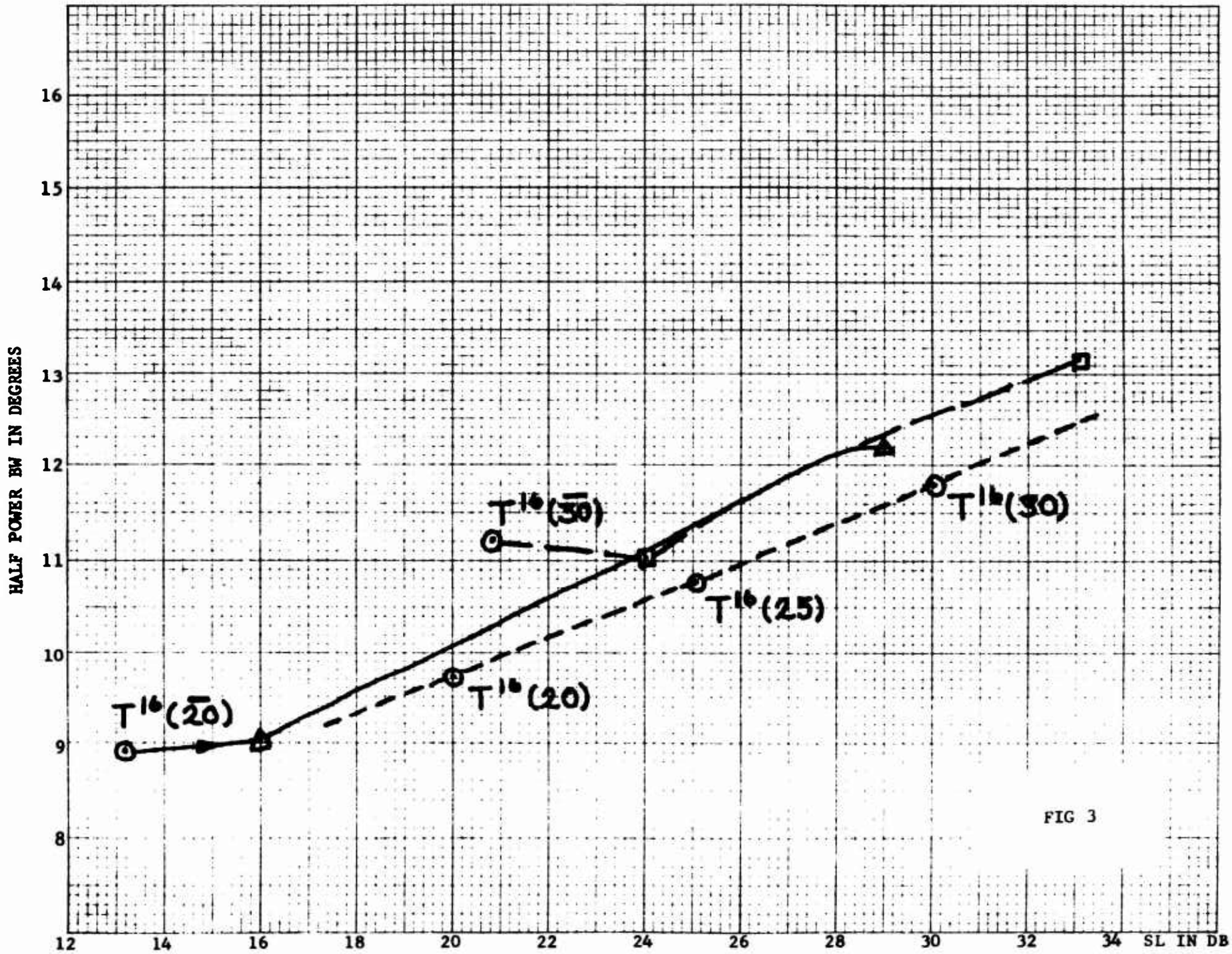

FIG 3

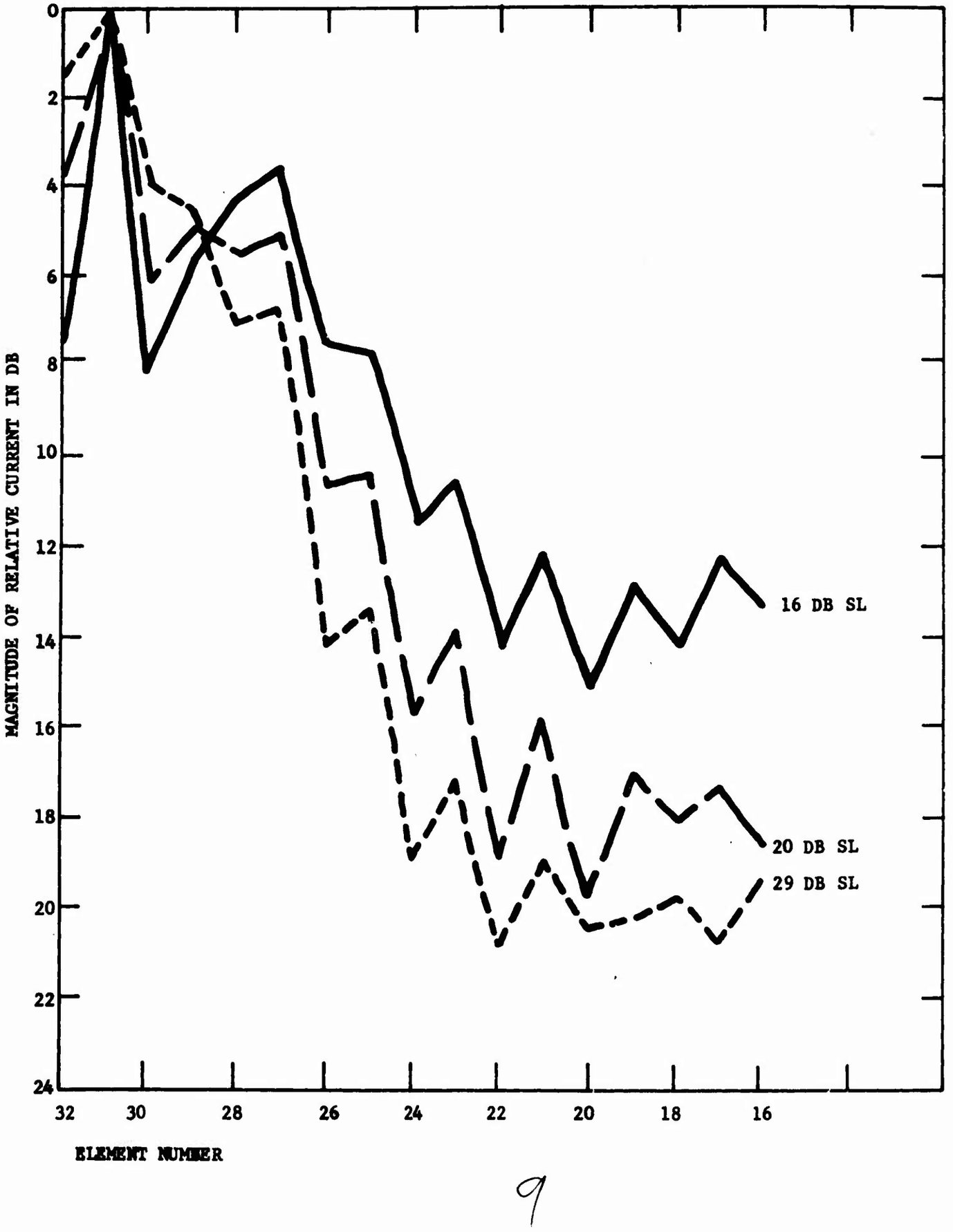
MAGNITUDE OF RELATIVE CURRENT IN DB
0
2
4
6
8
10
12
14
16
18
20
22
24
32
30
28
26
24
22
20
18
16
ELEMENT NUMBER
16 DB SL
20 DB SL
29 DB SL

FIGURE 4A

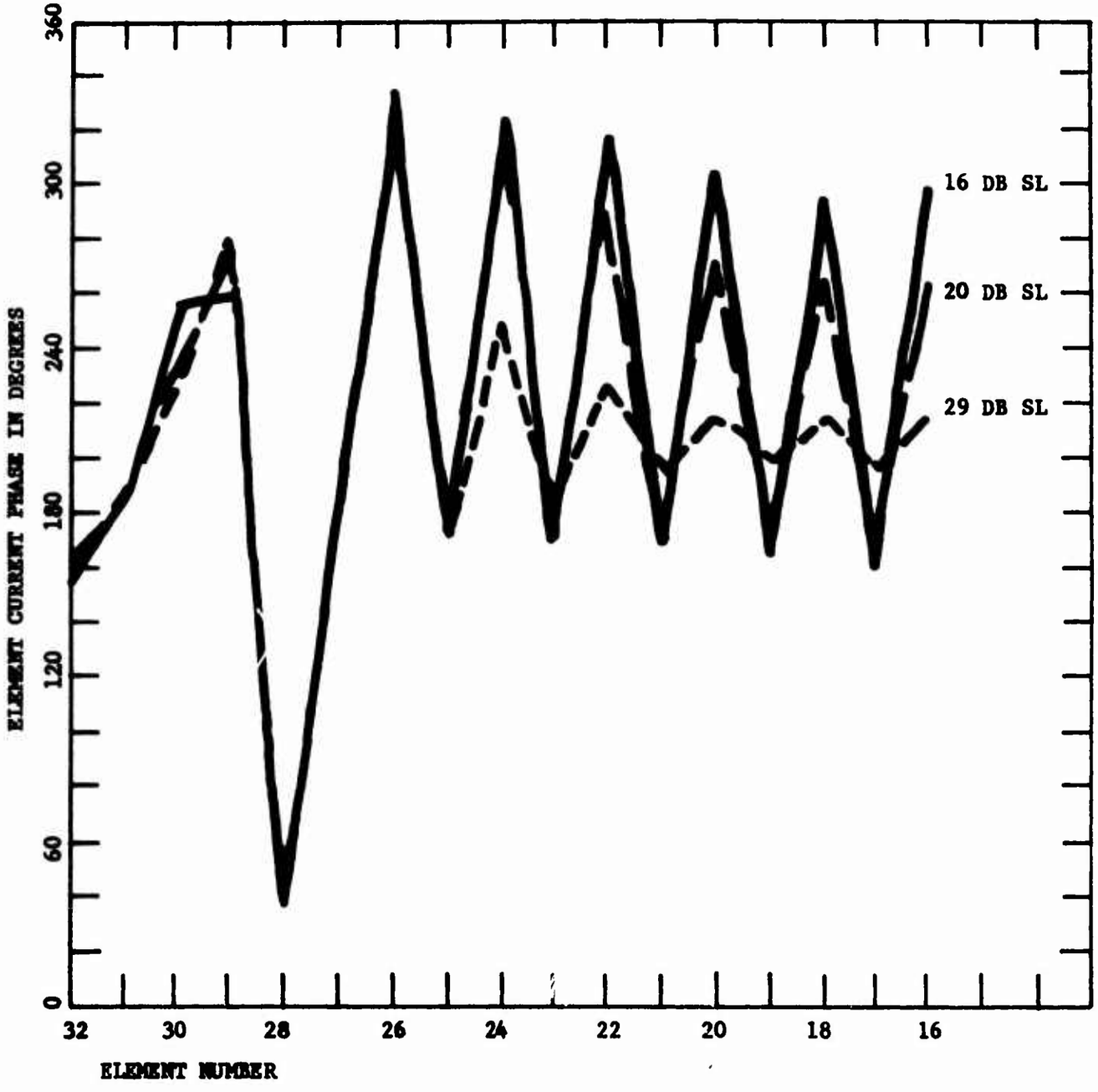
360
300
240
180
120
60
0
ELEMENT CURRENT PHASE IN DEGREES
16 DB SL
20 DB SL
29 DB SL
32
30
28
26
24
22
20
18
16
ELEMENT NUMBER

10

FIGURE 4B

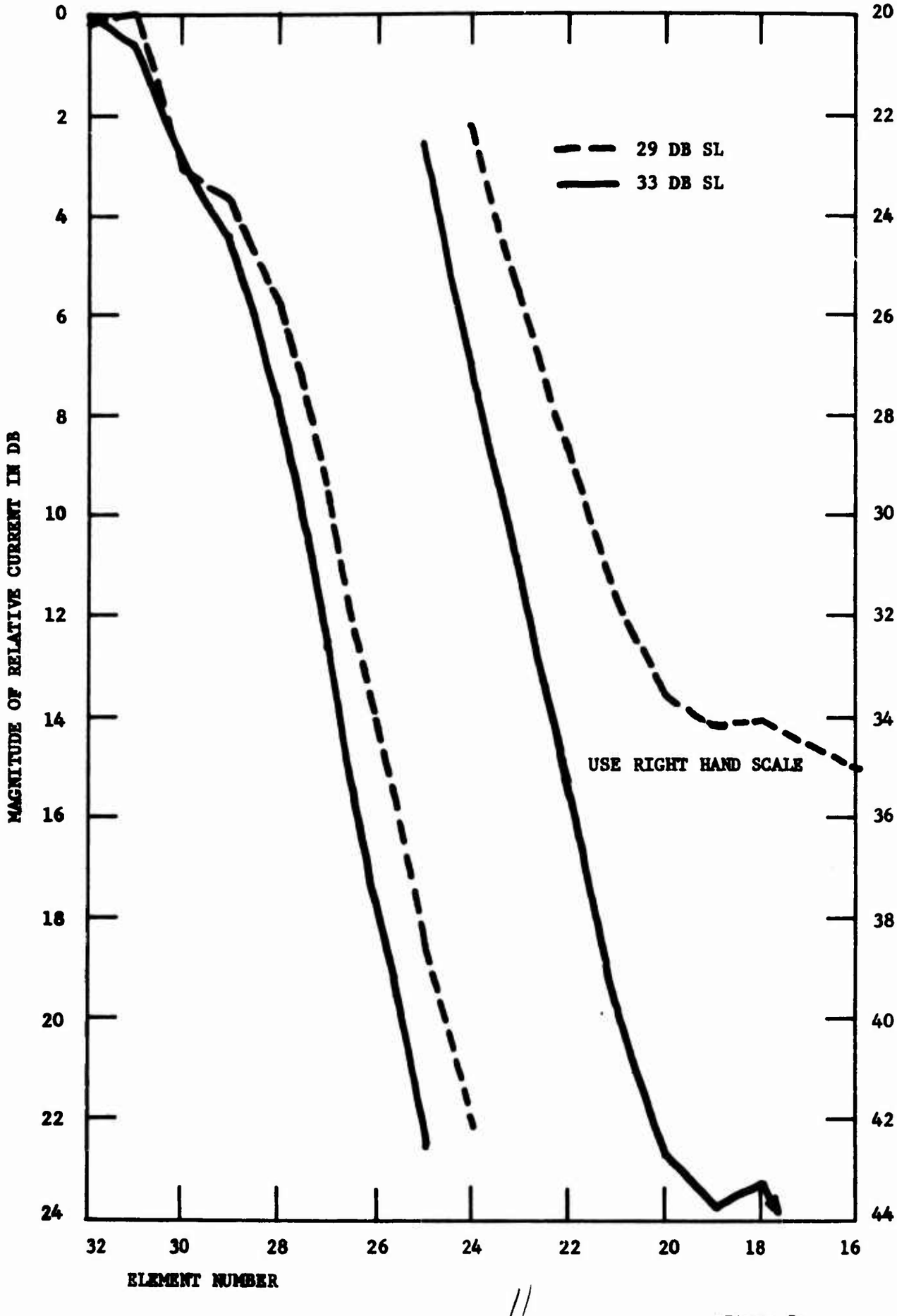
29 DB SL
33 DB SL
USE RIGHT HAND SCALE
MAGNITUDE OF RELATIVE CURRENT IN DB
ELEMENT NUMBER
0
2
4
6
8
10
12
14
16
18
20
22
24
20
22
24
26
28
30
32
34
36
38
40
42
44
32
30
28
26
24
22
20
18
16

FIGURE 5A

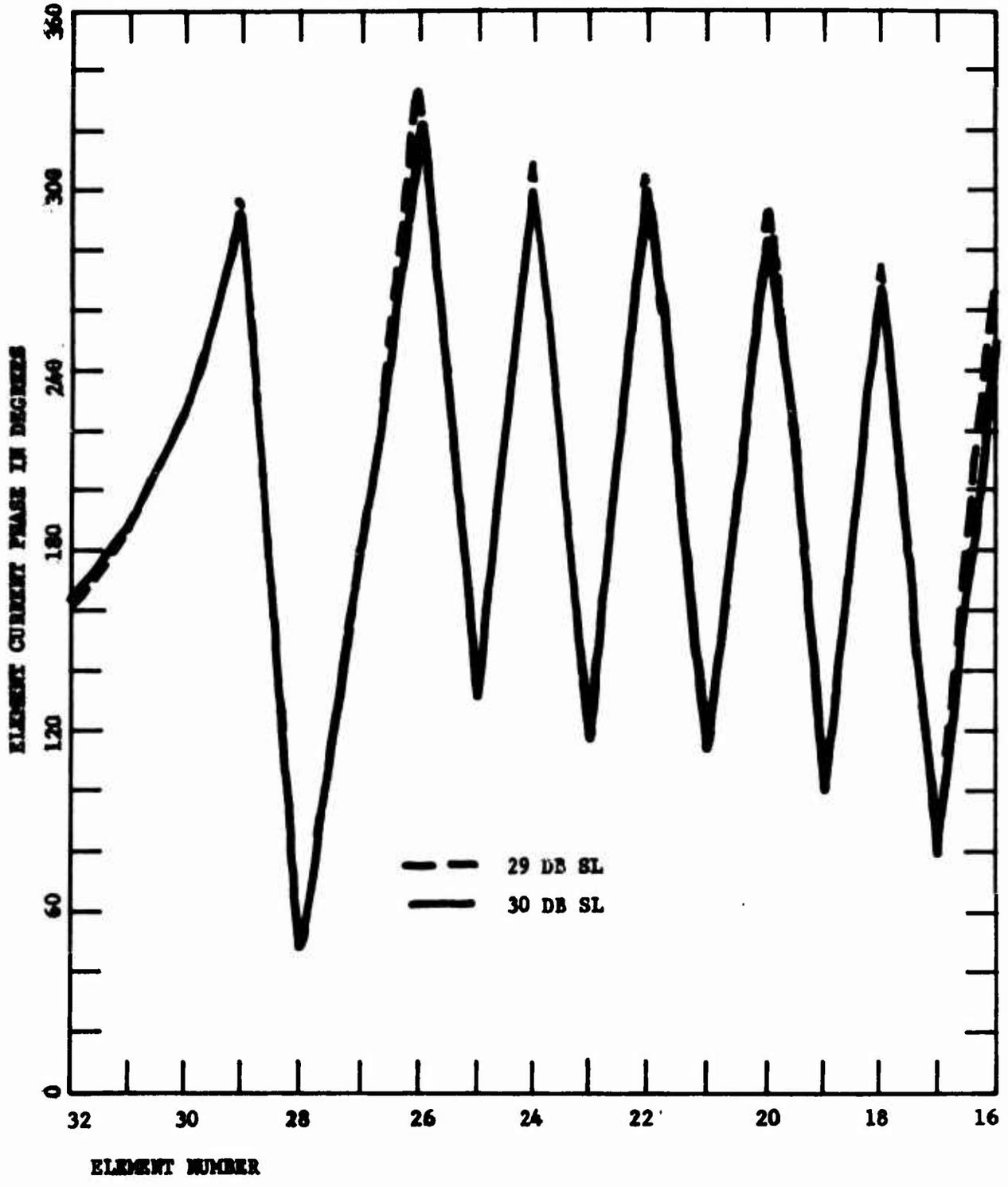
360
300
240
180
120
60
0
ELEMENT CURRENT PHASE IN DEGREES
29 DB SL
30 DB SL
32
30
28
26
24
22
20
18
16
ELEMENT NUMBER

FIGURE 5B

A SYMMETRICAL MULTIBEAM FEED NETWORK FOR CIRCULAR ARRAYS

J. Paul Shelton
Delex Systems, Inc.
Arlington, Va.

INTRODUCTION

Basic Concept

In previous papers the theory of obtaining simultaneous multiple beams from circular arrays has been described. In brief, the technique consists of cascading two Butler matrices with appropriate interconnecting phase shifts. The matrix connected to the radiating elements forms a set of ideally omnidirectional modes. These modes are phased properly at their inputs, the lines connecting to the second matrix. The second matrix combines the modes to form a set of multiple beams, just as a Butler matrix does when feeding a linear array, except that now the beams are distributed over 360 deg. It is noted that, if the beam forming matrix has N inputs and outputs, where N is the number of elements, the number of degrees of freedom in the feed network is N, corresponding to the phase shifts. Since the formation of a single beam depends upon the specification of amplitude and

phase for N elements, or 2N parameters, the existence of only N degrees of freedom is somewhat unexpected.

Assumptions

It is assumed that an acceptable element pattern is available for use in this analysis, and that this pattern is adequate for forming the modes used in forming the beams. It is felt that, as in the case of a linear array, there is an "ideal" element pattern, but the determination of such pattern for any given circular array is beyond the scope of this paper. The use of all N modes to form a multibeam array is analogous to a multibeam linear array covering 180 deg.

All analysis is two-dimensional and applicable in the plane of the array. Extension to three-dimensional cylindrical arrays is straightforward.

Objectives

The objective of this paper is to find a multibeam feed network that has the same symmetry as the circular array. That is, the network should appear the same to every input port. This characteristic is notably lacking in the cascaded Butler matrix configuration. This type of network has been termed cyclic, and one would expect a physically cyclic realization to be available.

SYMMETRICAL CYCLIC NETWORK

Derivation of Cascaded Network

If we arrange N straight parallel transmission lines along a cylinder, it is possible to imagine directional couplers among

all transmission lines as indicated in Figure 1. The coupling regions would all be at the same location along the lines, and it is seen that a symmetrical configuration can be achieved with N/2 separate coupling strengths. Recalling the previous allusion to N degrees of freedom in the tandem-matrix design, we note that the identical phase characteristics of the $e^{+nj\phi}$ and $e^{-nj\phi}$ modes reduce the actual degrees of freedom to N/2. Therefore, the network of Figure 1 is sufficient to realize the necessary multibeam aperture distributions and satisfies the symmetry requirement.

Unfortunately, the network of Figure 1 is physically impractical. A more reasonable approach is sketched in Figure 2. Cylindrical arrays of transmission lines are employed, but coupling is only between adjacent lines. If the input ports are numbered as indicated, each succeeding cylinder is seen to use a different coupling order, resulting in N/2 cylindrical coupling regions with N/2 degrees of freedom.

Synthesis

The objective of the synthesis procedure is to determine the coupling characteristics required to produce the same aperture distribution as that obtained from a tandem-matrix fed array. A brute-force approach would be to write the scattering matrix of each cylindrical coupling region, which is dependent upon coupling strength. Multiplication of the matrices for the overall network would give an output distribution that could be equated

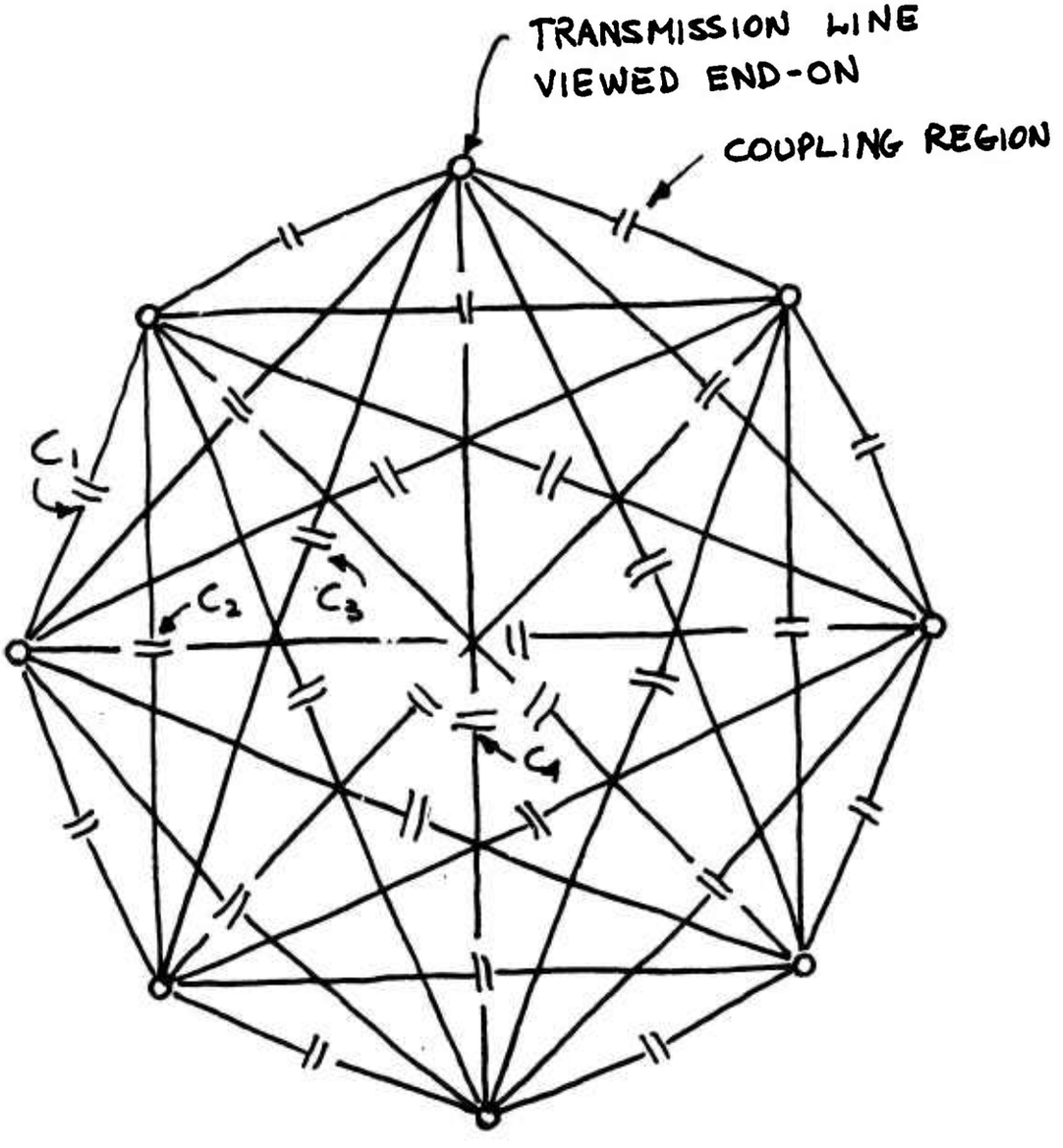

FIG. 1 SYMMETRICAL NETWORK WITH N/2 DEGREES OF FREEDOM

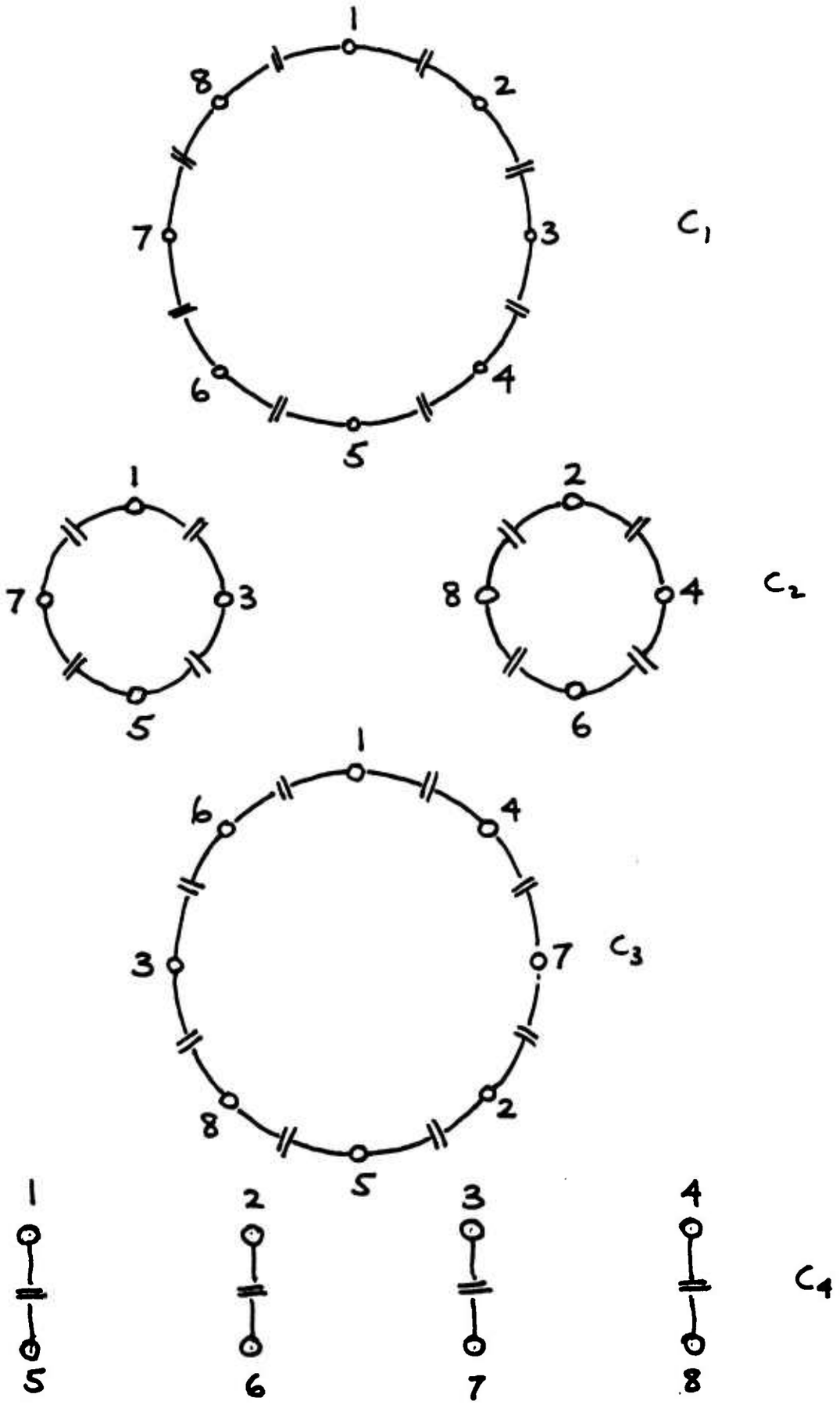

FIG. 2. MULTIPLE COUPLING REGIONS

with the desired aperture distribution. A normal mode analysis will prove more tractable.

The excitation of one input port is equivalent to simultaneous excitation of all of the progressive phase normal mode distributions. Furthermore, the scattering matrix for a normal mode passing through any one of the coupling regions is simply unity magnitude with phase shift, the value of which is dependent upon the mode and the coupling strength. Thus, on a normal-mode basis, the coupling regions are dispersive phase shifters. The analogy between the degrees of freedom in the tandem-matrix case and the configuration proposed here now becomes more clear. In each case the normal modes are phase adjusted to achieve beam collimation. A given mode is traced through the network and its phase is additively accumulated. N/2 simultaneous linear equations are obtained and the required coupling coefficients are found by matrix inversion.

Design of Coupling Regions

The first description of the cylindrical coupling region was in terms of directional coupling between parallel transmission lines, and one method for realizing such coupling is through branch lines, as shown in Figure 3(a). However, since by normal mode analysis the coupling regions are multimode phase shift networks, an alternative approach is illustrated in Figure 3(b), in which a set of Schiffman-type phase shifters is arrayed on a cylinder. Since maximum dispersion is required, the coupled sections

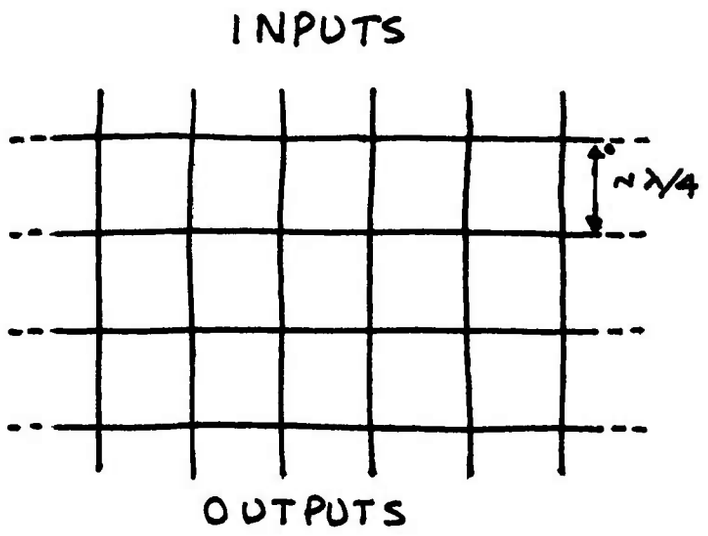

(a) BRANCH-LINE COUPLING

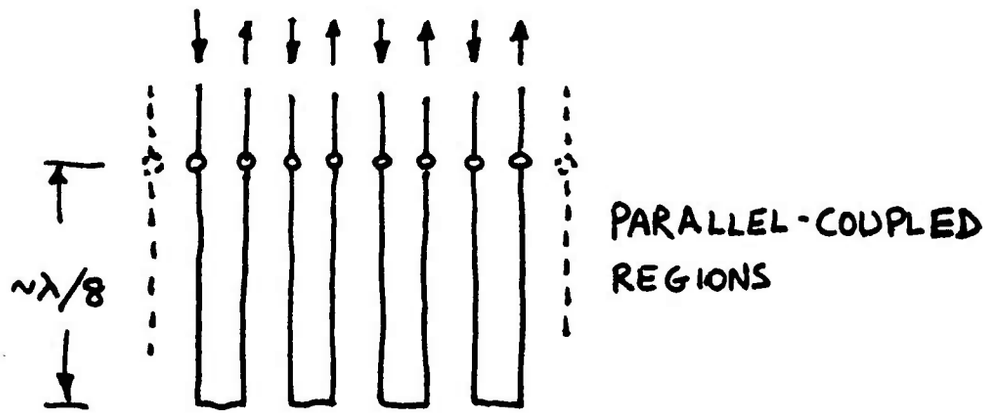

(b) SCHIFFMAN-TYPE DISPERSIVE NETWORK

FIG. 3. TWO POSSIBLE COUPLING CONFIGURATIONS

are approximately $\lambda/8$ in length.

For both of the cases of Figure 3, it can be shown that if the coupling between adjacent transmission lines is expressed by a coefficient c, the phase shift for an input mode with progressive phase θ between lines is given in terms of c and θ. For the branch-line network of Figure 3(a), the phase shift $\alpha(c,\theta)$ is to a first-order approximation of the form,

$$\alpha(c,\theta) \sim 2c \cos \theta.$$

For the network of Figure 3(b), the corresponding relation is

$$\alpha(c,\theta) \sim 2c \cos^2 \theta/2.$$

In either case the equations relating coupling coefficients for the coupled regions with mode phase characteristics will be linear.

Sample Design

A sample design is outlined in order to integrate some of the concepts presented here. The steps in the design are as follows:

1. Assume array size, number of elements, element pattern.
2. Calculate required mode phase corrections.
3. Set up cylindrical coupling regions and equations.
4. Invert coupling coefficient matrix.

For this example we assume an array of 32 elements with circumference of 16 wavelengths for element spacing of $\lambda/2$. The element pattern is assumed to be

$$E(\phi) = \frac{\cos \phi}{1+e^{5(\phi-\pi/2)}} ,$$

an expression selected not so much for credibility as for its approximation to an element backed by a cylindrical ground plane. The phase characteristic of the mth mode, referenced to the center of the array, is

$$\theta(m) = \text{atn} \left\{ \frac{-\Sigma' E(\phi_n) \cos m\phi_n \sin (z \cos \phi_n)}{\Sigma' E(\phi_n) \cos m\phi_n \cos (z \cos \phi_n)} \right\} \qquad (1)$$

where $\phi_n = 2\pi n/N$, $z = 2\pi R/\lambda$, and the primes on the summation signs indicate that the terms for n = 0 and N/2 are weighted by a factor of $\frac{1}{2}$.

A plot of the computed phases is shown in Figure 4. It is noted that the computed phase varies between plus and minus π, according to the limitations of the arctangent function. The result of adding or subtracting integral multiples of 2π is also shown in Figure 4. The new values closely approximate the function, $\sqrt{C_\lambda^2 - m^2}$, where C_λ is the circumference in wavelengths, 16 in this case. It is conjectured that if the element pattern had been more nearly optimum from the standpoint of being free of

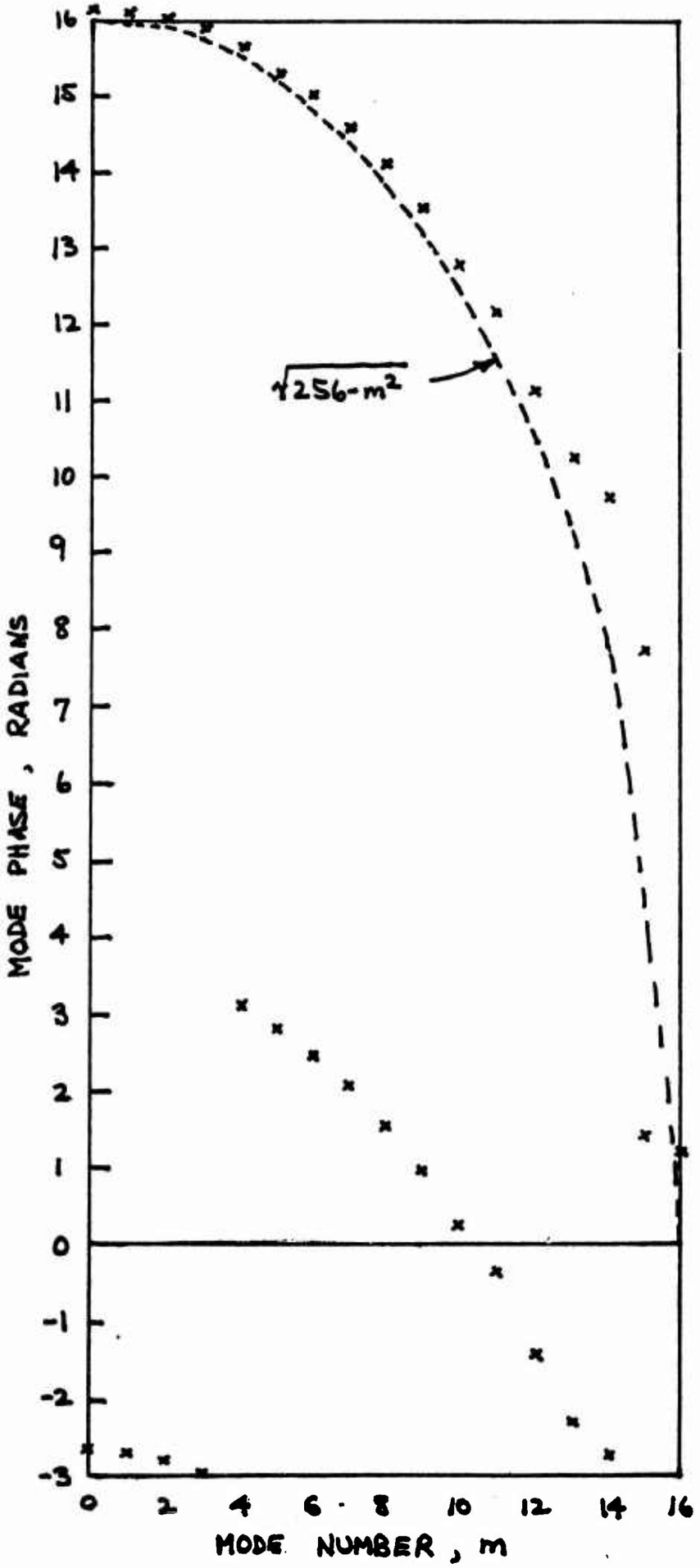

FIG. 4 MODE PHASE CHARACTERISTICS

mutual coupling, the match to this elliptical curve would have been better.

Turning now to the relation between phase dispersion for the various modes and the coupling networks, the following expression is found:

$$\beta(i,k) = 2c(k) \cos^2(\frac{ik\pi}{N}) ,$$

where i and k are the mode and coupling region indices, respectively. Since the modes run from 0 through N/2 and there are only N/2 coupling regions, an extra equation is obtained for the 0th mode:

$$\sum_{K=1}^{N/2} c(k) = \theta(0) \qquad (2)$$

If Equation (2) is subtracted from the remaining N/2 equations, the result is

$$\theta(i)-\theta(0) = -2\Sigma c(k) \sin^2(\frac{ik\pi}{N}) . \qquad (3)$$

Once the $\theta(i)$ have been found from Equation (1), solution of Equation (3) for the c(k) is straightforward.

However, it is readily seen from Figure 4 that the $\theta(i)$ are not unique. This is fortunate because direct solution of Equation (3) does not in general give positive values for all coupling coefficients c(k). It is readily shown that, for some constant p added to the left side of Equation (3), all the c(k) become positive.

Table I illustrates computed results for the phases of Figure 4. The first set of results is for $\theta(i) - \theta(0)$ ranging from zero to almost 16. Adding 11.372 rad to all modes produces the second set of results.

The third set of results is based on mode phases constrained to a range of 2π rad. Adding 7.048 rad to all modes produces the fourth set of results.

Discussion

Rather than continue into such considerations as bandwidth, partial arrays and networks, or reduced total number of beams, it seems preferable to discuss the results obtained and some of their implications. First, it is seen from Table I that the coupling coefficients are large, considering that a value of 0.3 corresponds roughly to 10 db coupling. Next, it is noted that a large variation of mode phase results in large coupling coefficients. These are aspects that need to be examined further. It may be that time-delay-related characteristics are simply not amenable to synthesis by dispersion-type networks, just as a Butler matrix produces a narrow-band linear array. Another point to be considered is the basic idea of coupling from the center of the aperture outward. Any coupling mechanism will inherently introduce delay, and the off-center elements need phase advance rather than delay. A possible alternative is to feed from the opposite side of the array.

In conclusion, a symmetrical multibeam feed network for circular arrays has been described and partially analyzed. The intention has been to introduce these networks and to suggest techniques for analyzing and synthesizing them.

TABELE I. COMPUTED RESULTS

COUPLING REGION	PHASE CORRECTION (RAD)	COUPLING COEFFICIENTS 1. With no additional phase.	2. With 11.372 RAD added.	PHASE CORRECTION (RAD)	COUPLING COEFFICIENTS 3. With no additional phase.	4. With 7.048 RAD added.
1	.033	4.020	5.442	.033	1.738	2.619
2	.125	-1.422	0	.125	.645	1.526
3	.286	.858	2.280	.286	-.881	0
4	.435	- .667	.755	.435	.673	1.554
5	.791	.570	1.992	.791	-.351	.530
6	1.151	- .545	.877	1.151	-.015	.866
7	1.568	.538	1.960	1.568	.325	1.206
8	2.04	- .511	.911	2.04	-.511	.370
9	2.633	.509	1.931	2.633	.602	1.483
10	3.297	- .465	.957	3.297	-.535	.346
11	3.951	.396	1.818	3.951	.348	1.229
12	5.014	- .351	1.071	5.014	-.122	.759
13	5.889	.300	1.722	5.889	-.133	.748
14	6.31	- .291	1.131	.027	.324	1.205
15	8.47	.295	1.717	2.187	-.446	.435
16	14.97	- .140	.571	2.404	.253	.694

SYSTEM CONSIDERATIONS AND DATA PROCESSING IMPLICATIONS OF COOPERATIVE CONFORMAL ARRAY SYSTEMS FOR ATC

NEAL A. BLAKE, TECHNICAL ASSISTANT - ATC DEV. DIVISION

Introduction

The ATC Advisory Committee was formed by the Secretary of Transportation in August of 1968 to define the improvements to the ATC system that will be required to meet the forecast 1980-1995 traffic demands. This committee concentrated its activities in the areas of increasing system capacity at the high density terminals and maintaining a high level of safety throughout the system. The committee report, submitted in August of 1969, concluded that:

. The required increase in traffic capacity could be provided in large urban areas largely by expanding existing airports. This requires implementation of close spaced (2500') dual lane runways (i.e., separate approach and departure lanes separated by 700'). In addition, the electronic guidance and surveillance systems must be upgraded so that independent all-weather landing operations can be conducted on these close spaced parallel runways. This upgrading includes development of an improved instrumert landing system based on microwave scanning beam technology.

. Maintenance of safety in high density areas as traffic increases requires extension of the ATC separation service to include all aircraft flying in medium and high density regions of controlled airspace. This is to be achieved by providing a new collision avoidance service called "Intermittent Positive Control (IPC)" to uncontrolled aircraft flying in controlled airspace.

. Increasing airspace capacity requires high levels of automation in order to increase the number of aircraft that can be handled by a controller team. Automation must provide increases of control system capacity of two times by 1980 and five times by 1995. This is to be achieved by automation of both routine and decision making tasks and implementation of an automatic air-ground digital data link. This will make it possible for computer generated control instructions to be transmitted directly to the pilot/autopilot.

. Achievement of the capacity and safety goals requires a substantial upgrading of the present ATC radar beacon system (ATCRBS) to provide increased aircraft capacity, reduced garbling and loss of reply data, increased aircraft position determination accuracy and a digital communications mode.

Requirements for the Upgraded ATCRBS

The approach taken by the ATC Advisory Committee was to define the changes to the existing ATCRBS which would be required to eliminate many of the deficiencies which exist in the present beacon system; to provide the capacity, accuracy, reliability and data rates required by the new services; to define the general requirements for the digital data link mode; and to provide a method that would permit a gradual phase-over from the present capabilities to the new services.

Present System Limitations

A significant amount of the computer capacity of the present FAA automation systems is used to compensate for deficiencies in the existing radar and radar beacon system. Some of the more serious of these are discussed briefly.

Synchronous garble results whenever two aircraft equipped with transponders exist within the same beamwidth and are within two miles of each other. Garbling conditions may also result when reply trains overlap due to reflection conditions. In this case, an aircraft on a different azimuth from the main beam may be interrogated due to energy reflected from ground objects such as hangar doors. This problem is particularly severe in terminal areas where aircraft are operating close to the ground. As aircraft densities increase, the synchronous garble problem will seriously degrade ATC operations in high density areas as identity and pressure altitude data, which are required by the ATC aircraft position monitoring and control process, will be lost for appreciable time intervals. The severity of this problem led the ATC Advisory Committee to recommend a range-ordered roll-call type of operation which is capable of greatly reducing or eliminating the garble problem.

The accuracy with which aircraft azimuth and range can be determined is degraded when an airborne transponder is exposed to over-interrogation; the aircraft antenna is shielded causing failure to reply to interrogation; reply trains overlap; fruit replies are received close to valid target data; and variable delays and reply jitter occur in the airborne equipment. As a result, the present system exhibits azimuth centermarking accuracies of $\pm$ .25° to $\pm$ .4° and range accuracies of $\pm$ 370'. As traffic densities increase, further degradation in system performance may be expected. Although use of the roll-call mode will reduce the degradation due to pulse train overlaps, any significant improvement in accuracy will require additional changes. Improvement of range accuracy will require better

control of the airborne transponder delay and reduction of reply jitter. Azimuth accuracy can be improved by use of large aperture phased array antennas and by control of the R.F. environment. The present beacon systems, both civil and military, are, in general, co-located with a primary radar and are sited to provide good primary radar coverage. This results in a considerable overlap in the beacon coverage. In addition, since civil and military interrogators operate on a common frequency, aircraft in high density areas or in areas of intense military training, are subject to multiple interrogation (e.g. in the New York area, aircraft in the low altitude airspace transitioning to land at one of the major airports, may be illuminated by up to 10 interrogators). Environment control requires that the number of interrogators operating simultaneously in an area be limited to the minimum number that can support the civil-military missions. Although much progress has been made in controlling the environment, further improvement is needed. Present processing systems can handle fruit counts in the tens of thousands per second. In many areas, however, the fruit counts are in the hundreds of thousands per second, and in some high density areas, the counts have reached into the millions per second. For this reason, video defruiters are used at most sites today. As the aircraft fleet grows, additional improvements, such as receiver side lobe suppression, may be required to reduce fruit levels.

The severity of the over-interrogation and fruit problems will be reduced in a system using a range-ordered roll-call mode of operation; however, due to the multiplicity of services, both civil and military, conducted on the present frequencies, it may be necessary to introduce the new services on a new pair of frequencies.

1980-1995 ATC System Improvements

Improvement of the ATC system to provide for automatic traffic control requires improved reliability and accuracy in determining aircraft position, short access time for digital communications relating to safety, variable data rates which increase as aircraft density and precision of control increase, and high traffic handling capacity. The ATC functions which affect the characteristics of the data acquisition and air-ground digital communications include conflict control and IPC, ATC sequencing and spacing of traffic and safety monitoring of aircraft on narrow high density routes and close spaced final approach courses.

Conflict control includes the detection of situations that may lead to collisions and the issuance of resolution control orders in adequate time to avoid the collision. The ATC Advisory Committee in studying the near mid-air collision data concluded that the collision rates would become

intolerable by 1980 if system changes were instituted. In evaluating various solutions, the committee concluded that the necessary improvement in safety could be achieved, at least for the densities forecast by 1980, if aircraft in a potential collision status were brought under control for the length of time required to resolve the conflict. The method selected used a digital data link to transmit the commands to the aircraft involved. Since the intent of uncontrolled aircraft is unknown, prediction and resolution of conflicts involving one or more uncontrolled aircraft presented the most challenging situation. The computer process selected projected all possible locations of each aircraft for the next 30 seconds. Whenever an overlap of any portion of the volumes occurred, the computer checked to see whether the aircraft would pass safely if they were constrained to fly "straight and level" or whether it was necessary to turn the aircraft. The appropriate command was then sent to the aircraft. Since the number of "false alarm" commands increases as the prediction time and volume increase, it is desirable to limit the prediction time to the minimum that will permit the pilots to recognize the commands, respond to them and pass no closer than 2000 feet from each other. This time interval is in the area of 20 to 30 seconds. Since the majority of this time (e.g. 14 to 20 seconds) represents evasion maneuver time, the data acquisition system must be capable of quickly accessing all aircraft in its area. Since any errors in determining aircraft position are reflected as errors in computed velocity, the size of the threat volume and the numbers of "false alarm" commands will increase as data accuracy decreases. The values for data rate and accuracy are related to traffic density and will vary as the aircraft progresses through the air environment.

Increasing the traffic capacity of large terminal areas while minimizing airborne delays requires use of computer assistance in the sequencing and spacing of terminal area traffic. The process used by the computer programs is to continuously monitor the early-late status of the aircraft relative to its arrival slot position and to issue control orders in the form of vectors, altitude changes and speed changes to achieve precision delivery of aircraft to the runway. As airport capacity is increased by implementation of close spaced dual runway systems, terminal route and final approach course spacings are reduced to two miles and 2500 feet respectively. As a result of the close spacings, aircraft deviations away from track must be detected quickly and corrective action, in the form of control orders, initiated within few seconds of the time of detection. The computer monitoring of these routes, and indeed, the feasibility of using such routes, is predicated on being able to achieve data rates of one message per aircraft per second for up to 2000 aircraft, accuracies of 100 feet in range and 1 to 2 mils in azimuth, and communications reliability better than 99% on the first interrogation. If these values can be

achieved, the computer can track each aircraft and compute the deviation from track and the rate of movement away from the track. Accurate determination of these two factors allows the computer to generate control instructions in time to bring the aircraft back on track (or initiate a go-around) and yet does not result in a high percentage of unnecessary control orders (false alarms) which would greatly reduce pilot acceptance of the monitoring system. The data acquisition site will also contain a fairly sophisticated data processing capability. Although the design of these sites is yet to be achieved, the processor will probably perform the function of tracking aircraft based on data not only from the upgraded ATCRBS system but also from non-co-located primary radar systems. The data from the various systems will be compared and position data representing aircraft not replying to interrogation will be extracted and sent to the control facilities along with data from cooperating aircraft. Since the conflict control process requires minimum delays, this function may well be carried out by the processor at the data acquisition site. Control orders resulting from this process would be sent to the control facility as well as to the aircraft. Performance of the conflict control routines at the data acquisition site will also permit conflict control to continue in the event that a control facility is lost. Redundant beacon coverage will permit servicing aircraft from alternate data acquisition sites in the event that a data acquisition site suffers a major failure.

Data Acquisition System Requirements

The general performance requirements for the data acquisition system were established by studying a traffic model for the Los Angeles area for the 1980-1995 time period to determine the traffic loading and by determining the accuracy and data rates required for automation of the ATC functions presented above. Although various alternatives are still under study that may modify the values, the ones resulting from the studies to date are presented with an indication of the major factor(s) that resulted in their selection.

The data rate varies as the aircraft approaches the high density areas. The time between interrogations for aircraft operating in the enroute area can be as low as 10 seconds; for aircraft in the transition area, 3 seconds; and for aircraft in the final approach area, 1 second. These rates are largely determined by aircraft proximity and required system reaction time.

The capacity of each beacon was determined from traffic forecast data which indicates a general increase of 5 times by 1995. The design requirements were based on a 10 times increase as traffic estimates have, in the past, tended to be low. On this basis, the Los Angeles data acquisition system for the terminal control facility would receive data from 4200 simultaneously airborne aircraft within the terminal airspace volume of 60 x 120 miles by 10,000 feet. The traffic count for the Los Angeles high density center using the same assumptions would include an additional 3800 aircraft. In order to obtain the required low level coverage and some system redundancy, it was assumed that the terminal volume would be serviced by two interrogators. These interrogators would be operated sequentially in the data link mode in areas where their simultaneous operation would cause interference.

In order to determine the technique to be used to service this number of aircraft, estimates were made of the message length required for the ATC service. It appeared that 50 bits would provide an adequate message structure for all of the ATC messages. Since these messages,which are transmitted as a part of the aircraft position determination messages, are relatively few in number (e.g. not over one per minute per aircraft even under the highest density conditions) considerable communications capability is available for future automation of additional services (e.g. transmission of selected weather data and detailed ATC clearance interchanges). It was readily apparent that the present scanning beam and statistical center marking process, which requires 18 to 20 replies per beamwidth to achieve the present accuracies, would not permit servicing of the required number of aircraft at the required rates. As a result, the committee selected the beam steering mode of operation for determining aircraft position. In this method, the beam is pointed at the predicted aircraft location during the interval when the reply is expected and then the beam is vernier steered during the reply period for accurate position determination.

The azimuth accuracy of 2 mils required for the terminal monitoring function can be achieved using a large aperture phased array system with a shaped reflector to generate a fan-shaped interrogation beam. A circular array with an aperture of about 60 feet can generate a 1^{o} beam at 1030 MHz and appears to be capable of providing the required accuracy.

Since the new data link mode must be introduced in parallel with the present beacon service, the interrogation modes must be interlaced. One possible method of operating, which was examined during the study, was based on the following assumptions:

. The message period per aircraft would be 50 microseconds long with 20 microseconds allowed for beam positioning and 30 microseconds for transmission of the message.

. The airborne transponder would have a one millisecond delay before replying in the data link mode.

. All messages transmitted during one data link period would be arranged in ascending range order by the processor.

. The beacon mode A and C interrogations would be interlaced with the data link mode.

. Beacon range would be limited to approximately 100 miles.

The system would then operate in the following manner. Aircraft entering the system and equipped with a standard transponder would reply to the standard mode A and mode C interrogations. Aircraft equipped with the new data link encoder-decoder would enter the system by replying with the aircraft discrete code to a data-link mode general call. Once entered in the roll-call, the aircraft would reply only when its discrete code was received. One possible interrogator sequence is as follows:

1. Transmission of 20 data link interrogations (1 ms)

2. Receipt of corresponding aircraft replies (2.2 ms)

3. Transmission of a mode A or mode C or data link general call interrogation and receipt of replies (1.2 ms)

4. Repeat the above sequence.

If a single beam were used 227x 20 = 4540 data link equipped aircraft could be serviced each second. In addition, a stepped 1^{o} beam would provide a 360^{o} search for data-link equipped aircraft entering the system every 1.6 seconds. Standard beacon interrogations would result in a 360^{o} scan every 16 seconds. Since it is possible to use multiple beams in the scanning modes, the standard beacon mode scan could be reduced to 4 or 5 seconds. This method of operation is only one of many that are possible. Other more sophisticated operating modes were examined during the study and further analysis is needed before the choice of method can be made.

Status and Summary

The ATC Advisory Committee defined the method of increasing airport capacity, the required level of automation and the general requirements for the upgraded beacon system. The Committee indicated that a large aperture phased array antenna system and associated processor would permit the necessary accuracy, data rate and communications capability to be achieved while at the same time permitting a smooth transition from the present beacon system operation to the future precision data acquisition and data link system.

The committee provided general guidance for the upgrading of the data acquisition system. The FAA is presently evaluating these recommendations and preparing the development plan not only for the data acquisition system, but also for the other elements of the upgraded ATC system.

HARDWARE DEVELOPMENT OF

CIRCULAR ARRAY ANTENNA SYSTEMS

FOR

IFF (L-BAND) FREQUENCIES

- - -

Presented by: Naval Ship Engineering Center
Department of the Navy
Center Building
Prince George's Center
Hyattsville, Maryland 20782

HARDWARE DEVELOPMENT OF CIRCULAR ARRAY ANTENNA SYSTEMS FOR IFF (L-BAND) FREQUENCIES

Naval Ship Engineering Center

Joseph L. Weis (NAVSEC 6175C05)

3 November 1969

ABSTRACT: In future shipboard IFF systems. the complete identification of all targets must be made in less time than it now takes with today's systems. One way to meet this shorter time would be to increase the scanning rate of the antenna. However, to meet the requirements, the antenna then must be turned at speeds greater than can be reasonably designed into combined radar/IFF antennas; or into slaved IFF antennas mounted on separate pedestals. The electronically steered antenna systems that position the beam without mechanical movement can meet—even greatly surpass—the high speeds required. With electronically steered antennas, the time for rotation is limited only by the electrical switching circuits and it is possible to achieve speeds that are hundreds of times faster than with mechanically rotated antennas.

The design of electronically steered antenna systems will almost always be a compromise made from several "trade-offs". Choice exists in beamwidth, diameter of the array, number of radiating elements energized, the type of RF feed system and switching matrices, and (very importantly) the accessibility of the array for maintenance after the initial installation. The design of two such electronically steered antenna systems has been undertaken by the Navy, and each system has unique features not found in the other.

GENERAL: The Navy decided to develop these two circular antennas (instead of one) because there were sufficient features and risks connected with each design that would make it unwise to proceed without first evaluating each antenna in an operating system. After proving the system performance of each antenna, the better design features will be combined into a final specification for production units. This simultaneous development of two systems protects against the risk of putting all the "design eggs" into one basket.

No attempt will be made to prove the theory behind each design. This paper will simply provide descriptions of both antennas, outline some of the problems encountered, and compare the pertinent technical features common to both systems.

HISTORY: Even in 1966, it was evident that the antenna of the future for shipboard IFF would have to be something other than a mechanically rotating device. The prime reason was the high speed scanning rates but another reason nearly as important was the need for operational reliability such as can be provided through solid state electronics. The elimination of moving parts was considered mandatory because such parts are notorious for the tendency to wear poorly and thereby require frequent refurbishment or replacement. Moving parts are also quite susceptible to additional degradation from the "at sea" environment of wind loading, salt spray, stack gas contamination, and ice loading. The speed of rotation of a mechanical antenna is usually limited to approximately 15 RPM, or 4 seconds per 360 degree rotation. It is impractical to design a "jump-scan" feature into a mechanical system that can change from one direction to another without rotating through all of the intervening positions. Therefore, the time to go from one direction to another is a function of rotational speeds rather than direct movement and consequently takes more time.

Electronically steered antennas have no moving parts so are not fettered to the mechanical problems. They are many times faster (up to 20,000 RPM), do not require frequent maintenance, and are not as adversely affected by the sea environment. Moving the beam directly from one position to another without passing through intervening positions is accomplished in microseconds. Control of the beam position through the use of digital signals permits computer programming techniques for efficient use of the antenna. Another feature of the circular array is the inherent ring or "doughnut" construction that permits mounting the array around a mast, on top of or around a deck house, or similarly affixed to other superstructures of the ship. The fixed circular antenna eliminates the turning clearances normally required by rotating planar arrays, and therefore is more versatile for installation on a ship. And lastly, the circular arrays can be readily "stacked" in layer fashion providing multiple antennas in one mounting location.

The original development plan of the Navy (started in 1966) specified that one design utilize magnetic reed switches and the other design use

RF diodes for the switching devices. The appeal of the reed switch was the low insertion loss and also the magnetic holding action (in either position) that eliminated the need for "holding power". The unattractiveness of the reed switches was the relatively long total switching time of a few milliseconds which was barely acceptable and was much longer than desired. The RF diodes were attractive because they had switching times in low microseconds, but in 1966, the reliability, unit cost, and insertion losses were unattractive. Therefore RF diodes were only conditionally acceptable. It was these pros and cons that prompted the decision to develop two circular antenna systems and prepare the final specification after the technical evaluation of the two systems.

It is an interesting fact that after several years of development, some of the parameters established in 1966 are not valid for 1970. The reliability and long life credited to the reed switches is now in question. The magnetic latching feature has been deemed unsatisfactory and holding current for one-half of the reed switches must now be provided. On the other hand, the RF diodes have been developed to a degree that reasonable reliability and satisfactory life times are achieved. Also, the diode insertion losses have been improved so that through judicious switching techniques, the total system losses can be reduced to acceptable levels.

From the foregoing, it can be seen that the design features—good and bad—recognized in 1966 are not patently true in 1970. The choice of one design over the other can now be made without being influenced strongly by a specific component choice such as reed switches versus RF diodes.

DESIGN: Design goals for electronically steered antennas for shipboard use do not differ greatly from design goals for similar antennas for land based installations. Platform stabilization is sometimes required for shipboard installations, and the design of the units must include protection against salt spray, stack gas temperatures, and stack gas contaminants. Access for maintenance of an array installed on a ship may require a different design treatment than required for a fixed land based installation. Some of the basic design parameters for shipboard systems is presented at this time (FIRST SLIDE ON) to serve as a prelude for the individual descriptions of the two developmental antennas that follow.

(Discussion of first slide-then SLIDE OFF)

ANTENNA # 1. The first circular antenna to be described was developed by the Scanwell Laboratories of Springfield, Virginia (SECOND SLIDE ON). This development will be described in greater detail by their engineers in a following paper. The array is twenty feet in outside diameter and provides a choice of two azimuthal beamwidths—either 4.5 or 8.8 degrees. The vertical beamwidth is 58 degrees and two identical circular arrays are stacked one on the other. Each array has the same

characteristics when fed separately. The purpose of the two arrays is to provide a continuous 360 degree scanning with one while using the other for jump scanning from one target to another for special data processing. The 360 degree scanning provides "all target" up-dating at about one second refresh rates, and the jump scan provides capability for immediate attention to pop-up targets or special security checks on a "target-by-target" basis at a switching time of approximately three milliseconds.

Electronic units are mounted above decks as well as below the decks. One electronic package, a scanner unit, is needed at each circular array—in the case of the dual arrays there are two such units—and the basic distribution of the RF energy is accomplished in this scanner unit. The RF paths are coax cables through reed switches to the radiating elements. The control of the switches is generated in the below deck electronic equipments, and on-line monitoring of the switching paths from the radiators is provided. The interconnections between the above deck and below deck equipments are a single RF cable 81 control leads, and 126 monitor leads for each array. The RF energy from the transmitter is first switched through an ISLS (Interrogation Side Lobe Suppression) switch for directing the energy into the sum or difference inputs of the scanner. There are 31 outputs from the scanner that feed 31 switches on the array which in turn feed 62 more switches that are connected to the 124 radiating elements. A monitor wire from each radiator is fed back to the below deck equipment to indicate when the radiator is being energized and serves as a monitor of array performance. The control of the ISLS switch comes from the IFF interrogator which is the transmitter/receiver connected to this antenna.

The inputs to the below deck electronic equipment are: (1) 10-bit digital control word, (2) manual controller 10-bit digital word, and (3) 60 cycle, 1 speed synchro data. Slaving or directing the array is accomplished by any one of the three inputs.

The weight of the array is approximately 2100 pounds, which is too heavy for nominal shipboard installations, but it must be remembered that there are two independent antenna systems in this construction, therefore a single array could be expected to be around 1200 pounds. (SLIDE OFF)

ANTENNA # 2. The second circular antenna is under development by Geotronics, Inc., a company in Falls Church, Virginia. (THIRD SLIDE ON) As built, this is a single array though a dual array construction is feasible. The outside diameter is 9.5 feet, the beamwidth is approximately 7.2 degrees horizontal and about 48 degrees vertical coverage. Like the system before it, this antenna beam can be positioned or slaved through a 10-bit digital control word, 60 cycle-1 speed synchro data, or manual controller 10-bit digital word. The array of radiating elements differs considerably. There are 180 radiators interspaced equally to provide three separate circular arrays each consisting of 60 radiating elements. Each array is spaced one-third electrical dimension from the other two—all are on the same periphery. The RF energy is fed through an R-2R lens system. Because there are three separate arrays, six

lenses are required—two for each array. The switching of the energy is through RF diodes and strip-line feed matrices. Thirty radiators are energized (to produce a beam) from one lens or a combination of two lenses. The beam steps in sixty major steps with 16 intermediate steps between each major step. This method provides a system capable of stepping the beam in 960 discreet steps of 0.375 degrees per step (6 lenses with 10 major steps each (60) multiplied by 16 intermediate steps for each major step). (THIRD SLIDE OFF)

Instead of providing sum and difference techniques, this second antenna provides an omni-directional pattern for the ISLS function. This is simply done by feeding two matching lenses through a centrally located input probe. (FOURTH SLIDE ON) The 360 degree coverage is better defined by this slide. Energy is fed directly into two ports of a lens, or one port of two lenses, depending upon the desired beam position. The step-type power divider provides 16 discreet positions ranging from one port direction to the other port direction. The switching diodes choose which two ports are used. When in the omni-directional position, the step-type power divider is removed and equal power is fed to the centrally located input ports of one pair of lenses.

The eight-throw diode switches provide a minimum RF path loss to the radiators. (FOURTH SLIDE OFF—FIFTH SLIDE ON). The general design of the switching matrix is shown by this slide with a schematic of the switch and strip-line feed system. Specific engineering details cannot be given at this time as some proprietary rights of both the Government and the contractor are involved.

(Discussion of slide, and then—FIFTH SLIDE OFF)

PROBLEMS: The design carried out under both contracts had the usual head-aches, false starts, and performance gliches attendant with development of electronic equipments. In addition to these, the following and somewhat unique problems were encountered. The relatively large number of switching devices required that a careful study be made to determine the optimum design of the switching matrix. The first impulse is to use a binary number but optimum design was found to use a number other than binary. For the first antenna the number was 124 (not 128) and for the second antenna the number was 60 (not 64). It is suggested that designers of similar systems keep an open mind concerning the number of radiating elements because a binary number might not be optimum.

Not having a binary number of elements operate against a 1024 (ten-bit) binary control signal requires special treatment in the logic. In the first antenna, the logic operating on the control signals of the ten bit input word perform a "skip" for every thirty-second position. This provides 992 steps for the 1024 input commands and each step is 0.363 degrees instead of 0.35 degrees which is the length determined by 1024 steps. The error is beam direction progresses to the 31st step and returns to zero on

the 32nd step. This process repeats itself as the beam rotates through 360 degrees. The maximum error is 0.21 degrees.

In the second antenna, the solution was to step 0.375 degrees instead of 0.35 degrees of the control word. Every 16th step was disregarded and 960 steps thereby resulted from the 1024 discreet orders from the digital 10-bit control word. The directional error produced by this method grows from zero to 0.18 degrees and returns to zero as the beam position advances from one through sixteen positions and repeats itself for every subsequent sixteen steps. This type of error has been considered acceptable to overall performance for shipboard IFF systems.

Stacking one antenna upon another required careful choke design so that vertical pattern interference would not degradate system performance of either antenna. Due to the relatively good isolation provided by the choke design, only some—but tolerable—interference is experienced. Also, when considering that the normal operating procedures cross beam positions quite rapidly, system performance continues even with the short term (microseconds) interference that occurs. There is only a low probability of this condition happening at a critical data acquisition period.

COMPARISON: In finale, a comparison is made of the features found in both systems. (SIXTH SLIDE ON) From this comparison one can see the features that appeal for a given antenna performance criteria.

(Discuss the slide, then-SIXTH SLIDE OFF)

CLOSING: If anyone desires more information about the two antennas described by this paper, it will be appreciated if all such requests are addressed to the Navy Department as follows:

Naval Ship Engineering Center
Center Building
Hyattsville, Maryland 20782

ATTN: Mr. Joseph L. Weis
Code NAVSEC 6175C05

BASIC DESIGN PARAMETERS

FREQUENCY	1030 MHz AND 1090 MHz, VERTICAL POLARIZATION
BEAMWIDTHS	AZIMUTH, 4 TO 8 DEGREES—ELEVATION, ~ +5 DEGREE
GAIN	MAIN BEAN > 18 db; MINOR LOBES < 20 db BELOW MAIN
BEAM CONTROL	10-BIT BINARY WORD
BEAM ERROR	ERROR < ONE DEGREE—RESOLUTION < ONE-HALF DEGREE
SWITCHING TIME	LESS THAN 3 MILLISECONDS—GOAL << 100 μSEC.
BORE SIGHTING	OPTICAL, OR ELECTRONIC
	PHYSICAL CHARACTERISTICS
ARRAY WEIGHT	500 POUNDS
OUTSIDE DIAMETER	10 TO 22 FEET GOAL = 10 FEET
INSIDE DIAMETER	1 TO 8 FEET GOAL = 8 FEET
ELECTRONICS	SOLID STATE WHEREVER PRACTICAL

SLIDE ONE

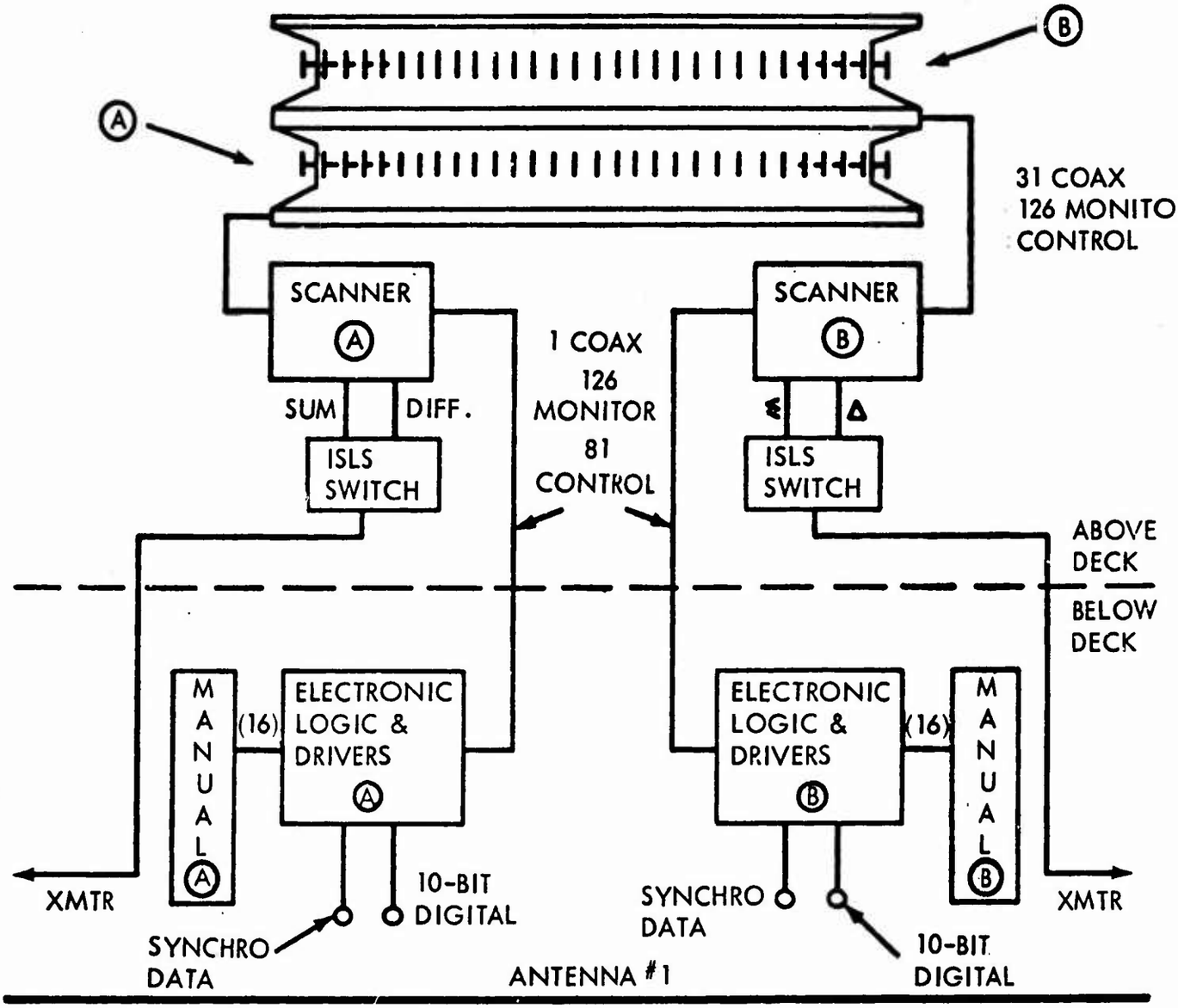

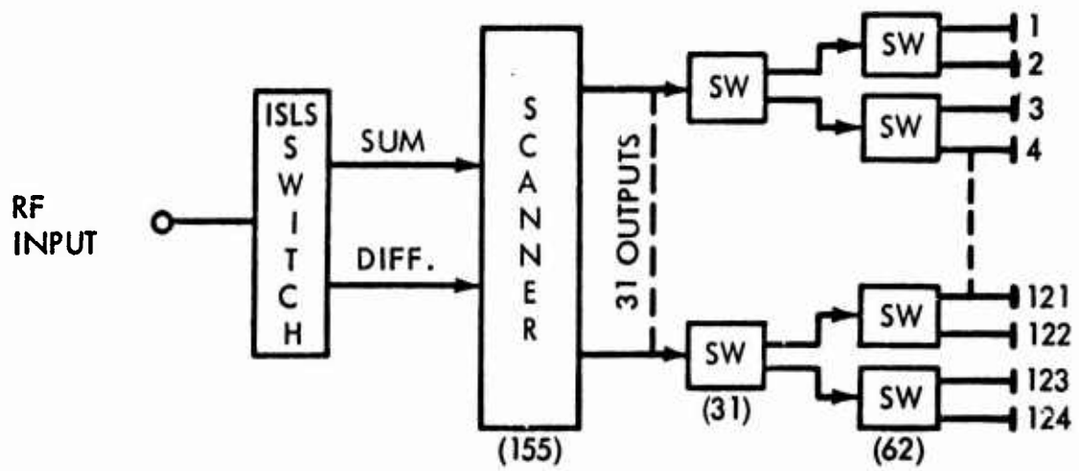

BASIC RF SWITCHING PATH

SLIDE TWO

8

ANTENNA #2

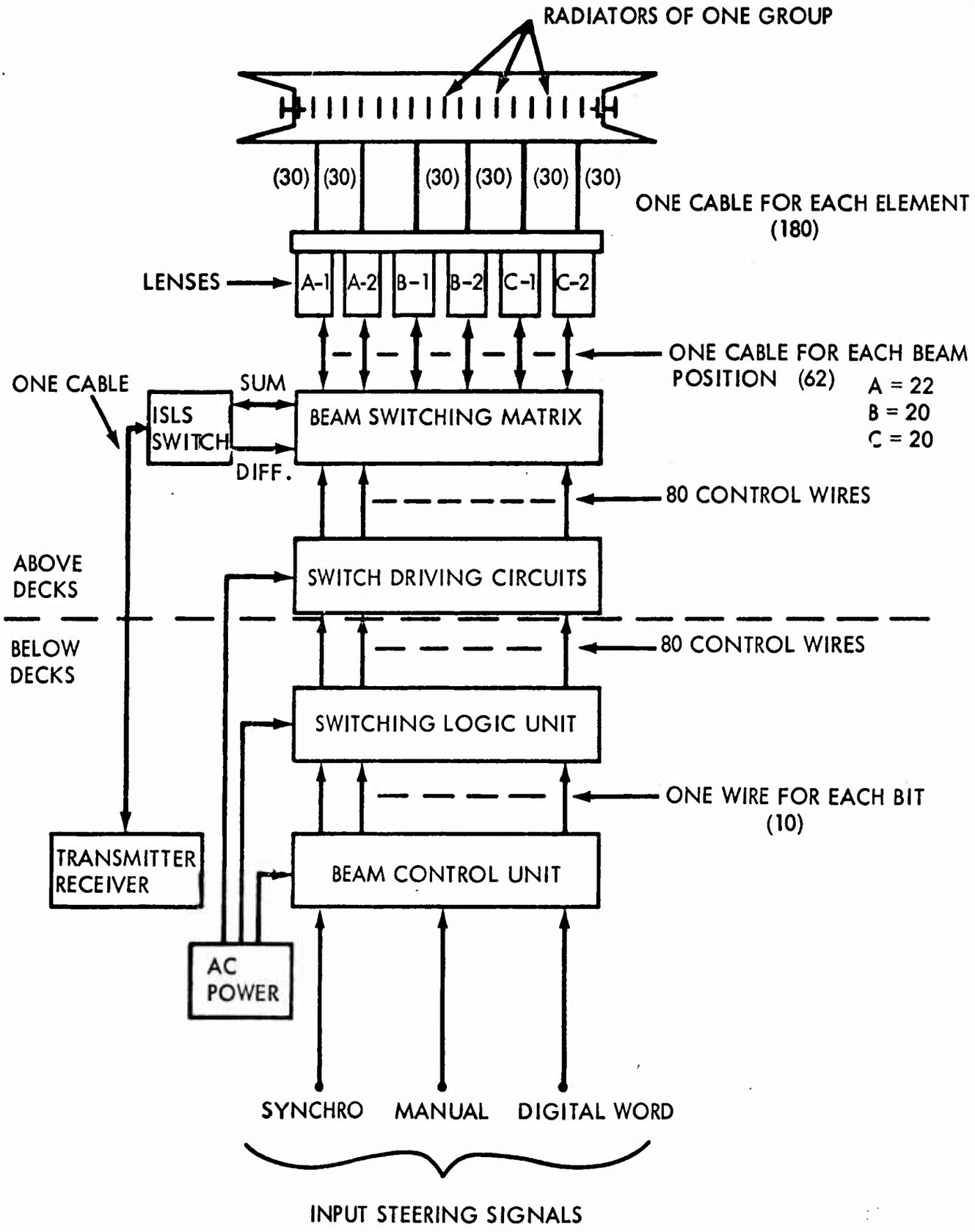

SLIDE THREE

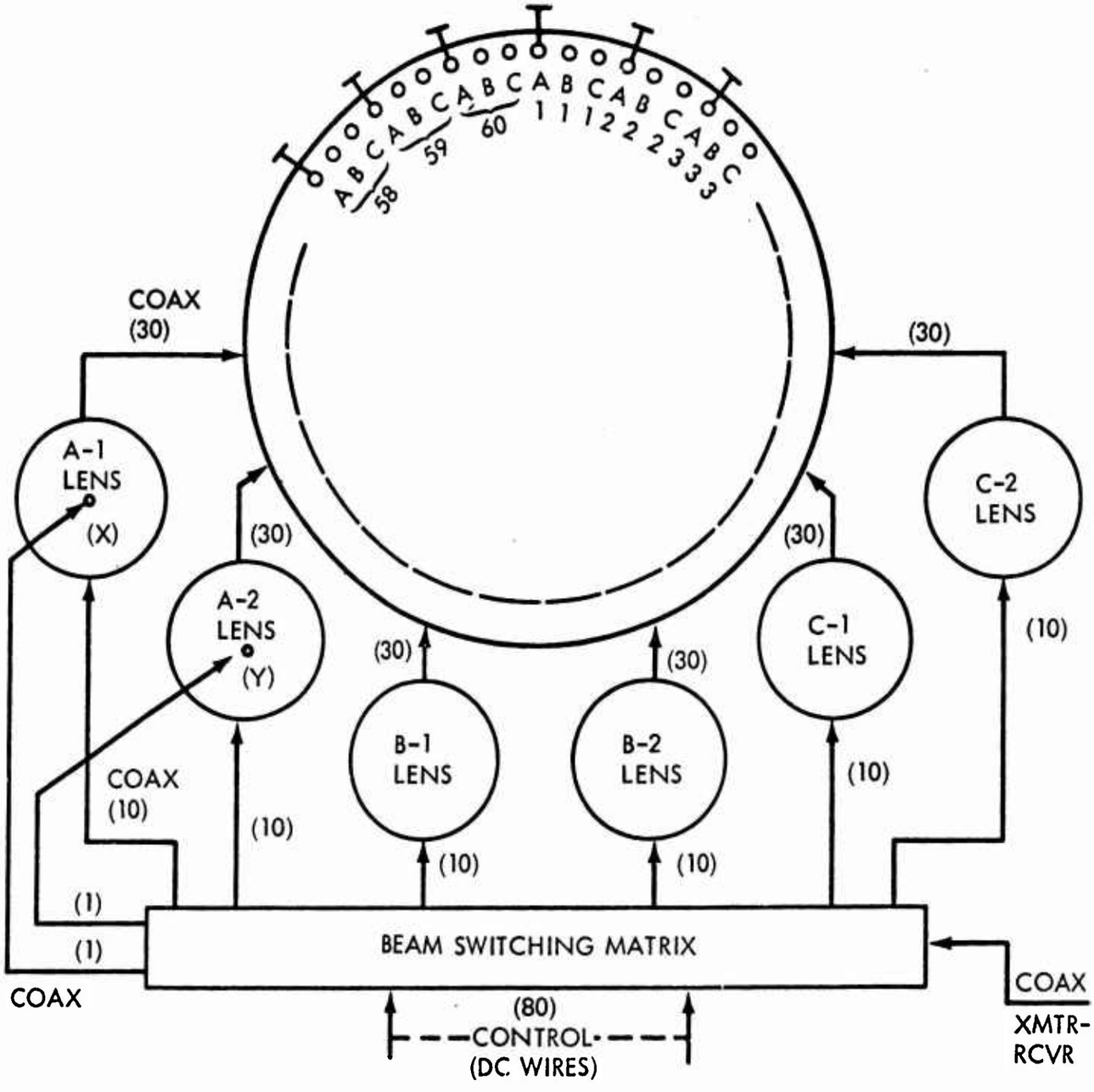
A B C A B C A B C A B C A B C A B C
1 1 1 2 2 2 3 3 3
58
59
60
COAX
(30)
(30)
A-1
LENS
(X)
A-2
LENS
(Y)
B-1
LENS
B-2
LENS
C-1
LENS
C-2
LENS
(30)
(30)
(30)
(30)
(10)
(10)
(10)
(10)
(10)
COAX
(10)
(1)
(1)
BEAM SWITCHING MATRIX
COAX
(80)
CONTROL
(DC WIRES)
COAX
XMTR-
RCVR

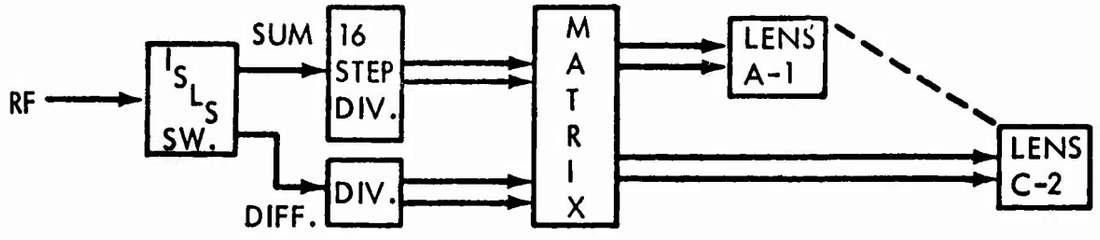
RF
SUM
DIFF.
SW.
16
STEP
DIV.
DIV.
MATRIX
LENS
A-1
LENS
C-2

SLIDE FOUR

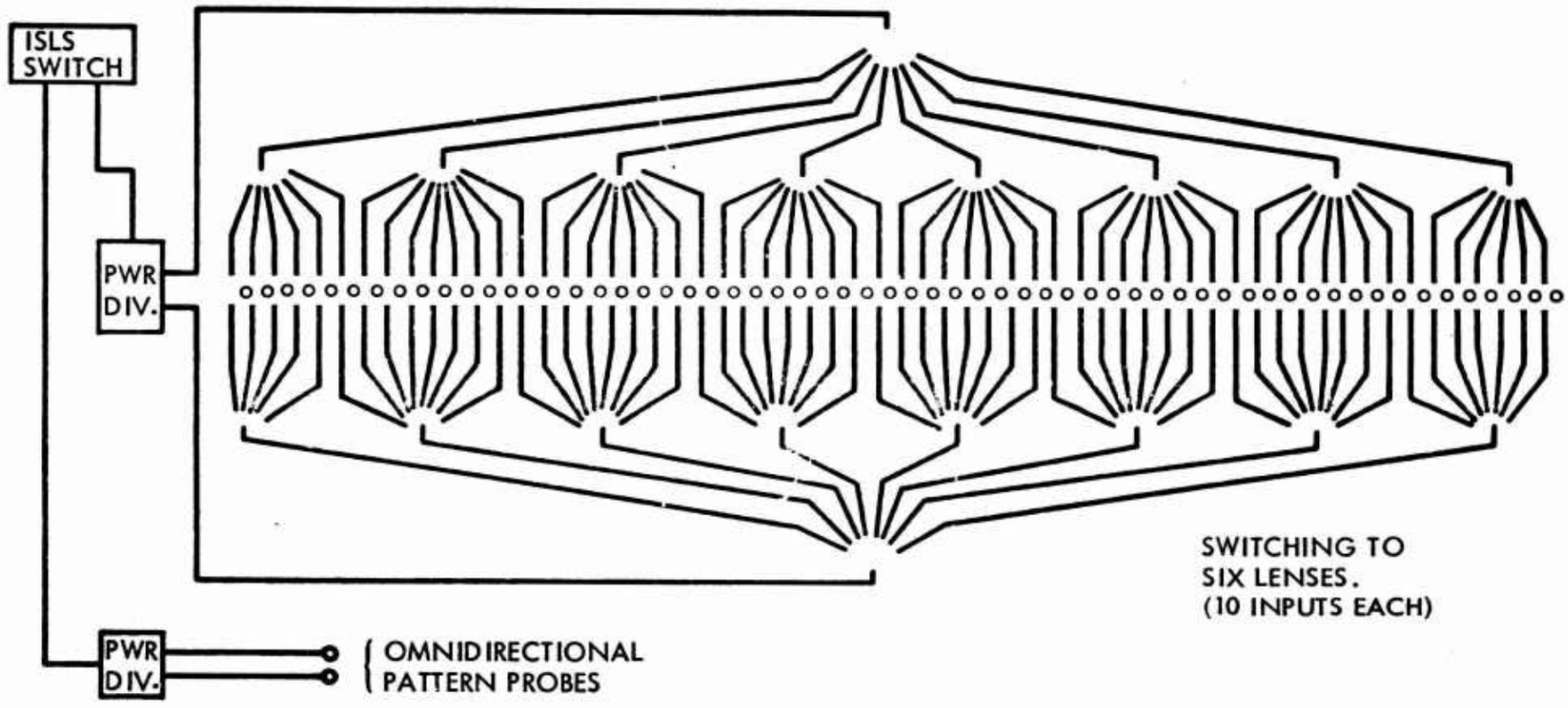
ISLS SWITCH
PWR DIV.
PWR DIV.
OMNIDIRECTIONAL PATTERN PROBES
SWITCHING TO SIX LENSES. (10 INPUTS EACH)

SLIDE FIVE

COMPARISON OF TWO ANTENNAS

	20' DIA.	10' DIA.
OUTSIDE DIAMETER	20'	10'
INSIDE DIAMETER	16'	7'
HEIGHT OF RING ARRAY	18"	18"
WEIGHT OF ARRAY	1200 LBS.	800 LBS.
HORIZONTAL BEAMWIDTH	4.5°	7.2°
VERTICAL BEAMWIDTH	50° (APPROX)	50° (APPROX)
ISLS METHOD	SUM & DIFFERENCE	OMNI
NUMBER OF RF SWITCHES	248 SPDT	18 - SP8T, 68 - SPDT
TYPE OF RF SWITCH	MAGNETIC REED	DIODE
METHOD OF RF POWER DISTRIBUTION	POWER DIVIDER	RF LENS
NUMBER OF ENERGIZED RADIATORS	30	30
SWITCHED PATH MONITORING	YES	YES
TOTAL SWITCHING TIME (MICROSECS)	3000	3
BORE SIGHTING METHOD	OPTICAL	OPTICAL
INTERCONNECTION RF	1	1
CONTROL LEADS	207	80

SLIDE SIX

ELECTRONICALLY SCANNED DUAL-BEAM WULLENWEBER ANTENNA

William F. Gabriel
Delex Systems, Inc.
Vienna, Virginia

William C. Cummings
Scanwell Laboratories, Inc.
Springfield, Virginia

SUMMARY

This antenna system[1], shown in Figure 1 at the completion of its construction, consists of a 20 foot diameter antenna ring, two (2) R.F. scanner units, an electronics cabinet rack, and two (2) remote beam controllers. The antenna ring was deliberately designed for a large open-center configuration and disassembly into two halves in order to facilitate mounting around structures. The ring contains two (2) Wullenweber type circular arrays of 124 elements each which are stacked vertically and are designed to permit operation either individually or in coherent combination. When operated individually, each array has the following design characteristics:

a) Frequency band - 1000 to 1100 megacycles

b) Polarization - Vertical

c) Elevation beamwidth - 58°

d) Azimuth beamwidth - Selectable 4.5° or 8.8°

e) Antenna gain - 19 db (not including system loss)

f) System attenuation loss - 4.5 db

g) Sidelobe characteristics - 26 db on sum pattern and smooth skirt coverage on difference pattern.

---

[1] The antenna described in this paper was developed and constructed by Scanwell Laboratories, Inc., Springfield, Virginia, under Contract NObsr-95040 with Naval Ship Systems Command, Department of the Navy. Construction was completed in December 1968, but field measurements and acceptance tests had not been performed as of the submission date of this paper.

h) Azimuth beam positions - 124 equally spaced positions

i) Beam switching speed - 3 milliseconds between any two azimuth beam positions

The present beam switching speed permits a stepping rate of at least 62 beam positions per second. These positions may be selected in arbitrary sequence from among the 124 available in azimuth. If it is desired to sweep the beam continuously in one direction, there would be at least 30 complete azimuth sweeps per minute.

The array elements consist of probe-fed flared horns with chokes. These are visible in Figure 2. The chokes are necessary in the vertical plane in order to achieve low back-radiation and, also, to prevent excessive coupling between the upper array and the lower array. In the azimuth plane, the elements radiate as a circular array of vertical probes backed by a ground plane. The design was developed by modeling at S-band, so that the radiation patterns of the model will be shown if field measurements have not been completed by the time of presentation.

The elements are fed through a special network of R.F. cable and distributed R.F. switch boxes. It required a total of 4900 feet of aluminum jacketed, semi-rigid, coaxial cable to implement the feed network. Figure 3 shows one of the 94 R.F. switch boxes which are distributed around the inside of the antenna ring. Each box contains two (2) R.F. switches, SPDT, in which the switching elements consist of magnetically energized, mercury-wetted reed capsules.

The heart of the feed network is a device termed a "Pass-Around", which is contained in the R.F. scanner unit shown in Figure 4. It has 31 input ports, 31 output ports, and consists of 155 interconnected SPDT switches. Its function is to switch the input distribution of 30 element signals into the proper sequence at its output ports so that they will be transferred by the feed network to correctly illuminate the particular group of 30 elements required in forming a given radiated beam. The amplitude illumination tapers required for the selectable azimuth beamwidths are set up by a dual directional coupler power divider.

The electronics cabinet shown on the left in Figure 1 contains the binary bit switches, a 64 position electronic switch, buffer stages, code circuits, driver stages for the R.F. switches, pulse circuits, and power supplies. Beam steering is accomplished by feeding a seven-bit digital signal into the electronics cabinet from the remote beam controllers. The two controllers are visible in the right foreground of Figure 1. They permit automatic beam command control from external digital or synchro inputs, and they can also be switched into a manual stepping or slewing of the beams via a binary analogue-to-digital encoder.

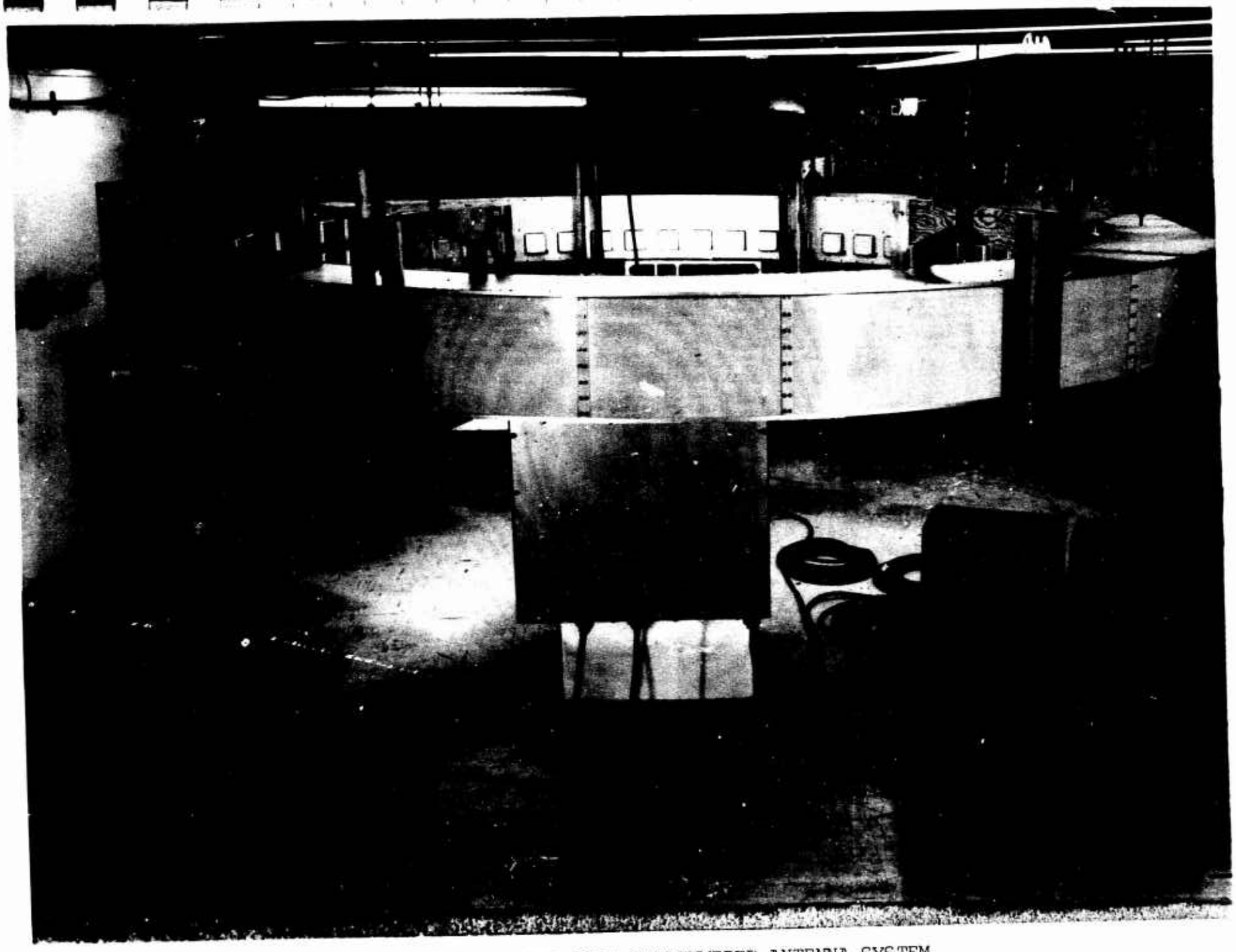

FIGURE 1 - IFF DUAL BEAM WULLENWEBER ANTENNA SYSTEM

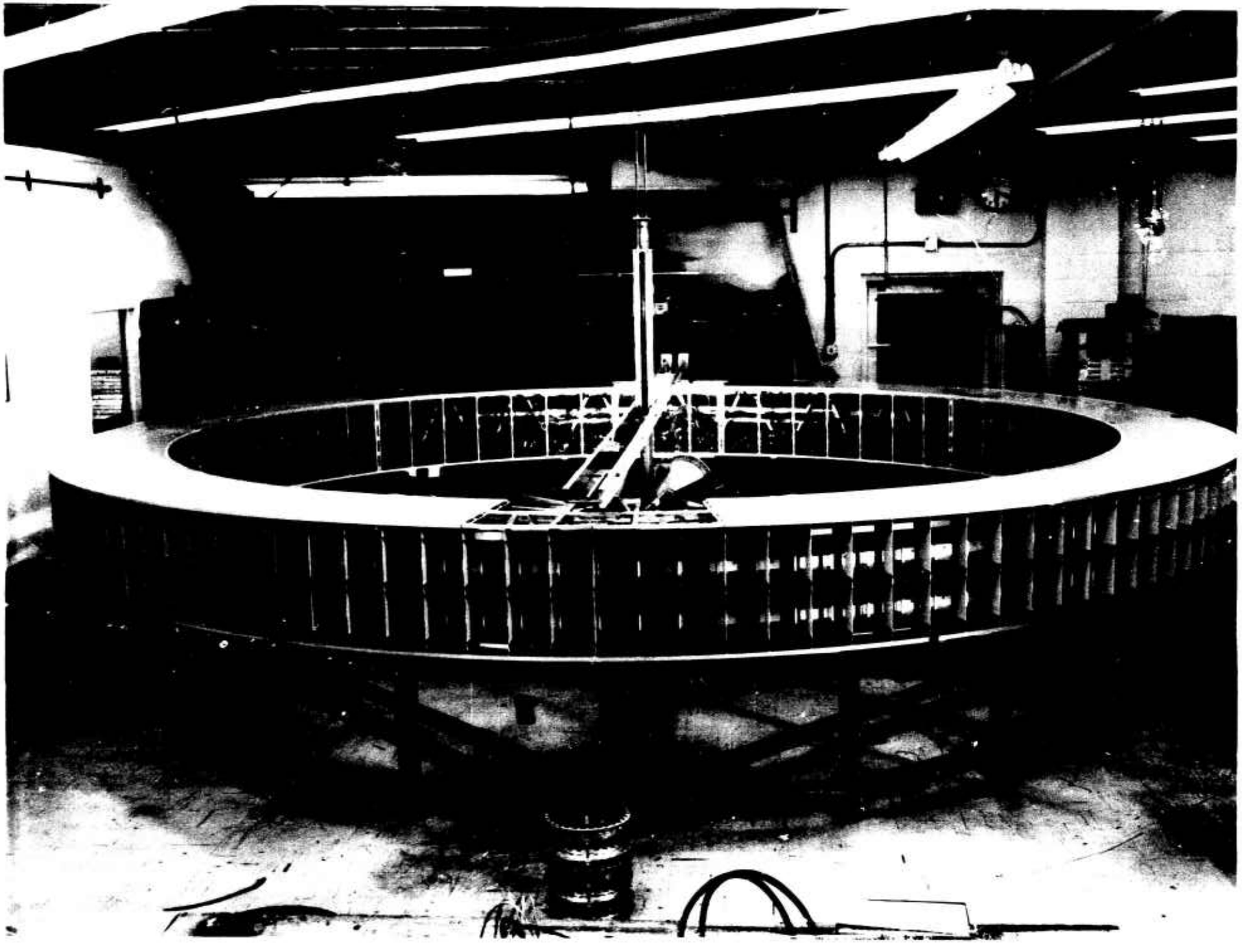

FIGURE 2 - ANTENNA RING WITH RADOME AND INSIDE COVER REMOVED

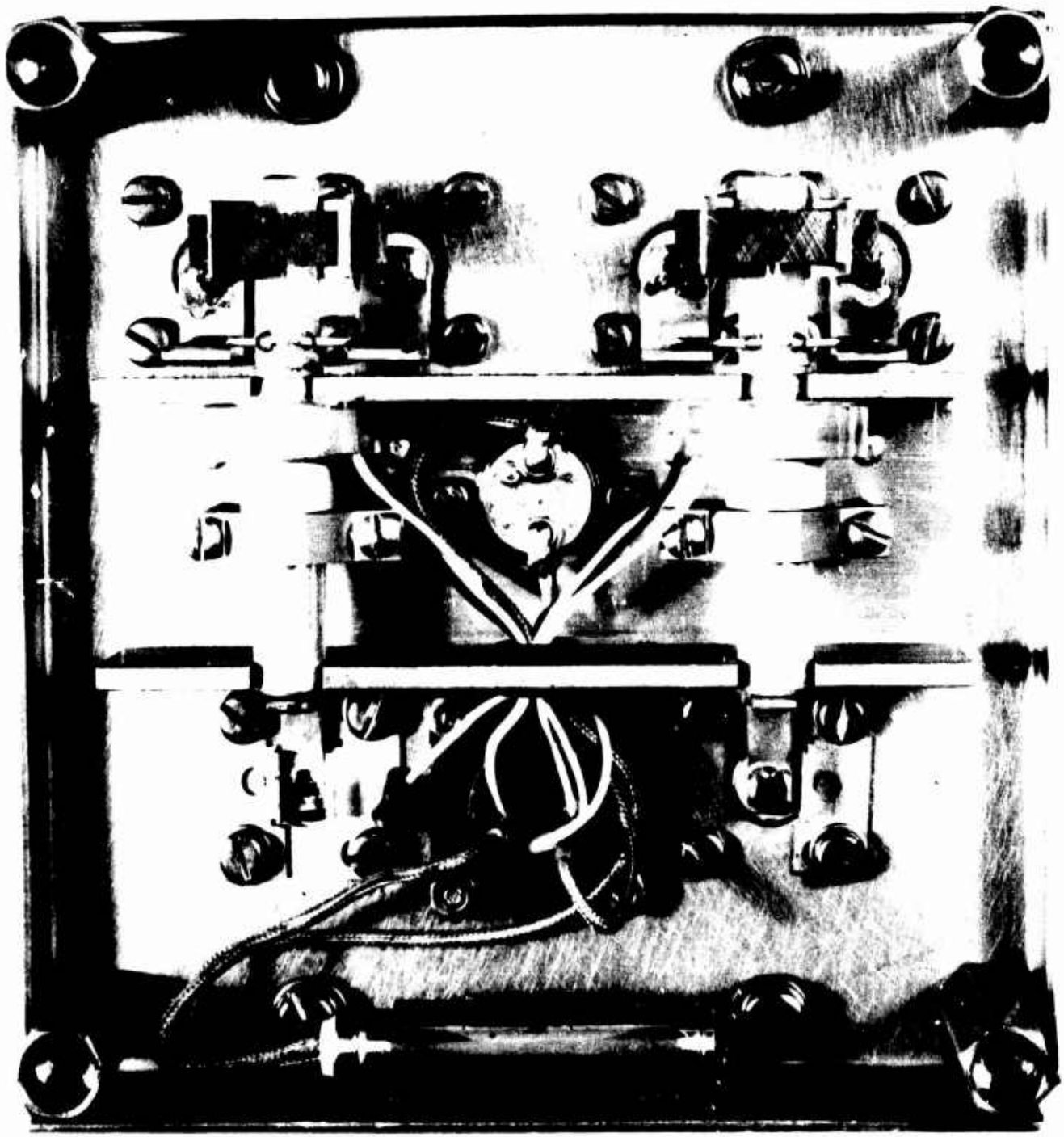

FIGURE 3 - RF SWITCH BOX WITH COVER REMOVED

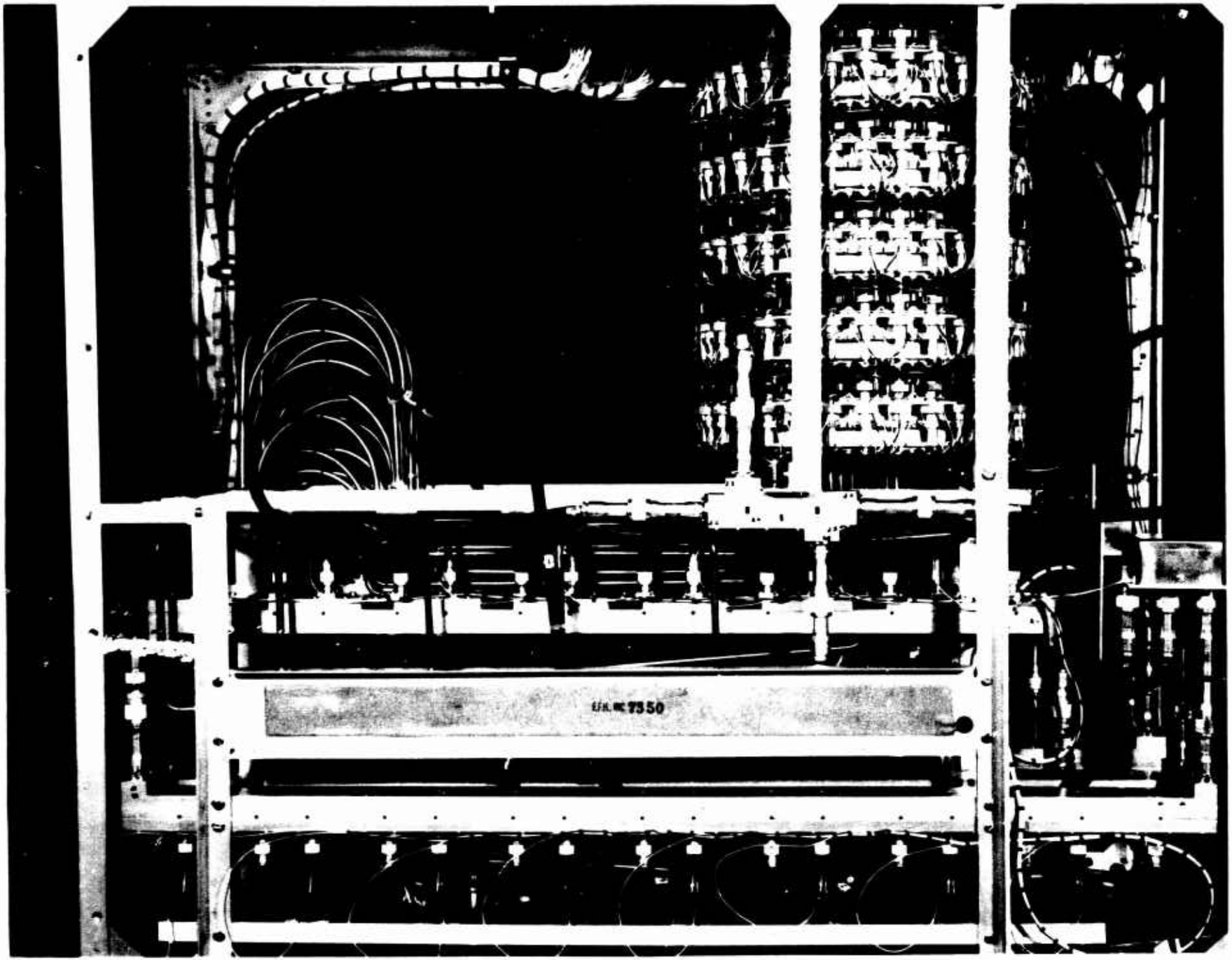

FIGURE 4 - SIDE VIEW OF UPPER ARRAY SCANNER UNIT

STEP-SCANNED CIRCULAR-ARRAY ANTENNA

by J. E. Boyns
C. W. Gorham
A. D. Munger
J. H. Provencher
J. Reindel
B. I. Small

U.S. Naval Electronics Laboratory Center
San Diego, California 92152

ABSTRACT

A circular-array radar antenna, designed for operation over a 20-percent bandwidth, has demonstrated improved performance over that of linear arrays. A major advantage is that the beam pointing angle is independent of frequency. The array developed and tested provides 128 beam positions with a beam crossover of about -2 dB, a half-power beam width on the order of 4 or 5 degrees, and a side-lobe level of -25 dB. Step increments of one element per beam position allow practical implementation of step scanning, i.e., simple commutation of the current distribution.

Two approaches are possible for feeding and scanning the ring array: (1) a vector-transfer system involving 3-bit phase and amplitude boards which are capable of amplitude attenuation (VT scan) and (2) a lens feed system employing an R-2R parallel-plate region, with the spacing between the plates less than one-half a free-space wavelength, so that only the electric-field component perpendicular to the plates is propagated. Energy is launched and extracted from the lens by means of monopoles mounted one-quarter wavelength in front of the circumferential ground plane enclosing the lens.

Computations involved in determining current distribution are based on a synthesis of Chebyshev patterns.

INTRODUCTION

It is well known that the radiation pattern produced by a planar or linear array deteriorates with increasing scan angle. To obtain 360-degree azimuth coverage from an electronically scanned array aperture, there are numerous advantages to the use of a circular array. When compared to a configuration of four linear arrays, for example, it can be shown that for the circular array the overall performance can be improved. Since the symmetry of the array is the same for all beam positions, the beam pointing angle is independent of the frequency. Numerous other advantages accrue depending upon the particular application.

Some of the problems involved with the design and implementation of the circular array are: (1) increased complexity in the mathematical analysis of the circular array as compared with the linear array; and (2) increased complexity in developing a feed system that both provides proper phase correction to a planar phase front and commutes the phase and amplitude distributions to step the beam. This paper describes some particular solutions to these problems.

The design goals of the array to be discussed here are: (1) 128 beam positions with a beam crossover of about -2 dB, (2) a half-power beam width on the order of 4 or 5 degrees, and (3) a side-lobe level of -25 dB. A step increment of one element per beam position will meet these goals and allow practical implementation of step scanning, i.e., simple commutation of the current distribution.

The project was undertaken in phases: (1) synthesis of current distributions and analysis of array performance with the aid of a high-speed computer; (2) development of a 128-element array; (3) development of a vector-transfer feed system and, independently, of a parallel-plate lens feed system, and (4) evaluation of the final experimental systems.

THEORETICAL CONSIDERATIONS

The first phase of this paper is concerned with some theoretical considerations involved in forming narrow-beam, low-side-lobe patterns from the ring-array aperture. It is well known that the Chebyshev pattern formulation for the linear array produces a pattern with the minimum beam width and lowest side-lobe level among all patterns which can be expressed as an N^{th} order polynomial. For the ring array, it cannot be proved that Chebyshev formulation is optimum, since the ring-array pattern is not expressible as an N^{th} degree polynomial. However, Chebyshev patterns can be synthesized on the ring-array aperture,[1] and the technique is useful for determining the current distribution required to form a good narrow-beam, low-side-lobe-level pattern.

Synthesis of Chebyshev patterns on the ring can be carried out by writing the pattern as a finite Fourier series of the form

$$T_N(\varphi) \sum_{n=0}^{N} C_n{}^N \cos n\varphi \qquad (1)$$

and finding the current modes, $I_n \cos n\alpha$, required to produce each component of the pattern. Only symmetrical patterns and current distributions are considered here. The synthesized current is a continucus distribution; approximation by discrete elements and the resulting pattern errors will be analyzed further on. The coordinate system is shown in figure 1. The frequency is ν and the radius is ρ.

Any element whose radiation pattern is expressible as

$$G(\varphi - \alpha) \quad K f(\theta) \sum_{m=0}^{\infty} F_m(\theta, \nu, \rho) \cos m(\varphi - \alpha) \tag{2}$$

can be used in the general synthesis problem. This expression gives the complex pattern in φ for an element located on the cylinder at the angle α. Assuming a continuous distribution of such elements excited by the current

$$I(\alpha) \quad \sum_{n=0}^{\infty} I_n \cos n\alpha \tag{3}$$

the far-field pattern is

$$E(\varphi, \theta) \quad \int_0^{2\pi} G(\varphi - \alpha) I(\alpha) d\alpha \tag{4}$$

Substituting equations 2 and 3 into 4, rearranging the summations, and noting the orthogonality of the resulting integral, we obtain

$$E(\varphi, \theta) = K f(\theta) \sum_{n=0}^{N} \frac{2\pi}{\epsilon_n} I_n F_n \cos n\varphi \tag{5}$$

Matching the coefficients of equation 5 with those of equation 1 yields the current mode amplitudes

$$I_n = \frac{\epsilon_n C_n^N}{2\pi K f(\theta) F_n(\theta, \nu, \rho)} \tag{6}$$

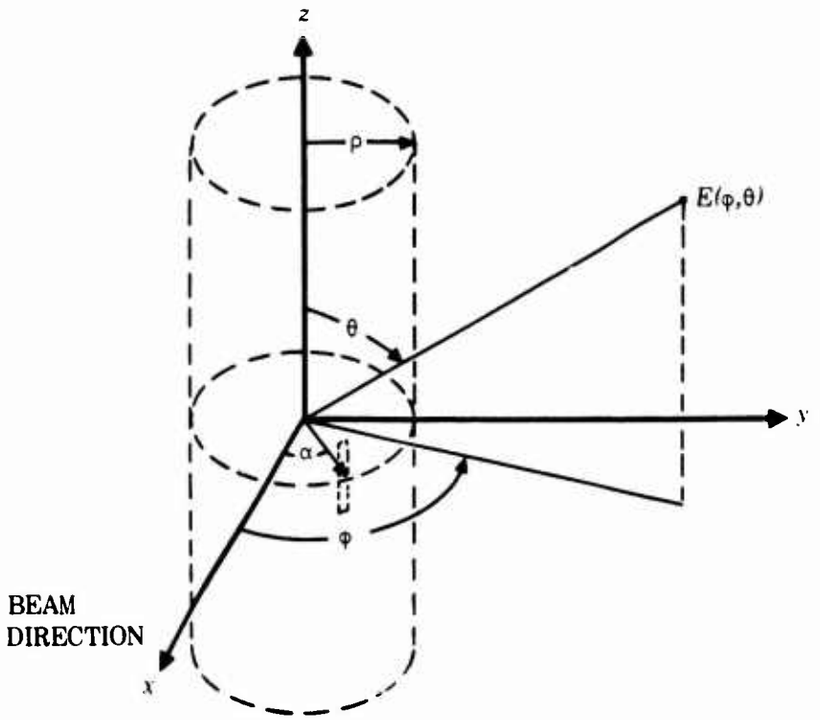

Figure 1. Coordinate system.

and the current

$$I(\alpha) = \sum_{n=0}^{N} I_n \cos n\alpha \tag{7}$$

where $\epsilon_n = 1$ if $n = 0$, and 2 if $n \neq 0$.

Now suppose that M identical elements are equally spaced on the cylinder at the angles

$$\alpha_p = \frac{2\pi}{M}(p + f) \tag{8}$$

where $p = 0, 1, \ldots, M-1$, and f is some fraction of the spacing that defines the location of the first element with respect to the beam direction $\alpha = 0$. Let the excitation currents be

$$I(\alpha_p)\Delta\alpha = \frac{2\pi}{M} \sum_{n=0}^{N} I_n \cos n\alpha_p \tag{9}$$

The far-field pattern due to the M elements is

$$E_D(\varphi) = \sum_{p=0}^{M-1} I(\alpha_p)\Delta\alpha\, G(\varphi - \alpha_p) \tag{10}$$

Substitution of equations 2 and 9 yield, after some manipulation,

$$E_D(\varphi, \theta) = K f(\theta) \sum_{n=0}^{N} \frac{2\pi}{\epsilon_n} I_n F_n(\theta, \nu, \rho) \cos n\varphi \tag{11}$$

$$+ K f(\theta) \sum_{n=1}^{N} I_n F_{M-n}(\theta, \nu, \rho)[\cos(2\pi f)\cos(M-n)\varphi + \sin(2\pi f)\sin(M-n)\varphi]$$

where we have assumed that $F_n = 0$ for $n > M$.

When the I_n's have been chosen by equation 6 and when we consider only symmetric element distributions ($f = 0$ or $f = \frac{1}{2}$),

$$E_D(\varphi,\theta) = T_N(\varphi) \pm K f(\theta) \sum_{n=1}^{N} \pi I_n F_{M-n} \cos(M-n)\varphi \qquad (12)$$

The positive sign applies when the first element is situated along the axis of the beam direction; the negative sign applies when the first and last elements straddle the beam direction. Expression 12 can be thought of as the desired pattern $T_N(\varphi)$ plus a "discrete error" which is due to the approximation of the continuous current distribution by discrete elements.

The Chebyshev polynomial is of interest because, of all polynomials of order N, it yields the minimum beam width for a given side-lobe level, or the minimum side-lobe level for a given beam width. In addition, it is a necessary and sufficient condition of the Chebyshev polynomial that all side lobes are equal. The polynomial is defined as

$$T_N(z) = \cos(N \cos^{-1} z) \qquad |z| \leq 1 \qquad (13)$$

$$= \cosh(N \cosh^{-1} z) \qquad |z| > 1$$

The pattern for a circular array can be obtained from the transformation

$$z = a \cos\varphi + b$$

where $a = \frac{1}{2}(z_0 + 1)$

$b = \frac{1}{2}(z_0 - 1)$

$z_0 = \cosh(N^{-1} \cosh^{-1} R)$

R = main-beam to side-lobe ratio (this ratio will be called L when given in dB)

The Fourier coefficients of the Chebyshev pattern may be computed exactly from the following:

$$C_n^N = \frac{\varepsilon_n}{2(N+1)}\left[R + (-1)^{N+n} + 2\sum_{i=1}^{N} T_i \cos\frac{n\pi i}{N+1}\right] \qquad (15)$$

where $T_i = T_N(a\cos\varphi_i + b)$

$$\varphi_i = \frac{\pi i}{N+1}$$

Exact expressions for the element patterns and their Fourier coefficients are available for various types of elements on a cylindrical ground plane. Computations for this study used an expression given by Wait[2] for a single axial slot on an infinitely high cylinder of radius:

$$G(\varphi - \alpha) = K f(\theta) \sum_{n=0}^{\infty} F_n \cos n(\varphi - \alpha) \qquad (16)$$

with $$f(\theta) = \frac{\cos(k\ell\cos\theta) - \cos k\ell}{\sin^2\theta}$$

and $$F_n = \frac{\varepsilon_n j^n}{H_n^{(2)'}(k\rho\sin\theta)} \frac{\sin\frac{n\alpha_0}{2}}{\frac{n\alpha_0}{2}}$$

where 2ℓ = length of slot

α_0 = angular width of slot

$k = \frac{2\pi}{\lambda}$

λ = wavelength

ρ = radius of cylinder

$H_n^{(2)'}(x)$ = derivative with respect to the argument of n^{th} order Hankel function of the second kind

When the amplitude pattern of the element is known, the complex F_n may be computed in the following manner if one assumes that the element has a point-phase

center on the circumference of the circle. Let g_n be the Fourier coefficients of the amplitude pattern $|G(\varphi)|$. The complex pattern can then be written

$$G(\varphi) = |G(\varphi)| \exp(jk\rho \sin\theta \cos\varphi) \tag{17}$$

$$= \sum_{n=0}^{\infty} g_n \cos n\varphi \sum_{m=0}^{\infty} \epsilon_m j^m J_m(k\rho \sin\theta) \exp(jm\varphi)$$

using the well known Bessel function expansion of the exponential. With some manipulation this becomes

$$G(\varphi) = \sum_{m=0}^{\infty} F_m(k\rho \sin\theta) \cos m\varphi \tag{18}$$

where $F_m(k\rho \sin\theta) = \dfrac{\epsilon_m j^m}{2} \sum_{n=0}^{\infty} j^n g_n [J_{m+n}(k\rho \sin\theta) + (-1)^n J_{m-n}(k\rho \sin\theta)]$

The curves of $F_n(\theta, \nu, \rho)$, from both the exact expressions for the element patterns, and from equation 18, are functions of the parameter $k\rho \sin\theta$. In general, it is true that the F_n converge rapidly for $n > k\rho \sin\theta$ and, except for isotropic elements, follow a reasonable smooth curve. The behavior of the magnitude for elements used in the experimental phase of this program is plotted in figure 2, computed from expression 16.

For synthesis of the continuous current distribution, only the first $N+1$ F_n are of importance (see equations 6 and 7). In order to restrict the magnitude of any single current mode I_n, N should be no larger than $k\rho \sin\theta$ so that the F_n do not converge in the region $n = 0$ to $n = N$. (The C_n^N are all of approximately the same order of magnitude.) A way of formulating this condition in terms of the radius

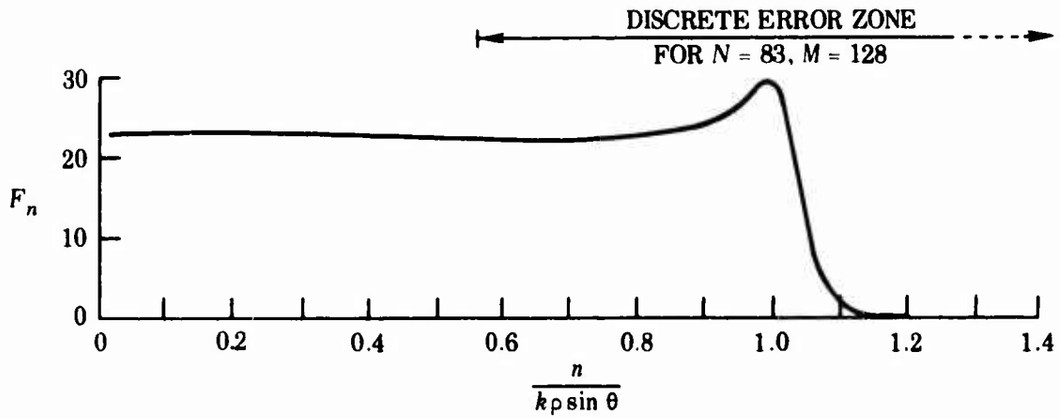

Figure 2. Magnitude of element factor F_n, with $k\rho \sin\theta = 83$.

is to avoid modes which require a phase shift between elements greater than their electrical separation along the arc of the circle. This again gives the requirement $N \leq k\rho \sin\theta$. This condition is necessary to avoid inefficient current modes (supergain) — that is, large currents that contribute little to the radiated pattern due to rapid phase shifts between elements.

It can also be shown that N times beam width is approximately constant for a given side-lobe level. Thus, to avoid supergain and yet maintain full aperture efficiency, one should have

$$N = k\rho \sin\theta \tag{19}$$

When the continuous current is approximated by M discrete elements, a discrete error arises as a result of the factor F_n over the range $n = M - N$ to $n = M$ (see equation 12). (In most practical designs, the F_n are negligible for $n > M$.) The discrete error can be reduced by requiring the F_n to be small in this range. With condition 19 in mind, we can consider the restriction $M = 2k\rho \sin\theta$ as being ideal; this will yield an interelement spacing of 0.5λ. For broadband systems, however, condition 19 should be satisfied for the lowest operating frequency so that $M = 2k\rho \sin\theta$ is not possible at midband. Hardware mounting requirements and mutual coupling problems also limit the minimum practical element spacing. Alternatively, the discrete error could also be reduced by decreasing N to a value less than the ideal. Hence, there is a trade-off between maximizing N and reducing the discrete error.

Figure 3 shows the results of the Chebyshev synthesis for $N = 40$ and $L = -28$ dB. The phase of the current

distribution is essentially beam cophasal out to 40 degrees, as should be expected. The uniform ripples beyond 40 degrees are due to the Chebyshev requirement of equal side lobes. Figure 4 shows the pattern as approximated by 128 elements, computed from equation 12. While the side lobes are above the -28 dB design level, they are still acceptable. Figure 5 shows the effect of increasing N and decreasing the side-lobe design level to -50 dB for a constant beam width at 4.7 degrees. While the inner side lobes are reduced to near the design level of -50 dB, the discrete error gives rise to a grating lobe. It can be shown that the position of this grating lobe is a function of the element spacing on the ring, in analogy to the linear array case. The element spacing for the array of figure 5 is about 0.65 wavelength. A spacing of about 0.5 wavelength would be needed to eliminate the grating lobe.

In practice it is not possible to implement the current distributions arrived at through the above synthesis. Furthermore, it would not be practical to excite elements in the back of the antenna, as they do not contribute to the main beam but only serve to excite side lobes in the back direction. In practice, then, one would use a beam cophasal distribution to excite an 80 or 90 degree sector of the ring with an amplitude taper approximating that of figure 5, which when smoothed is close to a $\cos^{6}\alpha$ amplitude taper. This yields a beam width of about 5 degrees and side-lobe level limited in practice only by the errors of implementation.

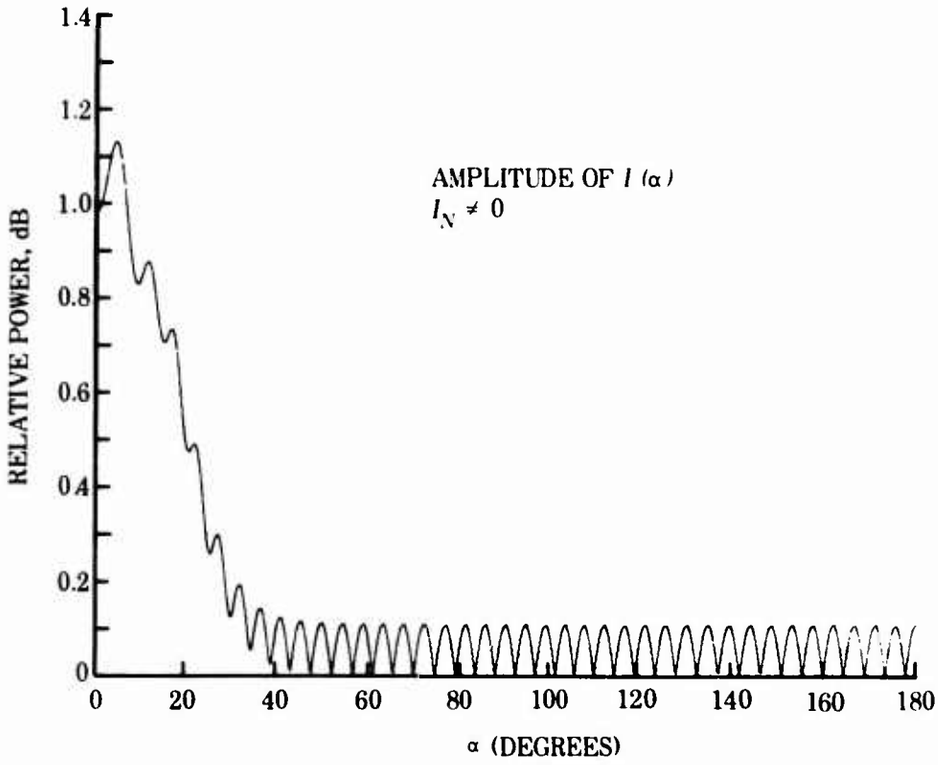

Figure 3. Amplitude of current synthesized for $N = 40$, $L = -28$ dB.

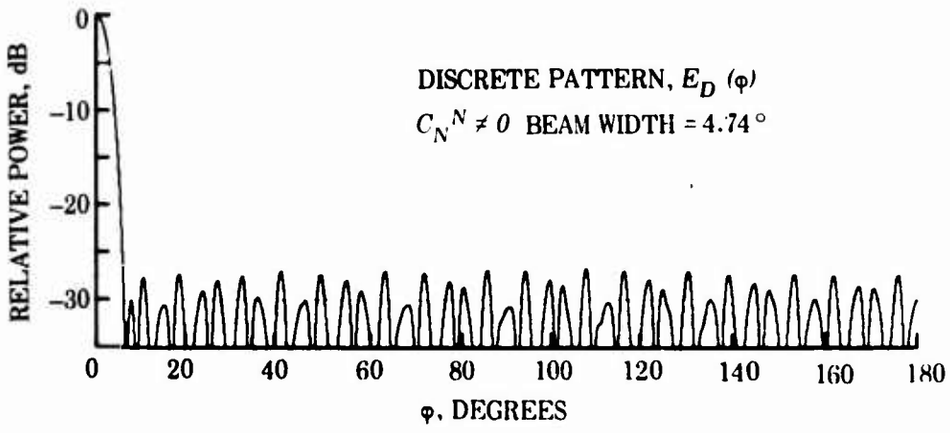

Figure 4. Pattern for approximation of continuous current distribution by 128 elements.

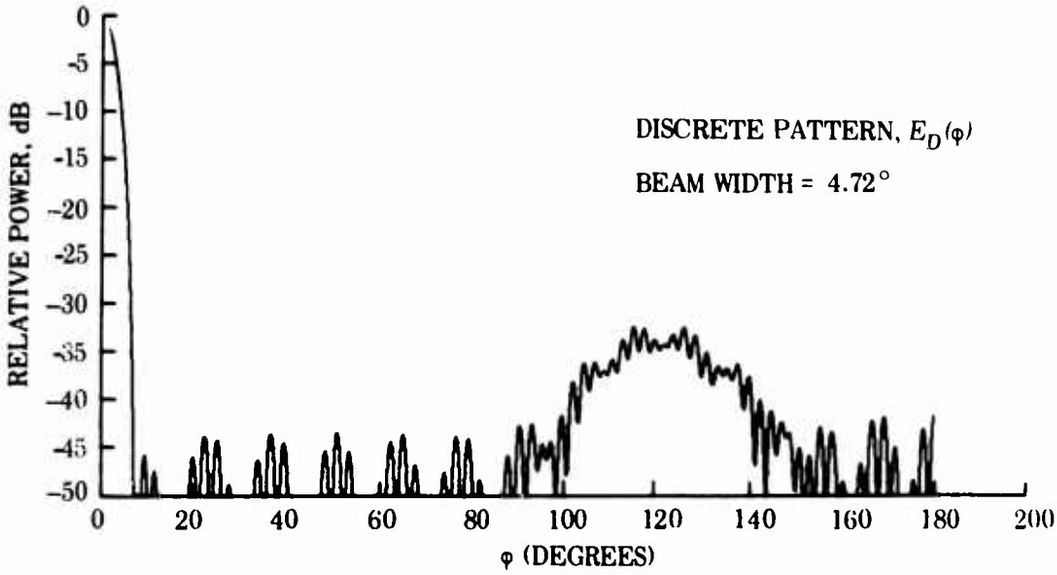

Figure 5. Pattern for N = 50, L = -50 dB distribution approximated by 128 elements.

THE EXPERIMENTAL SYSTEMS

RING ARRAY

The ring array designed and constructed for the experimental circular-array program is shown in figure 6. The array consists of 128 radiating elements equispaced at 0.65 wavelength and embedded in a ground plane of 13.2-wavelength radius at the center frequency f_0. The radiating elements are sectoral horns with a length of approximately 3 wavelengths and an aperture of about ½ wavelength in the *E*-plane and 1½ wavelengths in the *H*-plane. The elements have a bandwidth of ±10 percent of f_0 with a voltage/standing-wave ratio (VSWR) less than 1.5:1. The minimum half-power beam width (HPBW) in the *H*-plane is 40°. The gain of the element is 10.4 dB at f_0. Mutual coupling between adjacent elements in the array was measured at -22 dB.

VECTOR-TRANSFER FEED SYSTEM

Two approaches are presented to solve the problem of feeding and scanning the ring array. The first method involves 3-bit phase and amplitude boards which are capable of amplitude attenuation (VT scan). On transmit, the power is equally divided 32 ways and fed to 32 vector boards. Each is connected to a single-pole, four-throw (SP4T) switch with equal-length cables running to four radiating elements separated by 90° as shown in figure 7. Any 32 adjacent elements can be fed at the same time since no two elements of a 90° (32-element) sector of the ring

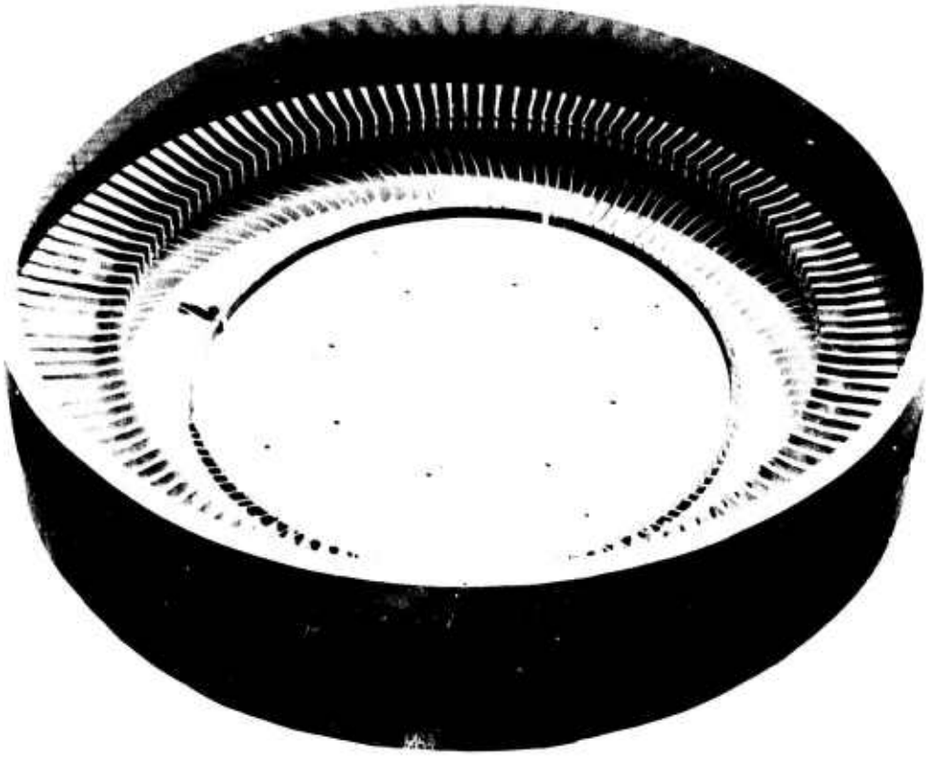

Figure 6. Ring array.

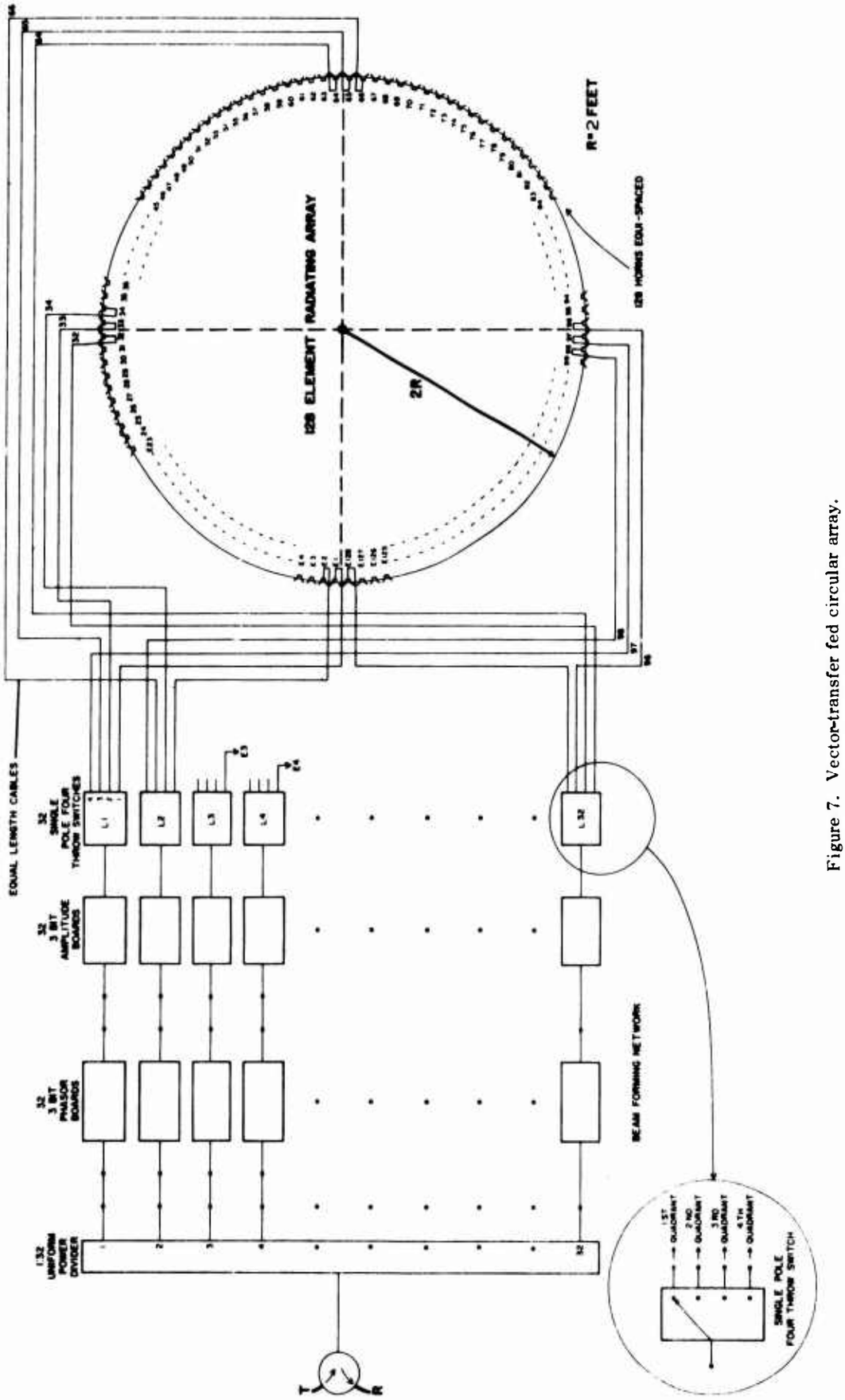

Figure 7. Vector-transfer fed circular array.

array are connected to the same vector board. The proper phase and amplitude are provided by the vector boards shown in figure 8.

The microwave SP4T transfer switches are built with shunt-mounted PIN diodes on stripline circuits. A SP4T switch is shown in figure 9. The circuit has the form of a corporate divider with shunt diodes placed at the junctions. The forward-biased diodes prevent transmission, the reverse-biased diodes permit transmission. Typically, a switch has a loss of 0.8 dB and a VSWR of 1.2:1 over the 20-percent band.

The vector boards consist of a 3-bit phasor and an attenuator, controlled by a 3-bit logic driver. The stripline circuit board has four cascaded hybrid couplers to which are connected four pairs of matched switches — three pairs for the phase switch and one pair for the attenuator.

The phasor circuit has been called the hybrid-coupled transformed phase shifter. It is widely used and has been fully described.[3] It is preferred over other circuits because it requires only two diodes per bit, has high-power handling capacity, is relatively simple, and has low loss.

The atten uator switch consists of a hybrid coupler that is terminated in a parallel circuit composed of a 50-ohm resistor and a diode switch. At low diode currents, the attenuation decreases as the diode current is increased in steps by a logic drive circuit. It is possible to eliminate the microwave resistor from the circuit and have PIN diodes absorb the power. However, it is more difficult

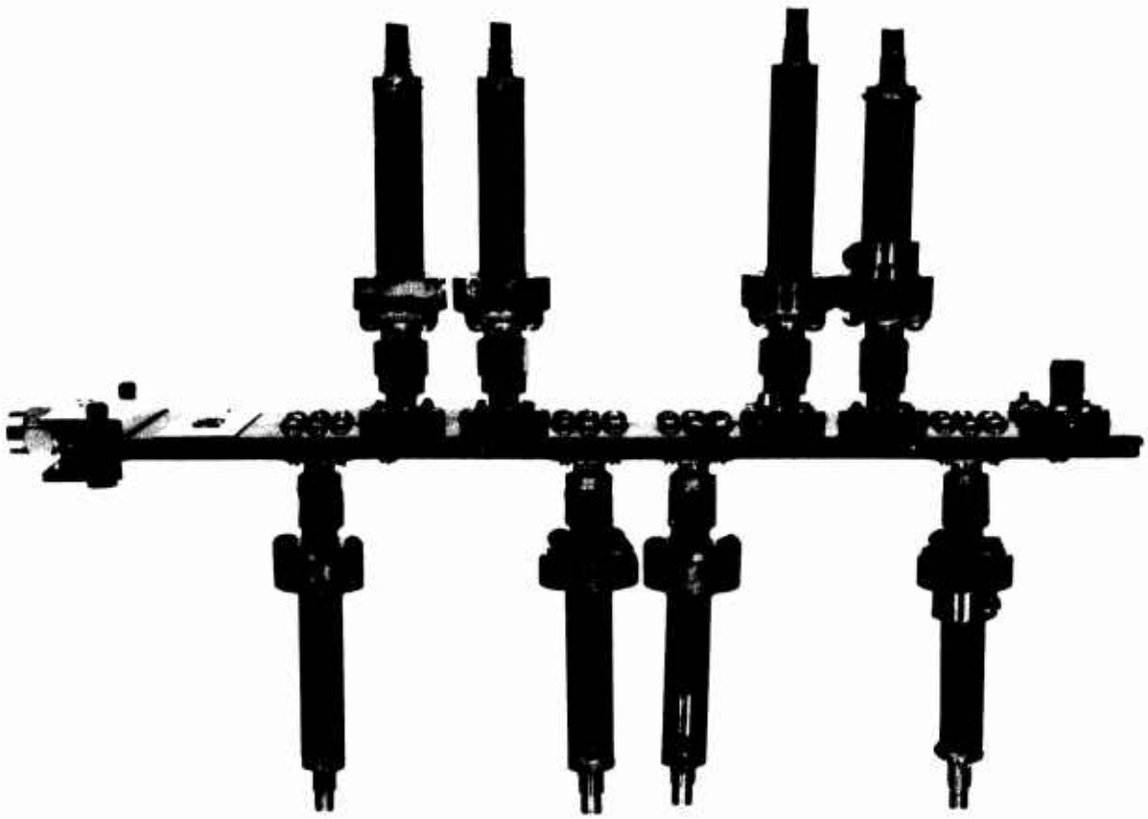

Figure 8. Vector switch with externally mounted diodes.

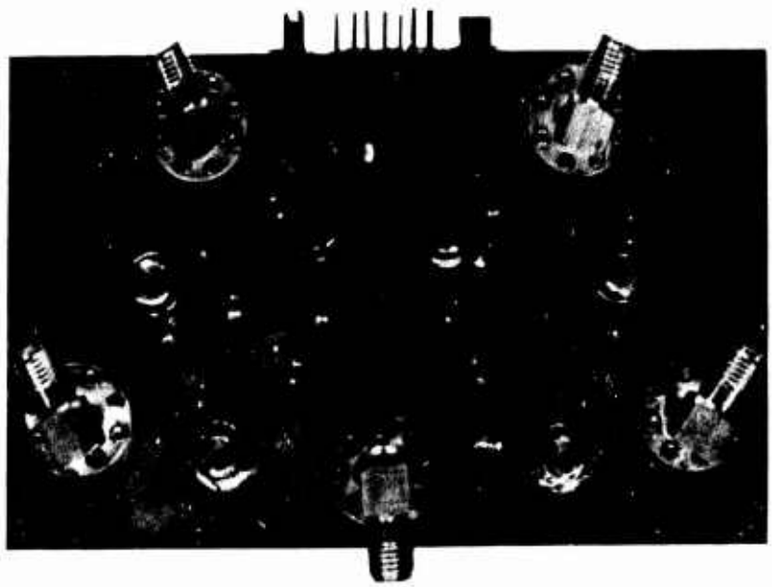

Figure 9. Single-pole, 4-throw switch.

to tune the circuit over the band without the resistor. The attenuation and phase shift of a hybrid-coupled attenuator are shown in figures 10 and 11. The vector boards and transfer switches are controlled by two shift registers. When the two registers are moved "n" places, the beam is stepped to the "n^{th}" beam position relative to the original.

Since amplitude taper is accomplished by attenuation, the amount of amplitude taper that can be practically used is limited. A $\cos^6\alpha$ taper gives about 3.5-dB loss in addition to the system loss. Computed patterns indicate that the three-bit phase approximation (45° steps) yields side lobes of -20 dB at best, when no errors are taken into account, and a HPBW of 3.7°. A slower taper with an overall attenuation of about 2 dB is shown in figure 12. For this taper, computed patterns indicate that -19 dB side lobes are available with HPBW of about 3.4°. Furthermore, approximation of the taper with eight discrete steps has negligible effect on the pattern but greatly simplifies implementation of the beam switching. Further computer studies indicated that the composite system errors are equivalent to random errors with a standard deviation of approximately 20°.

The above-mentioned vector boards could also be built with four bits at an increase in cost. Some patterns were computed on this assumption, with errors also considered, and the indications are that a four-bit phase quantization and a faster taper would significantly reduce the side-lobe level.

In summary, this method of feeding the ring array appears to have several desirable characteristics.

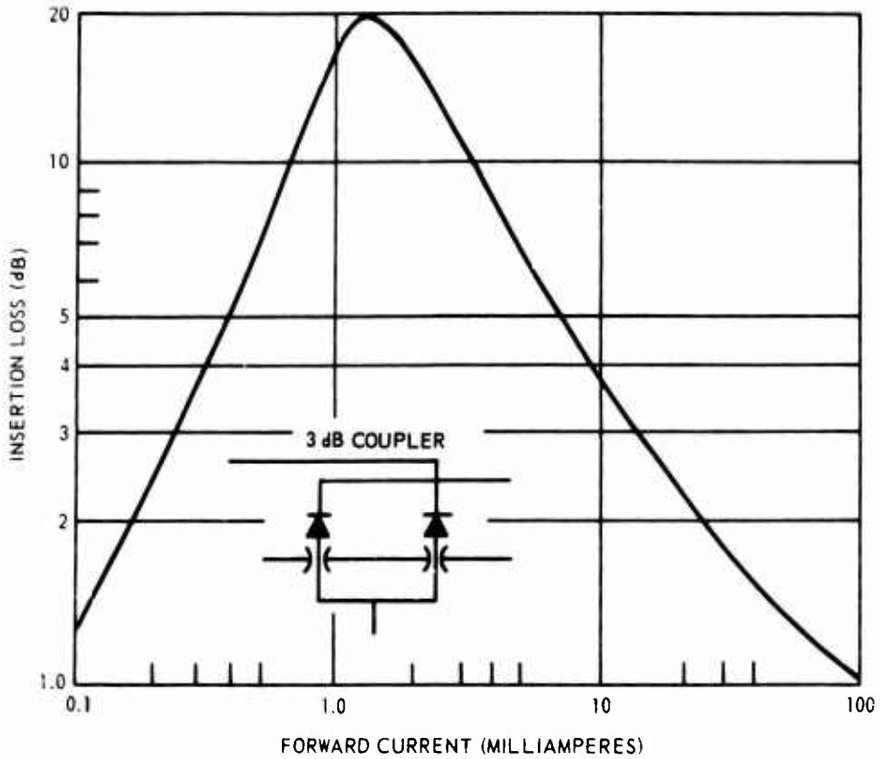

Figure 10. Dissipation loss of hybrid-coupled diode attenuator.

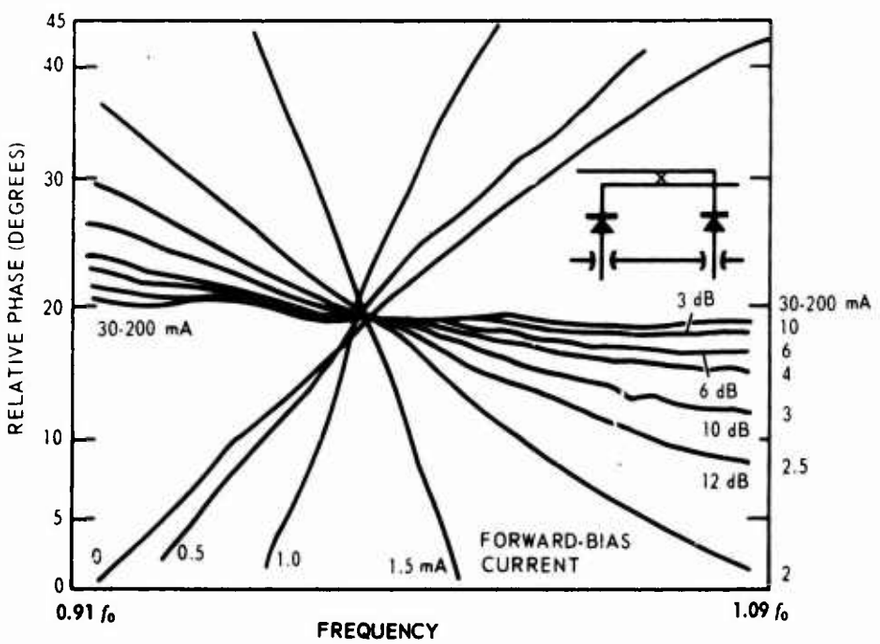

Figure 11. Phase shift of hybrid attenuator.

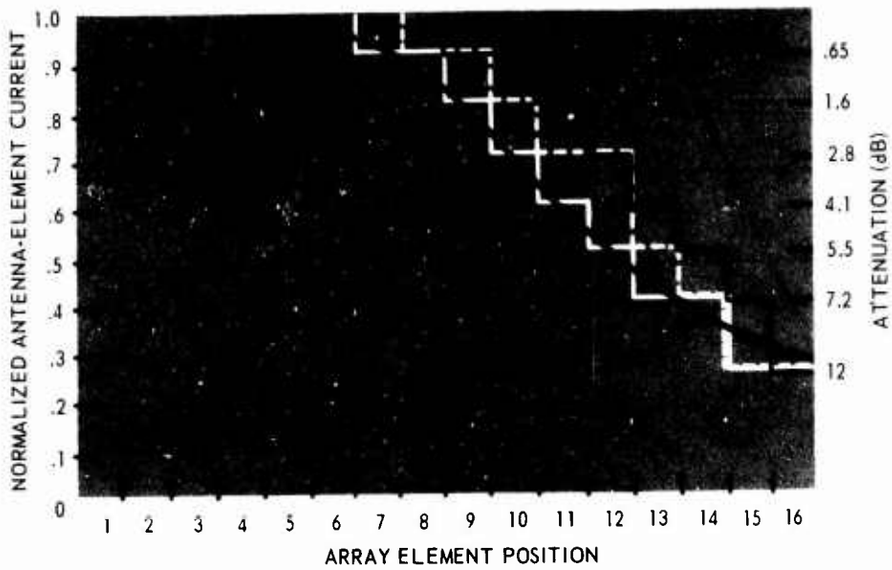

Figure 12. Amplitude taper of vector-transfer assembly.

First, in terms of power-handling capacity, the system allows the power to be divided into 32 equal parts; therefore, each component is required to handle only the power that is radiated by a single element. Second, a high degree of flexibility is achieved by having independent control of the phase and amplitude of each element in the excited sector. For example, the attenuators can be switched out during transmission to minimize transmission losses, and later switched to form a low-side-lobe beam for reception only; or, the phasing of all elements can be advanced an equal amount between transmission and reception (or from pulse to pulse) to redistribute the random errors and thus reduce the total apparent side-lobe level. Sum and difference can easily be obtained by dividing the input power dividers.

R-2R PARALLEL-PLATE LENS FEED SYSTEM

Another method of feeding and scanning the ring array can be referred to as an R-2R parallel-plate lens feed system.[4] The lens is a parallel-plate region of radius R, with the spacing between parallel plates less than ½ a free-space wavelength in order to propagate only the electric-field component perpendicular to the plates. Energy is launched and extracted from the lens by means of monopoles mounted ¼ wavelength in front of the circumferential ground plane enclosing the lens. From figure 13 it can be seen that energy introduced at a point "A" travels a distance $2R\cos\gamma/2$ when received by a pickoff probe at γ. For a beam-cophasal distribution on a ring array of radius ρ, the energy must be delayed a distance $\rho\cos\alpha$ for an

antenna element located at α measured from the beam direction. Thus the proper phase distribution will be provided by the lens if

$$R = \tfrac{1}{2}\rho \qquad (20)$$
$$\text{and } \gamma = \tfrac{1}{2}\alpha$$

The lens must be one-half the radius of the ring array as shown above. The lens angle will be twice the array angle if all the lens ports are used to illuminate one-half of the array aperture (180°). The illumination of the ring is accomplished with 64 equispaced probes on the lens, each switchable to one of two elements on the array separated 180° as shown in figure 14. Adjacent probes using equal-length cables must feed adjacent elements on the ring array.

The use of a single horn or probe is the usual method of feeding a parallel-plate lens, but this method provides little control over the amplitude distribution at the output terminals of the lens. A small linear array of probes, therefore, is fed to give a more directional pattern within the lens, and thereby a faster taper at the output probes. Good control of the amplitude at the output ports can be realized by varying the number of probes fed and also using an amplitude taper on their excitation. The probes are situated about ¼ wavelength in front of the enclosing ground plane so the pattern of a single probe at α can be approximated by $\sin\left[\frac{\pi}{2}\cos\frac{\gamma+\alpha}{2}\right]$, where α is measured from the center of the excited probes. The output of a probe at gamma can be roughly computed from

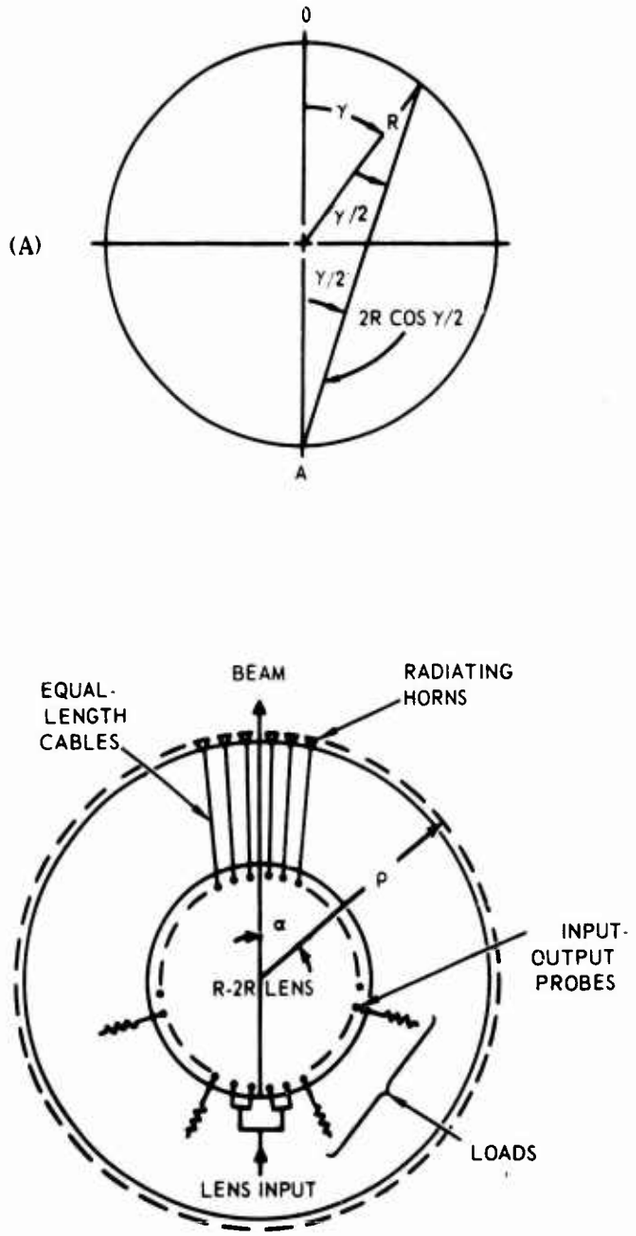

Figure 13. Parallel-plate lens: A, geometry; B, schematic of completed array.

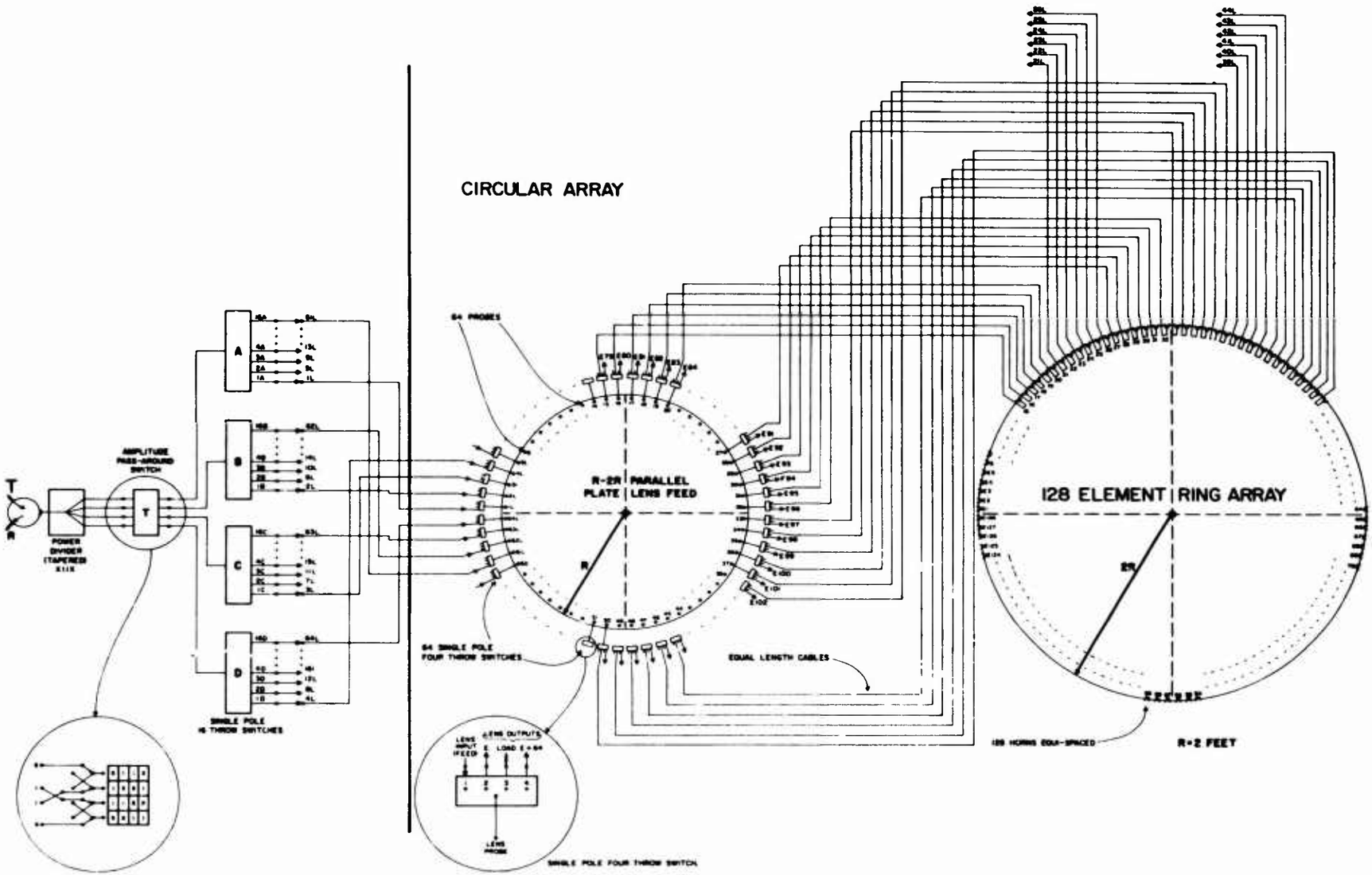

Figure 14. R-2R parallel-plate lens-fed circular array.

$$E(\gamma) = \sum_{\alpha} I(\alpha) \frac{\sin^2\left(\frac{\pi}{2}\cos\frac{\gamma+\alpha}{2}\right)}{\sqrt{2R\cos\frac{\gamma+\alpha}{2}}} e^{-j2\pi R\cos\frac{\gamma+\alpha}{2}} \qquad (21)$$

Figure 15 shows measured and computed phase distributions and figure 16 shows measured and computed amplitude distributions for feeding with $I(\alpha)$ = 1-2-2-1.

For the lens to properly function, it is necessary that internal reflections be minimized. Internal reflections can destroy the optical properties of the lens; thus, it is necessary to terminate nonactive ports in matched loads. Since each probe has a directional element pattern, it can only absorb all incident energy at normal incidence. At high angles of incidence — that is, for elements near the excited probes — most energy will be reflected. Therefore, the lens behavior is optimum when the primary probe array pattern is highly directional and has low side lobes. The 1-2-2-1 input amplitude distribution satisfies this criterion and gives near-optimum results. A discrepancy of the phase from the beam-cophasal curve resulted and can be interpreted as due to an apparent radius of the lens which is electrically smaller than the actual radius. It appears that the actual phase center of the probe radiators is slightly inside the lens rather than on the enclosing ground plane.

Three-hundred-sixty-degree azimuth beam steering is implemented by means of an SP4T switch at each input-output port of the lens. This switch selects one of the two radiating elements to which it is connected, a matched load when not active, or an input port when the probe is used to feed the lens. The SP4T switch has been previously

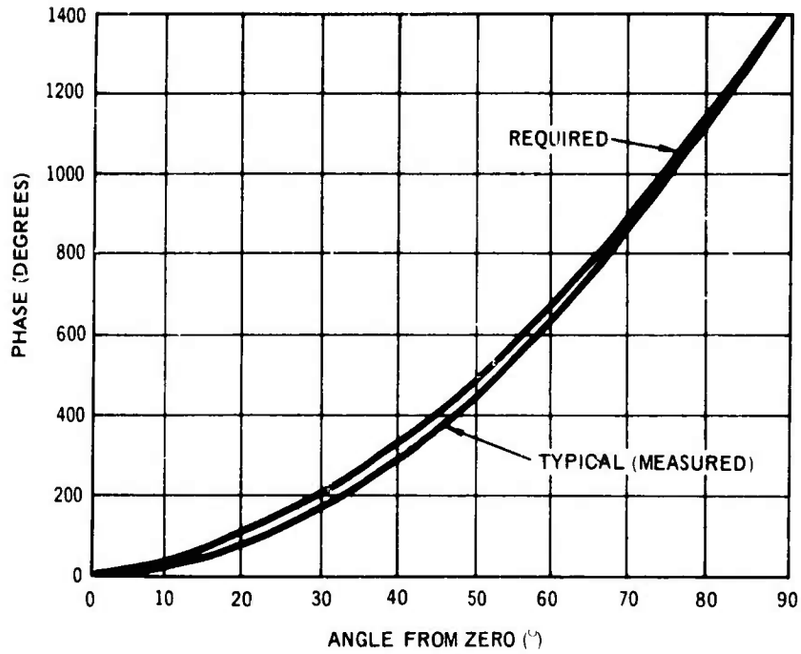

Figure 15. Measured and predicted phase distributions versus angle from beam direction.

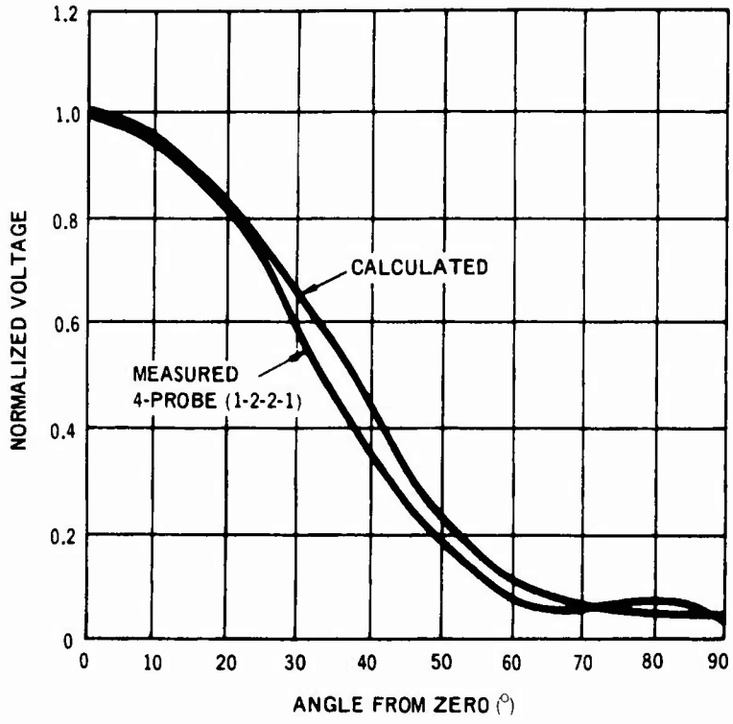

Figure 16. Measured and predicted amplitude distributions versus angle from beam direction for 1-2-2-1 input configuration.

described. A discussion of the double-pole, double-throw (DPDT) switch and the single-pole, sixteen-throw (SP16T) switch is given in detail in the following section.

SCANNING SWITCHES

DPDT Switches

The DPDT switches used in the parallel-plate fed system consist of a four-port transmission-line circuit and eight shunt diodes (fig. 17A). The four diodes in lines A and C are biased together and in opposite state to that of the remaining four diodes in lines B and D. Signals entering ports 1 and 4 are therefore transferred to either port 2 or 3. The effective circuit path for a single line is shown in figure 17B.

Isolation between the poles is obtained by two cascaded shunt diodes and is approximately 35 dB. The forward-biased diodes reflect open circuits at the circuit ports. The VSWR of the circuit was measured at less than 1.3:1. The insertion loss was measured at 1 dB.

SP16T Switches

The SP16T switches consist of five SP4T switches combined on a single stripline circuit board. The effective circuit path to any one of the 16 output ports is as shown in figure 18. The bandwidth of the switch is enhanced by spacing the diodes by ¼ wavelength.

The VSWR was measured at less than 1.5:1. The insertion loss was about 2 dB, and varied by ½ dB through the individual paths because of variations in diode characteristics. The circuit requires 30 diodes. Figure 19 is a photograph of an experimental SP16T switch.

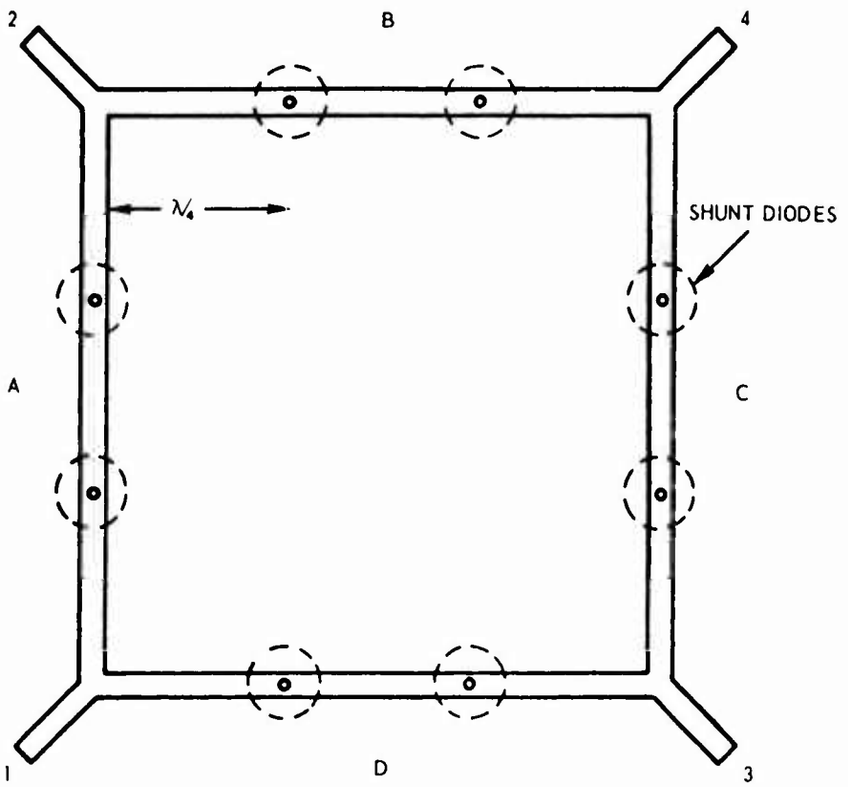

A. STRIPLINE CIRCUIT

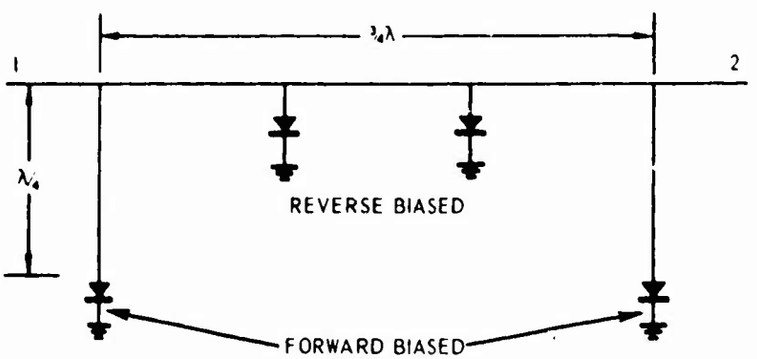

B. EFFECTIVE CIRCUIT PATH

Figure 17. Double-pole, double-throw switch: A, stripline circuit, B, effective circuit path.

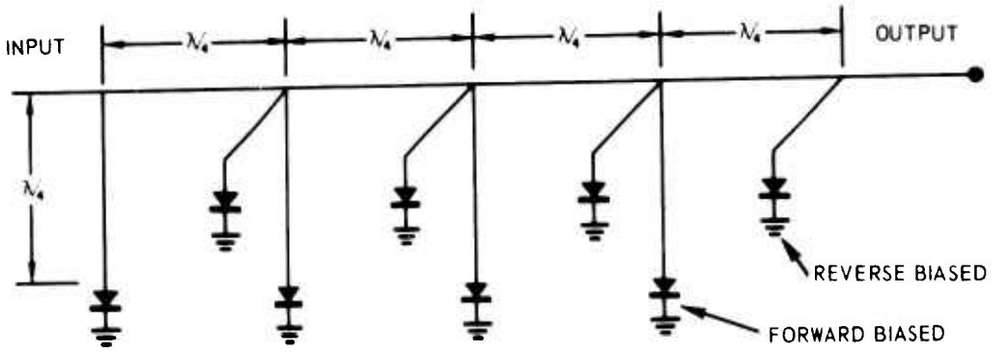

Figure 18. Equivalent circuit of SP16T switch.

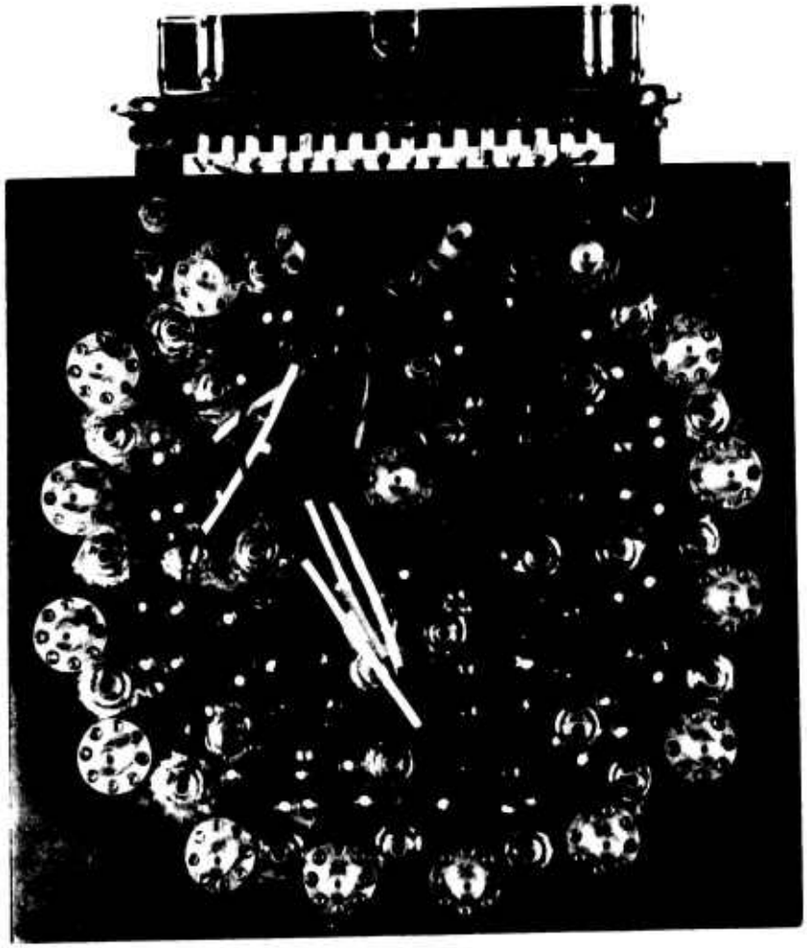

Figure 19. SP16T switch.

In summary, very-low-side-lobe patterns are achievable with the R-2R lens feed system. This is primarily a result of the optical characteristics and the amplitude-tapering techniques of the lens. The power-handling capability of this system is limited by the type of coaxial fitting used for the input-output ports on the R-2R lens. If a 1:4 power divider is used as an input to the lens to obtain the proper taper on the primary pattern of the lens input, each of the four probes must withstand one-quarter of the total input power. In principle the lens is an optical system, but an actual lens is bandwidth-limited because the probe must be maintained at about ¼ wavelength from the enclosing ground plane in order to provide a good match and to maintain a directional pattern in the lens. The use of ridged-waveguide techniques in the probe design will increase the effective bandwidth.

A partially implemented ring array fed with an R-2R parallel-plate feed system is shown in figure 20. Steering of the parallel-plate fed system was accomplished by manual switching. Computer control would be necessary for agile, rapid beam steering.

RADIATION PATTERNS

Predicted versus measured side-lobe levels and beam widths for the vector-transfer and parallel-plate feed systems with 32 elements illuminated are given in table 1. Figure 21 shows measured radiation patterns for the vector-transfer system, figure 21A being taken at 0.91 f_0, figure 21B at f_0, and figure 21C at 1.09 f_0. Figure 22A shows a measured radiation pattern taken at 0.91 f_0 for the parallel-plate

Figure 20. Partially implemented parallel-plate lens-fed circular array.

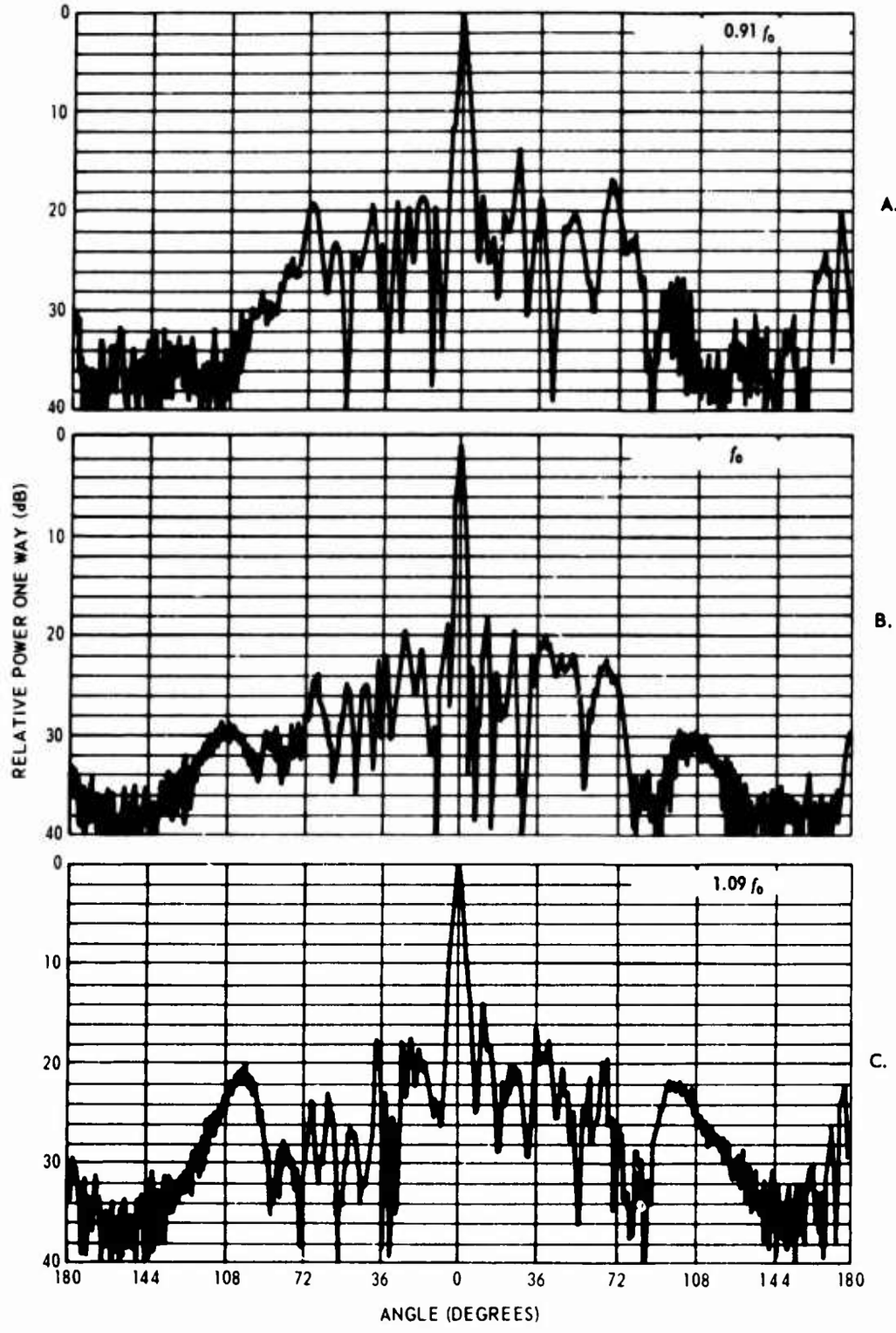

Figure 21. Measured radiation patterns for vector-transfer-fed circular array. Amplitude no. 2 (fig. 12).

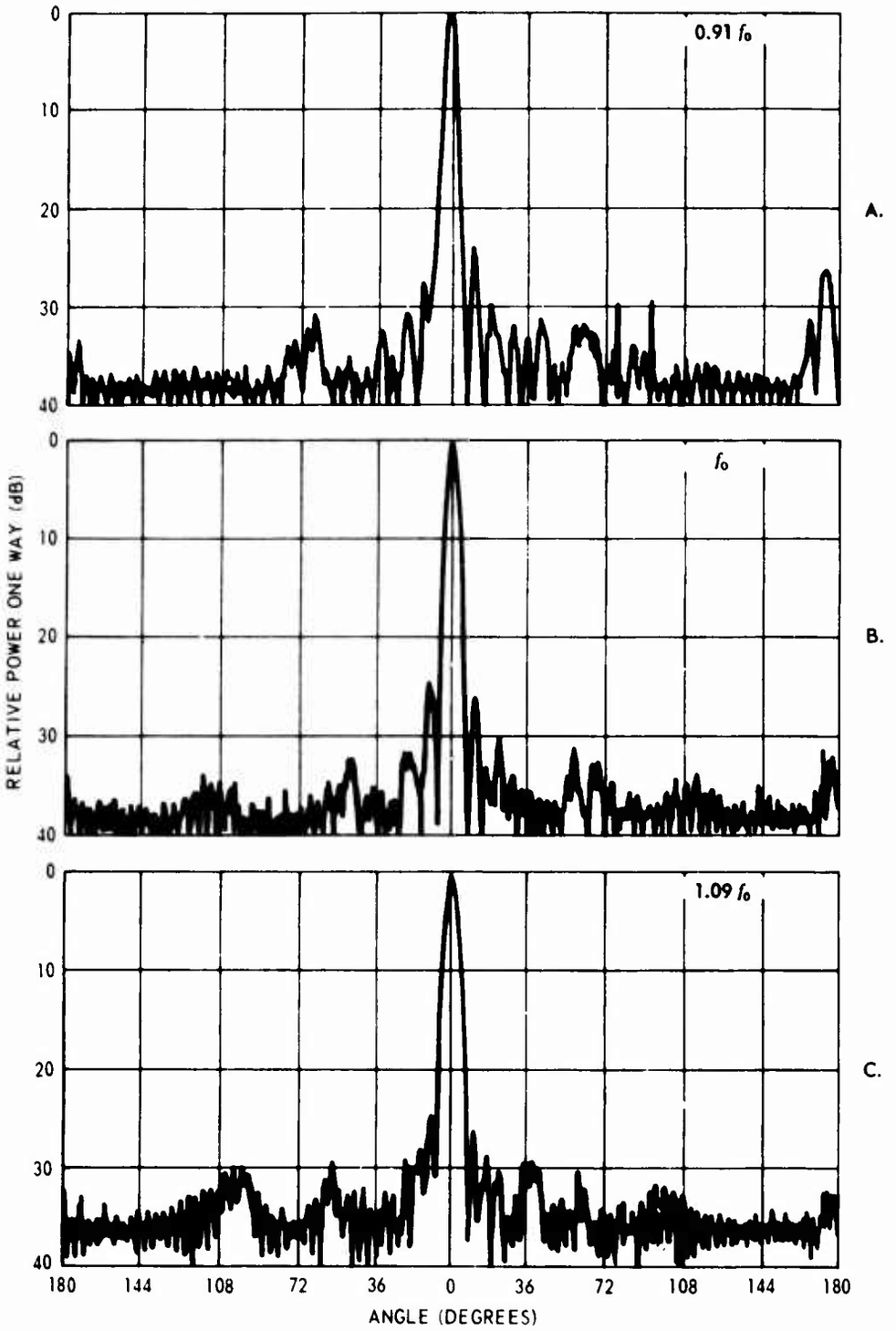

Figure 22. Measured radiation patterns for parallel-plate lens-fed circular array, 1-2-2-1 feed.

feed system. Figure 22B is a measured pattern at f_0, and figure 22C is a measured pattern at 1.09 f_0.

TABLE 1. PREDICTED AND MEASURED SIDE-LOBE LEVELS AND BEAM WIDTHS USING 90° APERTURE AND FREQUENCY = f_0

	Parallel-Plate Feed	Vector-Transfer Feed
Predicted (theoretical) side-lobe level	-28 dB	-19 dB
Measured side-lobe level	-24 dB	-18 dB
Predicted HPBW	5.98°	3.4°
Measured HPBW	5.2°	3.6°

CONCLUSIONS

Measured performance of both the vector-transfer and the parallel-plate feed systems compared favorably with computer predictions that take system errors into account. The largest source of error in both systems appears to be in the phase distribution scheme. The parallel-plate system gave the lowest phase errors and in addition is essentially true-time-delay. As a result it gave the lower side-lobe patterns and has a larger bandwidth capability. The vector-transfer system is to be preferred for high power-handling capabilities and lends itself to compact packaging. It also has a high degree of versatility for providing amplitude and phase distributions.

REFERENCES

1. Illinois. University. Electrical Engineering Research Laboratory Contract N6-ori-71, Task XV; Technical Report 16, Pattern Synthesis for Antenna Arrays on Circular, Elliptical, and Spherical Surfaces, by R. H. DuHamel, May 1952.

2. National Bureau of Standards Report 5553, Electromagnetic Radiation From Sources On and Near Cylindrical Surfaces, by J. R. Wait, 15 January 1958.

3. Burns, R. W., "PIN Diodes Advance High-Power Phase Shifting," Microwaves, v. 4, p. 38-48, November 1965.

4. Boyns, J. E., et al., "A Lens Feed for a Ring Array," Institute of Electrical and Electronics Engineers. Transactions: Antennas and Propagation, v. AP-16, p. 264-267, March 1968.

AN ELECTRONICALLY-SCANNED CYLINDRICAL ARRAY FOR IFF BASED ON A SWITCHING-AND-PHASING TECHNIQUE

Richard J. Giannini
Wheeler Laboratories, Inc.
Smithtown, New York

This paper describes the results of a study and measurement program which has demonstrated a technique for beam forming and electronic scanning of a cylindrical array antenna useful in IFF applications. The technique is based on a switching-and-phasing network which permits steering through 360° without beam distortion, and with steering increments much smaller than a beamwidth.

Various systems for feeding cylindrical arrays have been described recently in the literature. It is believed that the approach presented here is less complex than modal approaches for feeding cylindrical arrays (Refs. 1, 2), and allows more complete control of illuminations than lens approaches (Ref. 3). An IFF sidelobe-suppression difference pattern is easily provided with the present technique.

The switching network activates a contiguous set (usually 1/4 the total number) of the elements on the cylinder. The network consists of two parts; one part chooses the desired sector, and the other maintains the desired ordering of the elements. The switching network effects a "coarse" steering, moving the beam in angular increments corresponding to the element spacing (approximately 0.8 beamwidth steps). For any setting of the switches, phase tilt can be introduced by the phase shifters to provide "fine" steering. A distribution network is used to derive the aperture illumination as in the case of a linear array; fixed line lengths are used to correct for the curvature of the aperture. Sum and difference excitations are provided.

A schematic of the network used in a demonstration array is given in Fig. 1 for the case of 32 total elements with 8 elements activated at a time. In this case, the sector selection is provided by eight single-pole four-throw switches. The proper amplitude-and-phase ordering of the elements is maintained by the inter-connection of

1969 NOV 25

transfer switches, permitting cyclic permutation of the outputs from the distribution network. Phase shifters are included for fine steering; their location in the network requires as many phase shifters as there are excited elements. Eight phase tilt settings are provided in the demonstration model to obtain steering to 0.1 beamwidth. The distribution network is used to obtain desired sum and difference pattern illuminations. The excitations are then carried through the equal path-length switching network without distortion.

A photograph of the demonstration array model that was fabricated is shown in Fig. 2. This 32-element L-band array of dipoles around a 5 foot diameter cylindrical ground plane was selected to demonstrate feasibility of the technique. PIN diode switches and phase shifters, designed and fabricated in stripline, are used in the switching-and-phasing network which is contained within the cylinder formed by the ground plane. The control and biasing circuits are housed below the array, as seen in the photo.

Typical sum and difference patterns measured at 1030 Mhz are shown in Fig. 3. It was desired to provide a type of difference pattern which exceeds the sum pattern in the sidelobe region for an IFF sidelobe-suppression application. As seen in the figure, sum sidelobes are approximately 20 db below the peak, and the beamwidth is 16°, consistent with the 5-wavelength diameter antenna.

Fig. 4 shows scanned sum patterns for each of the 32 coarse steering positions offered by the switching network. In addition, the main beams for eight typical fine-steering positions are indicated (for clarity, only the top portion of each pattern is shown). Sidelobe suppression on the average is better than 20 db, and a minimum suppression of 17 db is observed. The latter is attributable to tolerance errors in cables and components for certain switching paths (no trimming was made after fabrication and initial measurements.) The level change at the peak of the patterns is partially the result of drift in the measurement equipment.

The feasibility of the switching-and-phasing technique for scanning a cylindrical array has been demonstrated. The principles may be directly extended to different size arrays. In general, with N total elements on the circumference of the cylinder and L excited

elements (L binary for purposes of the example), the number of sector ordering switches required to provide N coarse steering positions is $L/2 \log_2 L$. Simplifications in the switching network are possible when the number of beam positions are reduced. For $N/2^i$ beams, the number of sector ordering switches is given by, $(L/2)(\log_2 L - i)$. For the special case of uniform amplitude excitation, no sector ordering switches are needed. In all cases, L sector selecting switches with (N/L) throws are required.

For a 32-element array, 56 PIN diodes are required for the switches and 64 diodes for 4-bit phase shifters. If the modal approach, which is described elsewhere (Refs. 1, 2), were to be implemented for the same size array, 256 diodes would be required with 4-bit phase shifters.

This work was performed by Wheeler Laboratories supported as an in-house effort by the parent company, Hazeltine Corporation. C. Knowles contributed to the design effort and the measurements were performed by W. V. Polozzolo.

References

(1) W. Korvin, "Latest word in space talk: It can come from anywhere", Electronics, pp. 117-126; May 30, 1966.

(2) G. Sheleg, "Matrix fed circular array for continuous scanning", IEEE 1968 G-AP International Symposium, Program and Digest, pp. 7-9; Sept. 1968.

(3) J. E. Boyns, "A lens feed for a ring array", IEEE Transactions on Antenna and Propagation, Vol. AP-16, No. 2, pp. 264-267; March 1968.

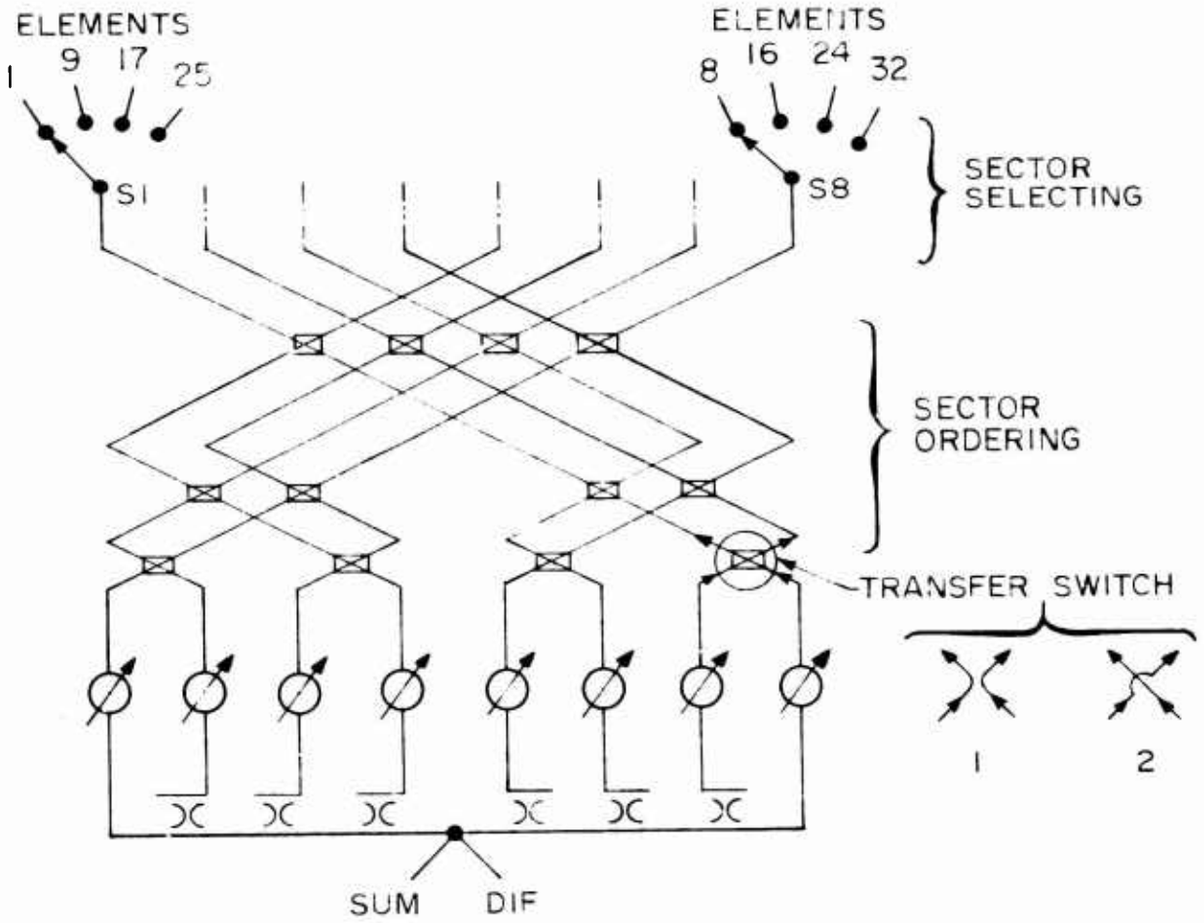

Fig. 1 - Schematic of network for 32-element array.

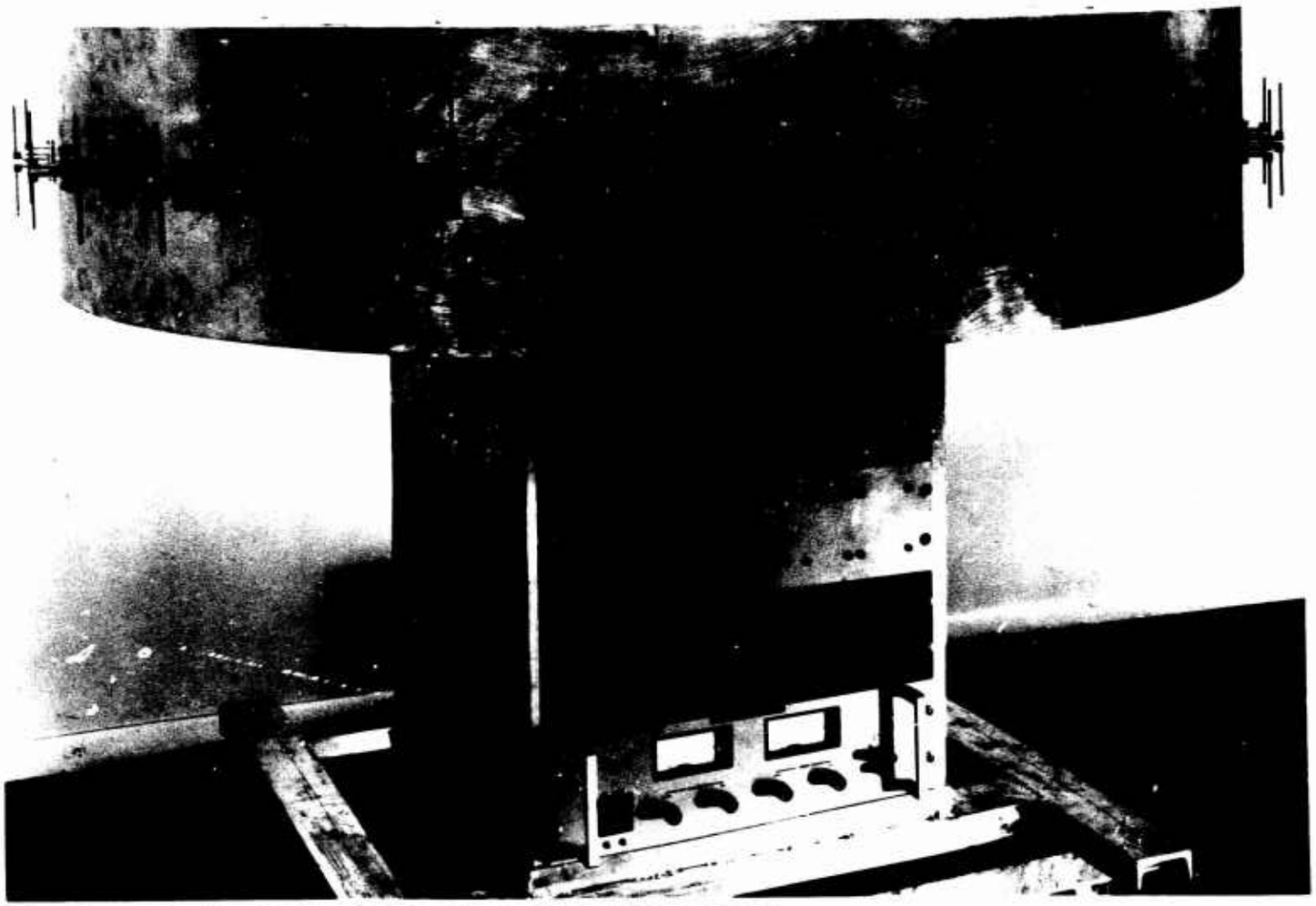

Fig. 2 – Photograph of 32-element L-band array.

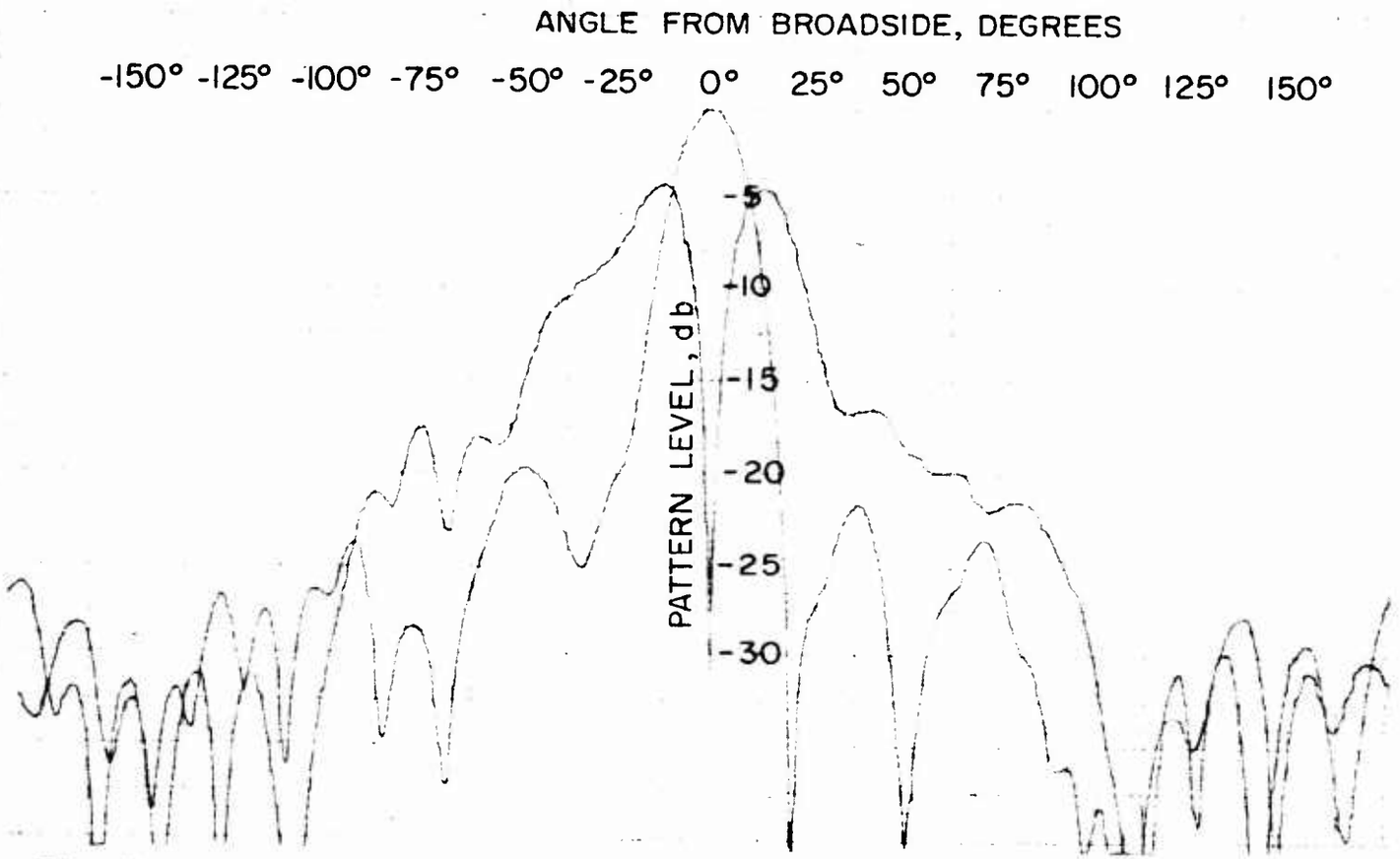

Fig. 3 - Sum and sidelobe-blanking difference patterns.

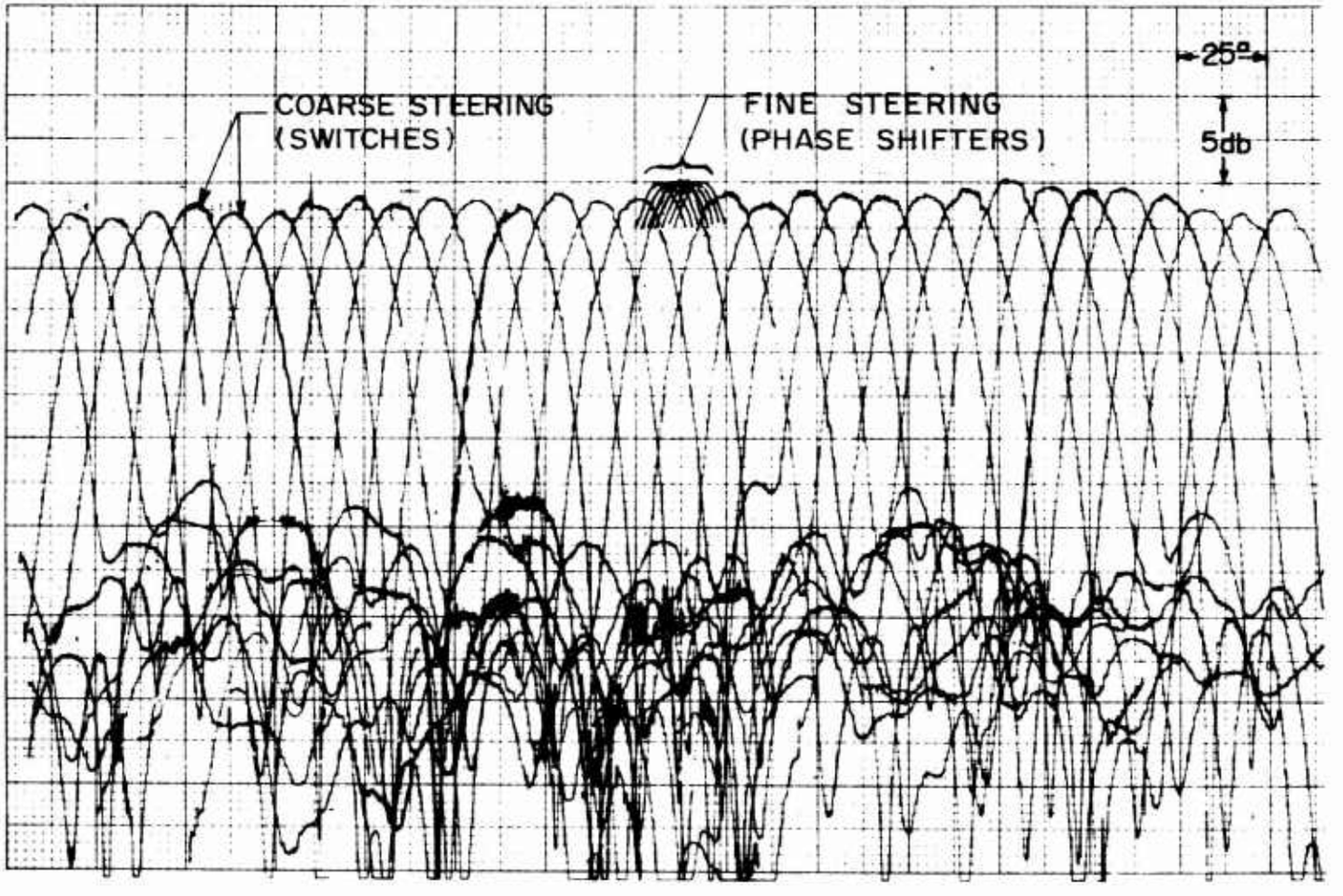

Fig. 4 — Scanned sum patterns.

AN ELECTRONICALLY SCANNED GEODESIC LUNEBERG LENS

by

R. P. Zimmer

Electronics Division
Georgia Institute of Technology
Atlanta, Georgia 30332

Introduction

In the field of radar antennas, the requirements and desired characteristics grow more sophisticated and diverse. No single method of antenna scanning serves all needs. The inertialess scan properties of phased arrays along with beam and scan flexibilities make their use appear attractive for many sophisticated radar systems. However, most linear or circular arrays employ complex networks consisting of power dividers, phase shifters, and beam-forming matrices. For many applications these complexities may be reduced by employing an electronically scanned geodesic Luneberg lens. Such a scanner would be a high-gain antenna with a step-scan agile beam and would represent an attractive alternative to many linear or circular phased array antennas.

A recent investigation at Georgia Tech entitled "An Inertialess Electronic Geodesic Scanner"[1] indicated that a rapid, 360 degree scan antenna could be developed by the design of feeds and switching networks to permit electronic scanning of a geodesic Luneberg lens. The system would employ two lenses, a secondary radiator and a switching network consisting of latching circulators arranged in a tree-type configuration. Although an inertialess antenna could be realized without employing two lenses, the use of two lenses

would result in characteristics superior to those of a system employing only one lens. Specifically, adjacent beam overlaps of less than 3 dB are readily obtainable only through the use of two lenses. In this paper, a brief description of the operation and performance characteristics of an electronically scanned geodesic Luneberg lens is given, and design considerations are presented for the various components and parameters of the antenna system.

Electronically Scanned Lens Concept

The geodesic Luneberg lens antenna consists of a pair of air-filled closely nested conducting surfaces of revolution which are parallel in the sense that their normal separation is everywhere constant. Such an antenna exhibits the property of transforming a point source on the periphery of the lens to a coherent line source which is tangent to the lens and located diametrically opposite the input. A suitable point source usually is realized by a flared horn feed, with a well-defined phase center. Its angular location along the periphery is arbitrary due to the symmetric properties of the lens. The feed radiation pattern is transformed by the lens to a corresponding aperture distribution at the lens output which in turn determines the far-field radiation pattern. This far-field radiation pattern generally exhibits high gain and low side lobes. A more detailed description of the geodesic Luneberg lens antenna and its characteristics is given by Johnson.[2,3] Although his analysis was based on a mechanically scanned geodesic Luneberg lens, it is also applicable to an electronically scanned lens.

Electronic scanning of a geodesic Luneberg lens consists of placing stationary feeds along the lens periphery and sequentially directing the input to the antenna to successive feeds through use of a microwave switching network.

Suitable microwave switches, appropriate switch configurations and suitable lens feeds are required for a practical antenna. Figure 1 shows a pictorial representation of an inertialess geodesic Luneberg lens antenna for sector scanning. For such an antenna, it is not possible to space feeds closely enough to achieve desirable overlaps of adjacent beams while maintaining a beam having high gain and low side lobes unless special techniques are used. As shall be seen, adjacent beam overlaps of less than 3 dB can readily be achieved with the use of two lenses.

For 360 degree scan, an array of feeds cannot be placed satisfactorily along the periphery of a lens without interference. The use of an alternative or secondary radiator which receives and re-radiates the energy from the lens results in an antenna system which does not have aperture blockage. Figure 2 gives a pictorial representation of such an antenna system. It consists of a beam positioning switching network, lens/radiator switches for switching between the lens and secondary radiator, a geodesic lens with feed horns and a secondary radiator with probe feeds. The switching network serves the same purpose as that shown in Figure 1 and is connected to a transmitter and a receiver through a duplexer.

With the aid of Figure 2, operation of the system during transmission can be explained as follows. A signal from the transmitter passes through the duplexer and enters the switching network. The switching network is of the proper state to route the signal to the selected lens/radiator switch which in turn is in the proper state to direct the signal to the desired lens feed. The signal radiated from the selected input feed propagates through the lens and enters the feeds in the opposite side of the lens. The lens/radiator switches associated with the output lens feed then route the signal to

corresponding probe feeds on the secondary radiator. Ideally, the aperture distribution of the lens will be transferred to the secondary radiator and its radiation pattern will be the same as that which would be obtained for radiation from the lens itself. On reception, the switches employed during transmission are repositioned so that the input signal to the secondary radiator is passed back through the lens to the selected lens feed and from there to the duplexer. Since the radiated system is circularly symmetric, the same principle of operation holds for any direction of propagation. Thus, as each feed around the periphery of the lens is sequentially activated, the radiated beam moves through the full 360 degrees. As in the sector scan case, the technique used for reducing the scalloping between adjacent beams beyond the 3-4 dB otherwise attainable, consists of using two geodesic lenses rather than one.

Figure 3 shows a basic mechanical layout of a full 360 degree scanner employing two lenses. The number of feeds used in each of the two lenses is such that the feed-to-feed spacing is 1.0λ; this spacing permits the use of a flared feed horn to obtain a desirable feed pattern from a single active feed. The secondary radiator has twice as many feeds spaced 0.5λ apart to achieve the required overlap. Probes are used for the feeds of the secondary radiator and every other probe feed is connected to the same lens; the two probes adjacent the active one are passive and act as parasitic radiators.

Conceptual and experimental studies of an inertialess scanner of the type shown in Figures 1, 2, and 3, were made at Georgia Tech and consisted of a detailed investigation of possible switching networks, feed designs, and mechanical layouts of the system. The mechanical layout shown in Figure 3 is only

one possible configuration; other combinations of circulators and interconnecting waveguide are possible to achieve further reduction in overall size and weight. However, the system as illustrated is composed mainly of conventional components which are commercially available and any significant refinement probably would have to be realized with specialized components. Designs of the lens itself were not studied implicitly because design techniques for geodesic lenses have been developed at Georgia Tech which should eliminate problems in this area.

Switching Network

The beam switching network of Figure 2 consists of microwave switches interconnected such that the rf signal path through the network can be changed rapidly and sequentially in a specified manner. Two general categories of switches may be used, the semiconductor type and the ferrite type. In general, the advantages of semiconductor switches are multi-throw capability and low switching times. Conversely, their disadvantages are high insertion loss, particularly at high frequencies, and low power-handling capability. Ferrite switches are limited to two or possibly three positions and require longer switching-times than semiconductor devices, but their power-handling capabilities are high and their insertion losses are low even at wavelengths extending into the millimeter region. Finally, ferrite switches are usually non-reciprocal, whereas semiconductor switches are reciprocal.

In analyzing switching networks which might be suitable for use in electronic scanning, several parameters need to be considered. These include the total insertion loss contributed by the network, the total number of switches required to implement the particular network, and the special switch characteristics required by the configuration.

Two simple and straightforward switch arrangements may be designated as the series and the pyramidal configurations. Each network may be made up of single pole, double throw semiconductor or ferrite switches. Alternate forms of the basic series and pyramidal configurations include a double pyramidal arrangement in which the signal follows a different path on transmission and reception; this switching network circumvents the requirement for switching between transmit and receive which arises when non-reciprocal ferrite switches are employed in the simple pyramidal configuration.

Although the lens antenna is potentially applicable to a wide variety of radar systems, the particular system in which it is to be used can impose restrictions on the switching network to be employed. For example, the use of semiconductor switches would probably be limited to low power systems and to systems operating at S-band or below since at higher frequencies the insertion losses currently attainable are not competitive with those of ferrite devices. Insertion loss limitations will normally restrict the simple series configurations to a scan-sector antenna or to an antenna with a large beamwidth in which only a few feeds are required. Where large numbers of feeds are required, some form of pyramidal arrangement is almost essential to achieve an insertion loss which is practical for system application. Consequently, for an X-band scanning antenna such as shown in Figure 3 ferrite switches arranged in a pyramidal configuration would normally be used; and latching circulators would be employed in radar applications requiring short switching times.

Parameters

If the shape of the beam radiated from an electronically scanned geodesic Luneberg lens is parabolic, then the expected adjacent beam crossover level

(scallop) may be determined from the equation

$$dB_s = 3\left(\frac{\Psi}{N \times \theta_B}\right)^2 \qquad (1)$$

where Ψ is the scan sector in degrees, N is the number of beam positions, and θ_B is the 3 dB beamwidth. Past experience at Georgia Tech has shown that the 3 dB beamwidth of a properly focused geodesic Luneberg lens depends on the effective lens aperture according to the empirical equation

$$\theta_B = 70\ \lambda/D \qquad (2)$$

where λ is the operating wavelength and D is the diameter of the effective lens aperture. The arc length between feeds is equal to the circumference divided by the number of probe feeds and, after combining Equations 1 and 2, the arc length is

$$S = 0.61\lambda\sqrt{dB_s/3} \qquad (3)$$

Hence, for a given scallop level, the required spacing is explicitly dependent only on the operating wavelength. Equation 3 is also true for any sector scan.

A frequency of 10 GHz and a scallop level of 2 dB were design parameters. From Equation 1, it may be determined that this scallop results in a 3.5° beamwidth for the case of 128 beam positions. Calculations using Equation 2 show that a lens diameter of 24 inches is required for a 3.5° beamwidth at 10 GHz. Equation 3 predicts a necessary spacing between feed positions of 0.5λ or 0.590 inch. If 128 beam positions were to be realized with a single lens and independent feeds, the required spacing would prevent the use of a flared feed which is desirable for good lens performance.

Although the spacing of 0.5λ required for a 2.0-dB beam overlap is impractical with a single lens, it is in effect realizable through the use of two geodesic lenses rather than one. If, as shown in Figure 3, half the number of feeds or 68 are located on each lens, the feed-to-feed spacing between lens feeds would be approximately 1.0λ. This spacing then would permit the use of a flared feed horn to obtain a desirable feed pattern. The spacing required to achieve the 2.0-dB scallop is effectively realized by employing on the secondary radiator probe feeds spaced 0.5λ apart with alternate probe feed connected to the feeds of each of the lenses.

Radiation Characteristics

Mathematical relationships between the radiation pattern of a feed and the corresponding far-field pattern for an inertialess scanner with and without a secondary radiator were derived. These relationships were used in evaluating the various feed designs. Each probe feed consists of a modified miniature panel connector mounted on one side of the radiator with the center conductor extending into the interior of the radiator. Each lens feed has a 1.20 inch aperture and an H-plane flare. Based on the patterns of these feed designs, anticipated characteristics of 360 degrees and 90 degrees, two-lenses, inertialess scanners were calculated and are listed in Table I. The overall diameter of a 360 degree scanner is equal to that of the secondary radiator since all the other components can be fitted within a circle of this radius. The total weight of switches is based on an existing latching circulator whose weight has not been minimized and the weight of the lenses assumes the use of conventional metalized, plastic materials for the lens surfaces. Both the size and weight of a sector scanner

would be significantly less than those of a 360 degree scanner since no secondary radiator would be needed and fewer switches and feeds would be required.

Concluding Remarks

In general, an inertialess geodesic Luneberg scanner has most of the advantages that cylindrical array antennas possess. These advantages include the following: (1) The beamwidth, side-lobe level, antenna gain, and cross-over points of adjacent beams are constant with scan angle, (2) the lens and secondary radiator components form a rotationally symmetric configuration which would facilitate simple manufacturing and production techniques, (3) the inherent broad bandwidth of a lens permits a wide operating frequency range, and other inherent properties offer mechanical ruggedness and operation over a wide temperature range.

In addition to the above, other advantages are that the beam positions are highly stable, the ferrite switches being two-state devices provide relative simplicity in electronic programming, and for X-band applications, the losses are relatively low.

REFERENCES

1. R. P. Zimmer, M. E. Wallace, and F. Q. Herschelman, "Inertialess Electronic Geodesic Scanner," Georgia Institute of Technology Final Technical Report on Contract DAAH01-67-C-0463, May 1969.

2. R. C. Johnson, "The Geodesic Luneberg Lens," Microwave Journal 5, 76, August 1962.

3. R. C. Johnson, "Radiation Patterns from a Geodesic Lunberg Lens," Microwave Journal 6, 68, July 1963.

TABLE I

ANTICIPATED CHARACTERISTICS OF INERTIALESS SCANNERS
EMPLOYING TWO LENSES

A. 360° Scanner

1. Electrical Characteristics

Frequency, GHz	10
Number of lens feeds	128
Secondary radiator required	Yes
Azimuth beamwidth	3.8°
Adjacent beam overlap, dB	2
Vertical beamwidth	20°
Minimum gain, dB	25
Maximum first side-lobe level, dB	20
One-way insertion loss, dB	2.85
Bandwidth, per cent	8
Maximum switching time, μsec	2
Peak power, KW	20
Average power, watts	100
Number of switches	256

2. Physical Characteristics

Size:

Height	20 inches
Lens diameter	24
Secondary radiator diameter	48
Overall diameter	48

Weight:

Switches (8 oz/ckt)	128 pounds
Waveguide and coaxial lines	40
Lenses	50
Secondary radiator	50
Total weight	268

(Continued)

TABLE I (Continued)

ANTICIPATED CHARACTERISTICS OF INERTIALESS SCANNERS
EMPLOYING TWO LENSES

B. 90° Sector Scanner

Secondary radiator required	No
One-way insertion loss, dB	1.6
Number of switches	32
Number of lens feeds	64
(Other characteristics same as those of 360° scanner)	

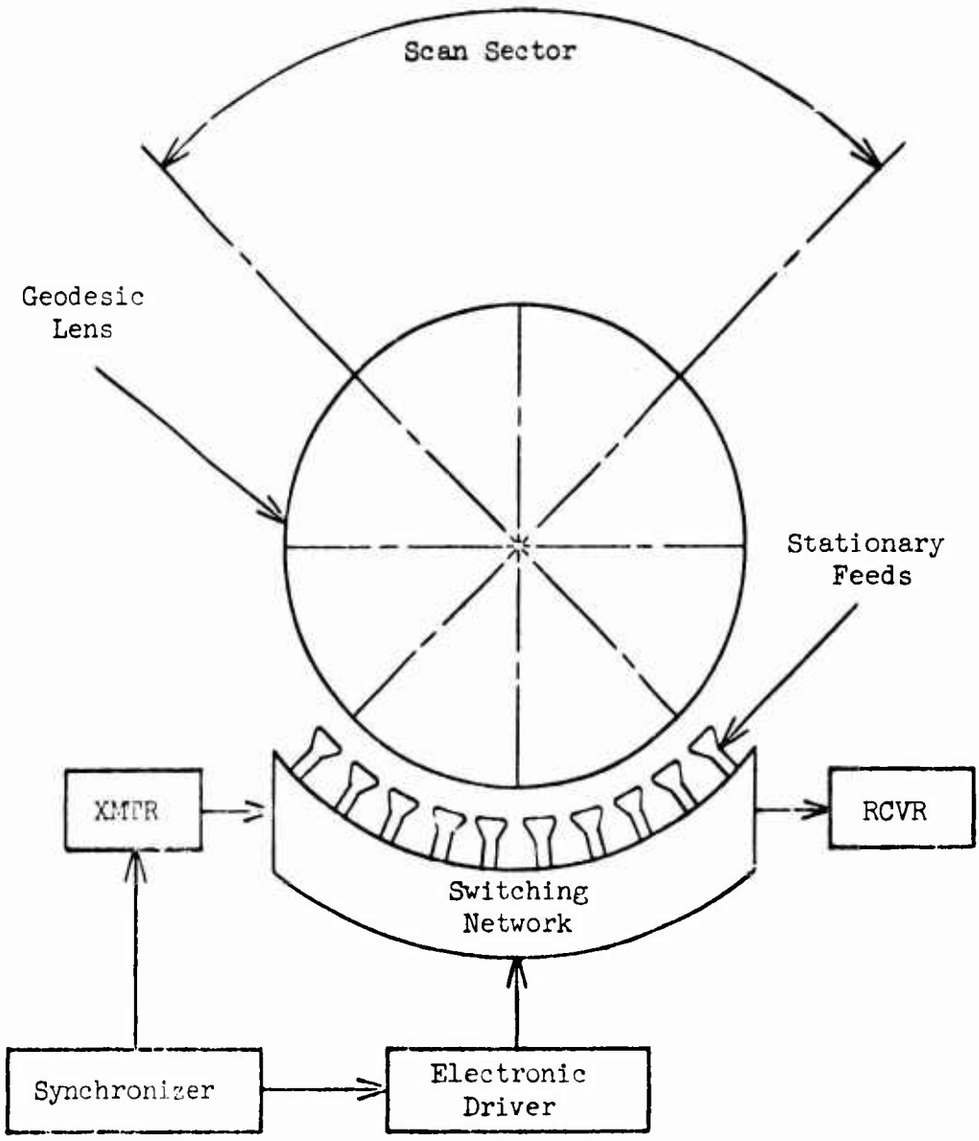

Figure 1. Pictorial representation of inertialess geodesic Luneberg lens antenna.

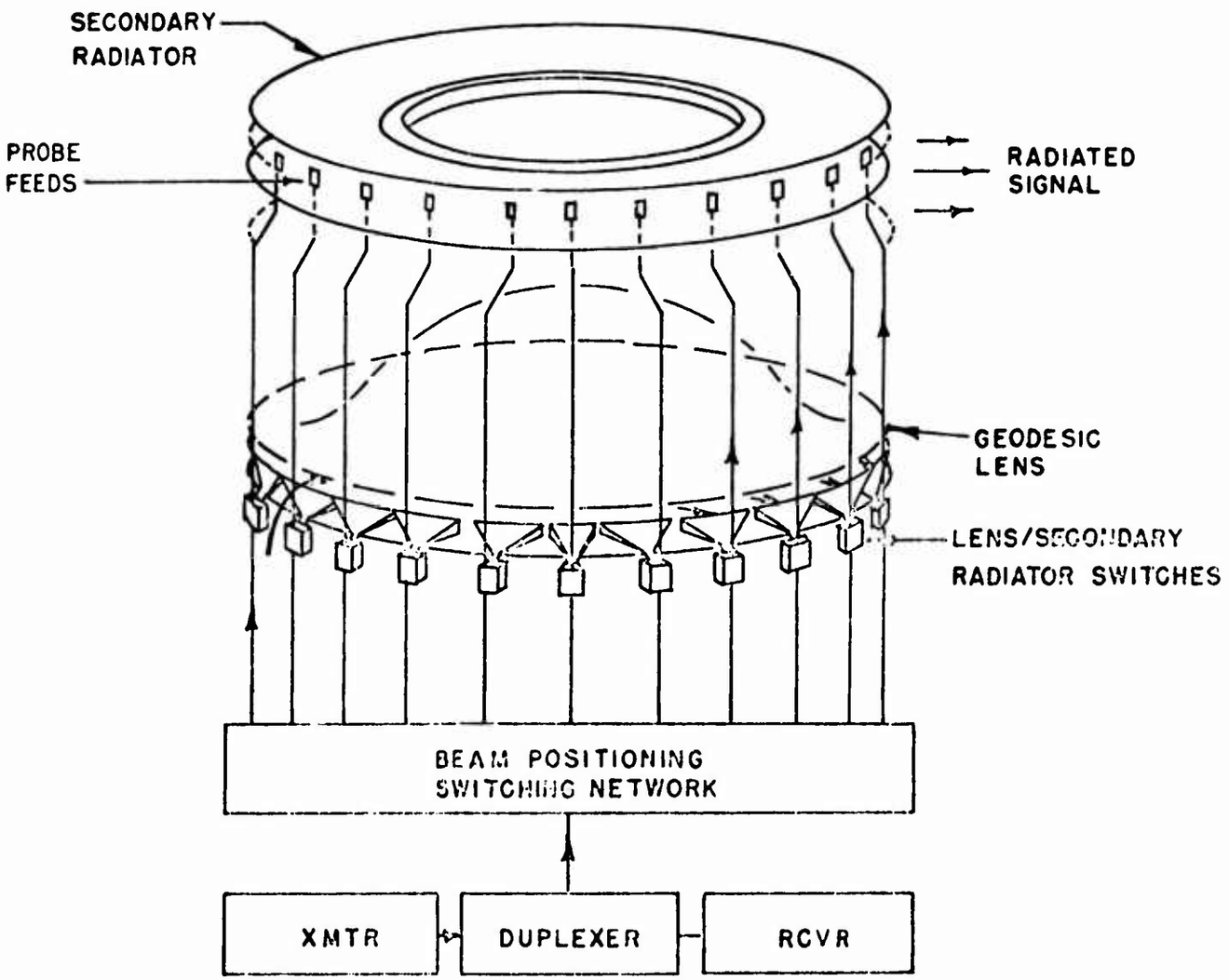

Figure 2. Pictorial representation of a geodesic lens and secondary radiator. Arrows indicate direction of signal flow during transmission.

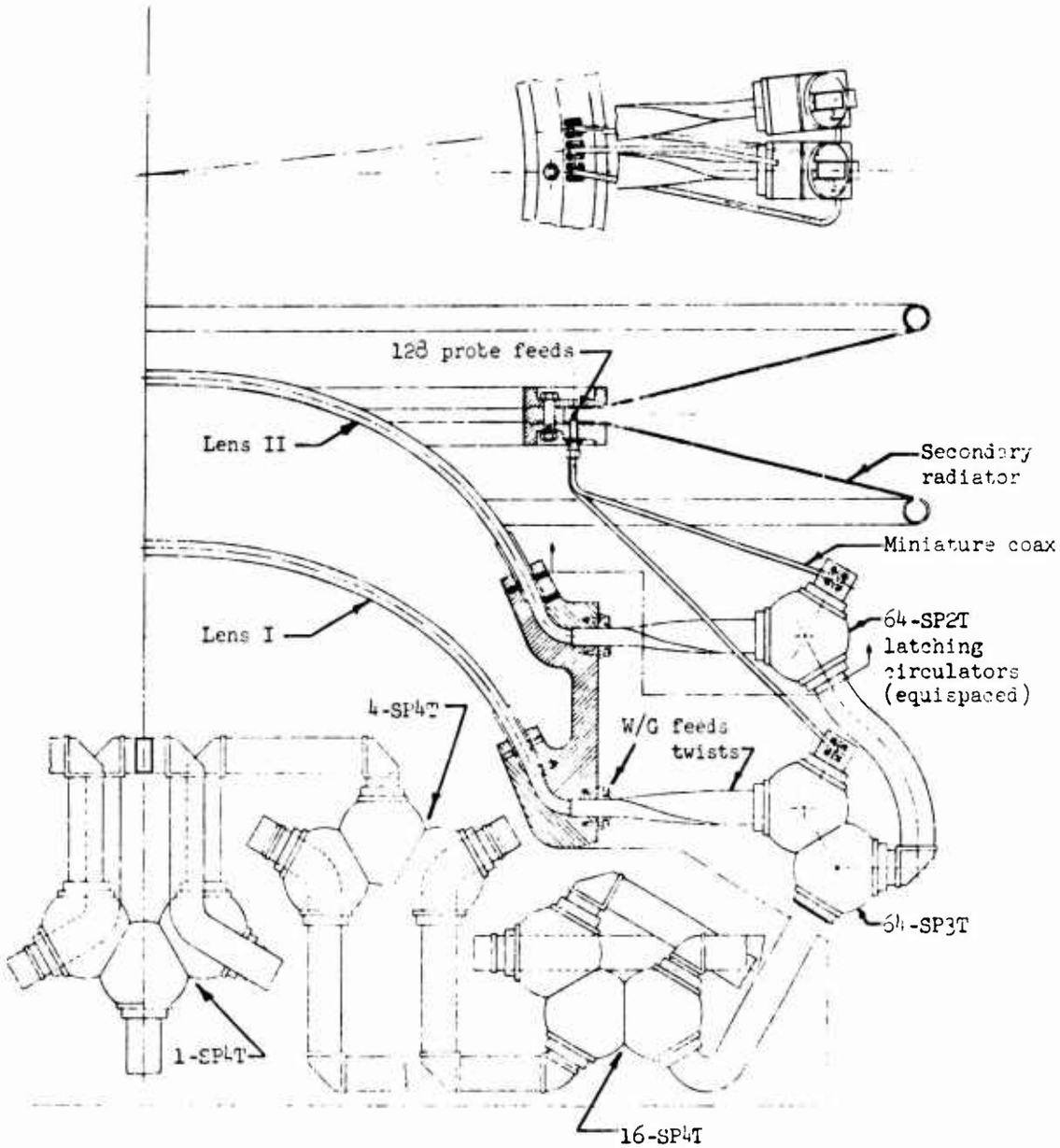

Figure 3. Mechanical layout of a 360° scanner employing two lenses and a secondary radiator; system is symmetric about center line.

RECENT THEORETICAL AND EXPERIMENTAL RESULTS ON DETERMINATION OF ANTENNA PATTERN AND GAIN FROM NEAR-FIELD MEASUREMENTS

by

Dr. David M. Kerns
National Bureau of Standards
Boulder, Colorado 80302

ABSTRACT

Recent theoretical and experimental results obtained at NBS on determination of antenna pattern and gain from near-field measurements will be outlined. (Here "near" means typically a distance of the order of 1 meter--a small fraction of the Rayleigh distance.) The theoretical results include a technique for correcting for the effects of the measuring antenna ("probe"). Experimental results include measurements on three antennas, all operating at $\lambda = 6$ mm.: an electrically large horn-lens, a standard-gain horn, and a duplicate of the measuring antenna itself. Measurements on the latter two antennas were also made by conventional far-field techniques. In view of the rigorous basis and theoretical structure one must conclude that the near-field measurement technique is inherently capable of high accuracy; our experiments are confirming this. The method is applicable in principle to any type of antenna (thus including conformal arrays!). The suitability of the method naturally depends on the antenna to be measured and the amount and precision of pattern information desired. The number of input data required for one complete pattern determination tends to be proportional to the area of the antenna in square wavelengths and may be large. In return the method is capable of giving complete vectorial far-field patterns and effective gain function (referred to antenna input power), including side lobes down 50 dB or more. Possibilities for determination of a multiplicity of patterns of an electronically steerable array are intriguing.

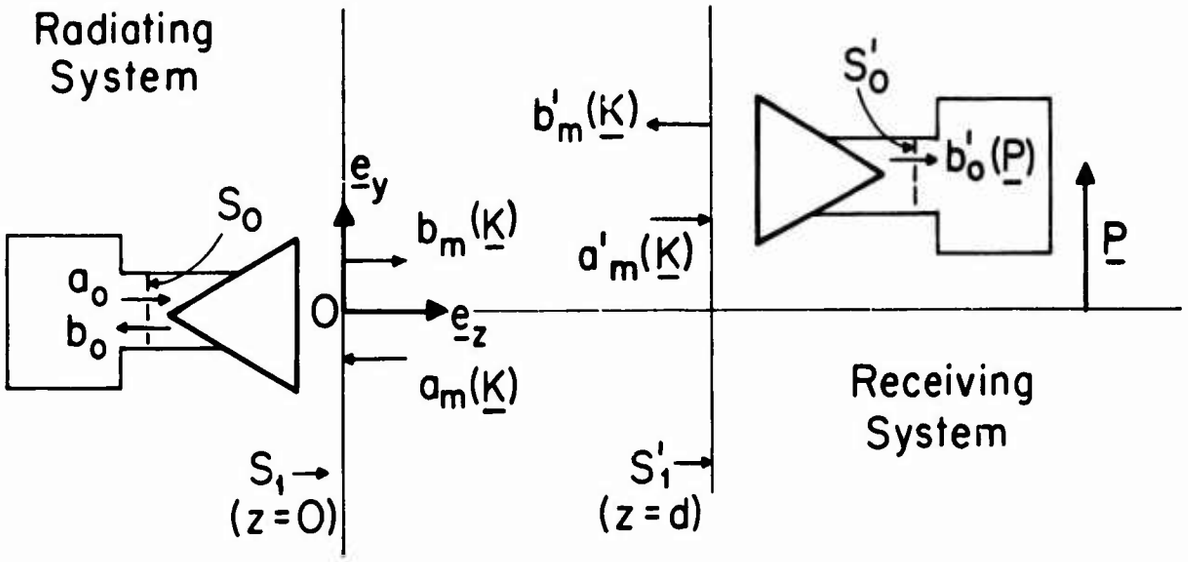

Figure 1

Transmission system -- schematic.

1. Introduction -- As implicit in the title and abstract, the main emphasis in this paper is upon the use of certain techniques to obtain antenna measurement results, rather than upon the results themselves. In order to make the techniques reasonably intelligible, it will be necessary to give a number of basic equations and to introduce a good deal of notation. Derivations and additional details may be found in a previously published paper[1] and in a group of papers now in the process of publication.[2,3,4]

2. Basic equations and notation -- Consider the transmission system consisting of two antennas shown schematically in Fig. 1. We assume that the antenna on the left is transmitting and that the one on the right is receiving. As far as the general formulation of the measurement techniques is concerned, the antennas may be of arbitrary types, arbitrary sizes, in arbitrary relative orientation, and may be separated by an arbitrary distance.

Let us consider the antenna shown schematically at the left in Fig. 1. We define the usual phasor wave amplitudes a_o and b_o for incident and emergent travelling waves at the terminal surface S_o in the input waveguide to the antenna. We choose characteristic impedance equal to unity and power normalization such that the net time-average power input to the antenna at S_o is

$$P_o = 2\pi^2 \eta_o (|a_o|^2 - |b_o|^2), \qquad (1)$$

where η_o is the wave admittance of the single mode involved and the vertical bars indicate absolute values.

We choose a coordinate system Oxyz with unit vectors $\underline{e}_x$, $\underline{e}_y$, and $\underline{e}_z$ in the space to the right of the antenna being considered, and let $\underline{k}$ denote the propagation vector for plane waves in this space. $\underline{k}$ will be regarded as a function of its transverse components k_x, k_y (throughout this discussion "transverse" means perpendicular to the z-direction); the z-component of $\underline{k}$ is then

$$k_z = \pm \gamma, \tag{2a}$$

where $\gamma = (k^2 - k_x^2 - k_y^2)^{1/2}$ and $k^2 = \omega^2 \mu \epsilon$. The transverse part of $\underline{k}$ is denoted by $\underline{K}$, so that $\underline{K} = k_x \underline{e}_x + k_y \underline{e}_y$, and

$$\gamma = (k^2 - K^2)^{1/2}, \tag{2b}$$

where γ is taken positive for $K^2 < k^2$ and positive imaginary for $K^2 > k^2$ [time dependence: $\exp(-i\omega t)$]. We need the transverse unit vectors

$$\underline{\kappa}_1 = \underline{K}/K, \quad \underline{\kappa}_2 = \underline{e}_z \times \underline{\kappa}_1, \tag{3}$$

which are respectively in, and perpendicular to, the plane of $\underline{k}$ and $\underline{e}_z$. For the transverse electric and magnetic field components $\underline{E}_t(\underline{r})$ and $\underline{H}_t(\underline{r})$ at the point $\underline{r}$ in $z \geq 0$, we introduce the vectorial plane-wave (= Fourier integral) representation

$$\left.\begin{aligned} \underline{E}_t(\underline{r}) &= \int \sum (b_m e^{i\gamma z} + a_m e^{-i\gamma z})\, \underline{\kappa}_m\, e^{i\underline{K} \cdot \underline{R}}\, d\underline{K}, \\ \underline{H}_t(\underline{r}) &= \int \sum (b_m e^{i\gamma z} - a_m e^{-i\gamma z})\, \eta_m\, \underline{e}_z \times \underline{\kappa}_m\, e^{i\underline{K} \cdot \underline{R}}\, d\underline{K}, \end{aligned}\right\} \tag{4}$$

where $\underline{R}$ denotes the transverse part of $\underline{r}$. Here and in subsequent expressions of this type summation over the values 1 and 2 of the polarization index m and integration over the infinite k_x, k_y plane will be understood. The spectral density functions $a_m(\underline{K})$ and $b_m(\underline{K})$ for incoming and outgoing waves, respectively, are defined by eqn. 4; these are the modal terminal variables, analogous to a_o and b_o, for traveling waves at the plane $S_1(z = 0)$ regarded as a terminal surface.

Limiting our consideration to (electrically) linear, passive antennas, we can now write

$$b_o = S_{oo}\, a_o + \int \sum S_{01}(m, \underline{K})\, a_m(\underline{K})\, d\underline{K}, \qquad (5a)$$

$$b_m(\underline{K}) = S_{10}(m, \underline{K})\, a_o + \int \sum S_{11}(m, \underline{K}; n, \underline{L})\, a_n(\underline{L})\, d\underline{L}, \qquad (5b)$$

thereby defining the scattering matrix [having the elements S_{oo}, $S_{01}(m, \underline{K})$, $S_{10}(m, \underline{K})$, and $S_{11}(m, \underline{K}; n, \underline{L})$] for the antenna considered. If the antenna is reciprocal, then the receiving characteristic $S_{01}(m, \underline{K})$ is related to the transmitting characteristic $S_{10}(m, \underline{K})$ by the reciprocity relation

$$-\eta_o\, S_{01}(m, \underline{K}) = \eta_m(\underline{K})\, S_{10}(m, -\underline{K}). \qquad (6)$$

where $\eta_1 = \omega\epsilon/\gamma$ and $\eta_2 = \gamma/(\omega\mu)$ are the wave-admittances associated with the polarizations $\underline{\kappa}_1$ and $\underline{\kappa}_2$ respectively. We define the vectorial transmission spectrum $\underline{S}_{10}(\underline{K}) = S_{10}(1, \underline{K})\, \underline{\kappa}_1 + S_{10}(2, \underline{K})\, \underline{\kappa}_2$, and note that the transverse part of $\underline{E}$ is given

asymptotically at large distances r by

$$\underline{E}_t(\underline{r}) \sim - 2\pi ik \cos\theta \, \underline{S}_{10}(\underline{R}\, k/r) \; a_o \; e^{ikr}/r \, ; \quad (7)$$

the angle θ introduced here is the polar angle of $\underline{r}$ relative to the z-axis. Another important asymptotic quantity, here called the "effective gain function" and denoted by G_e, is defined as

$$G_e = \frac{\text{power radiated per unit solid angle as a function of direction}}{(\text{power input to antenna})/(4\pi)}$$

and is given in terms of S_{oo} and $S_{10}(m, \underline{K})$ by

$$G_e(\underline{K}) = \frac{4\pi \, k^2 \cos\theta \, [\,|S_{10}(1, \underline{K})|^2 \, \eta_1 + |S_{10}(2, \underline{K})|^2 \, \eta_2\,]}{\eta_o (1 - |S_{oo}|^2)} \quad (8)$$

In view of eqns. 6, 7, and 8, which respectively give the receiving characteristic, the far-field pattern, and the gain in terms of $\underline{S}_{10}(\underline{K})$; we shall consider $\underline{S}_{10}(\underline{K})$ as our measurement objective.

We now consider a transmission system (Fig. 1) operating in a homogeneous, isotropic, and dissipationless medium. The receiving antenna has the terminal surfaces S'_o and S'_1, the latter being at $z = d$. (Primes are used throughout to refer to the receiving antenna.) In many practical cases the effects of multiple reflections between two antennas, even when set up for near-field measurements, are found to be (or may be made to be) negligible. Here we assume that the effects of multiple reflections are indeed negligible. Let the (passive) termination on the receiving antenna have reflection coefficient Γ'_L; then a'_o will be equal to $b'_o \Gamma'_L$.

The measurement technique being presented requires measuring the field of the transmitting antenna in a transverse plane $z = d$. Let the displacement of the receiving antenna from a reference position be denoted by the transverse vector $\underline{P} = x\underline{e}_x + y\underline{e}_y$ (Fig. 1). Then[2]

$$b_o'(\underline{P}) = F'a_o \int e^{i\underline{K}\cdot\underline{P}} \sum S_{01}'(m, \underline{K})\, S_{10}(m, \underline{K})\, e^{i\gamma d}\, d\underline{K}. \quad (9)$$

Here F' is a "mismatch factor" equal to $1/(1 - \Gamma_L' S_{oo}')$. Note that $b_o'(\underline{P})$ is what is observed in the measurement process: it may or may not be simply related to $\underline{E}_t(\underline{P}, d)$.*

Equation 9 is the immediate basis for two new antenna measurement theorems pertaining to two different antenna measurement problems.

First let us suppose that a receiving antenna of known characteristics is being used to measure the properties of the transmitting antenna. That is, $\underline{S}_{10}(\underline{K})$ is sought and $\underline{S}_{01}'(\underline{K})$ is known. Inasmuch as eqn. 9 is a Fourier integral transformation, its formal inversion is immediate:

$$\sum S_{01}'(m, \underline{K})\, S_{10}(m, \underline{K}) = D'(\underline{K}). \quad (10a)$$

Here $D'(\underline{K})$ is an abbreviation for the determinate function of $\underline{K}$ given by

$$D'(K) \equiv \frac{e^{-i\gamma d}}{4\pi^2 F'a_o} \int b_o'(\underline{P})\, e^{-i\underline{K}\cdot\underline{P}}\, d\underline{P}$$

Equation 10a determines one linear combination of the two components of $\underline{S}_{10}(\underline{K})$; in the general case one must make two sets of measurements

*If the measuring antenna were to give a response precisely proportional to the x or y component of $\underline{E}_t$, then these equations reduce essentially to a rigorous form of the well-known Fourier transform relation between $\underline{E}_t$ and the spectrum.

with "independent" measuring antennas. (In many cases a single antenna used in two different orientations, differing say by a 90° rotation around the z-axis, would serve the purpose.) Then one would obtain the additional equation

$$\sum S''_{01}(m, \underline{K})\, S_{10}(m, \underline{K}) = D''(\underline{K}) ; \qquad (10b)$$

the double primes distinguish the second set of measurements. For each value of the parameter $\underline{K}$ for which the determinant $S'_{01}(1, \underline{K})\, S''_{01}(2, \underline{K}) - S''_{01}(1, \underline{K})\, S'_{01}(2, \underline{K})$ is not zero, the eqns. 10 can be solved for the two unknowns $S_{10}(1, \underline{K})$ and $S_{10}(2, \underline{K})$. At least this is true mathematically; practically one may expect difficulty if the equations are ill-conditioned, but we have not yet encountered this in our work.

Once $\underline{S}_{10}(\underline{K})$ is found, one can incidentally obtain $\underline{E}_t(\underline{P}, d)$, corrected for probe effects, by making the appropriate Fourier transformation. However, $\underline{E}_t$ has not been of direct interest in our work.

The second application of eqn. 9 leads to a new method of measuring on-axis pattern and on-axis gain using two identical antennas.[3] The two antennas must obey reciprocity*, but may otherwise be arbitrary; the usual requirements in the conventional two-antenna gain measurement method, that the polarization be known a priori and that the separation be large compared to the Rayleigh distance, are eliminated. Again, the effects of multiple reflections must be avoided. (This requirement is by no means peculiar to the techniques being described here.)

Here we shall give only the equation for determining $G_e(0)$, and this only in the case in which the on-axis polarization is considered known.

---

*More precisely (and more generally) what is needed is a known relation between the transmitting and the receiving characteristics.

The polarization is conveniently specified by means of the complex polarization ratio

$$\rho \equiv \frac{S_{10y}(0)}{S_{10x}(0)} \quad , \tag{11}$$

where the subscripts x and y denote the x and y components of $\underline{S}_{10}(0)$. (The state of polarization at the point $\underline{K} = 0$ of the spectrum has immediate physical significance in terms of the on-axis asymptotic $\underline{E}$; cf eqn. 7.) Let us suppose that the placement of the receiving antenna to serve in reception is derived from that of the identical transmitting antenna by a 180° rotation around the y-axis. (For an arbitrary antenna, the y-axis is an arbitrary axis.) Then the on-axis gain is given by

$$G_e(0) = \frac{k^2}{\pi} \frac{\left|1 - \Gamma'_L S'_{oo}\right|}{1 - |S_{oo}|^2} \frac{|\rho|^2 + 1}{|1 - \rho^2|} \frac{1}{|a_o|} \left| \int b'_o(\underline{P})\, d\underline{P} \right|. \tag{12}$$

If we assume a "polarization match" ($\rho = 0, \infty$, or $\rho = \pm i$), $\Gamma'_L = 0$, and use the well-known theorem relating effective gain and effective receiving cross-section σ_e, we obtain the remarkably simple formula

$$\sigma_e = \frac{1}{|a_o|} \left| \int b'_o(\underline{P})\, d\underline{P} \right| \tag{13}$$

We note that both eqn. 12 and eqn. 13 are wholly independent of d, the distance between the antennas. The gain and cross-section given by these equations include the effect of whatever losses there may be in the antennas (in accordance with the definition 8); to obtain this result the relative amplitudes of a_o and $b'_o(\underline{P})$ must of course be properly determined in the measurement process.

3. Evaluation of integrals -- Clearly the utility of the results given in eqns. 10, 12, and 13 de · nds upon the ability to evaluate the integrals in the equations in a satisfactory manner. We have used two methods of determining these integrals from data taken at the discrete points of a rectangular lattice in the measurement plane. One method determines the coefficients of a double Fourier sine series giving a least-square fit to the data over the measurement lattice. The other is an application of the sampling theorem (or the "cardinal theorem of interpolation theory") stated in two-dimensions.

In both methods of fitting one determines the coefficients C_i in a representation of $b_o'(\underline{P})$ of the form

$$\epsilon_N(\underline{P}) = \sum_{i=1}^{N} C_i f_i(\underline{P}) \quad , \tag{14}$$

where the summation goes over the total number N of suitably indexed basis functions $f_i(\underline{P})$. When the sampling theorem is used, the coefficients are simply the measured values of $b_o'(\underline{P}_{rs})$, and the summation actually goes over the M points of the measurement lattice. When the statistical least-squares method is used, the coefficients are determined by minimizing the sum of the absolute squares of the residuals

$$\sum_{r,s} |\epsilon_N(\underline{P}_{rs}) - b_o'(\underline{P}_{rs})|^2 \quad , \tag{15}$$

taken over the measurement lattice. If, as is the case for the trigonometrical functions used, the f_i are in the Hermitian sense normalized and mutually orthogonal with respect to summation over the measurement lattice, the least-square requirement leads to

$$C_i = \sum_{r,s} b_o'(\underline{P}_{rs}) \overline{f_i(\underline{P}_{rs})} \qquad (16)$$

In eqns. 15 and 16, one must have $N \leq M$ and ordinarily one has $N < M$ -- or else the fitting is not statistical. We have in some cases employed the F-test of mathematical statistics as an aid in judging whether certain f_i of higher spacial frequencies should be retained or rejected.[5]

Although the excellence of the representation achieved with eqn. 14 is of crucial importance in that it determines the excellence of the final result (assuming that the data themselves are sufficiently accurate), the final result itself depends upon the Fourier transform of $b_o'(\underline{P})$. The basis functions used in both methods of fitting the data possess simple known analytical Fourier transforms, which we may denote by $F_i(\underline{K})$. Then the desired transform of eqn. 14 is obtained directly as a weighted sum,

$$\sum_{i=1}^{N} C_i F_i(\underline{K}) \ , \qquad (17)$$

and the fitting of the near-field data can remain implicit.

The sampling theorem enables us to give an explicit expression for the evaluated integral. If we assign band limits $k_1 = 2\pi/\lambda_1$ and $k_2 = 2\pi/\lambda_2$ for k_x and k_y, respectively, then

$$D(\underline{K}) = \frac{e^{-i\gamma d}}{4 k_1 k_2 F' a_o} \sum_{r,s} b_o(\underline{P}_{rs})\, e^{-i\underline{K} \cdot \underline{P}_{rs}} \ . \qquad (18)$$

In this expression the vectors

$$\underline{P}_{rs} = \frac{r\lambda_1}{2} \underline{e}_x + \frac{s\lambda_2}{2} \underline{e}_y, \quad (r, s = \ldots -1, 0, 1, 2 \ldots\ldots)$$

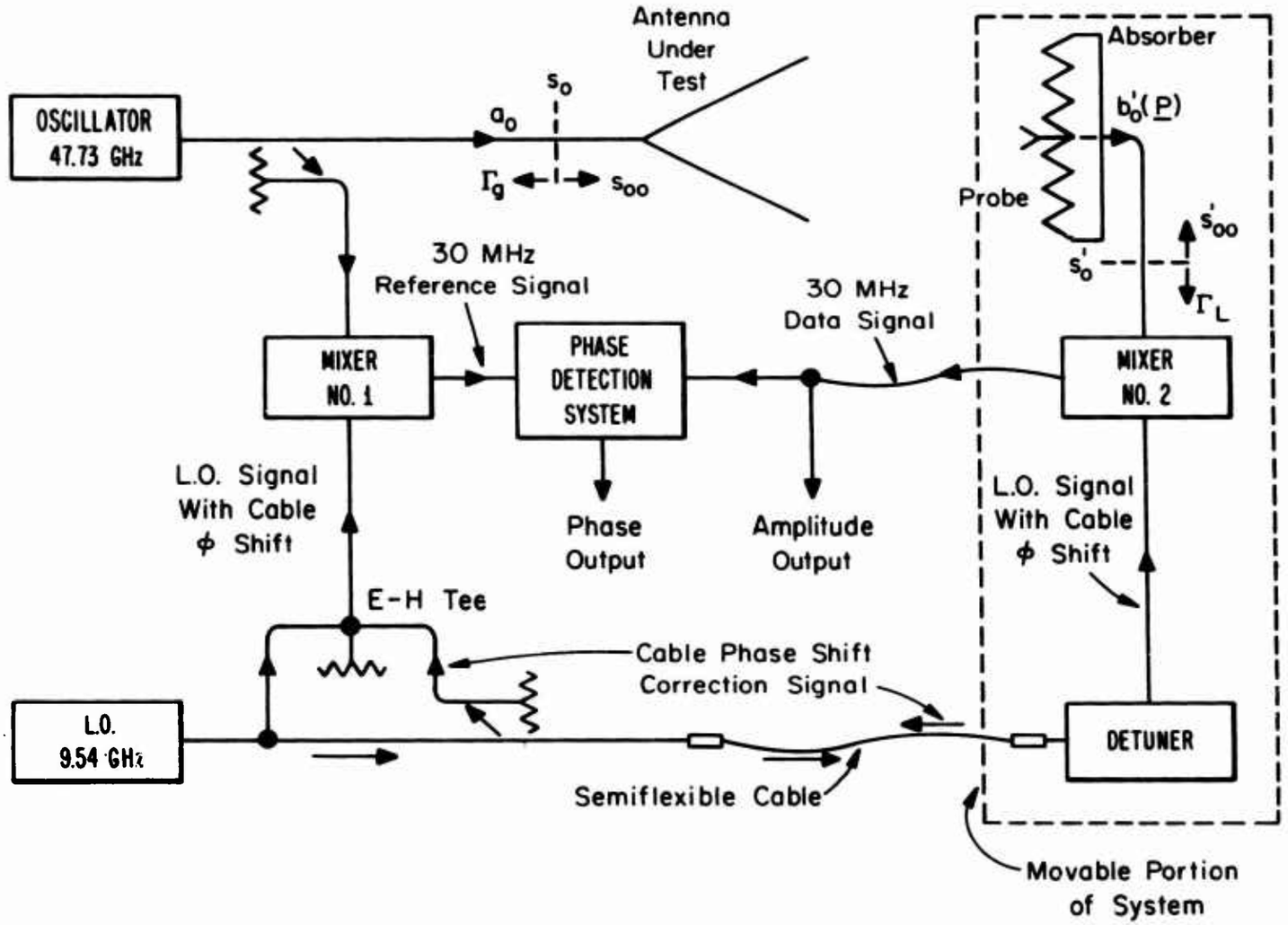

Fig. 2. Functional block diagram of near-field phase and amplitude measurement system.

define the measurement lattice, the quantities $b_o(\underline{P}_{rs})$ are the (complex) values of receiving antenna output directly observed at the points of the lattice, and the summation goes over the points of the lattice. The theorem requires an infinite sum, but empirically we have found that not even all values measurable above noise are needed. Ordinarily, band limits $k_1 = k_2 = k$ would be conservative. (There is a lot more to multi-dimensional sampling than might be suspected from what is said here. See the interesting paper by Petersen and Middleton.[6])

To all indications, excellent results have been obtained using both methods of treating the data.

It can be shown that the relative statistical precision of calculated far-field results tends to be improved over that of the input data at the individual measurement points by a factor of $\sqrt{M_e}$, where M_e is an effective number of independent data points. M_e is less than M as a consequence of the normalizing "tie-scans" noted below, but nevertheless is typically large enough so that random error is essentially eliminated.

4. Experimental apparatus and technique -- A functional block diagram of the near-field measuring apparatus is shown in Fig. 2. The 47.73 GHz operating frequency (λ = 6.281 mm) was chosen because of existing equipment capabilities and the desirability of working with an electrically large antenna that is physically small enough to manage in a laboratory. The 47.73 GHz oscillator is phase locked to a stable 9.54 GHz local oscillator (L.O.) in order to provide coherent phase measurements as well as a stable frequency.

A portion of the input energy is combined with the L.O. signal in Mixer No. 1 where fifth harmonic mixing produces a 30 MHz reference signal. The energy collected by the small scanning antenna (probe) is combined with the L.O. signal in Mixer No. 2 to produce a 30 MHz

signal containing the desired phase and amplitude information. Part of this data signal is fed to the amplitude recording system and the remainder is compared with the reference in the phase detection system. The digital data are recorded automatically during a series of horizontal scans. Numerous vertical scans are also made to "tie" the horizontal scans together and correct for drift. Accuracies of better than 1% in amplitude and a few tenths of a degree in phase are attainable. The overall dimensions of the measurement lattice are determined by the required accuracy in the computed far-field results and by the transverse area over which $\underline{E}_t$ is significant. (In the measurements made thus far it has been found sufficient to include the 1-percent-of-maximum contour of $|\underline{E}_t|$.)

The circuitry enclosed by the broken line moves with the probe, and some means must be found to eliminate, or correct for, changes in the L.O. signal caused by the flexing of the connecting cable. Any amplitude changes are small and the L.O. input to Mixer No. 2 is optimized so that a large change in L.O. power is required to produce a small change in the Mixer output. Consequently, there are no observable amplitude changes in the data signal when the cable is flexed.

We obtained the smallest cable phase shifts with a semiflexible cable having a solid outer conductor and a solid dielectric. The maximum phase shift observed at 47.73 GHz was 2 or 3 degrees ($\sim$ 0.5 degrees at 9.54 GHz). The effects of this remaining phase shift were eliminated as follows: A multistub tuner (detuner) at the moving end of the cable is adjusted to produce a reflected wave, and a portion of this reflected wave is combined with the direct L.O. signal in the E-H tee so that any cable phase shift produces an equal phase shift in the L.O. input to Mixer No. 1. The net result is that the phases of the reference and data signals are both shifted an equal amount but the phase difference remains unchanged. When all adjustments are properly made this correction is essentially exact, and remains so, for cable phase shifts up to at least 20 degrees at 9.54 GHz.

In order to determine absolute (rather than merely relative) values of the far-field quantities $\underline{S}_{10}(\underline{K})$ and $G_e(\underline{K})$, in accordance with the equations given previously, it is necessary to determine the relative amplitudes of the transmitting antenna input a_o and the receiving antenna output $b_o'(\underline{P})$. In the experimental technique adopted, a "transfer normalization" base was established by determining $|b_o'(\underline{P})/a_o| \equiv \tau$ at the one probe position $\underline{P} = 0$. Then, apart from an immaterial constant phase factor, the desired quantity $b_o'(\underline{P})/a_o$ is given in terms of relative values of $b_o'(\underline{P})$ taken over the measurement lattice:

$$\frac{b_o'(\underline{P})}{a_o} = \tau \frac{b_o'(\underline{P})}{b_o'(0)} \quad . \tag{19}$$

To obtain τ a form of substitution loss measurement was made: A known two-port (actually a section of waveguide) was substituted for the system of two antennas between the desired reference planes, and the ratio of the transmitted wave amplitudes before and after the substitution was measured using precision calibrated attenuators included in the system. It can be shown that

$$\tau = \left| \frac{M_{21}(1 - \Gamma_g S_{oo})}{(1 - \Gamma_g M_{11})(1 - \Gamma_L M_{22}) - M_{12} M_{21} \Gamma_g \Gamma_L} \right| \cdot \left| \frac{b_o'(0)}{b_2} \right| . \tag{20}$$

Here b_2 is the transmitted wave after substitution, the M_{ij} are the elements of the scattering matrix of the substituted two-port, and the other quantities are defined in Fig. 2. Although the needed quantities were very carefully evaluated, the error in τ (approximately 0.05 dB 2-sigma value) is the largest single error contribution in the measurements reported here. (Relative values of G_e, i.e. directive gain, could be obtained more precisely and more easily.)

In the measurements to be described here the receiving antenna (hereinafter called the "probe") is an open-ended straight section of WR-22 (rectangular) waveguide 45.72 cm. long, with the walls of the open end tapered to a sharp edge to reduce back-scattering. The probe passes through and protrudes from a section of microwave absorbing material which moves with the probe and is large enough to intercept almost all the radiation from the transmitting antenna whatever the probe position. Additional pieces of absorbing material were strategically placed on various surfaces in the laboratory, and no difficulties with scattered radiation were experienced.

The above-described apparatus and techniques have been used to measure three antennas: (A) a nominal duplicate of the probe, (B) a standard-gain pyramidal horn, and (C) an electrically-large horn-lens antenna. All three antennas were fed by the TE_{10} mode in WR-15 waveguide so oriented that the $\underline{E}$ of the waveguide mode was in the y-direction (cf Fig. 1). The probe output observed with the probe similarly oriented is denoted by b_o' and is termed y-component data; the probe output observed with the probe rotated by 90 degrees around the z-axis is denoted by b_o'' and is termed x-component data. In cases A and B, the x-component data were observed and considered negligible; this information is embodied approximately in the assumption that $S_{10x}(\underline{K})$, the x-component of $\underline{S}_{10}(\underline{K})$, was identically zero. In case C, x-component data were taken and the contribution was evaluated (see below).

Some basic data pertaining to the three cases are given in Table 1.

Table 1. Basic measurement data

Measurement	Aperture, λ's*	Separation, cm	Rayl. dist. $a^2/2\lambda$, cm	Meas. lattice, x x y, cm	Point Spacing, λ's
Probe to Probe:	0.95λ x 0.395λ	2.54	N.A.	20.3 x 37.5	0.5λ x 0.5λ
Std.-gain horn:	6.5λ x 5.3λ	2.54 & 7.62	13.1	20.3 x 37.5	0.5λ x 0.5λ
Horn-lens:	90λ x 90λ	50.8	2840	118 x 151	1.0λ x 0.75λ

*λ = 6.281 mm.

Probe to probe measurements: Considering the two antennas to be identical, on-axis effective gain, $G_e(0)$, was calculated from eqn. 12 utilizing cardinal-function fitting and centerline (x = 0, y = 0) y-component input data. [This use of centerline data is equivalent to the assumption of probe response pattern separability, i.e., $b_o'(\underline{P}) = f(x)\,g(y)$.] The result was 6.83 dB, with an estimated 2-sigma accuracy of about 0.1 dB. The effective gain was also measured using the conventional two-identical-antenna method. This yielded 6.80 dB with about the same accuracy. The agreement is better than might be expected considering the stated assumptions. (These were used at the present stage of our work for simplicity only; none is imposed by limitations in the theory or in measurement capability.)

The previous assumption of $S_{10x}(\underline{K}) = 0$ and the additional assumption of symmetry with respect to y (or k_y), e.g., $S_{10y}(k_x, k_y) = S_{10y}(k_x, -k_y)$, enable one to determine an approximate vectorial spectrum

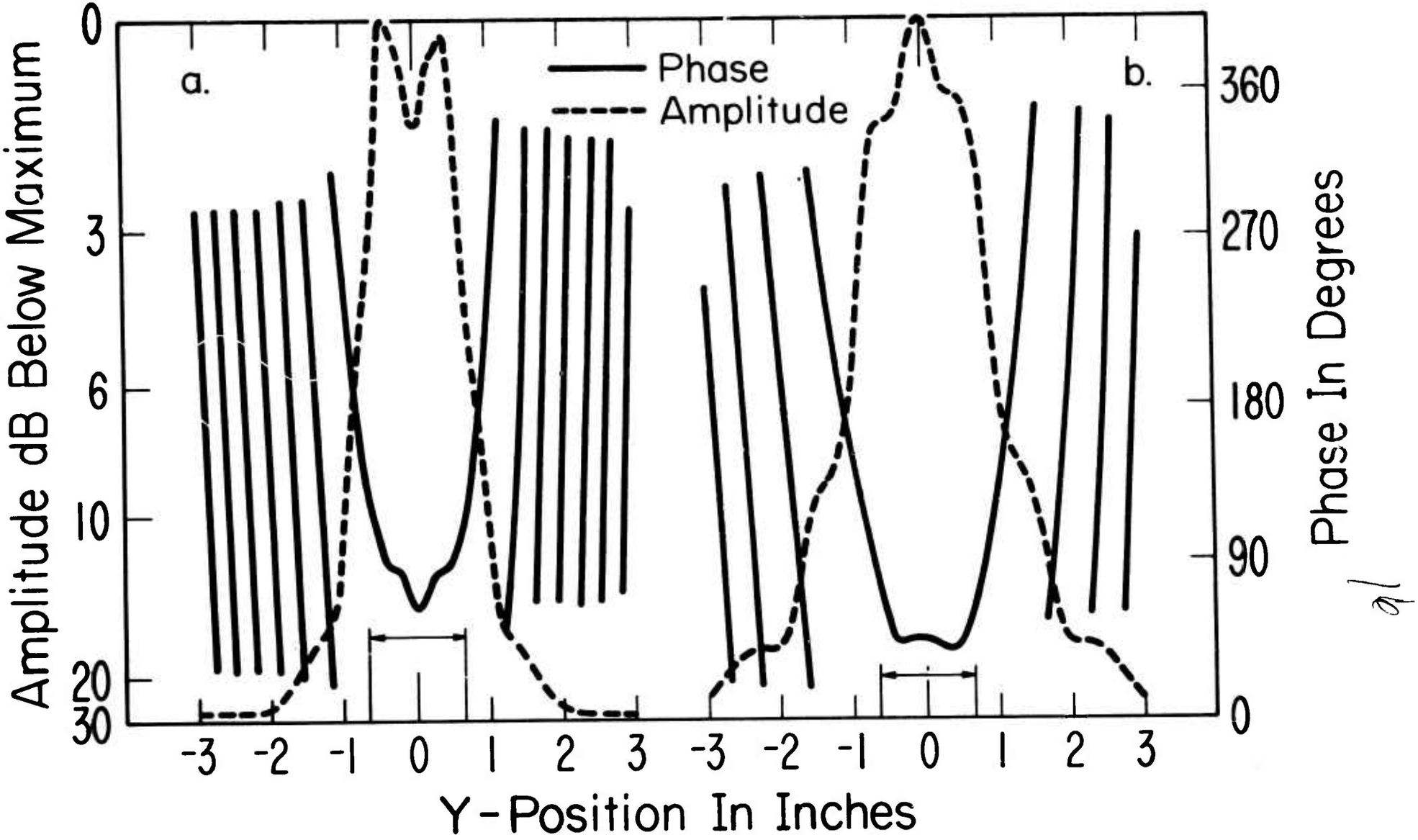

Fig. 3. Standard-gain horn near-field x = 0 centerline data attwo antenna separation distances: (a) 7.62 cm, (b) 2.54 cm. Apparent asymmetry in phase data is due primarily to plotter inertia.

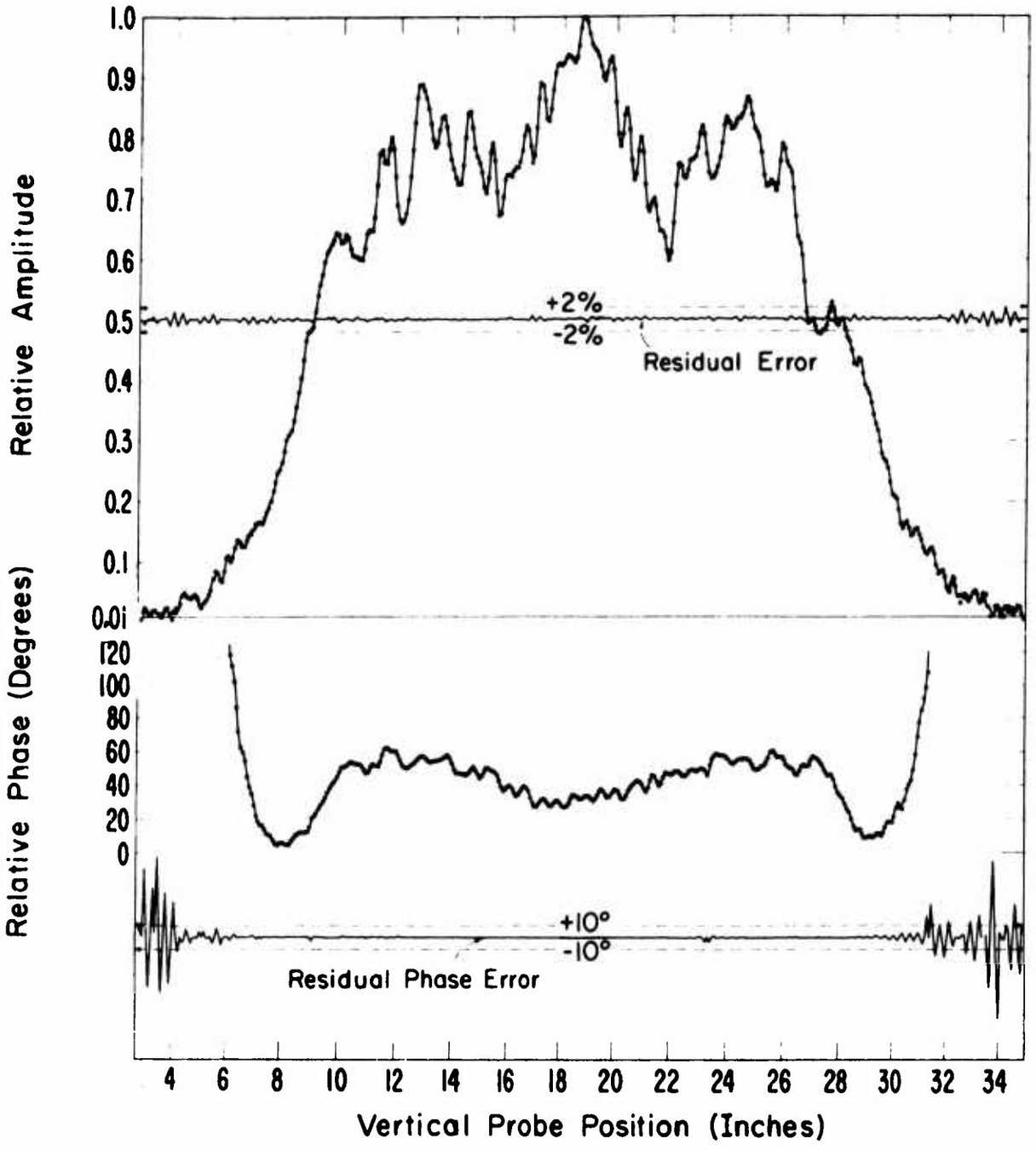

Fig. 4. An example of non-statistical curve fitting (horn-lens antenna).

Digital vertical (E-plane) centerline data taken with the RG-98 probe at z = 50 cm. The data were recorded at 399 points. The smooth curves were obtained by fitting 200 Fourier basis functions to 200 of the equally spaced points. In each case the residual curve represents the difference between the amplitude or phase obtained from the fitted curve and the actual data.

16A

for all values of k_x and k_y. (Note that this is a considerable extension of previous two-identical-antenna measurement technique.) The basic equation for this may be derived from eqns. 10a and 6, with due consideration of the probe as a reoriented transmitting antenna. One finds

$$\left[S_{10y}(\underline{K})\right]^2 = \frac{\eta_o K^2 e^{-i\gamma d}}{\eta_1 k_y^2 + \eta_2 k_x^2} \frac{1}{4\pi^2 a_o} \int b_o'(\underline{P})\, e^{-i\underline{K}\cdot\underline{P}}\, d\underline{P} \quad (21)$$

Again, centerline data were used in an approximate evaluation of the integral.

The simplifying assumptions used in these probe-probe measurements are frequently considered applicable in antenna work and may be considered "good," even though little evaluation has been done. Here we are using the approximate results to apply a probe correction in the next-described measurement.

Standard-gain horn measurements -- The transmitted spectrum $\underline{S}_{10}(\underline{K})$ of the standard-gain horn was calculated from eqns. 10a and 18 using centerline data taken at two separation distances, 2.54 cm and 1.72 cm, and using the previous probe-probe data to obtain the probe receiving pattern $S_{01}'(\underline{K})$. Figure 3 shows (contrasts) the $x = 0$ centerline input data for the two distances. The calculated far-field amplitudes ($\sim\sqrt{G_e}$) for the two distances were compared with each other and with directly measured results on the $k_x = 0$ centerline. The maximum disagreement among the three was approximately 2 percent of the maximum amplitude for elevations between 0 and 50 degrees.

Horn-lens measurements -- The measurement plane was chosen at 50 cm from the physical aperture. This choice represents a compromise between the somewhat greater detail in the near-field closer to the antenna and the somewhat greater scan area required at larger distances. Fig. 4

illustrates the complicated structure of the near-field and shows the successful fitting of a one-dimensional (y-direction) sample of the field by means of a 200-term Fourier series (Fig. 4 relates to earlier experimental work than the bulk of that reported here).

Preliminary measurements and computations were made using centerline data to determine the density of data points and the length of scan required in the x and y directions. This was done by starting with density of points and scan lengths both clearly greater than necessary, and then simultaneously reducing the density (by deletions) and the scan range until significant degradation of the computed approximate far-field pattern occurred. Results are given in Table 1.

Measurements of phase and amplitude of both $b_o'(\underline{P})$ and $b_o''(\underline{P})$ were made over the 24,157 points of the measurement lattice, and computations of the far-field amplitude ($\sim\sqrt{G_e}$) using both the statistical-trigonometric (with use of F-test) and the cardinal-function data-fitting processes were made. In these computations an approximate analytical expression for the probe pattern was used. In particular, calculations were made for 11 slices of the far-field amplitude obtained by fixing k_x at values corresponding to (azimuthal) angles of $0(0.2)\,1.2^\circ$ and fixing k_y at values corresponding to (elevation) angles of 0, 0.2, 0.4 and 1.0°. On these 11 slices the maximum difference between the trigonometric and the cardinal computations was 0.066 percent of maximum amplitude. This good agreement must be considered as a measure of precision, not accuracy, and certainly is due in part to the improvement in precision produced by averaging.

The completeness of the measurement and computation just outlined enabled us to evaluate two simplifying assumptions frequently used in antenna work, as applied to our antenna. Thus, omitting the x-component

data input produced a maximum change of 0.254 percent of maximum amplitude over the set of 11 slices of the far-field amplitude. Omitting the x-component data and also assuming a product pattern led to a maximum error of approximately 6% over a set of four slices at 0 and 1° azimuth and at 0 and 1° elevation.

Direct far-field measurements of the horn lens antenna have not been made -- nor are they likely to be made. Such measurements have not been feasible with the range facilities available to us. Moreover, we feel that the results for the horn-lens antenna obtained from the near-field measurements are at least as accurate and as easily obtained as any of equal completeness that could be obtained directly. In other words, for the particular antenna measured, near-field measurements made indoors and not requiring an anechoic room obviate the need for direct measurements even if such were feasible.

REFERENCES

1. Kerns, D. M., and Dayhoff, E. S., 'Theory of diffraction in microwave interferometry', J. Res. NBS, 1960, 64B, pp. 1-13.

2. Kerns, D. M., 'Correction of near-field antenna measurements made with an arbitrary but known probe', (to be published). Presented at the 1963 Spring URSI meeting, Apr. 29-May 2, Washington, D. C.

3. Kerns, D. M., 'A new method of gain measurement using two identical antennas , (to be published). The basic theorem was given in the NBS High-Frequency and Microwave Field-Strength Precision Measurement Seminar, held Mar. 7-9, 1966, in Boulder, Colorado.

4. Baird, R. C., Newell, A. C., Wacker, P. F., and Kerns, D. M., 'Recent experimental results in near-field antenna measurements,' (to be published).

5. Mandel, J., "Statistical Analysis of Experimental Data," Interscience, 1964.

6. Petersen, D. P., and Middleton, D., 'Sampling and reconstruction of wave-number-limited functions in N-dimensional euclidean spaces,' Information and Control, 1962, 5, pp. 279-323.

SUPERSTRUCTURE BROADBAND DISCAGE ANTENNA

by

R. L. Goodbody

Naval Electronics Laboratory Center
San Diego, California 92152

INTRODUCTION

The purpose of this paper is to describe a concept for using a single, large self-supporting superstructure on a ship as a dual band hf antenna. The object is to improve ship hf antenna radiation pattern characteristics by reducing the number of structures acting as major parasitic radiators in the hf range and to more efficiently utilize the limited available topside space on ships.

The old method has been to mount several hf radiators on and around the various superstructures, masts, and towers on a ship. The resulting environment of major parasitic radiators results in very poor radiation pattern control on most ships.

DESCRIPTION AND OPERATION

Figure 1 shows a sketch of a typical configuration of the superstructure dual band antenna. The structure shown is for operation 2-6 MHz fed at the bottom (a) and 4-12 MHz fed at the top (b). It will provide a matched VSWR of less than 3:1 in the range 2 to 12 MHz. Figures 2, 3, 4, and 5 show the feed point and matched impedances as measured on a 1/48th scale model. Using existing multicouplers, this structure will provide for simultaneous operation of up to 16 transmitters in the 2 to 12 MHz band.

The structure modeled in this case was one approximately the size and shape of the major superstructure existing on CGN-9, USS LONG BEACH. A salient feature of the invention is that it has shown that very large structures can be utilized. The structure can be self-supporting on the large central conducting cylinder or shaft (c) up to at least 15 feet in diameter. Access to the structure is provided through the cylinder (c) which is large enough for elevators, stairs, pipeways, and cableways. The maximum diameter of the cylinder is limited only by the degradation suffered in the impedance and radiation pattern shape resulting from the large feed ring (d) and the necessity for the large offset from center of the feed (a). The diameter and length of the supporting cylinder or shaft (c) has been chosen to provide a shunt inductance just small enough so that the 2 MHz point can be matched 3:1 with a matching series capacitor. Within the conducting surfaces, the entire volume shown cross-hatched in figure 1 can be utilized as access, equipment, living or operating space. All the surfaces shown are conducting unless otherwise indicated in figure (1). The upper or discone portion fed at (b) has a large shunting 50-ohm shorted stub (e) of length chosen to provide a shunt reactance which will allow a series capacitor to match the antenna to a 2:1 VSWR over most of the 4 to 12 MHz range. The disc (f) is formed by yardarms

and platforms. Electrical cables, wave guides, and piping for the equipment above the disc are lead through the inner cylinder (g).

ADVANTAGES AND NEW FEATURES

A single structure can be installed on a ship which, besides performing other functions of ship superstructure, integrates a dual band antenna into the structure. This is a major advantage in terms of efficient use of topside space and reduction of parasitic radiators over the old methods. An entire, very large superstructure is made into a broadband discage hf antenna on which almost all antennas such as those for radar and ECM functions can be mounted in a concentric or colinear manner. This eliminates much of the antenna blockage which occurs on present ships due to the presence of masts, platforms and equipment.

ALTERNATIVES

The conducting surfaces can be formed of solid sheet, welded pipe, or wires spaced at suitable intervals depending on mechanical requirements. The dimensions shown in figure (1) are not all necessarily critical. They can be changed on an experimental basis to provide the desired impedance characteristics in the desired frequency range. The more critically determined dimensions in figure 1 are the dimensions of the shunt stub (e), the shaft (c), and the 45° angles shown chosen for a 50-ohm characteristic impedance. The diameter of the disc (f) and the overall height of

the structure have minimums determined by the desired low frequency response. The shape is not critical--the structures can be either rectangular, pyramidal or cylindrical-conical, the cylindrical-conical shape being optimum for all-round symmetry. Equipment such as conformal arrays can be installed external to the conducting surfaces indicated, limited only by the tolerance for discontinuities resulting in impedance perturbations. If desired, the structure can also be supported by insulated guy wires.

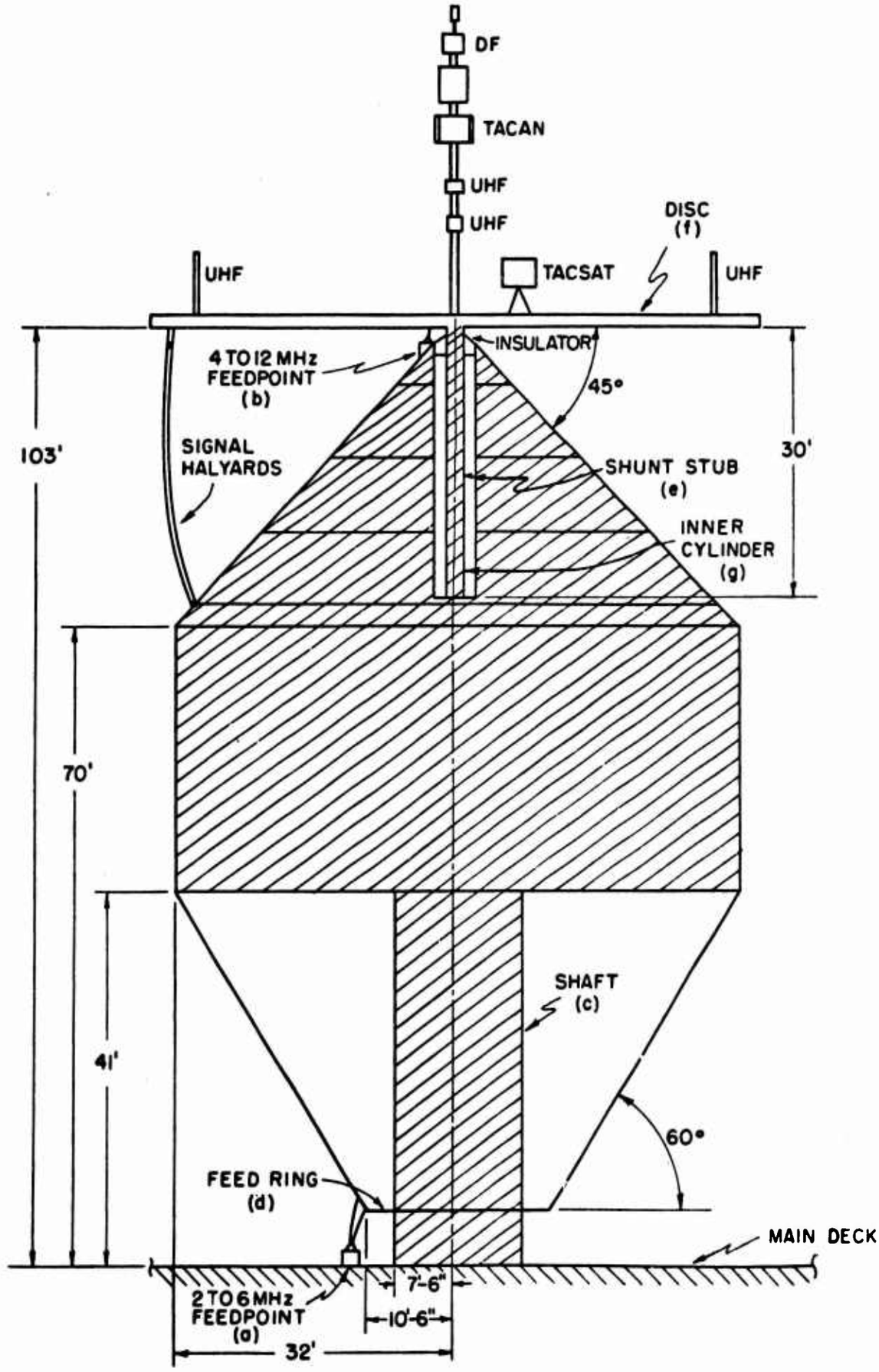

FIGURE 1. SUPERSTRUCTURE BROADBAND DISCAGE ANTENNA

IMPEDANCE DIAGRAM (SMITH)
I IND-NEL-3900/8 (REV 10-65)

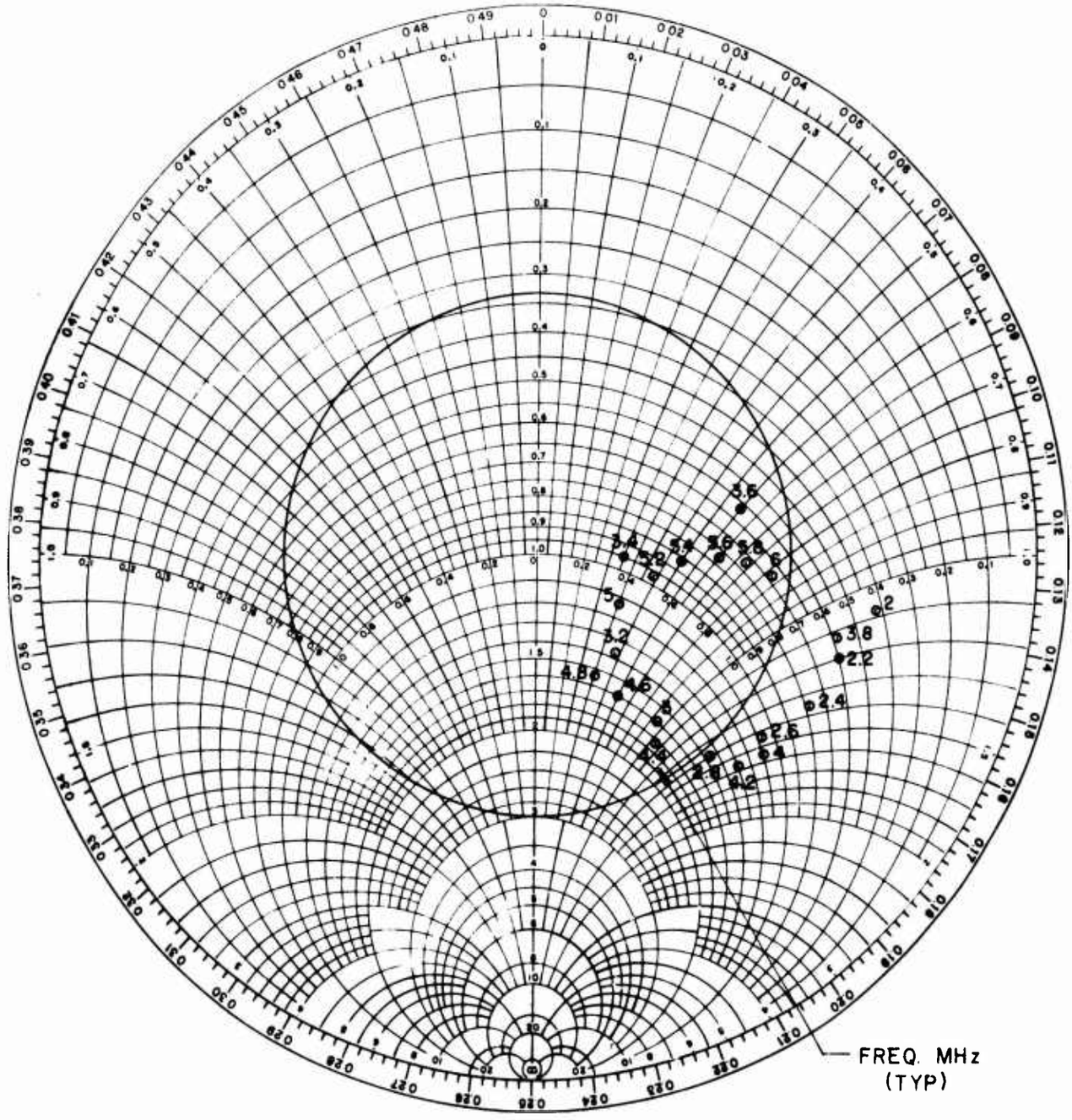

FIGURE 2. SUPERSTRUCTURE BROADBAND DISCAGE ANTENNA CAGE PORTION 2-6Mc FEEDPOINT IMPEDANCE

IMPEDANCE DIAGRAM (SMITH)

IND-NEL-3900/6 (REV 10-65)

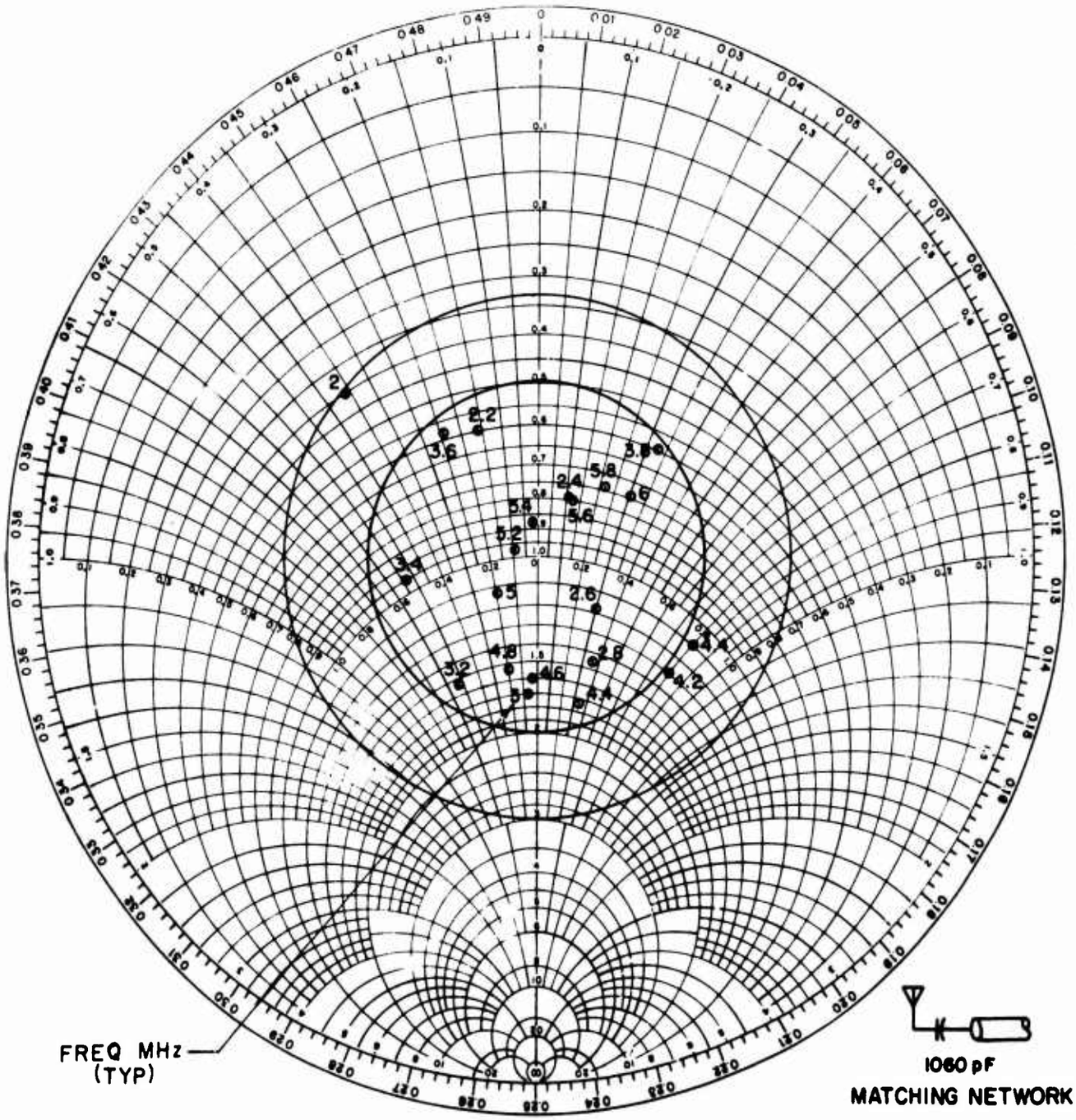

FIGURE 3. SUPERSTRUCTURE BROADBAND DISCAGE ANTENNA CAGE
PORTION 2-6Mc MATCHED IMPEDANCE

IMPEDANCE DIAGRAM (SMITH)
I IND-NEL-3900/8 (REV 10-65)

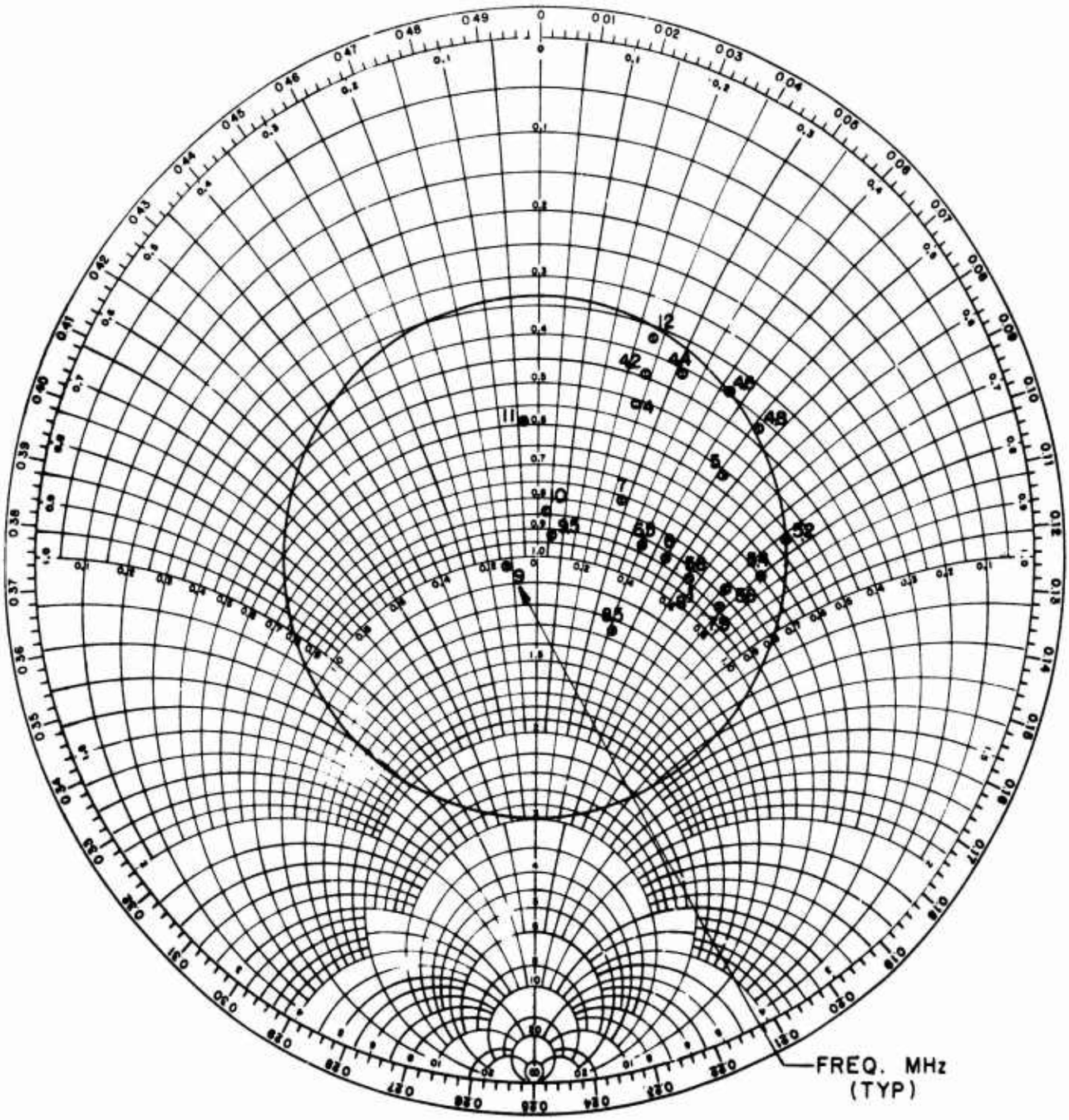

FIGURE 4. SUPERSTRUCTURE BROADBAND DISCAGE ANTENNA DISCONE PORTION 4 - 12Mc FEEDPOINT IMPEDANCE

IMPEDANCE DIAGRAM (SMITH)
LIND-NEL-3900 6 (REV 10-65)

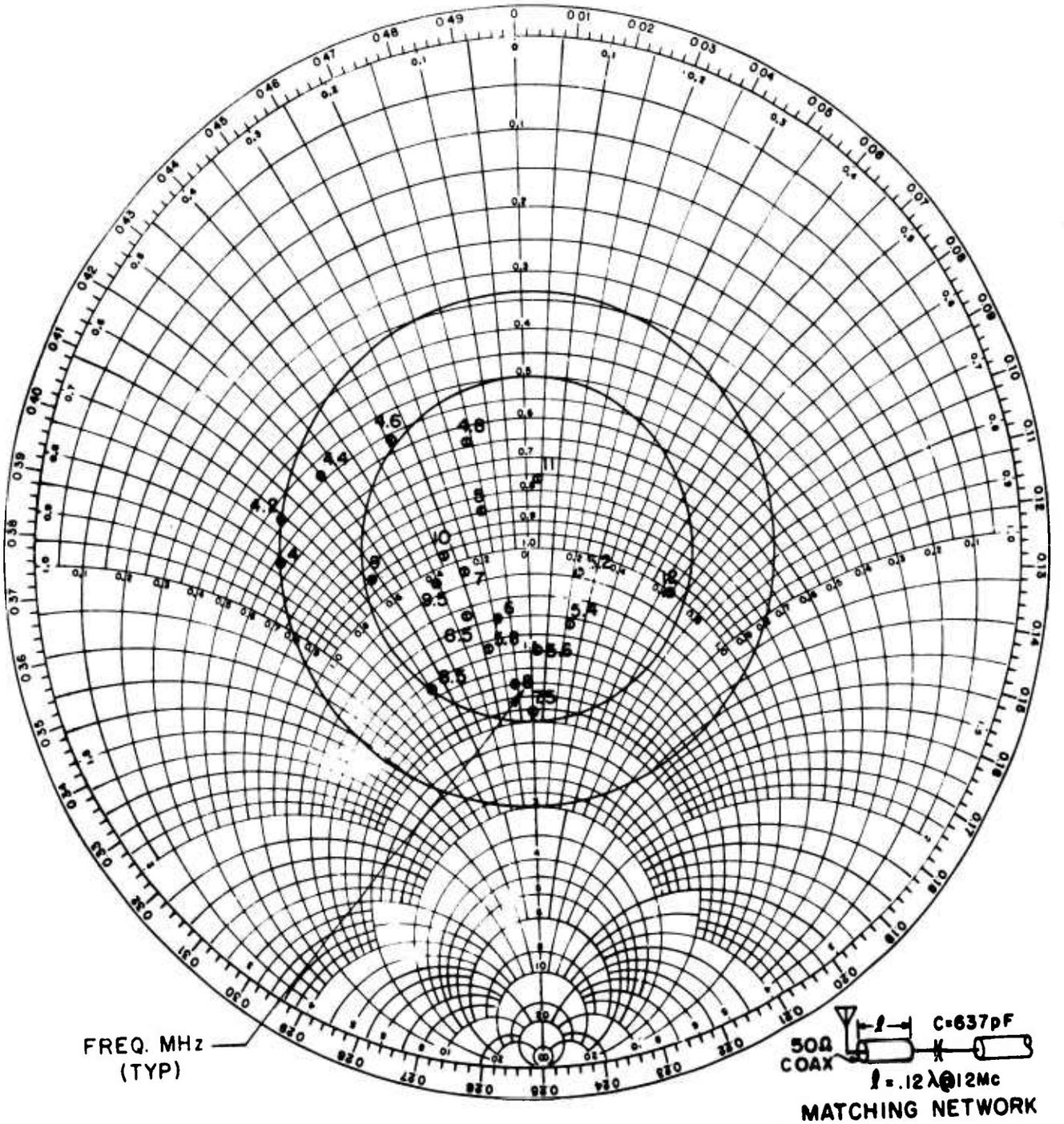

FIGURE 5. SUPERSTRUCTURE BROADBAND DISCAGE ANTENNA DISCONE PORTION 4-12Mc MATCHED IMPEDANCE

DUAL CIRCULARLY POLARIZED MODULAR ARRAY ANTENNA FOR TACSAT COMMUNICATIONS

AUTHORS:

C.A. BRAMBLE - USASCA

E.J. PERROTTI - ITT DEFENSE COMMUNICATIONS DIV.

J. RANGHELLI - ITT DEFENSE COMMUNICATIONS DIV.

FORWARD

The work described in this paper was performed under Contract No. DAAB07-68-C-0018 awarded by Department of the Army, United States Army Electronics Command, Fort Monmouth, New Jersey.

1. Introduction

This paper describes the feasibility models of an Alert Receiver Antenna and a Basic Module Antenna, which were fabricated by utilizing four of the Alert Receiver Antenna configurations. These models are the result of a study and development effort for advanced Tactical Satellite Communications that involve transportable terminals consisting of team pack and vehicular mounted configurations. Emphasis has been placed upon weight, size, efficiency and a modular concept that will allow expansion to larger antenna size through the use of additional modules.

2. Antenna Description

The modular array antenna described is required to operate with TACSAT. As such, its overall operational requirements are as follows:

1. To provide simultaneous transmit, receive and tracking functions in two planes.
2. Operational frequency range 7.2 to 8.4 GHZ.
3. Polarization - right hand circular in the transmit band left hand circular in the receive band.
4. Maximum power - 250 watts CW.

The mechanical considerations included:

1. Aperture modular construction to aid logistics, repair, and contingency modes of operation.
2. Minimum aperture depth.
3. Light weight, low cost construction.
4. Method of connection to be compatible with future integration with transmitter and receiver to be rear mounted.

These requirements were met with the planar array design described herein.

The array is composed of 1000 crossed dipole elements positioned above ground planes. The elements are contained in a two by two matrix of identical modules which are interconnected by waveguide circuitry. The circuitry located at the rear of the modules serves to locate the modules while providing the required transmit, receive, and tracking functions.

An extremely flat, minimum weight, rugged module design was achieved by employing a novel construction technique using printed circuits. These circuits have the further advantages of repeatability and low cost in volume production.

Module Array

The modules which comprise the full array are complete antennas in themselves. A single module is capable of simultaneous transmit and receive operation by virtue of the mechanism which affords the dual circular polarization. Each module is a 250 element square, planar array with a uniformly illuminated aperture. The construction of the module features a novel arrangement of 2 linearly polarized printed circuit arrays including their corporate feeds in a layered structure, fed by a hybrid for circular polarization. The resulting package has an aperture of 15 by 15 inches, an overall depth including waveguide flanges of 2.5 inches, and a weight of 3.5 pounds. It is estimated that by use of a printed circuit hybrid and molded plastic case, the depth will be 1.75 inches and the weight 1.5 pounds. Figure 1 shows a complete module antenna.

The electrical circuitry features two linearly polarized arrays oriented in space with their respective polarizations in quadrature. The arrays are driven with a 90° type hybrid to simultaneously generate left and right circular polarization. The basic antenna element used in the array is a printed dipole backed by a ground plane for unidirectional radiation. All the dipoles of one polarization are excited from a two wire balanced transmission line corporate feed. This corporate feed is connected to a hybrid port via a balun structure. The corporate feed uses binary power division and equal path length to achieve uniform dipole excition. Both the dipole array and corporate feed are printed in the aperture plane thereby realizing a very flat structure. The electrical performance of a single linearly polarized array included 28 db gain at mid band and maximum first sidelobes of 11.5 db below the peak of the main lobe. A typical pattern of a linearly polarized array is shown in Figure 2a. Figure 2b shows a comparable pattern for a circularly polarized module formed from two of the linearly polarized arrays.

The measured performance of the circularly polarized module is as follows:

mid band gain	28 db
first side lobe	11 db down from main lobe
polarization isolation	20 db
VSWR	1.55:1
axial ratio	< 3.1 db

In addition to these characteristics, tests showed that continuous power of 250 watts(CW) can be radiated. Destruction tests indicate even higher powers are possible by a redesign of the impedance levels of the corporate feed branches.

4. Four Module Array

The largest aperture tested utilizes 4 modules in a 2 by 2 matrix array. The modules are driven by waveguide circuitry designed to give uniform aperture illumination and symultaneous transmit, receive, and autotrack functions. Figure 3 shows the complete 4 module array. The antenna face dimensions are approximately 30 by 30 inches and the depth to the outermost flange of the waveguide network is approximately 9 inches.

The four module design used a total of 1000 elements arrayed in a square planar aperture. The array elements are driven with uniform illumination. The feed circuitry provides right hand circular polarization for transmit and left hand for receive, also provided are functions for simultaneous transmit, receive and 2 axis tracking.

The electric circuitry to develop the required aperture excitation and input-output functions is shown schematically in Figure 4a. The four identical module antennas are treated as terminations for the system via their respective transmit and receive ports. Module transmit inputs of equal amplitude and phase were developed by a two step binary power division of the system input carried to the modules by equal length transmission paths. Rectangular waveguide was used with Magic Tee hybrids for power division. The module receive signals were carried through equal length waveguide paths to a microwave comparator circuit.

In the comparator, 3 Magic Tee hybrids and a power summing Tee combine the 4 module receive signals to produce a sum output, an azimuth difference output, and an elevation difference output. As depicted in Figure 4a, the comparator network achieves a uniform illumination for the sum output and a bi-polar illumination for each of the difference outputs.

The modular antenna performance was measured over the full SHF communications band. The performance characteristics included a mid-band gain of 33 db and maximum sidelobes of 10 db below the main lobe. The receive difference pattern null depths were greater than 30 db while the maxima were 3 db below the peak of the main lobe of the receive sum pattern. Typical sum and difference patterns are presented in Figure 4b. In addition, both axial ratio and VSWR were measured across the transmit and receive bands. The axial ratio was no greater than 3.2 db across the transmit and receive bands. The VSWR was less than 1.6 to 1 across both bands.

At present it is estimated that 1 KW CW can be radiated by the modular antenna in its present form. This estimate is based on the power tests performed on a module as previously mentioned.

A final indication of performance was successful voice communication tests utilizing the TAC-SAT satellite. This included side-by-side comparison tests with a 3 foot parabolic antenna. The results showed the modular antenna performance to be equal to or better than the paraboloid despite the 10 percent larger aperture area of the paraboloid.

Conclusions

The feasibility of a modular, highly mobile SHF antenna has been demonstrated. By utilizing printed circuit techniques, a light weight antenna with a superior form factor has been built and tested successfully. The technique has great potential for military tactical communication systems.

Emmanuel J. Perrotti

Present Position: Section Head, Advanced Development
ITT Defense Communication Division

Mr. Perrotti is responsible for the development of advanced antenna systems and microwave networks. This responsibility includes the development of multifunction descrete and continuous apertures utilized in communications systems. Prime consideration in such systems lies not only in maximizing gain but also to minimize antenna noise temperature.

Prior to joining ITT, Mr. Perrotti was engaged in radar antenna work at the Westinghouse Surface Division in Baltimore, Maryland.

Mr. Perrotti received a BME from the City College of New York in 1958 and a BSEE from Johns Hopkins University in 1962. He also served as a second lieutenant with the U. S. Army Corps of Engineers.

Joseph Ranghelli

Present Position: Senior Member, Tech 'cal Staff

Experience:
Mr. Ranghelli is currently doing work on advanced antenna systems including array and continuous aperture antennas and their associated microwave components.

Prior to employment at ITT, Mr. Ranghelli was employed with Bogart Manufacturing, PRD Electronics, and Blass Antenna Electronics, all in the capacity of microwave development engineer.

Education:

Mr. Ranghelli received his BEE and MEE Degrees from the Polytechnic Institute of Brooklyn.

Military Experience:
Mr. Ranghelli served in the U. S. Army Signal Corp for two years during which time he attained the rank of Second Lieutenant.

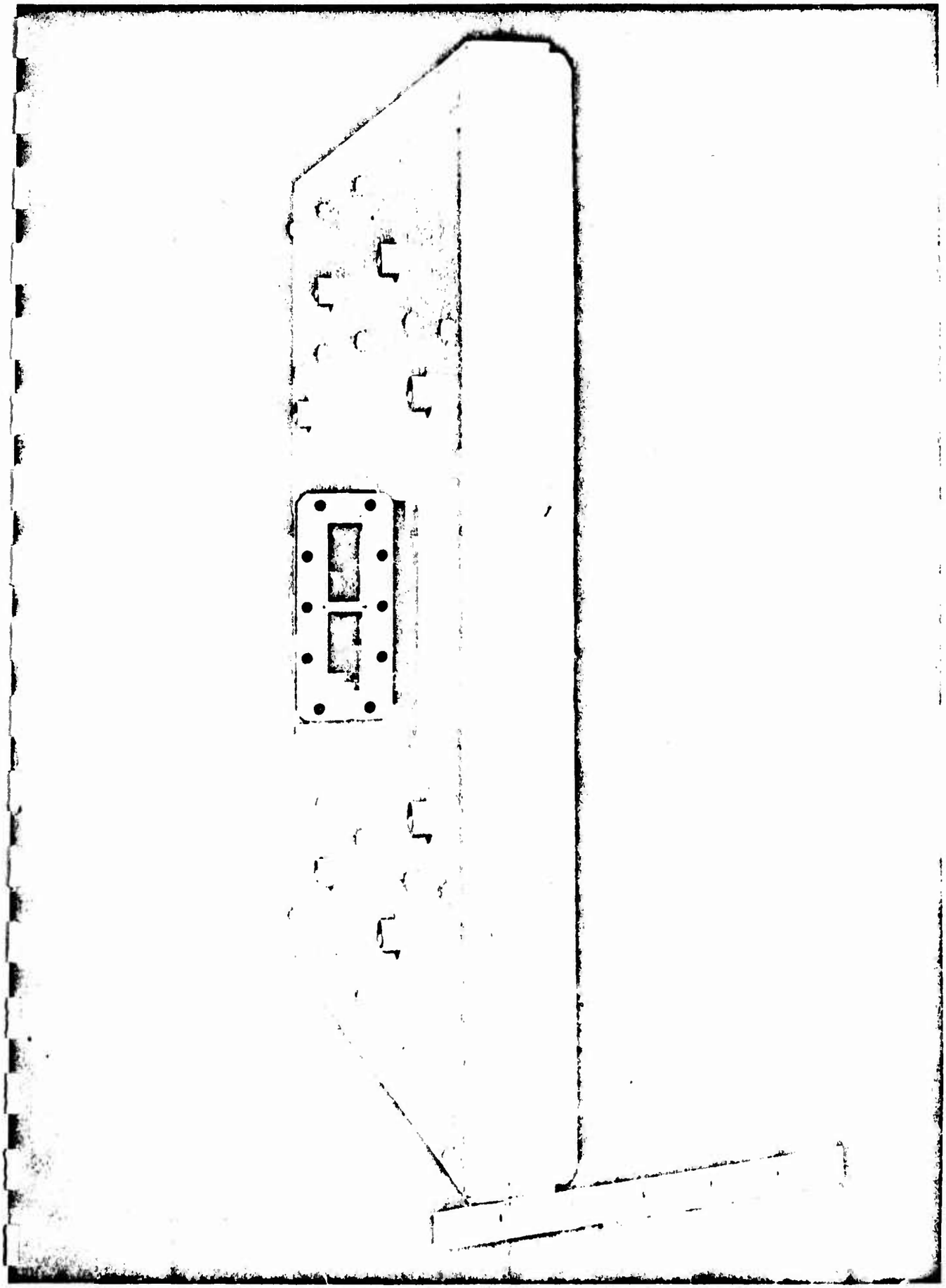

FIGURE 1 ALERT RECEIVE ANTENNA

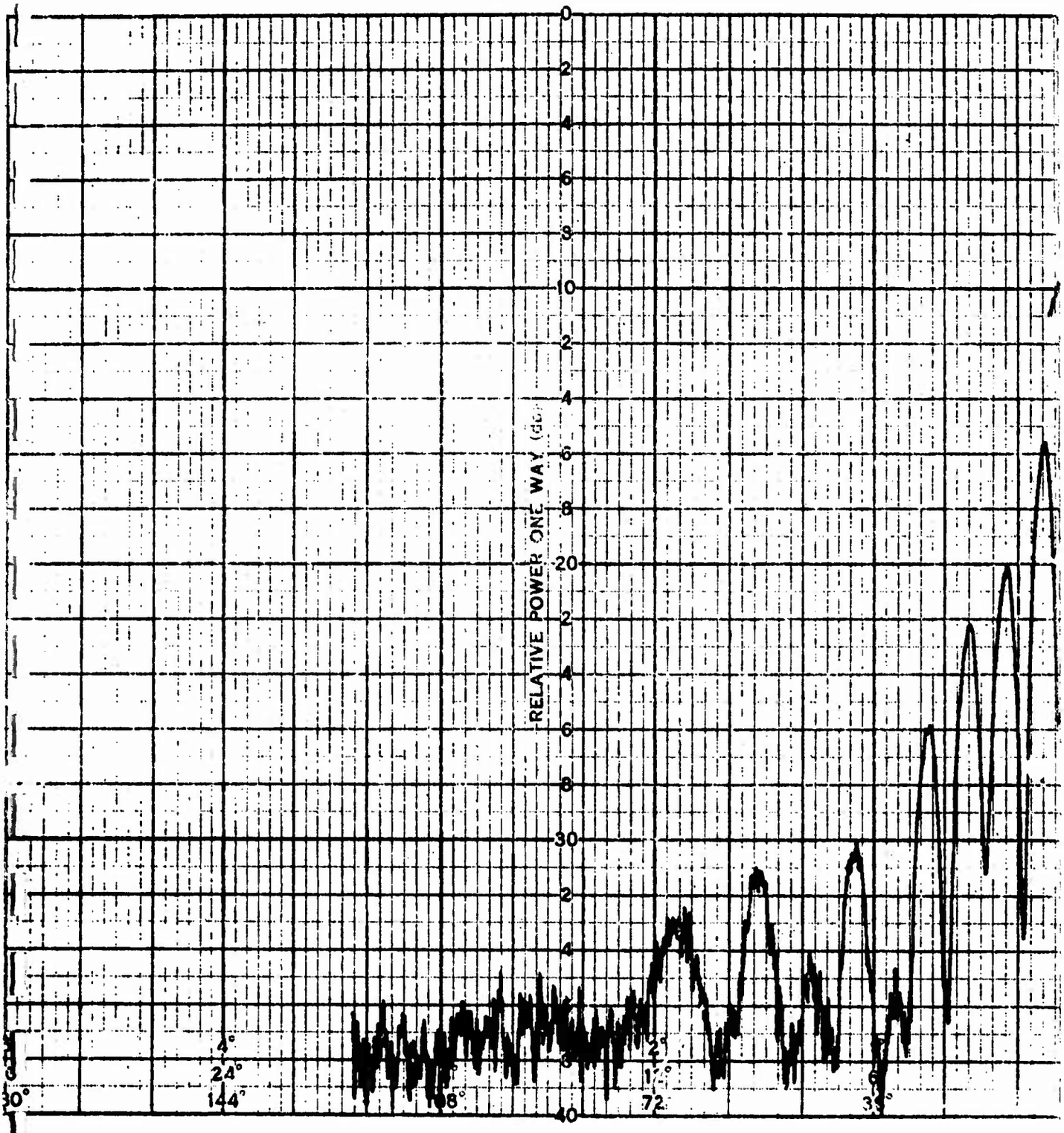

FIG.2A LINEARLY POLARIZED MA

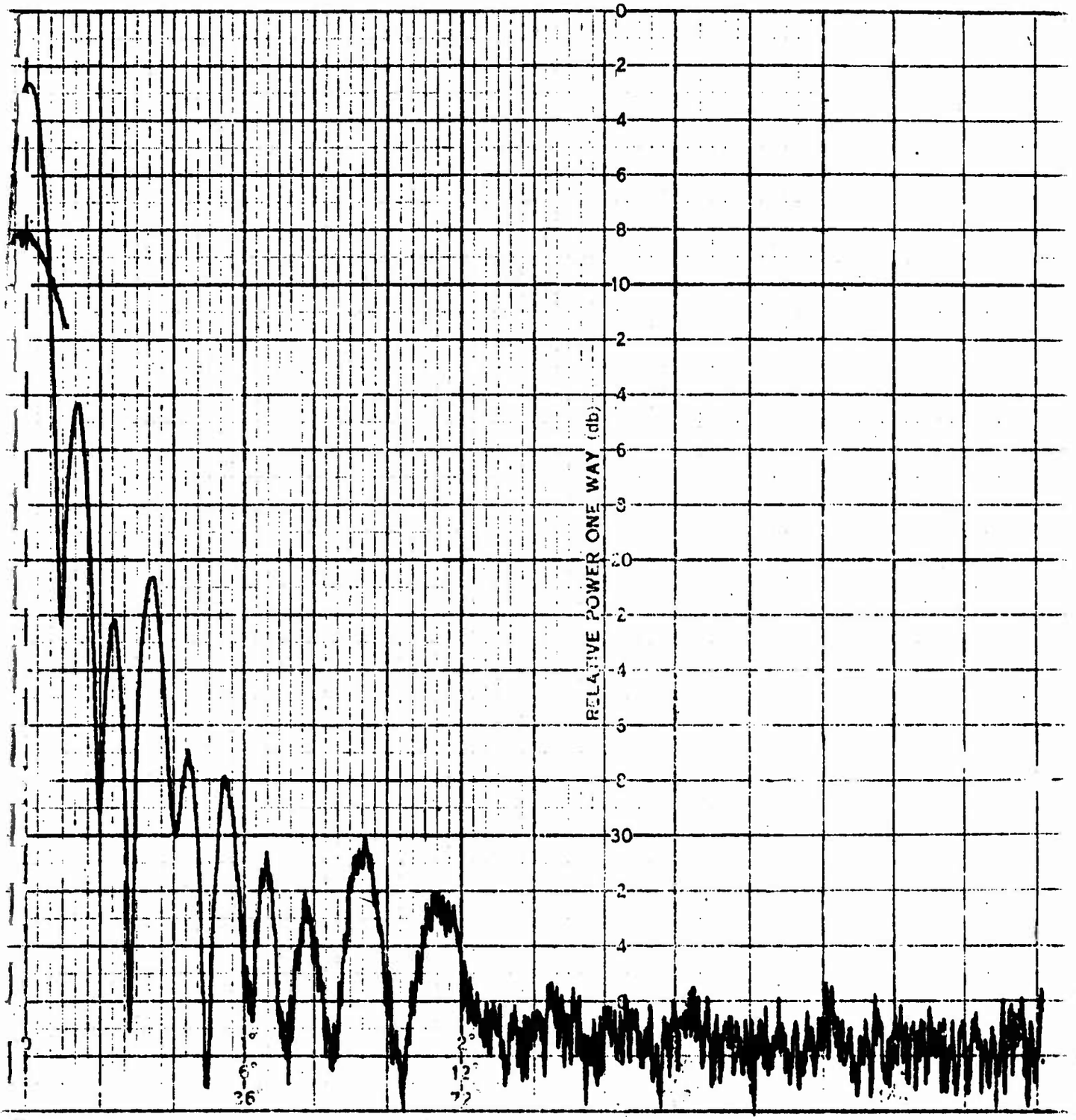

STRIP ARRAY AFTER SPURIOUS LOBE SUPPRESSION

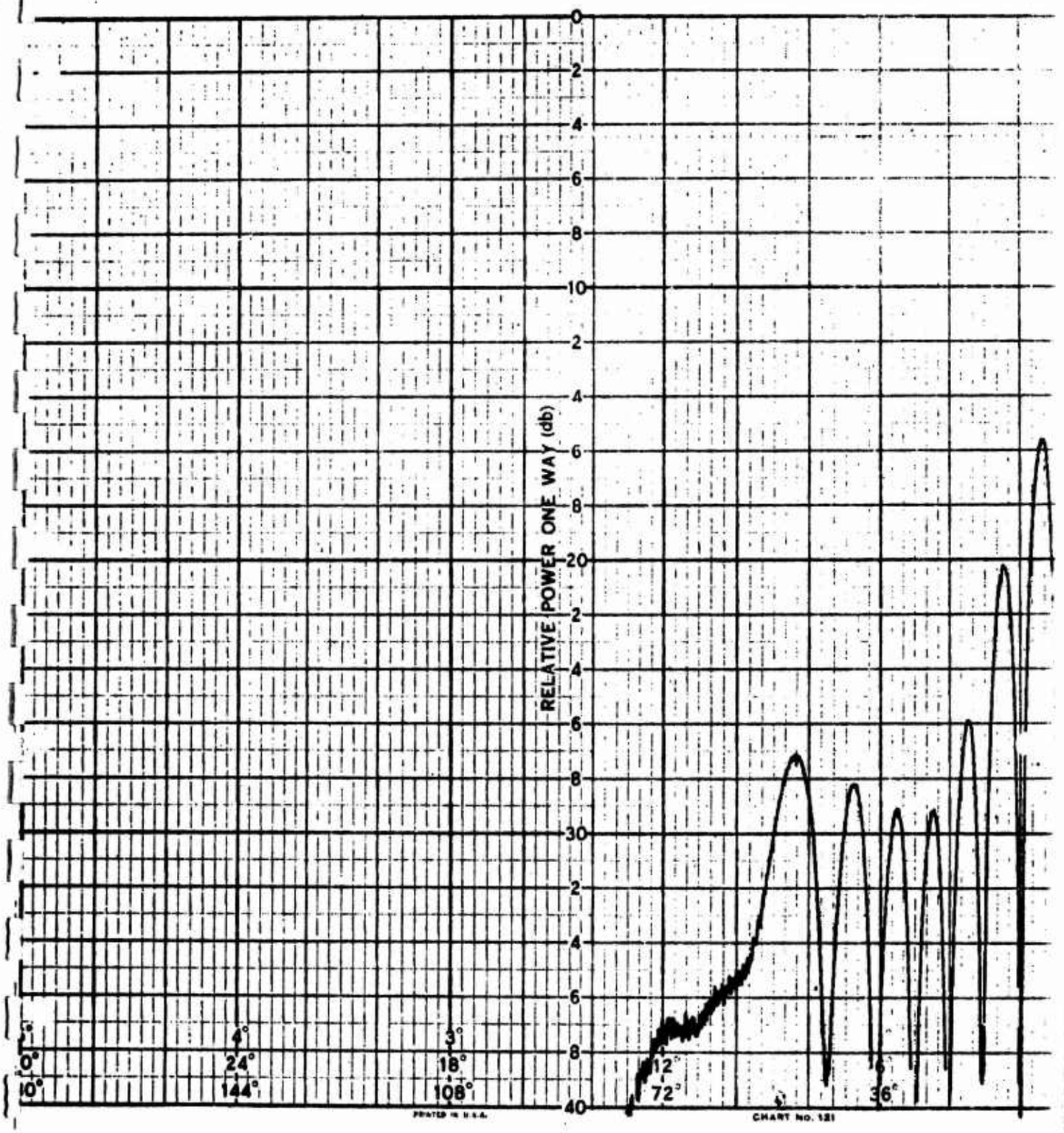
RELATIVE POWER ONE WAY (db)
0
2
4
6
8
10
2
4
6
8
20
2
4
6
8
30
2
4
6
8
40
0°
10°
6°
24°
144°
3°
18°
108°
12°
72°
36°
PRINTED IN U.S.A.
CHART No. 121

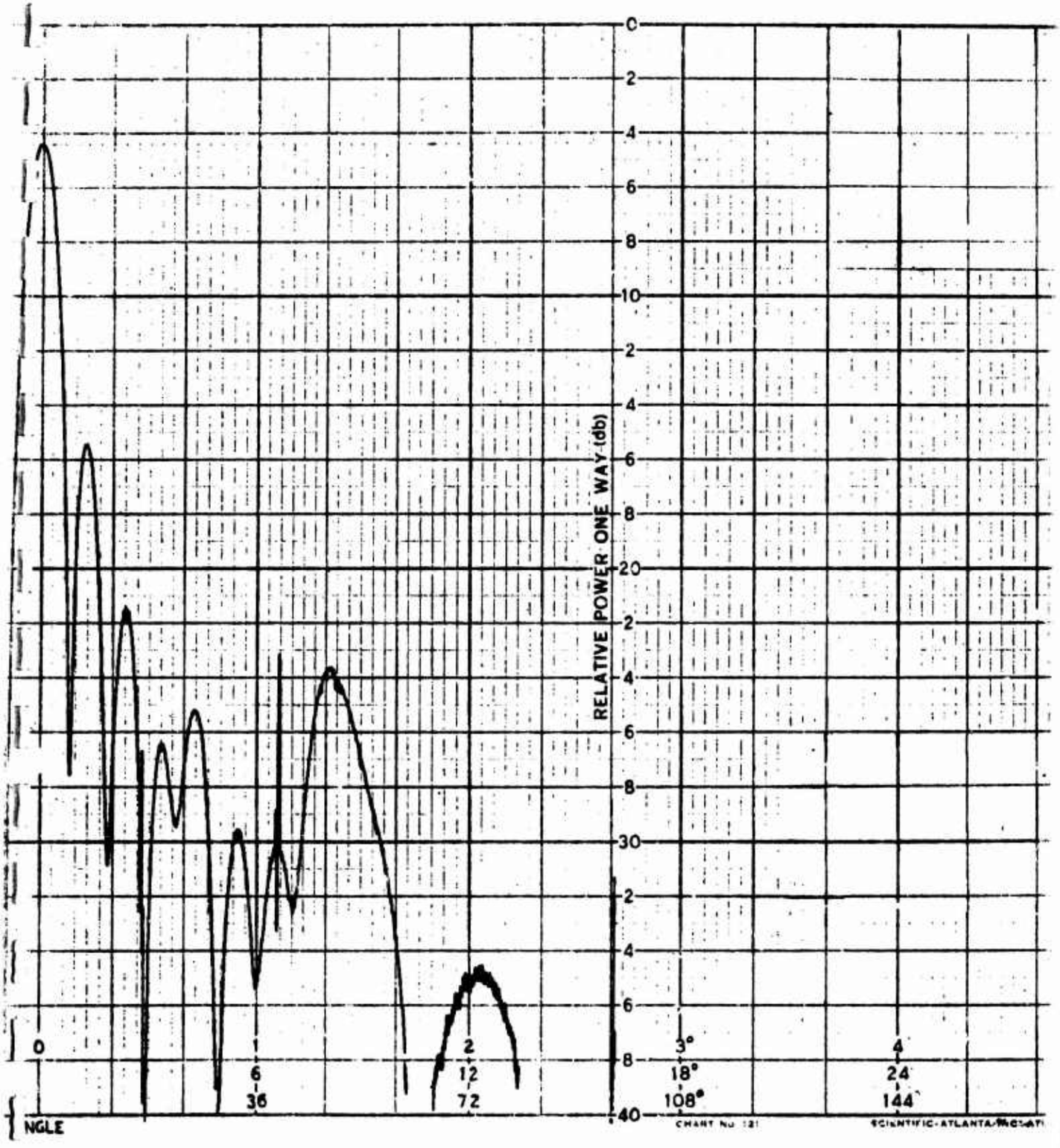

FIG. 2B SUB-MODULES ,CIRCULAR POLARIZATION ARRAY

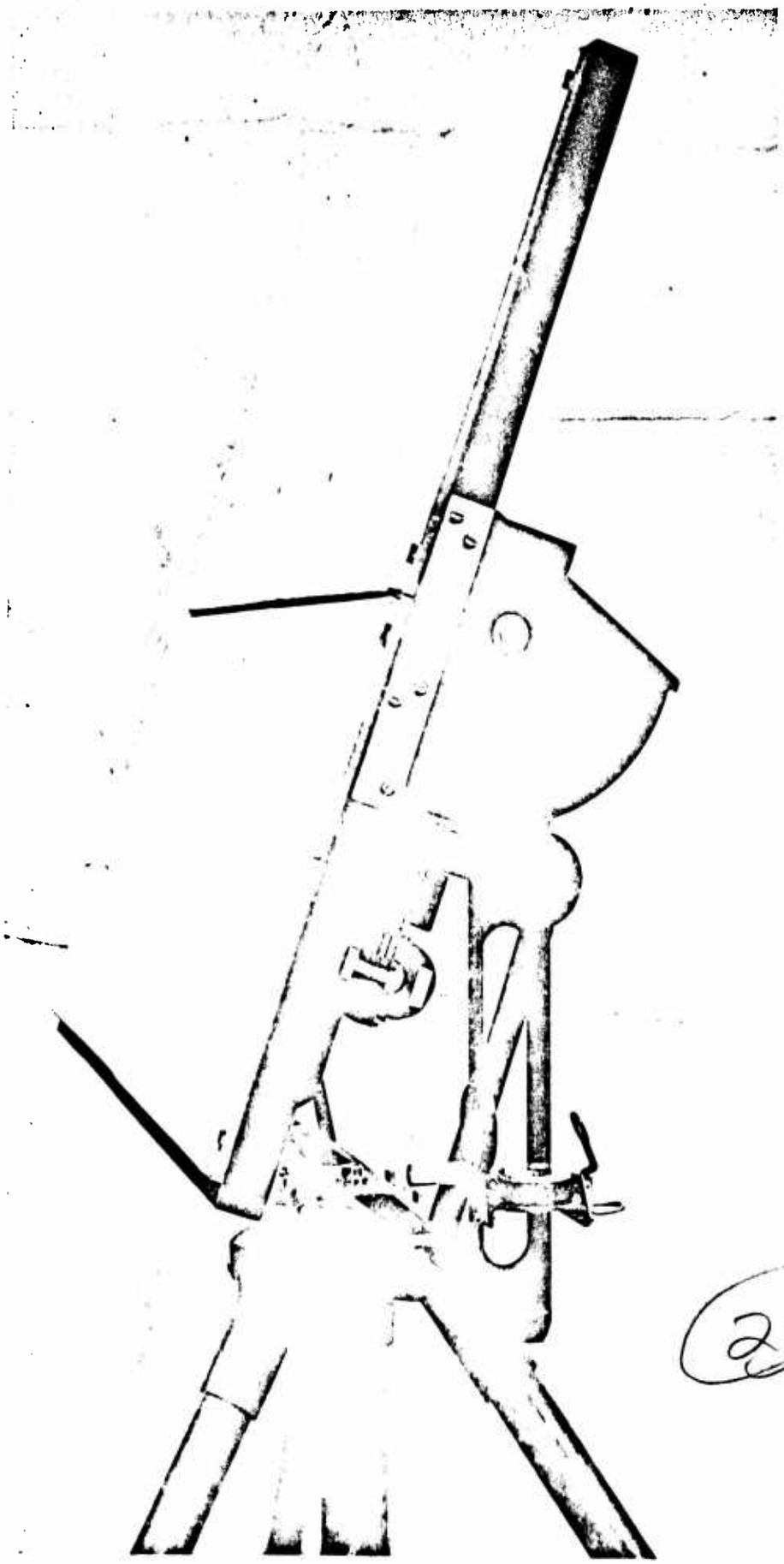

24

FIGURE 3 BASIC MODULE ANTENNA

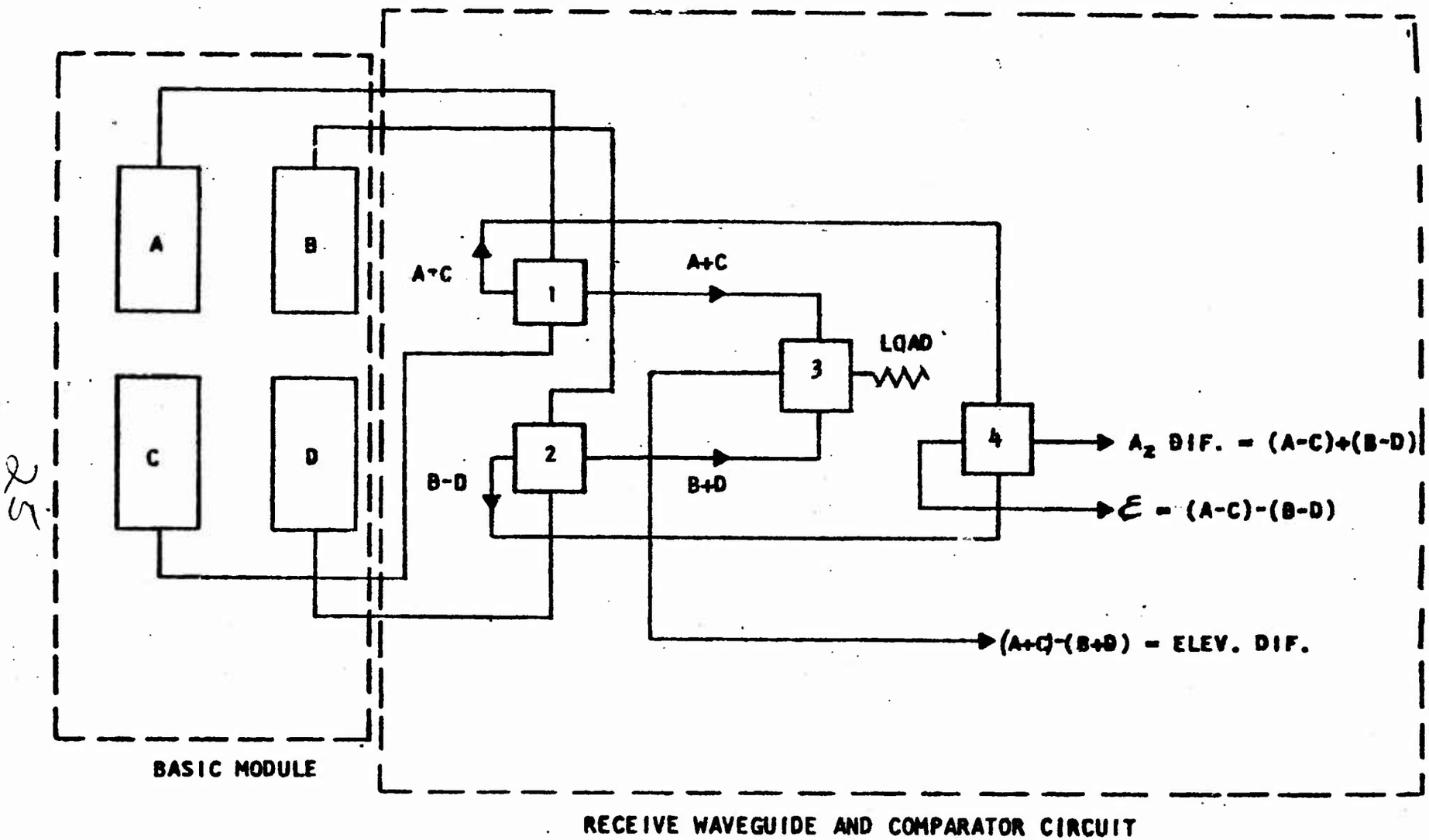

FIGURE 4a SCHEMATIC OF RECEIVE NETWORK

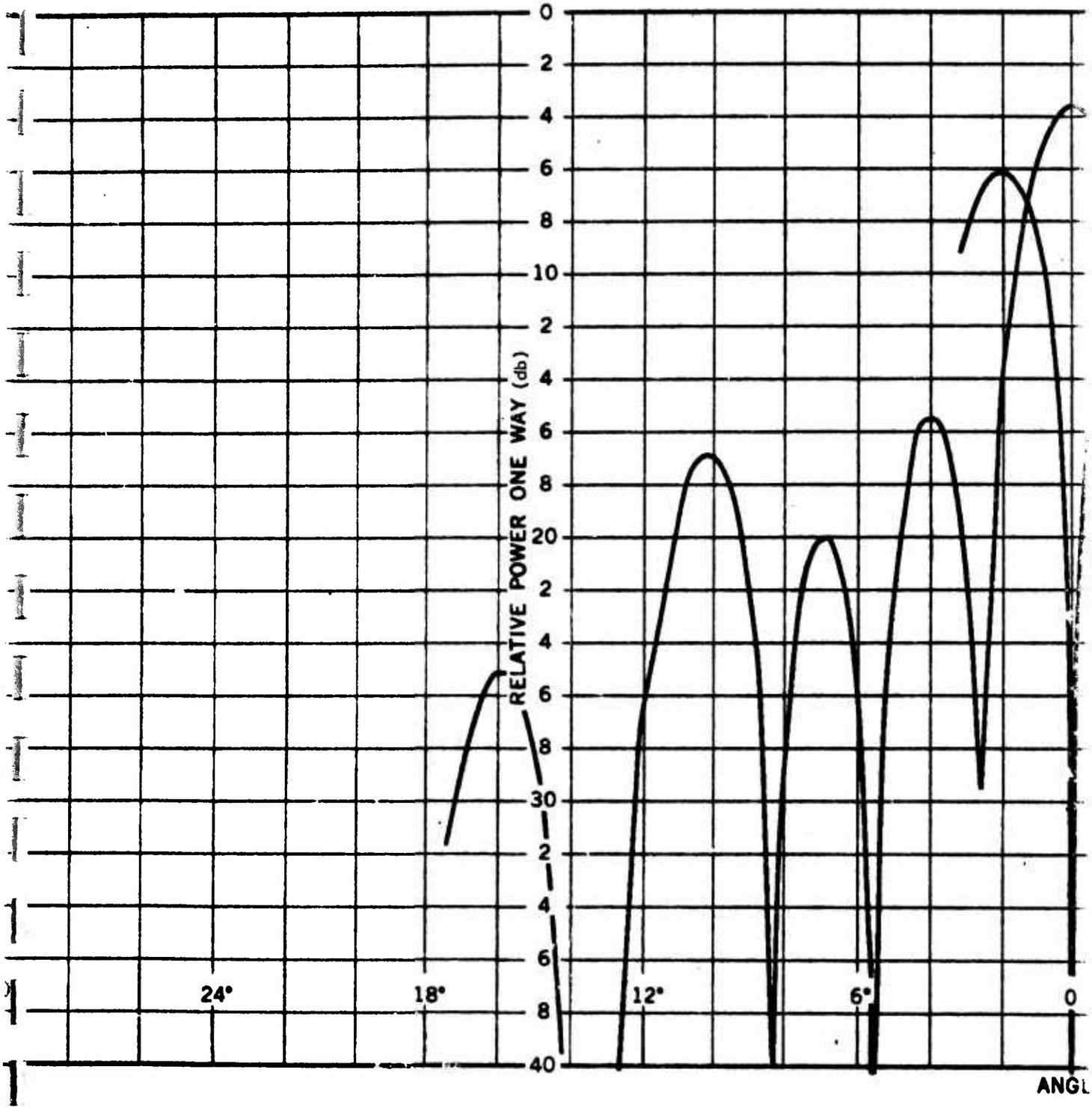
0
2
4
6
8
10
2
4
6
8
20
2
4
6
8
30
2
4
6
8
40
RELATIVE POWER ONE WAY (db)
24°
18°
12°
6°
0
ANGL

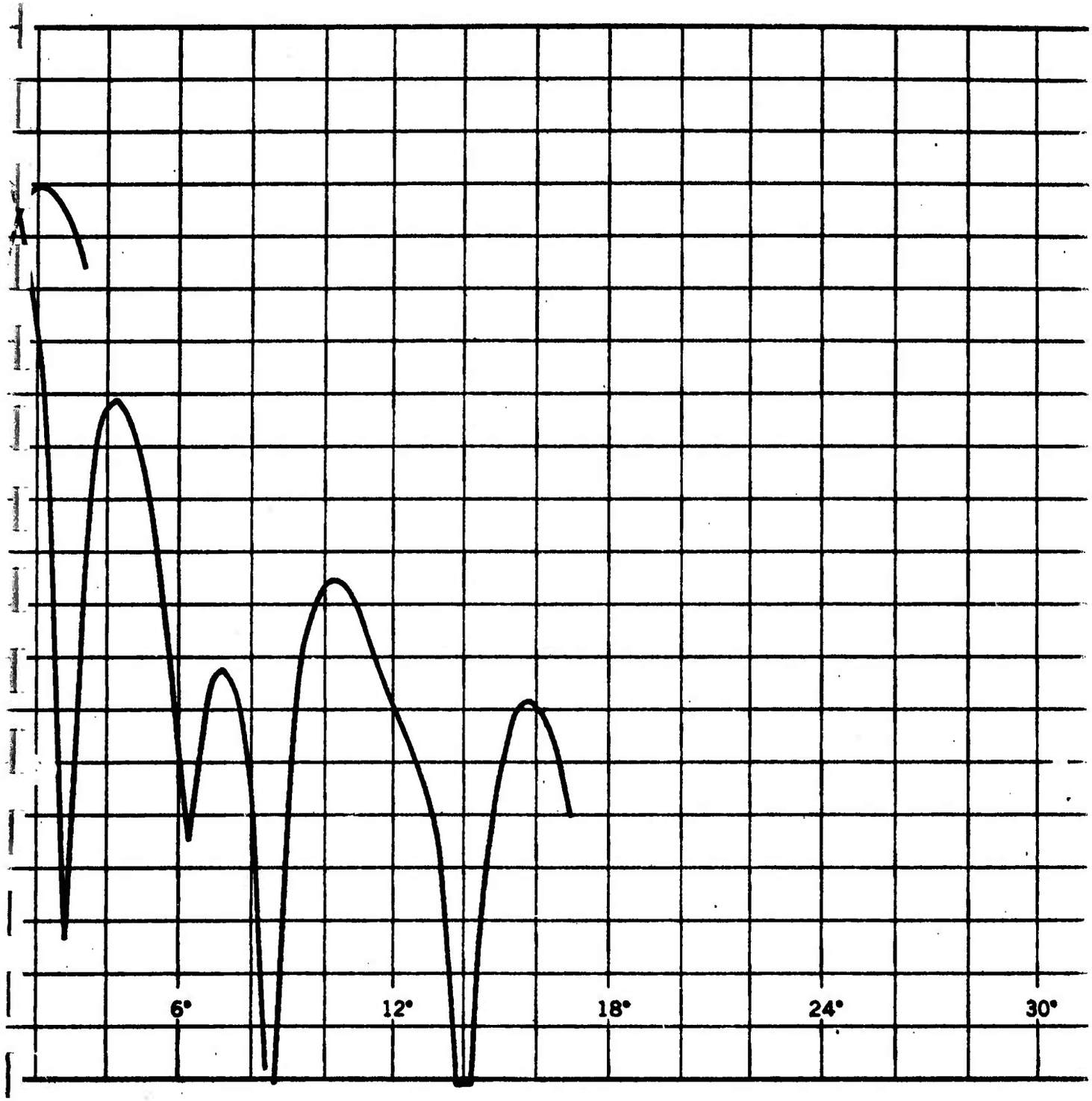

G 4B BASIC MODULE ARRAY TYPICAL DIFFERENCE PATTERNS

END